

DISSERTATION

Silicon Sensor Development for the CMS Tracker Upgrade

Ausgeführt zum Zwecke der Erlangung des akademischen Grades eines Doktors
der technischen Wissenschaften unter der Leitung von

Univ.-Doz. DI Dr. Manfred Krammer

E141

Institut für Hochenergiephysik der OeAW / Atominstitut

eingereicht an der Technischen Universität Wien

Fakultät für Physik

von

DI GEORG AUZINGER

0326064

Franz Arnbergerweg 9

3500 KREMS

Wien, am 21. Oktober 2013

PhD Thesis

Silicon Sensor Development for the CMS Tracker Upgrade

Georg Auzinger*

October 21st, 2013

*georg.auzinger@cern.ch

For my parents Susanne and Josef Auzinger

Abstract

The Large Hadron Collider at the European Council for Nuclear Research in Geneva is scheduled to undergo a major luminosity upgrade after its lifetime of ten years of operation around the year 2020, to maximize its scientific discovery potential. The total integrated luminosity will be increased by a factor of ten, which will dramatically change the conditions under which the four large detectors at the LHC will have to operate.

The Compact Muon Solenoid, which has contributed to the recent discovery of the Higgs boson, is one of them. Its innermost part – the so-called tracker – is a high-precision instrument that measures the created particles' trajectories by means of silicon detectors. With a total surface of more than 200 square meters it is the largest device of its kind ever built.

The increase in instantaneous luminosity in the upgraded LHC will lead to a dramatically increased track density at the interaction points of the colliding beams and thus also to a much more hostile radiation environment. As a consequence, the tracker of CMS will require a major upgrade and redesign of the sensors and read-out electronics, as the components installed at present do not have sufficient granularity and radiation tolerance.

An extensive research- and development campaign has therefore been started by the CMS collaboration to identify and assess suitable radiation-hard silicon substrates and sensor technologies that could be implemented in the future tracker.

This thesis, carried out at CERN and the Vienna University of Technology, will present aspects of this campaign, especially the investigation of a prototype structure called Multi-Geometry Silicon-Strip Detector or MSSD in laboratory measurements and tests with accelerator beams. It has been designed to identify materials and strip geometries that will meet the stringent requirements for sensors in the outer part of the upgraded CMS tracker.

After a brief introduction to the CMS experiment and silicon sensors in high-energy physics, the specific experimental setups and facilities that have been used during the research for this thesis will be described. The obtained results have been extensively analyzed, interpreted and compared to earlier work with the goal of submitting a recommendation for a suitable material and technology.

Zusammenfassung

Der Large Hadron Collider am Europäischen Zentrum für Kernforschung in Genf soll nach seiner geplanten Lebensdauer von zehn Jahren um das Jahr 2020 aufgerüstet werden, um dessen wissenschaftliches Entdeckungspotenzial voll ausschöpfen zu können. Die integrierte Luminosität, also die Gesamtmenge an aufgezeichneten Daten, soll dabei um den Faktor zehn vergrößert werden, was sich auch auf die vier grossen Detektoren auswirken wird.

Das CMS¹ Experiment ist eines dieser vier grossen Experimente, das zur kürzlichen Entdeckung des Higgs Bosons beigetragen hat. Der innerste Teil des Detektors – der sogenannte Spurdetektor oder Tracker – ist ein hochpräzises Instrument, das die Teilchenbahnen misst. Er besteht aus Silizium-Pixel- und -Streifensensoren mit einer Gesamtfläche von über 200 Quadratmetern, womit er das größte derartige Instrument ist, das jemals gebaut wurde.

Die Luminosität im zukünftigen Höchststraten-LHC führt zu einer signifikant größeren Spur- und Teilchendichte in der nächsten Umgebung des Kollisionspunktes und dadurch auch zu einem dramatisch erhöhten Strahlungsfeld. Deshalb muss der CMS Spurdetektor ebenfalls überarbeitet und teilweise neu entworfen werden, da die derzeit verwendeten Komponenten den Ansprüchen an Segmentierung und Strahlenhärte nicht gerecht werden.

Die CMS Kollaboration hat aus diesem Grund eine großangelegte Kampagne gestartet, um strahlenharte Siliziummaterialien und -technologien zu untersuchen, die im zukünftigen Experiment Verwendung finden könnten.

Diese Dissertation – ausgeführt am CERN und der Technischen Universität Wien – behandelt einige Aspekte dieser Kampagne: Konkret befasst sie sich mit der Untersuchung und Qualifizierung eines Prototyp-Sensors mit dem Namen 'Multi-Geometry Silicon-Strip Detector' (MSSD) in Labor- und Testbeam Messungen. Dieser wurde entworfen, um verschiedenste Streifen-Geometrien und Materialien zu testen, die den Ansprüchen an Sensoren im zukünftigen CMS Spurdetektor gerecht werden können.

Nach einer kurzen Einleitung und der Beschreibung des CMS Experiments, sowie von Siliziumsensoren in der Hochenergiephysik werden die speziellen Messapparaturen und Testbeam Einrichtungen beschrieben, die im Zuge dieser Dissertation verwendet wurden. Die gewonnen Resultate werden genau analysiert, interpretiert und mit bisherigen Arbeiten verglichen, mit dem Ziel, eine Empfehlung für geeignete Materialien und eine erfolgversprechende Technologie abgeben zu können.

¹Compact Muon Solenoid

Acknowledgements

I want to thank my supervisor at the Vienna University of Technology *Univ.-Doz. DI Dr. Manfred Krammer* for giving me the chance to write this dissertation under his guidance. He has been a very patient and encouraging advisor and has read this thesis in very limited time.

Furthermore, I acknowledge the contributions from my supervisor at CERN *Dr. Anna Elliott-Peisert*, who has patiently introduced me to the matter, has provided much appreciated help and advice on a day-to-day basis and has been a great support in the process of compiling this thesis from the work I have done.

Very special thanks go to my colleague, mentor and advisor *Dr. Stefano Mersi* for guiding me and teaching me the business of data analysis. This work has greatly profited from his invaluable experience and creative ideas, not only in extracting the relevant information from data but also in presenting it. Without his help I could not have written this thesis in the presented form.

Many friends and colleagues at CERN have made my time there an unforgettable experience, not only at work but also when exploring the peaks and faces of the French Alps.

My partner *Verena Kuhn* has been a great support and source of inspiration. She gave me comfort and strength when I needed it the most and has made the past three years the best time of my life.

Everything I have achieved, I owe to my parents *Susanne* and *Josef Auzinger*. From as early as I can think they have challenged and supported me and my interests. They have given me the opportunity to study and to pursue my interests with great freedom, which has enabled me to follow a career in a field I am passionate about. For that and everything else they have done for me I am grateful beyond words.

Statutory Declaration

I declare that I have authored this thesis independently, that I have not used any other resources than the declared ones, and that I have explicitly marked all material which has been quoted either literally or by content from the used sources.

Eidesstattliche Erklärung

Ich erkläre an Eides statt, dass ich die vorliegende Arbeit selbstständig verfasst, keine anderen als die angegebenen Quellen/Hilfsmittel benutzt, und die den verwendeten Quellen wörtlich und inhaltlich entnommenen Stellen als solche kenntlich gemacht habe.

Wien, 21. Oktober 2013

Signature / Unterschrift

Contents

1	The Large Hadron Collider	1
1.1	Physics Goals	1
1.2	Design Parameters and Technical Specifications	4
1.2.1	Design Parameters	5
1.2.2	Operational History and Achievements	6
1.3	The High-Luminosity Upgrade	7
2	The CMS Experiment	9
2.1	CMS Physics	9
2.1.1	Higgs Production and -Decay	9
2.1.2	Supersymmetric Searches	12
2.2	The Detector	14
2.2.1	The Tracker	15
2.2.2	The Electromagnetic Calorimeter	15
2.2.3	The Hadron Calorimeter	16
2.2.4	The Magnet	17
2.2.5	The Muon System	18
2.2.6	The Trigger	19
2.3	Results	19
2.4	The CMS Upgrades	21
2.4.1	The Phase-1 Upgrade	23
2.4.2	The Phase-2 Upgrade	23
3	The CMS Tracker	25
3.1	Description	26
3.1.1	The Pixel Tracker	26
3.1.2	The Silicon-Strip Tracker (SST)	28
3.2	Tracker Readout	33
3.3	Performance	35
3.4	The Tracker in the HL-LHC Scenario	38
4	Silicon Sensors in High-Energy Physics	43
4.1	Working Principle and Limitations	43
4.1.1	Silicon as a Semiconductor and the pn-Junction	43
4.1.2	Energy Loss – Signal Creation	46
4.1.3	Design of Position-Sensitive Devices	48
4.1.4	Parameters	50

4.2	Radiation Damage	52
4.2.1	Bulk Damage – Microscopic and Macroscopic Consequences	52
4.2.2	Surface Damage	56
4.2.3	Annealing	56
4.3	Radiation-Hard Sensor Technology	57
4.3.1	p-Type Silicon	58
4.3.2	Oxygen-Rich Silicon	59
5	The HPK Project	65
5.1	Motivation and Goals	65
5.2	Materials, Technologies and Structures	67
5.2.1	Strip Isolation on p-Type Sensors	68
5.2.2	Thin Materials	68
5.2.3	Wafer and Structures	70
5.3	Irradiation	72
5.4	The Multi-Geometry Silicon-Strip Detector	74
6	Electrical Qualification of the Multi-Geometry Silicon-Strip Detector	77
6.1	Measurements & Parameters	78
6.1.1	Measurements	78
6.1.2	Parametrization of Results	80
6.2	The Experimental Setup	85
6.2.1	Hardware	85
6.2.2	Control Software	86
6.2.3	Calibration	90
6.3	Results	91
6.3.1	Depletion Voltage	92
6.3.2	Total Strip Capacitance	98
7	Beam Tests	105
7.1	The Beam-Test Setup	105
7.1.1	The Silicon Beam Telescope	106
7.1.2	Test-Beam Facilities	109
7.2	The Analysis	109
7.2.1	Tracking with the EUTelescope Framework	110
7.2.2	MSSD Analysis	113
7.2.3	Parameters	121
7.3	Results	126
7.3.1	Data-Taking Conditions	127
7.3.2	Signal and Noise	129
7.3.3	Resolution and Efficiency	139
8	Simulation of Binary Clustering with the CBC	151
8.1	Binary Clustering Algorithms	151
8.2	Simulation of the CMS Binary Chip	153
8.3	Results	154

9	Selected Results from the Collaboration	161
9.1	Diodes and Material Properties	161
9.2	Other Aspects of Strip-Sensor Performance	162
9.3	Random Ghost Hits	163
10	Summary & Conclusions	165
10.1	Summary of the Presented Study	165
10.2	Conclusions from the Electrical Qualification	166
10.3	Conclusions from the Beam-Test Results	168
10.4	Implications for the Binary Readout	169
10.5	Recommendation	170
	Appendix: Detailed Results	173

1 The Large Hadron Collider

1.1 Physics Goals

Over the past decades the Standard Model (SM) of Elementary Particle Physics has been proven a powerful and reliable theory. It relies on gauge invariance and symmetries and has allowed physicists to make precise predictions of new particles that have been confirmed experimentally to stunning accuracy, such as the discovery of the Top quark at the Tevatron at Fermilab in 1994 and the vector bosons of the weak interaction (W^\pm & Z^0) at the SPS at CERN in 1983.

Up to this day there has been no experimental contradiction of the Standard Model and it is able to describe three out of four of nature's fundamental forces. These are the electromagnetic force, which can be unified with the weak force to the electroweak model, and the nuclear (or strong) force, which is described by quantum chromodynamics. The unification of the electroweak- and the strong force is predicted at a higher energy range than is accessible today. The combination of quantum mechanics and the laws of relativity yields the so-called quantum field theory, which describes the interaction of matter by the exchange of field quanta. According to this theory each fundamental interaction is based on one of nature's fundamental symmetries and couples to a field with its quanta being the bosons of the Standard Model.

However, the Standard Model relies on 19 free parameters and cannot explain the open questions physicists face today such as symmetry breaking, dark matter, matter-antimatter asymmetry or the mechanism by which the fundamental particles acquire their mass.

According to theory, the quanta of the weak interaction, the W^\pm and Z^0 bosons, should be massless and the range of the weak interaction should be infinite, but their mass has been measured at precisely $80.4 \text{ GeV}/c^2$ and $91.2 \text{ GeV}/c^2$ respectively, which yields a very short range. This contradicts the symmetry underlying the electroweak interaction and would require the breaking of the latter. To resolve this discrepancy the Brout-Englert-Higgs formalism has been introduced, which explains the particles' mass by their coupling to a scalar field – the Higgs field – and spontaneous symmetry breaking. As each field requires an exchange quantum an additional particle, the Higgs boson, must exist.

In order to produce new particles like the Higgs boson or supersymmetric particles experimentally, very powerful accelerators are needed as the predicted masses are very

large. The Large Hadron Collider (LHC) that was built at CERN¹ in Geneva was designed as a 'discovery machine' capable of hopefully producing these new particles. It is the collider with the highest center-of-mass energy in the world and has already produced a very promising result — the discovery of the Higgs boson with a mass of $\sim 125 \text{ GeV}/c^2$.

Higgs Physics

One of the main physics goals of the LHC is the production and discovery of the Higgs particle. Previous experiments at the Large Electron Positron Collider (LEP) at CERN, Tevatron at FNAL and theoretical considerations have restricted the possible mass range for a Higgs particle between $114 \text{ GeV}/c^2$ and $1 \text{ TeV}/c^2$.

In the Standard Model, at high enough energies the electromagnetic- and weak interaction can be unified to the electroweak model. In this energy range all elementary particles are massless. However, below a certain energy threshold the electroweak symmetry is spontaneously broken and the gauge bosons of the weak interaction become massive through the Higgs field, while the photon as the carrier of the electromagnetic force stays massless and thus the range infinite.

There are several extensions of the Standard Model introducing the Higgs field of which many are supersymmetric and thus many different Higgs particles are theoretically possible. Previous experiments have restricted the mass range for a light non-supersymmetric Standard Model Higgs to values between 115 to $130 \text{ GeV}/c^2$ and $180 \text{ GeV}/c^2$ [1].

The Minimal Standard Model (the simplest model introducing the Higgs field) does not predict a mass for the Higgs boson and if it is found to be between the values quoted above it might act as an indication that the model is valid up to the Planck scale (10^{19} GeV) or, if not, that a supersymmetric theory might be more favorable. However, a neutral Higgs boson at a mass of approximately $125 \text{ GeV}/c^2$ – just like the one discovered – is also compatible with supersymmetry.

Supersymmetry

Supersymmetry, or abbreviated SUSY, is a theory that describes a certain symmetry in particle physics. It basically relates every elementary particle with a super partner whose spin differs by $1/2$. This means that every fermion (constituents of matter) has a super partner that is a boson and every boson has a super partner that is a fermion.

The theory is motivated through its possible ability to solve several theoretical problems in physics but since super particles have not been observed experimentally up to this date, supersymmetry must be a broken symmetry, which would allow the super partners of all known particles to be considerably heavier than their Standard Model counterparts. However, the most favorable models work with super partners at a mass

¹Conseil Européen pour la Recherche Nucléaire / European Council for Nuclear Research

scale of around $1 \text{ TeV}/c^2$, which would allow the unification of the electroweak- and the strong interaction at very high energies.

The incorporation of supersymmetry into the Standard Model leads to the Minimal Supersymmetric Standard Model (MSSM), which knows exactly one super partner to every known particle. Many supersymmetric Standard Models also know a heavy neutral particle, the so-called neutralino, which is considered a promising candidate for the Weakly-Interacting Massive Particle (WIMP) and thus cold dark matter, which is required by cosmology.

However, recent results of the Large Hadron Collider Beauty experiment (LHCb) have dramatically restricted the parameter space in which supersymmetry is possible. The collaboration has observed a very rare B meson decay ($B_S^0 \rightarrow \mu\mu$) and measured the branching ratio in agreement with the Standard Model prediction [2].

This fact, the mass of the discovered Higgs-like particle and the absence of any hints of supersymmetric particles in the LHC data up to this date – indicate that supersymmetry might not be one of nature’s fundamental symmetries and some theorists think it should better be abandoned.

CP Violation

Many fundamental laws of physics can be attributed to the conservation of symmetries under certain transformations. The three fundamental symmetries in particle physics are:

- **Charge symmetry:** Each particle is exchanged with its antiparticle of opposing charge.
- **Parity symmetry:** The inversion of all three spatial coordinates of every particle. This is equivalent to an inversion of one coordinate and subsequent rotation of 180° around that particular axis. Everything appears as if reflected in a mirror.
- **Time symmetry:** On a microscopic scale all physical processes should be the same when the direction of time is reversed.

This basically means that our universe would be indistinguishable from one that was transformed under all three symmetries. Electromagnetic- and gravitational processes are invariant under these transformations but some weak interactions, such as the decay of K^0 discovered in 1964, were found to violate CP symmetry.

Theoretically matter and antimatter should have been produced in equal parts after the Big Bang, which would mean that they would have instantly annihilated again. But as a consequence of CP violation there was slightly more matter (which constitutes our universe) and experiments have shown that today less than 0.01 % of the observable universe are made of antimatter.

CP violation is incorporated into the Standard Model by a complex phase in the Cabibbo-Kobayashi-Maskawa Matrix V_{CKM} that describes flavor mixing of up-type (up, charm, top) and down-type (down, strange, bottom) quarks. The existence of at least three generations of quarks and leptons is a necessary requirement for its occurrence.

At the LHC a dedicated experiment called LHCb precisely measures the V_{CKM} matrix elements by observing the decays of rare C and B mesons and thus the strength of CP violation [3] but also the general purpose experiments ATLAS and CMS do flavor physics [4].

Quark - Gluon Plasma and QCD

Quark-gluon plasma is a possible state of matter predicted by the theory of the strong interaction called quantum chromodynamics (QCD). It is believed to consist of asymptotically free quarks and gluons which normally cannot be observed as they are confined in baryonic matter. Unlike ordinary plasma, quark-gluon plasma behaves more like an ideal fermi liquid due to the strength of the color force and can only occur at extremely high temperatures and densities.

It is believed that the primordial universe before the baryogenesis (the formation of matter) consisted of quark-gluon plasma, as the temperatures and energies were too high for the gluons to keep the quarks together. Only when the universe cooled down considerably after some tiny fractions of a second they formed nucleons and quarks were not free any more.

Quantum chromodynamics is part of the Standard Model but while the theories of the electromagnetic- and weak interactions have experimentally been confirmed to extreme accuracy, QCD has only been tested to an accuracy of a few percent. By investigating quark-gluon plasma physicists hope to gain a better understanding of the strong interaction.

At the LHC it is produced by colliding heavy lead ions (208 nucleides) with an unprecedented energy. In these collisions the temperatures reach several trillion degrees Celsius, which is approximately 100,000 times hotter than the center of the sun and hopefully sufficient to free the quarks and gluons. Although there is a dedicated heavy-ion experiment called ALICE, also ATLAS and CMS take data during the LHC's lead runs.

1.2 Design Parameters and Technical Specifications

The Large Hadron Collider is the largest scientific instrument ever built by mankind and at the same time the most powerful particle accelerator in the world. It was constructed in an underground tunnel with a circumference of 27 kilometers that was initially excavated for the LHC's predecessor, the Large Electron Positron Collider, beneath the

French-Swiss border in the Geneva region. The project was planned over several decades, as the initial decision to build the machine was taken in 1984. Actual construction started in 1998 and took until 2008. The first proton beams circulated in the ring on September 10th in 2008 but nine days later a faulty electrical connection caused a magnet quench which led to an explosive expansion of liquid helium that damaged many of the superconducting dipole magnets. More than one year later, after the damage was repaired beams were circulated again in November 2009 and the first proton collisions were recorded three days later.

1.2.1 Design Parameters

The LHC tunnel features eight access points, where the four experiments are located. Inside the tunnel there is the actual accelerator with two separate beam pipes, included in the same magnet structure, which intersect at 4 interaction points in the middle of the detectors. The protons circulating in opposite directions are kept on a circular trajectory by 1,232 superconducting dipole magnets, which produce a magnetic field of 8.33 Tesla, while 392 quadrupole magnets focus the proton beam. The whole ring is kept at an operating temperature of 1.9 Kelvin using almost 100 tons of liquid helium (Figure 1.1). Superconductivity is necessary to achieve such high magnetic fields which in turn are necessary to keep the beams on their circular trajectory at the maximum energy of 7 TeV. This results in a center-of-mass energy of 14 TeV and a proton speed of 0.999999991 times the speed of light.

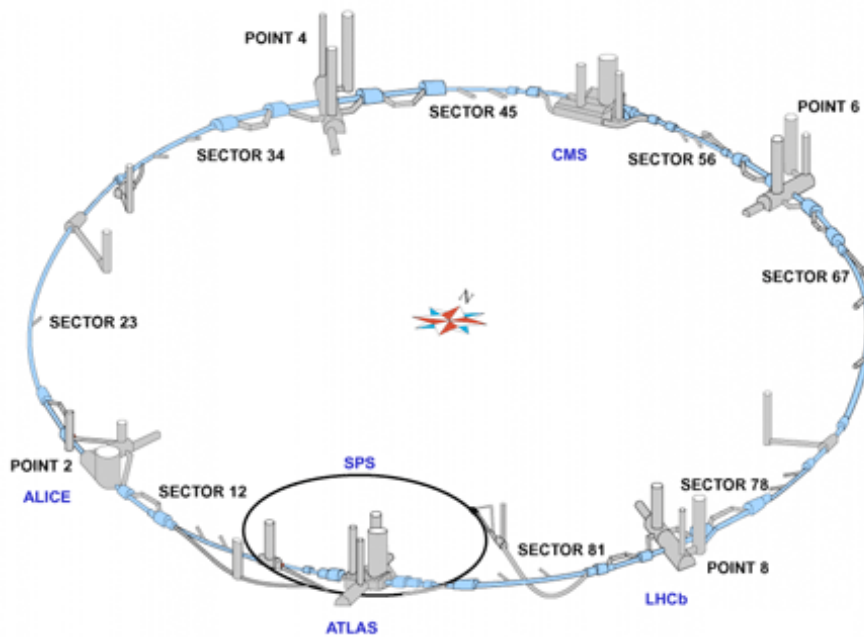


Figure 1.1: Schematic drawing of the LHC tunnel with experiment caverns. The superconducting parts are drawn in blue. http://www.quantumdiaries.org/wp-content/uploads/2009/11/0910_LHC_cold1.gif

The design luminosity is $10^{34} \text{ cm}^{-2}\text{s}^{-1}$, which is necessary for the study of very rare events, and achieved by dividing the beam into 2,808 bunches with 115 billion protons in each bunch and a collision rate of 40 MHz [5]. The luminosity for a Gaussian beam profile can be written as [6]

$$\mathcal{L} = \frac{N_b^2 n f_t \gamma}{4\pi \epsilon_n \beta^8} \quad (1.1)$$

with N_b the number of particles per bunch, n the number of bunches per beam, f_t the revolution frequency of a bunch, γ the relativistic γ factor, ϵ_n the normalized transverse emittance of the beam, and β^* the beta function at the collision point.

Table 1.1 summarizes the most important parameters of the LHC in proton-proton- and heavy-ion modes.

Table 1.1: LHC design parameters [5]

Parameter	Symbol	Unit	p-p Injection	p-p Collision	HI Collision
Energy per nucleon	E	[TeV]	0.45	7	2.76
Dipole field	B	[Tesla]	0.53	8.33	8.33
Nominal luminosity	\mathcal{L}	$[cm^{-2}s^{-1}]$	-	10^{34}	10^{27}
Bunch separation		[ns]		25	100
Number of bunches				2808	592
Particles per bunch	n			1.15×10^{11}	7.0×10^7
Beam current	I	[A]		0.582	
Beam energy	E_{Beam}	[MJ]	23.3	362	

In order to achieve these energies the particles have to undergo a whole chain of pre-accelerators before they are filled into the LHC itself. Protons are created from gaseous hydrogen in a proton source and are then accelerated to 50 MeV in a linear accelerator. Next they are passed to the Proton Synchrotron (PS) through the Proton Synchrotron Booster (PSB) (extraction energy of 1.4 GeV), where they reach a total energy of 25 GeV. The final step before the injection into the LHC is the Super Proton Synchrotron, which accelerates the particles to 450 GeV. This injection chain had to undergo several upgrades for the LHC era and two new transfer lines from the SPS to the LEP tunnel had to be constructed.

For heavy-ion operation the LINAC extraction energy is 4.2 MeV/nucleon and instead of the Booster, an Ion Accumulator is used before the ions are injected into the PS.

1.2.2 Operational History and Achievements

Shortly after the first successful circulation of low-energy beams in the tunnel in mid-November 2009 the LHC set the world record as the world's strongest particle accelerator with an energy of 1.18 TeV per beam. In early 2010 the energy was slowly increased up to a value of 3.5 TeV per beam and the main research program was started with the

first successful proton-proton collisions at a center-of-mass energy of 7 TeV. In late 2010 the proton run was stopped for heavy ion operation.

The accelerator continued operation throughout 2011 with 3.5 TeV per beam and after a technical stop at the end of that year the energy was further increased to 4 TeV for the 2012 run. In 2013 the LHC will enter a long shutdown of 2 years for the upgrade to 7 TeV per beam and for maintenance (LS1).

On April 21st 2011, the machine became the world's highest luminosity hadron accelerator beating a record set by the Tevatron with a peak luminosity of $4.67 \times 10^{32} \text{ cm}^2 \text{ s}^{-1}$.

Some intermediate milestones have already been reached well ahead of time, for example the total integrated luminosity of 1 fb^{-1} ² was reached half a year before scheduled in June 2011. By the end of that year, the high-luminosity experiments CMS and ATLAS had already recorded 5 fb^{-1} of data.

1.3 The High-Luminosity Upgrade

The LHC will require a major upgrade around the year 2020 to extend its potential for physics discoveries. When the machine has reached its full design luminosity of $10^{34} \text{ cm}^{-2} \text{ s}^{-1}$ after the energy increase to 14 TeV, it is expected to deliver $\sim 40 \text{ fb}^{-1}$ to the experiments per year, resulting in a total of 200 to 300 fb^{-1} over the scheduled lifetime of 10 years. After 2019/2020 the increase in statistics will become negligible if the accelerator is still operated at its design luminosity value. For example a reduction of the statistical error by a factor of 0.5 would require more than 10 years of further operation (Figure 1.2) [7].

For that reason a high-luminosity upgrade is scheduled for the year 2020, which will introduce a number of technological advances since the design of the original LHC, such as 13 T superconducting focussing magnets.

The design goal for this upgrade is a total integrated luminosity of 3,000 fb^{-1} over the lifetime of 10 to 12 years, while keeping the center-of-mass energy the same (all hadron colliders have so far produced a total luminosity of $\sim 10 \text{ fb}^{-1}$!). This implies major challenges to the experiments as they will have to cope with a pileup³ of up to 100 events per bunch crossing (as compared to 19 for nominal LHC parameters). If the bunch spacing of 25 ns is maintained this means a peak luminosity of $5 \times 10^{34} \text{ cm}^{-2} \text{ s}^{-1}$, thus increasing the present LHC's design value by a factor of 5 [9]. There are also studies with bunch spacing of 50 ns and twice the number of particles per bunch but this would increase the pileup even further.

In order to achieve this, several adjustments to beam parameters will be necessary:

- Maximize the number of particles per bunch;

²inverse barn (b^{-1}) is a unit for integrated luminosity) $1 \text{ fb} = 10^{-39} \text{ cm}^2$

³Overlap of events



Figure 1.2: Integrated luminosity and halving-time of the statistical error of results for the LHC lifetime [8].

- Minimize the size of the beam at the interaction points (i.e. experiments);
- Increase the number of bunches in the ring;
- Make sure that the overlap of the bunches at the interaction points is maximal.

The latter could be achieved by rotating the bunches with special cavities (crab-cavities) just before the collisions so that the geometric restrictions of the angle at which the two beams collide are compensated. Anyhow, all of the above require some major changes to the existing beam-optics infrastructure, especially in the vicinity of the experiments. This includes the development of new focussing magnets, RF cavities, collimators, shielding and cryostats.

Also the injection chain described in action 1.2 will need some serious upgrades to meet the demands of the HL-LHC in terms of beam intensity and -quality. This includes the construction of the new LINAC 4 as injector, increasing the Proton Synchrotron Booster extraction energy to 2 GeV and updating the PS and SPS infrastructures.

2 The CMS Experiment

The Compact Muon Solenoid is one of the four large LHC experiments, situated in a cavern especially excavated 100 meters underground. It is a multi-purpose detector and its design – as the name suggests – is very compact as opposed to the other multi-purpose experiment ATLAS, which is much larger in overall volume. The philosophy behind this is to have two detectors with similar abilities but quite contrary designs to record redundant data to back up potential discoveries. The magnet coil in CMS is of solenoid type and reaches a field strength of four Tesla.

The main purpose of CMS is the general search for new physics beyond the Standard Model with a special focus on Higgs searches and supersymmetry but it also records data during heavy-ion operation. The main physics goals will be presented in section 2.1, while the individual detector components will be introduced in section 2.2. The recent discovery of a Higgs boson with a mass of ~ 125 GeV, will be discussed in section 2.3 and section 2.4 will introduce the proposed upgrades for the high-luminosity phase of LHC.

2.1 CMS Physics

The process for creating all kinds of exotic or unknown particles in collider experiments is always the same. Basically, two particles get accelerated to extremely high energies and speeds close to the speed of light. Then they collide and the interaction of the elementary particles (leptons in lepton colliders and quarks/gluons in hadron machines) creates an extremely high energy density from which new particles can emerge.

The LHC in particular collides protons and lead ions, thus the main process is the interaction of gluons and quarks. In these interactions many new particles are produced and can be detected, but only very rarely a process that is of interest for the search for new physics takes place. The estimated production rate of the Higgs boson for example is one in ten billion events.

2.1.1 Higgs Production and -Decay

In the following, the most important processes for the production and decay of the Higgs boson will be discussed for the case of the minimal Standard Model, not considering supersymmetry. In a hadron collider like the LHC there are four main production

channels, of which one is dominant [10]. Their respective cross-sections as a function of Higgs mass are shown in figure 2.2.

Gluon-Gluon Fusion

In this process two gluons from the colliding protons interact and produce a Higgs particle through the formation of a virtual heavy-quark loop. Since the coupling to the Higgs field is proportional to the particles' mass this process is dominated by the heavy top quark with a bottom quark contribution smaller than 10 %. This process is approximately 10 times more likely to happen than any of the following processes (Figure 2.1a).

Vector-Boson Fusion

In this case two fermions collide and exchange a virtual vector boson, which then emits a Higgs. The two participating fermions need not be of the same type and at the LHC they will most likely be quarks (Figure 2.1b).

Higgs Strahlung

An elementary fermion collides with an antifermion of the same type and they merge to form a virtual vector boson (W^\pm & Z^0), which then, provided it has sufficient energy, emits a Higgs boson. The involved fermions are quarks and antiquarks in the case of the LHC (Figure 2.1c).

Top Fusion

This is by far the most unlikely process and involves two colliding gluons that decay into heavy quark- antiquark pairs and a quark and anti-quark of each pair combine to form a Higgs boson (Figure 2.1d).

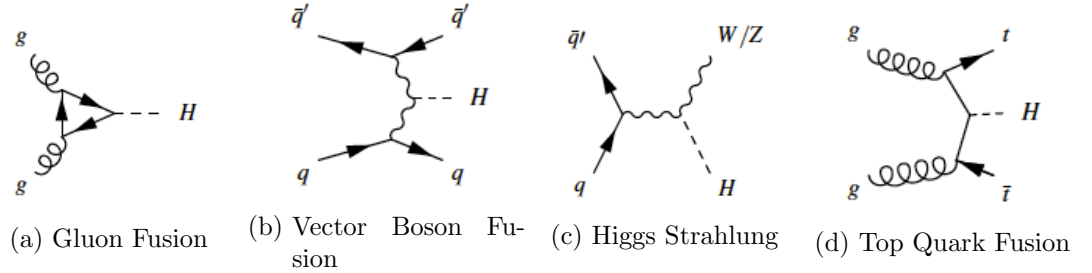


Figure 2.1: Higgs production processes

The decay modes of the Higgs particle depend on the mass of the decay products and the strength of the different interactions. All these parameters are fixed by the Standard Model except for the mass of the Higgs itself. There is a quantum-mechanical uncertainty relation between the mass of a particle and its lifetime, the lifetime τ is given as

$$\tau = \frac{\hbar}{\Gamma} \quad (2.1)$$

with \hbar the reduced Planck quantum and Γ the width of the relativistic Breit-Wigner distribution, also called decay width. For a Higgs particle with a mass of 126 GeV/c² this results in a mean lifetime of $\tau = 1.26 \times 10^{-22}$ seconds.

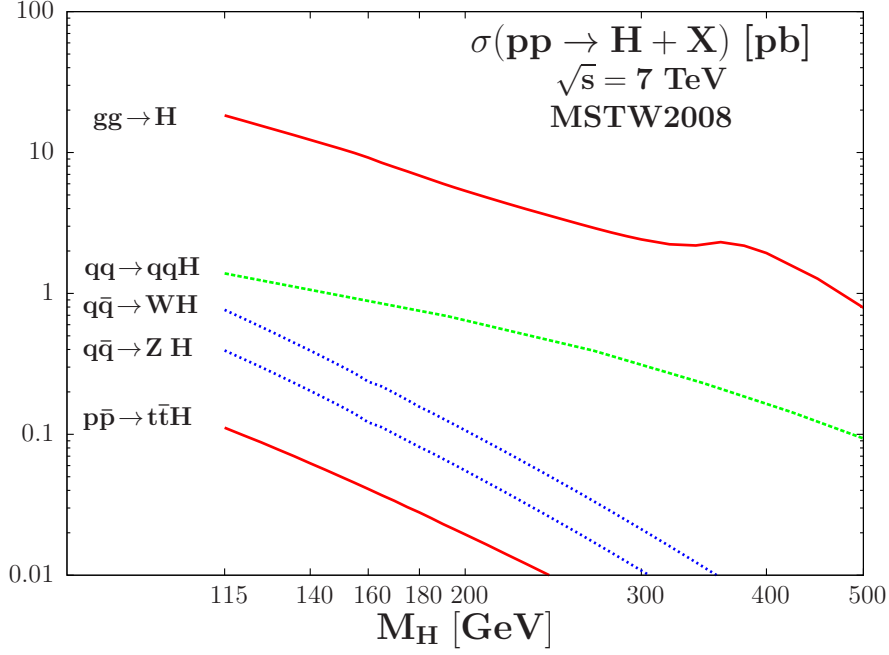


Figure 2.2: Cross-sections of the different Higgs production mechanisms as a function of the Higgs mass m_H at the LHC with $\sqrt{s} = 7 \text{ TeV}$ [10]

Since the Higgs boson interacts with all massive elementary particles, there are many possible decay modes of which some are more likely and others are less so. The fraction of decays through a particular channel is called branching ratio and an overview of the most important Higgs decay modes as a function of mass can be found in figure 2.3.

For the CMS experiment some decay modes are more favorable because they are easier to detect and have higher mass resolution and lower background. The most important ones are described here in brief [11]:

$H \rightarrow \gamma\gamma$

In this mode the Higgs boson decays into two high-energetic photons. It is one of the most promising channels since it offers a very good mass resolution by measuring the invariant mass of the two photons but also has a large irreducible QCD background.

$H \rightarrow ZZ \rightarrow 4\ell$

Here the Higgs decays into two Z^0 vector bosons which then further decay into four leptons. The combinations $2e2\mu$, $4e$ and 4μ are possible. The main background arises from direct ZZ production via a quark and an antiquark. Also this channel has a very high mass resolution as the electromagnetic calorimeters of the LHC experiments are very precise.

$H \rightarrow WW \rightarrow 2\ell + E_T^{miss}$

Another probable channel is the decay of the Higgs into two W vector bosons.

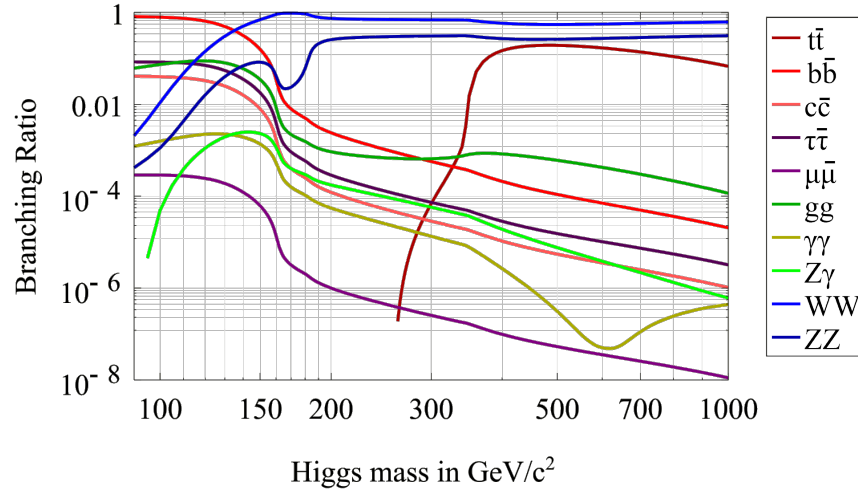


Figure 2.3: Branching ratios for the most important Higgs boson decay channels as a function of the mass m_H .

These have several decay modes themselves but in CMS the one where the W bosons decay into two leptons and undetected neutrinos, which manifest themselves in high missing transverse energy, is exploited.

$H \rightarrow \tau\tau$

This Higgs decay mode has four sub-channels that correspond to the possible τ decays. These are $e\mu$, $\mu\mu$, $e\tau_h$ and $\mu\tau_h$, with the first two leptonic τ decays and τ_h indicating a tau decaying into hadronic jets (pions). It is the second-most-probable channel but it is really hard to explore experimentally since there is a huge background from other hadronic interactions.

$H \rightarrow b\bar{b}$

This decay mode is the most likely one with more than 50 % of all decays. However, it offers a very low mass resolution as the decay products manifest themselves in hadronic jets which cannot be measured with high resolution and the background is very large.

As there are several other extensions of the Standard Model with a varying number of Higgs particles – the Minimal Supersymmetric Standard Model features a quintet of scalar Higgs bosons – the investigation of coupling strengths and branching ratios can give hints to what kind of particle is under investigation.

2.1.2 Supersymmetric Searches

It is believed that – if supersymmetry is one of nature’s fundamental symmetries – it will be discovered at the LHC. According to the Minimal Supersymmetric Standard Model there are five classes of super particles: squarks, gluinos, charginos, neutralinos

and sleptons. Since the LHC is a hadron machine, the search is focussed on strongly interacting super particles, namely squarks and gluinos. According to theory the MSSM has R parity¹, which means that the lightest supersymmetric particle (LSP) is stable and only interacts weakly (WIMP).

Therefore each decay chain of a squark or gluino will contain at least one LSP, which cannot be detected by the experiments and will manifest itself in the detector as large E_{miss}^T .

Typical decay channels for squarks, which are always produced in pairs, are

$$\tilde{q}\tilde{q} \rightarrow q\tilde{N}_1^0\bar{q}\tilde{N}_1^0 \rightarrow 2 \text{ jets} + E_{\text{miss}}^T \quad (2.2)$$

with the squark-antisquark pair decaying to a quark-antiquark pair and 2 LSPs (neutralinos), which appear in the detector as two hadronic jets and large E_{miss}^T and

$$\tilde{q}\tilde{q} \rightarrow q\tilde{N}_2^0\bar{q}\tilde{N}_1^0 \rightarrow q\tilde{N}_1^0\ell\bar{\ell}\bar{q}\tilde{N}_1^0 \rightarrow 2 \text{ jets} + 2\ell + E_{\text{miss}}^T \quad (2.3)$$

with ℓ denoting leptons.

Gluinos decay to a quark and squark, thus typical signatures look like

$$\tilde{g}\tilde{g} \rightarrow (q\tilde{q})(\bar{q}\tilde{q}) \rightarrow (q\tilde{q}\tilde{N}_1^0)(\bar{q}\tilde{q}\tilde{N}_1^0) \rightarrow 4 \text{ jets} + E_{\text{miss}}^T \quad (2.4)$$

Since gluinos are their own antiparticles they can decay to quark-antisquark and squark-antiquark with equal probabilities.

$$\tilde{g}\tilde{g} \rightarrow (\bar{q}\tilde{q})(q\tilde{q}) \rightarrow (q\tilde{q}\tilde{C}_1^+)(q\tilde{q}\tilde{C}_1^+) \rightarrow (q\tilde{q}W^+)(q\tilde{q}W^+) \rightarrow 4 \text{ jets} + \ell^+\ell^+ + E_{\text{miss}}^T \quad (2.5)$$

The purely hadronic events above are most sensitive to supersymmetry but have a very large background from SM processes like QCD multi-jet events, Z boson production with associated hadronic jets, and neutrinos and W boson production. Adding the requirement of 2 isolated leptons eliminates the background from multi-jet QCD and W boson production. The last signature 2.5 is a very distinctive one, since the background from SM processes is very low [12].

So far (July 2013) experimental evidence for supersymmetry has not been found yet. Squarks have been excluded to 1.1 TeV and gluinos to 500 GeV (meaning that if they exist, their mass is greater than 1.1 TeV and 500 GeV respectively). Figure 2.4 shows the present experimental limits obtained with the CMS detector.

¹In supersymmetric Standard Models the baryon- and lepton numbers are not conserved any more. R parity is defined as: $P_R = (-1)^{2s+3B+L}$ and all Standard Model particles have R parity of 1 and super particles have R-parity of -1.

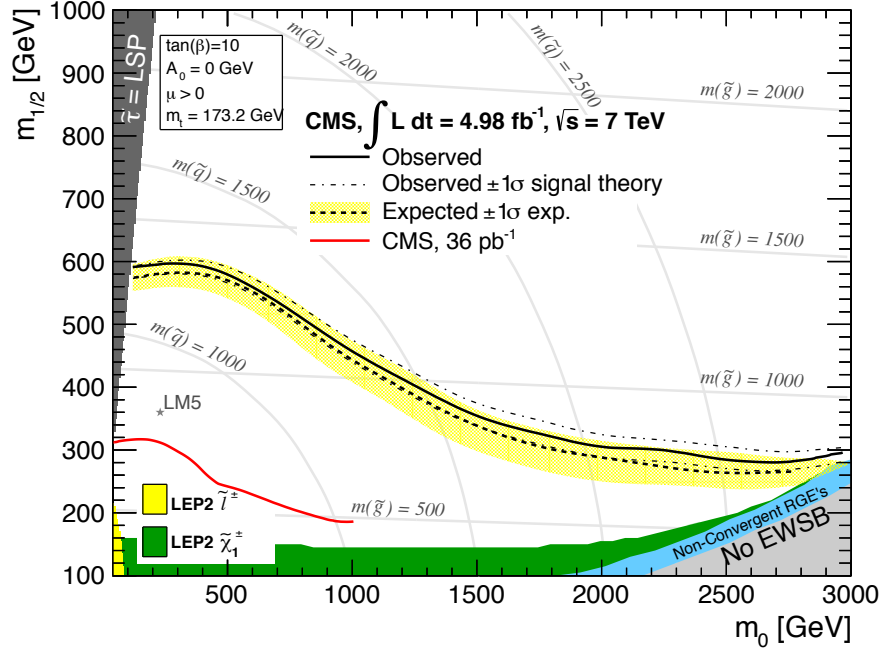


Figure 2.4: Experimental limits for supersymmetry at $\sqrt{s} = 7 \text{ TeV}$ [12].

2.2 The Detector ²

The CMS detector is designed as a hermetic 4π detector where several sub-detectors surround the point of the particle collisions. Each of these sub-systems serves another purpose and their order is given by the range and properties of the particles that are measured. Hermeticity is necessary for event reconstruction and for efficient detection of missing transverse energy (E_{miss}^T). Figure 2.5 shows all important detector systems. The main design goals were (all from [13]):

- Good muon identification and momentum resolution over a wide range of momenta; explicit muon-charge identification for momenta $< 1 \text{ TeV}/c$ and good dimuon-mass resolution
- Good charged-particle momentum resolution and reconstruction efficiency in the tracker; efficient triggering and tagging of τ 's and b-jets
- Good electromagnetic-energy resolution; good diphoton- and dielectron-mass resolution
- Good E_{miss}^T and dijet-mass resolution; hadron calorimeter with large geometric coverage and fine lateral segmentation

²Numbers and figures in this section are all from [13] unless otherwise stated.

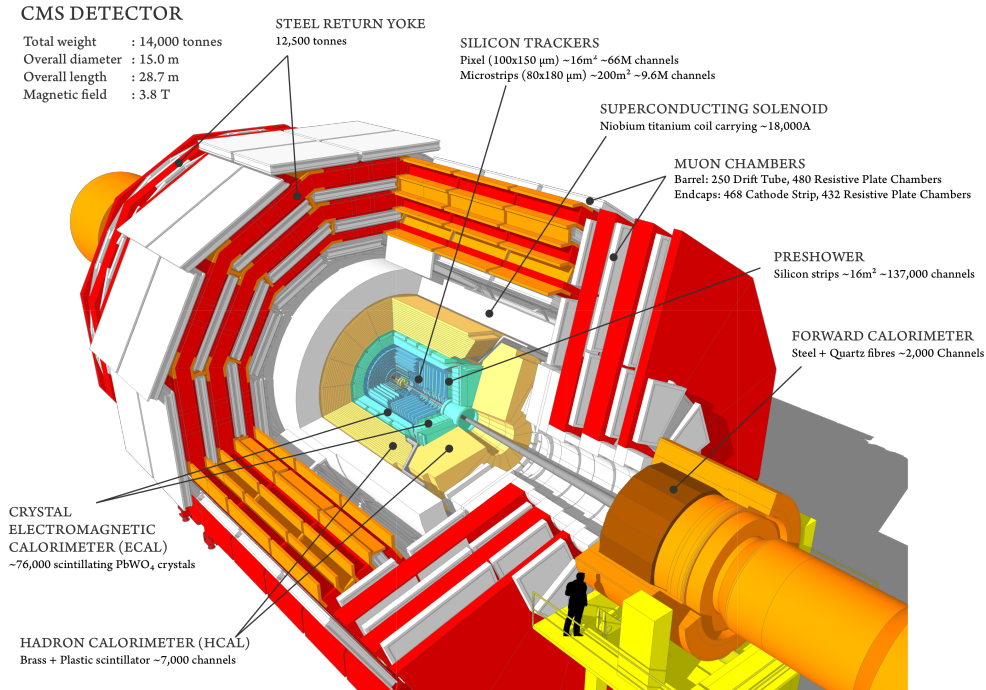


Figure 2.5: Schematic drawing of the CMS detector with all sub-systems. [14]

The main features of CMS that distinguish it from other experiments are the high-field super-conducting solenoid, a full-silicon inner tracker and a homogenous electromagnetic calorimeter based on scintillating crystals without non-active absorbers.

The design was driven by the choice of the magnetic-field layout which features a solenoid-type field with a field strength of 4 Tesla. This immense bending power is necessary to achieve the good momentum resolution for muons, which are an important indicator for interesting physics processes. The individual sub-components of CMS will be presented in the following sections.

2.2.1 The Tracker

CMS has an all-silicon tracker with a total surface of 210 m^2 . Its main purpose is to measure the trajectories of the particles that are created in the proton collisions and the reconstruction of secondary vertices. Details about the tracker will be presented in chapter 3.

2.2.2 The Electromagnetic Calorimeter

The electromagnetic calorimeter of CMS (ECAL) is a hermetic and homogenous calorimeter constructed of 61,200 lead-tungsten crystals (PbWO_4) in the barrel region and 7,324

crystals in each of the end-cap regions. This means that the absorber material is also the signal-producing material. Its purpose is to measure and absorb electromagnetically-interacting particles.

PbWO₄ was chosen because it has a very short radiation length ($X_0 = 0.89$ cm) and Molière radius (2.2 cm) and because the crystals are very fast (80 % of the light is emitted within 25 ns) and radiation-hard. The crystals are read out by avalanche photodiodes in the barrel region and vacuum phototriodes in the end caps. These photodetectors have intrinsic gain and can operate in a magnetic field, which is required by the ECAL's location inside the solenoid magnet and because of the relatively low light yield of the PbWO₄ crystals. The size of the individual crystals is 22×22 mm² in the barrel region and 28.6×28.6 mm² in the end caps with respective lengths of 230 mm and 220 mm ($\sim 25 X_0$) [13].

The end-cap region also features an additional pre-shower detector in front of the crystal calorimeter. These are 2 layers of silicon-strip sensors with a pitch of 1.9 mm, which are mounted behind discs of lead at depths of $2 X_0$ and $3 X_0$.

The energy resolution as a function of incident particle energy of the calorimeter can be parametrized as

$$\left(\frac{\sigma}{E}\right)^2 = \left(\frac{S}{\sqrt{E}}\right)^2 + \left(\frac{N}{E}\right)^2 + C^2 \quad (2.6)$$

with S denoting the stochastic term, N the noise and C the constant contribution. Figure 2.6 shows the measured energy resolution of an ECAL supermodule obtained in a beam test.

2.2.3 The Hadron Calorimeter

The hadron calorimeter (HCAL), like the ECAL, is mostly situated inside CMS's magnet coil, outside the ECAL, and therefore the properties of the magnet system govern the design of HCAL. The requirements are good containment and hermeticity for E_{miss}^T measurement, which requires a maximum amount of absorber material and thus interaction lengths.

For that reason it has been designed as a so-called sampling calorimeter with alternating absorber- scintillating material. The absorber is 5 cm thick brass interleaved with 4 mm thick layers of plastic scintillators. An additional layer of 10 mm thick scintillators is located outside the magnet coil, which serves as the last absorption layer and increases the effective thickness of HCAL to over ten interaction lengths. Wavelength-shifting fibres connect the scintillator tiles to multi-channel hybrid photodiodes that act as readout. [13] and [15].

An additional Hadron Forward (HF) calorimeter is located more than 11 meters away from the interaction point in deep-forward direction. It is built from steel and quartz fibres, as this design leads to narrower and shorter hadronic showers, which is desirable for the forward region. The signal-creation mechanism is Cherenkov radiation in the

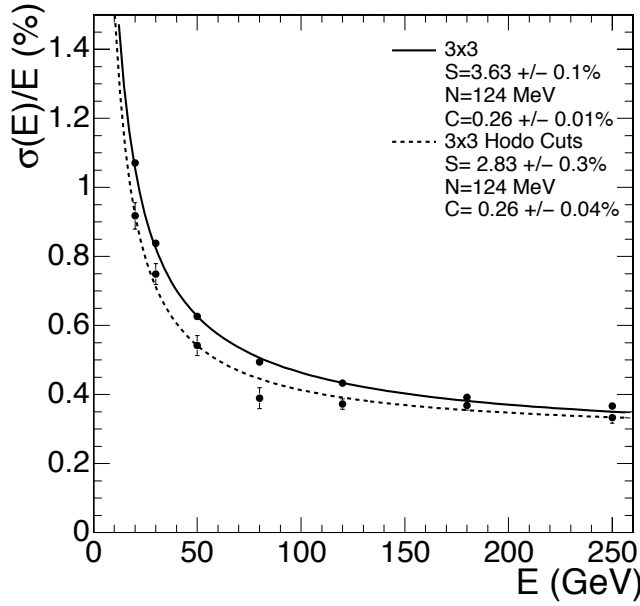


Figure 2.6: Measured ECAL supermodule energy resolution as a function of incident electron energy. [13]

quartz fibres, which is detected by photomultipliers.

2.2.4 The Magnet

One of the most important factors for the overall performance of a particle detector is the magnet system. It determines the momentum resolution, as the curvature of the tracks depends on the magnetic field strength. As quoted in section 2.2, the CMS design concentrates on good momentum resolution for muons with momenta around 1 TeV. To achieve this a very strong field is required, while still maintaining compact detector dimensions.

Consequently CMS has a superconducting solenoid coil made out of niobium-titanium (Nb_3Ti is a Type II superconductor with a critical temperature of 10 Kelvin and a critical field of 15 Tesla), which creates a field of 3.8 Tesla (nominally 4 T) and is housed inside a vacuum vessel with liquid-helium cooling. The coil is surrounded by a huge steel structure that acts as return yoke for the magnet and also as structural support. Together they account for a large part of the experiment's overall weight of 12,500 tons.

One big advantage of the solenoid geometry is that the field on the inside is parallel to the beam axis and therefore the bending of the particle's track already starts at the vertex.

2.2.5 The Muon System

The muon system is one of the key components of CMS, since high-energetic muons are important signatures for interesting events. Muons, apart from neutrinos, are the only particles that can traverse the whole detector without being stopped and therefore are very important for triggering and event selection. One of the key requirements of the detector is good muon identification and momentum resolution, which is achieved by combining the information from the tracker, where muons are measured the first time, and the muon system. The momentum resolution for the lower range is governed by the tracker but the muon chambers at the outside of the detector play an important role for large momenta.

The muon system uses three types of gaseous detectors adapted to the different radiation environments where they are installed, interleaved inside the hollow parts of the magnet return yoke. In the barrel region drift-tube chambers are used because the neutron background, residual magnetic field, and muon flux are low.

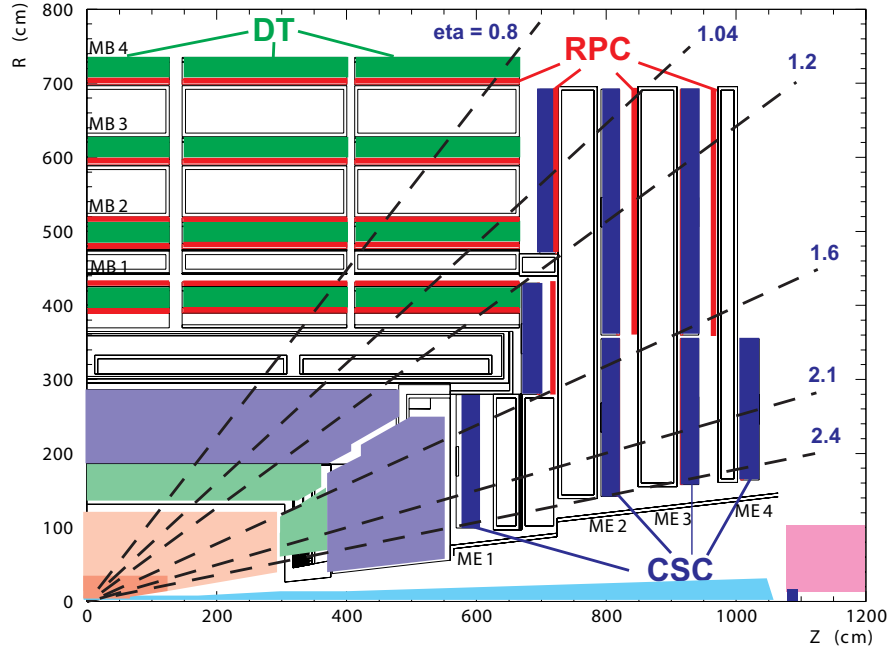


Figure 2.7: The layout of the CMS muon system with drift tubes (DT), cathode strip chamber (CSC) and resistive plate chambers (RPC) [13].

The end-cap regions, in contrast, use cathode strip chambers because of higher particle rates and background. Additional resistive plate chambers, that operate in avalanche mode, are used all around the detector as they provide good time resolution for event selection and perform well at high rates (Figure 2.7). The combined information of all three systems provides very fast and robust trigger information [13] [16].

2.2.6 The Trigger

Since the LHC is a hadron machine with an extremely high event rate and high occupancy the trigger system is a key component of the whole detector. The bunch-crossing frequency of 40 MHz leads to $\sim 10^9$ interactions per second, while only 100 events per second can be written to data storage. To achieve this reduction a very sophisticated trigger system is used that consists of several levels [13].

Level-1 Trigger

The average transit time of signals from the experiment to the service caverns that house the logic for the Level-1 trigger and back is about $3 \mu s$, which means that all event data needs to be stored in the front-end electronics until a decision from the trigger logic is received. This also means that there is only a very short time window for the trigger decision itself.

For that reason custom hardware circuits are used which, take into account data from the calorimeters and the muon system and look for particles and jets with very high E^T or p^T or large E^T_{miss} . A reduction to a rate of 100 kHz is achieved within about one microsecond [13].

High-Level Trigger (HLT)

If the front-end electronics receive a Level-1 trigger decision, the event data is read out, processed and forwarded to the Data Acquisition System (DAQ). The amount of data corresponding to one proton-proton collision is about 1.5 MB. A processor farm then starts reconstructing the interesting parts of the events with information from only a fraction of the detector sub-components, making it possible to discard events as soon as they are deemed uninteresting. This HLT software is highly flexible, can be changed over time and reduces the data rate even further to 100 Hz for mass storage.

2.3 Results

On July 4th, 2012 CERN held a joint seminar of the ATLAS and CMS collaborations involving much speculation by the media and the general public about the content. Rumors had circulated that a confirmation of preliminary hints of a new particle, which were published late in 2011, was about to happen.

The spokespersons of the two experiments actually announced the discovery of a new particle with a mass around $125 \text{ GeV}/c^2$ with a significance of 5 sigma, which is widely considered the threshold for claiming a discovery. In the following section the result as presented by CMS will be summarized in brief.

The talk and publication [11] are based on data taken during the 2010 and 2011 runs with $\sqrt{s} = 7 \text{ TeV}$ and the 2012 run with $\sqrt{s} = 8 \text{ TeV}$ with integrated luminosities of

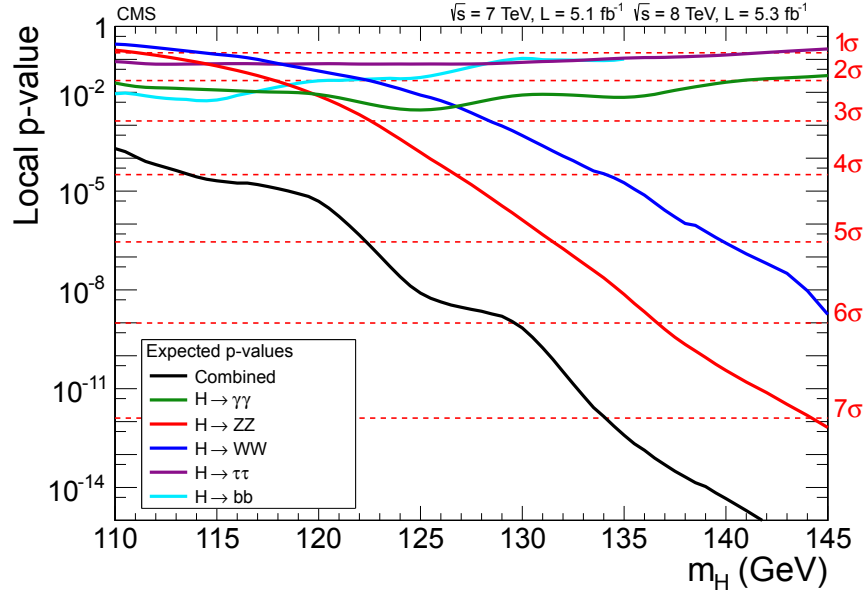


Figure 2.8: Expected local p -value for a Standard Model Higgs boson as a function of Higgs mass m_H for all observed decay modes [11].

5.1 fb⁻¹ and 5.3 fb⁻¹ respectively. The observed decay modes are (see Section 2.1):

$$H \rightarrow \gamma\gamma, H \rightarrow ZZ, H \rightarrow W^+W^-, H \rightarrow \tau^+\tau^-, H \rightarrow b\bar{b}$$

During the 7 TeV runs of 2010 and 2011 the CMS experiment managed to reproduce and verify previous results (from earlier experiments) and Standard Model predictions to stunning accuracy, which built a fabulous baseline for the Higgs search, as it allowed for a very precise calibration of the detector.

In particle physics the probability of a background fluctuation to be at least as large as the observed excess is called the local p -value and that for an excess anywhere in the observed range is called global p -value [11]. This probability is evaluated using simulations, and can be expressed as a corresponding number of standard deviations σ . Figure 2.8 shows the expected local p -value for a Standard Model Higgs boson as a function of its mass for all decay modes quoted above. The strength of a possible Higgs boson signal is quantified as the product of the production cross-section and the branching ratio relative to the expected Standard Model signal strength σ/σ_{SM} [11].

According to the analysis presented in [11] the two decay modes with high mass resolution in the low Higgs mass range $H \rightarrow \gamma\gamma$ and $H \rightarrow ZZ \rightarrow 4\ell$, which is also called the 'golden channel', reach local p -values of 4.1σ at a mass of 125 GeV and 3.2σ at a mass of 125.5 GeV. The combined significance for these two is 5.0σ , whereas the Standard Model expectation is 4.7σ .

If the other three channels with low mass resolution are added, taking the respective

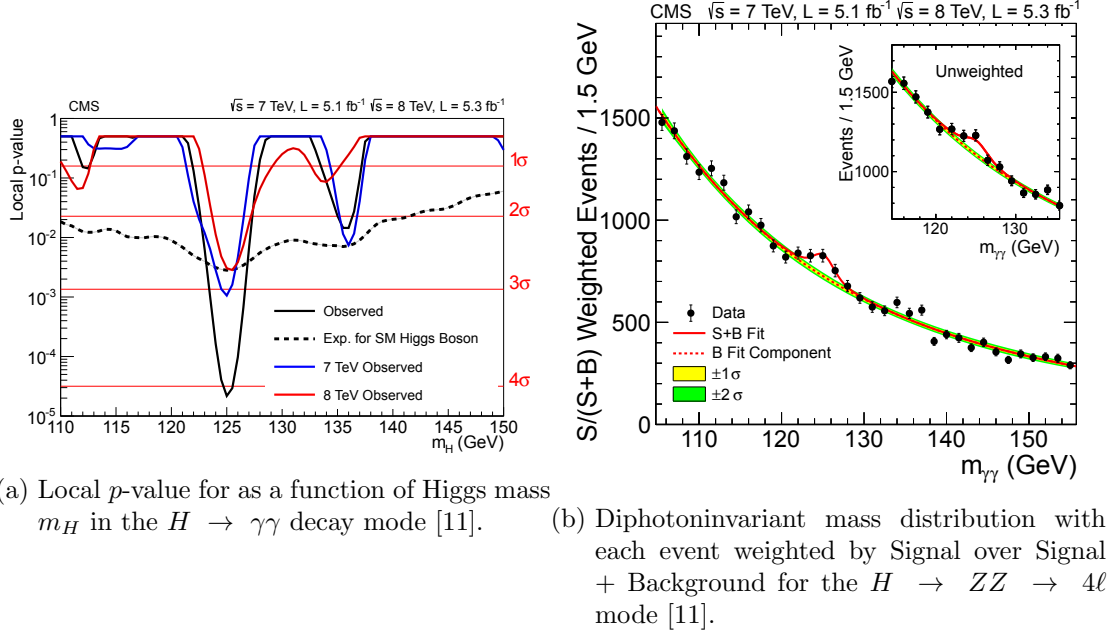


Figure 2.9

fraction of branching ratios into account, the local p -value of the combined results is 5.0σ for $m_H=125.5 \text{ GeV}/c^2$ (Figure 2.11). The confidence level of the exclusion of a Standard Model Higgs boson below a mass of 121.5 GeV is 95 % and between 121.5 and 128 GeV a significant excess is observed, as shown in figure 2.10.

The two decay modes $H \rightarrow \gamma\gamma$ and $H \rightarrow ZZ \rightarrow 4\ell$ indicate that the observed particle is a boson and the decay into photons implies a spin different from 1. The best value for the mass extracted from the results is $m = 125.3 \pm 0.4 \text{ (stat.)} \pm 0.5 \text{ (sys.) GeV}/c^2$ [11], which is compatible with a Standard Model Higgs boson.

2.4 The CMS Upgrades

The operation of the CMS detector is governed by the operating parameters of the LHC, which change over time. During the Phase-1 operation, denoting the period before the high-luminosity upgrade, which is scheduled around 2020, the energy of the collisions will be increased to 14 TeV after the long shutdown 1 (LS1) and the luminosity will be further increased towards and after the long shutdown 2 (LS2). After the year 2020, when the High-Luminosity LHC (Section 1.3) will enter operation, the luminosity increase will be even higher. In order to keep up with these ever-increasing demands, also the CMS detector will need several upgrades. These are divided into the so-called Phase-1 Upgrades, which concern the detector before the high luminosity era of LHC and Phase-2, which is optimized for that era.

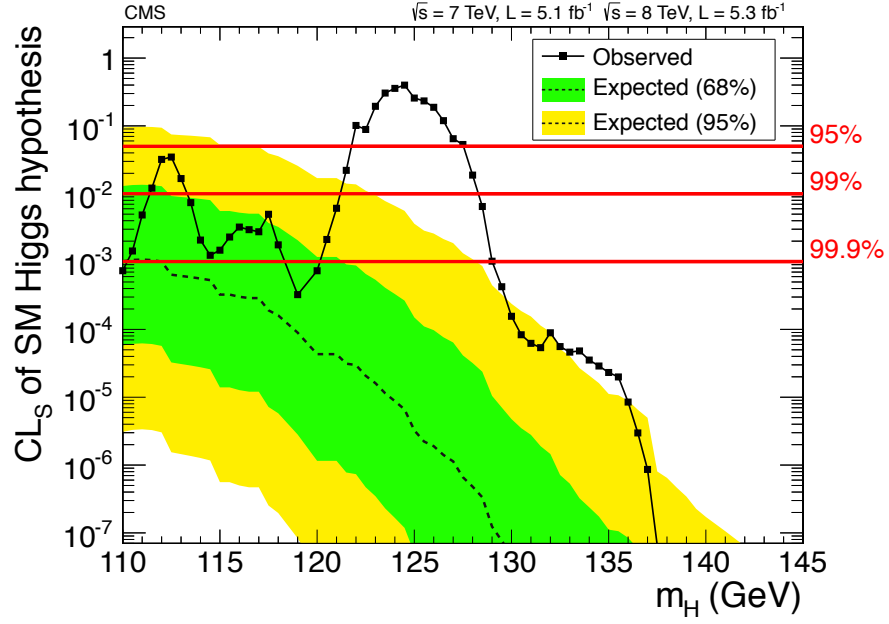


Figure 2.10: Confidence levels for the Standard Model Higgs boson hypothesis as function of the mass m_H [11].

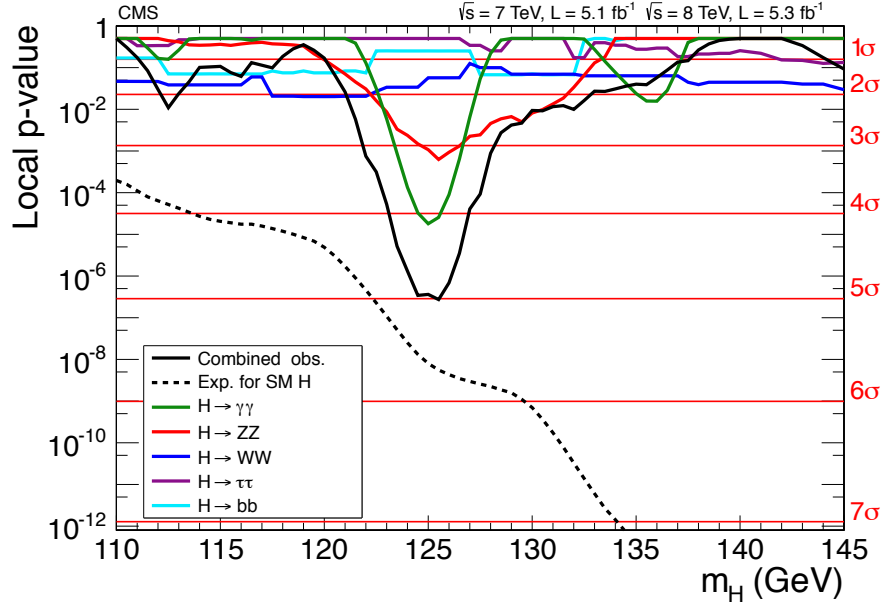


Figure 2.11: Observed local p -value for all five decay modes and their combination [11]

2.4.1 The Phase-1 Upgrade

These upgrades are scheduled to be implemented between the present day and the end of the long shutdown 2 around 2017. The affected subdetectors are (all from [17]):

The Muon System

The increase of the instantaneous luminosity to $10^{34} \text{ cm}^{-2}\text{s}^{-1}$ will increase the pileup of events to a level where it will become difficult for the muon system to provide efficient triggering information. For that reason an additional layer of cathode strip chambers will be added along with improvements of the readout- and trigger electronics. Also in the end caps a fourth layer of resistive plate chambers will be added to cope with higher particle rates.

The Hadron Calorimeter

The hadron calorimeter will see an exchange of the photodetectors as well as the back-end electronics. The current hybrid photodiodes are scheduled to be exchanged with silicon photomultipliers, which are compact in size and have better efficiency. The forward hadron calorimeter will be upgraded with another type of photomultipliers, which detect the Cherenkov light from the quartz tubes (Section 2.2) to reduce fake signals.

The Pixel Detector

The present pixel detector has a limited lifetime and was designed for luminosities up to $10^{34} \text{ cm}^{-2}\text{s}^{-1}$. At a later stage of LHC operation it will have to deal with twice that value and therefore the exchange of the whole pixel system is scheduled for LS2. The current 3-barrel-layer- and 2-end-cap layers layout will be replaced by 4 barrel- and 3 end cap layers, the cooling will be switched to CO_2 , the electronics boards will be removed from the tracking volume and a new readout chip is to be developed to reduce data loss at higher collision rates.

Trigger

The trigger system will be switched to a new, more flexible and capable hardware solution, which will allow the use of more sophisticated algorithms and thus the handling of higher rates and more complex events.

2.4.2 The Phase-2 Upgrade

The five-fold increase of luminosity during the HL-LHC operation will require significant R&D for some of CMS's detector-components upgrades. This Phase-2 upgrade will build on the Phase-1 in some cases but in other cases whole components will have to be exchanged. While the Phase-2 tracker upgrade will be discussed in detail in chapter 3, section 3.4, an overview of the proposed upgrades for other components will be given here.

The Calorimeters

The radiation damage in the CMS calorimeters in the HL-LHC era will be far beyond the design specifications and thus major upgrades and changes to the systems will be required. While the Phase-1 upgrades to the barrel hadron calorimeter will address most issues of the current design, allowing for operation well into the High-Luminosity Phase, the R&D effort for the ECAL will be significant. Although PbWO_4 crystals are relatively radiation-hard, hadronic interactions will reduce their transparency, which leads to an increase of the stochastic- and constant terms in the energy resolution. Also the avalanche photodiodes in the barrel region will suffer from radiation damage in the silicon, which will increase the dark current [17].

The biggest problem of ECAL, though, is the presence of anomalous signals caused by hadronic interactions in the avalanche photodiodes. This effect will increase with fluence and become dominant. To overcome it, mainly upgrades of the readout electronics and increased redundancy are planned.

The forward calorimeters will likely take more damage than the barrel region and therefore, if the excellent energy resolution shall be maintained, the complete system will have to be rebuilt with more radiation-hard crystals and photodetectors. Candidates are $\text{LYSO}(\text{Ce})$ and PbWMO for the crystals and silicon-photomultipliers and GaAs photodetectors as readout [17].

The Muon System

For the Phase-2 upgrade, the drift-tube component of the muon system itself should be able to cope with the higher luminosity but the electronics will need revision in terms of radiation tolerance and processing power for high rates. This is crucial, as the drift tubes are an important part of the Level-1 trigger and the only way to maintain the rejection power of the system is an improvement of its p^T resolution, which is achieved by including track information from the tracker.

The resistive plate chambers in the barrel region have successfully been tested to the expected rates in the high-luminosity scenario, but in the forward region, which is presently vacant in terms of RPCs, instrumentation with a new detector type would be desirable. Promising candidates are micro-pattern gas detectors (MPGD), which have the potential to be built industrially in large sizes and to deal with high rates [17].

Finally the cathode strip chambers, in conjunction with a future track trigger, should be sufficient to provide robust Level-1 trigger information on muons. But the readout electronics would likely require upgrades, especially in terms of high-rate capability.

3 The CMS Tracker

The inner tracking system of the CMS detector, also called tracker, has to fulfill several tasks. These are the measurement of the momentum and charge of created particles, the reconstruction of their trajectories and the measurement of the impact parameter and thus the identification of secondary vertices. To achieve these goals, the tracker measures space points of the tracks in a high magnetic field of 3.8 Tesla.

The curvature of a charged particle travelling in a magnetic field is related to the momentum and charge, which allows for indirectly measuring both parameters according to the formula $p_T = qBR$ with p_T being the transverse momentum, q the charge of the particle, B the magnetic field and R the radius of the curvature.

The geometric layout of the tracker was designed such that each track is measured independently in the different sub-systems several times. The number of measurement points is typically between eight and 13, which allows for robust track reconstruction provided that the precision of these measured space points is high and they are unambiguous.

The impact-parameter resolution is determined by two contributions. One is the granularity of the sensors and the other is multiple scattering in the detector layers. To achieve a good performance, the granularity of the tracking layers should be high and the distance of the first layer to the beam pipe has to be minimal. Thin layers also reduce the contribution of multiple scattering.

The momentum resolution also has two contributions that govern the performance in different regimes of momenta. For high momenta, the resolution depends on the point resolution of the individual tracking layers and the number of measurement points, the arc length of the track in the magnetic field, the measurement points and the momentum itself. For lower momenta the resolution is dominated by multiple scattering and can be increased to a certain limit by using less material in the tracking volume. The design resolution of the individual layers of the CMS tracker ranges from 15 to 40 μm from the inner to the outer regions and combined with the large tracking volume and strong magnetic field leads to excellent impact-parameter- and momentum resolution.

The following chapter will give a detailed summary of the tracker, its components and the readout system. Then the performance measured with data from early LHC operation will be presented, followed by a summary of the current status of the upgrade plans.

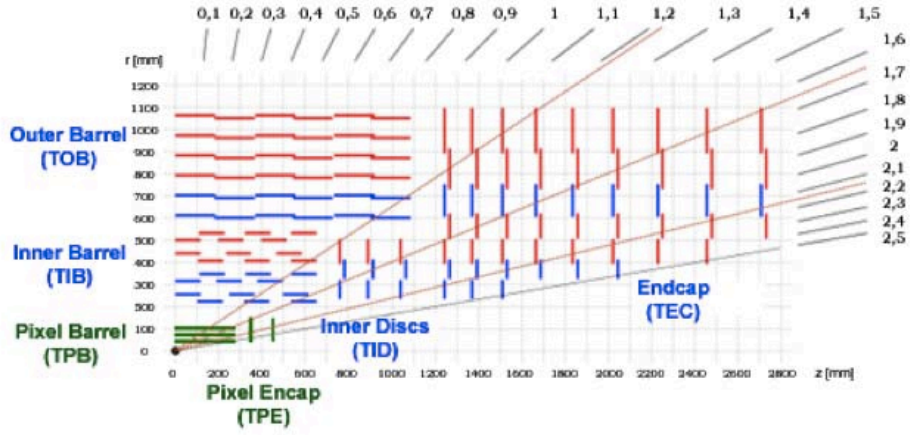


Figure 3.1: The tracker layout. 1/4 of the z view is shown. [13]

3.1 Description

The total surface of the CMS tracker is 210 m^2 divided into 13 barrel layers and 14 forward discs. It is radially divided into three regions according to particle flux and track density.

The innermost layers are designed as silicon-pixel detectors with very high granularity and the two outer sections are made of silicon-strip detectors with the strip pitch¹ and detector thicknesses are adapted to the particle rate. The outer section uses larger pitches, longer strips and thicker detectors to compensate for the higher noise caused by the longer strips. The whole tracker is divided into the barrel region, where the layers are situated around the interaction point in a barrel-like geometry, and the end-cap region, where they are parallel circular discs. The individual regions will be described in the following section.

The tracker extends from as close as four cm to a radius of 110 cm from the interaction point and has an overall length of 540 cm [13]. Figure 3.1 shows one quarter of the tracker and the nomenclature of the individual regions.

3.1.1 The Pixel Tracker

The part closest to the primary vertex, where the particle flux is highest, is the silicon-pixel tracker. It has to meet extreme requirements in terms of rate capability and radiation tolerance whilst providing high-precision, three-dimensional space points for track reconstruction and the identification of secondary vertices. When a short-lived particle like a b -quark or τ is created in a collision it will not live long enough to be directly

¹The size of the 'detection-cell'; the distance between two strips

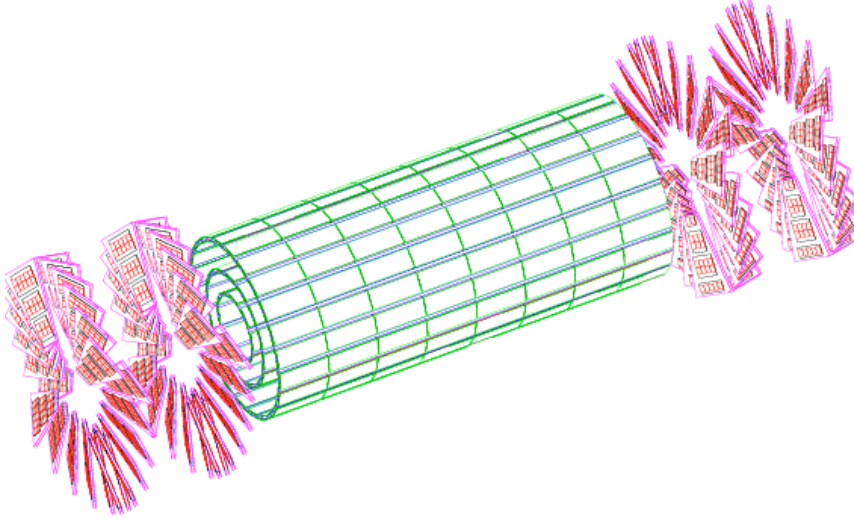


Figure 3.2: Schematic view of the CMS pixel detector. [13]

measured by one of the detector layers but it is possible to extrapolate the trajectories of the decay products and thus reconstruct the original secondary vertex. This requires an exceptional impact parameter resolution between 100 and $10\ \mu\text{m}$, depending on the particle momentum, which is achieved by high spatial resolution of the pixel system [18].

The CMS pixel tracker is composed of three barrel layers at radii of 4.4 cm, 7.3 cm and 10.2 cm and two end-cap discs in a slanted geometry (rotated at an angle of 20°) covering a radius from 6 to 15 cm. The overall length of the barrel ladders is 53 cm and the pixel tracker has a total of 66 million readout channels (Figure 3.2).

The individual pixel cells are rectangular with a size of $100 \times 150\ \mu\text{m}^2$, which was found optimal since due to the high magnetic field in CMS significant Lorentz effects² occur which lead to charge sharing between the pixels and thus improved resolution. Consequently, analog readout of the pixel sensors is necessary to take advantage of these effects. The achieved resolution of the CMS pixel tracker is $10\ \mu\text{m}$ in $r - \phi$ direction and $20\ \mu\text{m}$ along the beam (z direction) [13].

Sensors

The 270 and 285 micrometer-thick sensors are based on the n-in-n process, which means that the signal is read out from n^+ -doped electrodes in a high resistivity n-doped substrate. The p implant at the back requires a double-sided production process but this design has the advantage of allowing under-depleted operation – as opposed to the p-side readout adopted in the strip tracker – after type inversion with increasing radiation damage (see Chapter 4). The electron readout of the n-in-n concept allows for the large

²Due to the magnetic field in the experiment charge carriers in the silicon experience the Lorentz force, which changes the drift path, and the signal is distributed over several electrodes.

Lorentz angle due to the increased mobility of the electrons as compared to holes.

Front-End Electronics

The front-end chip of a pixel system is one of the key elements in its performance as it has to be highly integrated and fulfill tasks like identifying detector signals created by a passing particle, store time, position and analog signal height and has to send out data if a trigger is received [18]. The chip developed for the CMS pixel system is the PSI46 [19], which makes use of an integrated threshold to identify particle hits, which greatly reduces the amount of data as not the whole chip has to be read out.

The chip reads an array of 52 times 80 pixels and also has a peripheral section that houses the buffers for event-data storage and the bond pads for connection to the hybrid. The individual pixel readout cells of the chip consist of a pre-amplifier stage, a shaper and a comparator circuit [19].

Modules and Mechanics

A barrel pixel module consists of a sensor which is bump-bonded to 16 readout chips(ROC) in two rows of eight chips. Since the peripheral section of the ROC extends over the edge of the sensor, it is possible to feed the signals through wire bonds to a hybrid that is glued to the other side of the sensor. This so-called high-density interconnect (HDI) distributes the bias voltage, control signals and the detector signals. At the back of the ROC there are base strips that serve as mechanical support and mounting structure [18]. For reasons of geometric coverage also modules with only one row of 8 ROCs exist in the barrel region (3.3).

The end-cap discs have 24 wedge-shaped modules that hold sensors of different sizes and varying ROC numbers to maximize the covered surface.

The readout of the pixel modules is done with a similar system as is adopted in the strip tracker, which will be described in section 3.2. Due to the intense radiation environment in the pixel region of the tracker, the pixel system requires operation at low temperature and therefore a cooling system. The cooling tubes, together with some carbon fibre parts, also act as mechanical support for the detector layers.

3.1.2 The Silicon-Strip Tracker (SST)

In the outer regions of the central tracking volume of CMS, where the particle rate is considerably lower than in the pixel region and extreme granularity is not required, silicon-microstrip detectors are used. They are arranged in cylindrical layers outside the pixel volume and provide $r - \phi$ information, with some layers providing additional z information. The silicon-strip tracker must measure the momenta of particles precisely, separate electrons and photons reliably and localize calorimeter showers exactly while

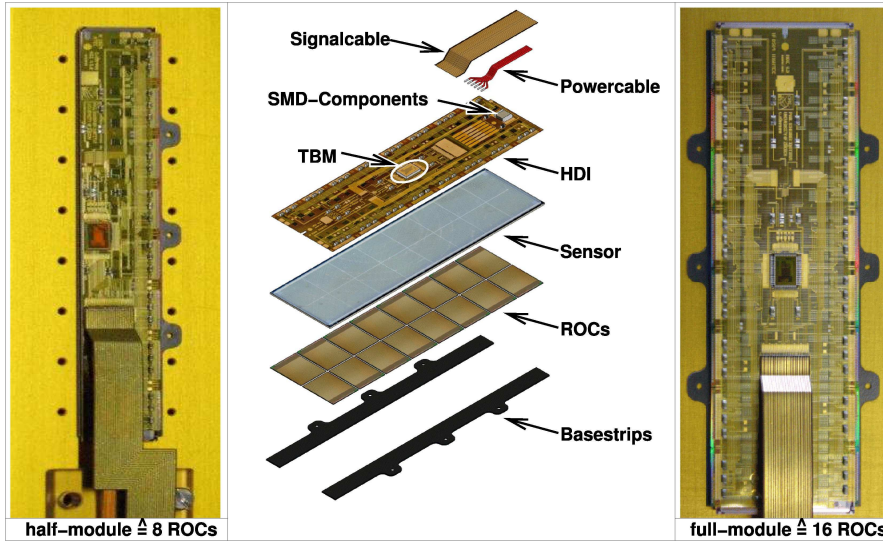


Figure 3.3: Components of barrel pixel modules. [18]

keeping the general occupancy of the readout channels at the percent level. Together with the space points of the pixel tracker the strip tracker provides robust tracking information.

The radiation environment in this region of CMS is a lot less hostile than in the pixel tracker, therefore the strip system was designed and built for the full nominal ten years of LHC operation before the high-luminosity upgrade.

Some design choices that were made include high modularity for relatively easy mass production of the huge number of modules, simple and relatively cheap detectors and fully analog readout electronics together with low-mass support structures and service infrastructure [20].

Layout

The CMS silicon-strip tracker is divided into four individual parts that can be seen in figure 3.1. The barrel region is divided into the Tracker Inner Barrel (TIB) and Tracker Outer Barrel (TOB), which feature different support structures and sensor parameters. The TIB consists of four layers of silicon-microstrip detectors made of 320 micrometer-thick silicon and a strip pitch between 80 and 120 μm . The two innermost layers are made up of stereo modules where two single-sided sensors are mounted back-to-back, slanted at a stereo angle of 100 mrad to provide two-dimensional position resolution. The resolution that is achieved is between 23 and 34 μm in $r - \phi$ direction and 23 μm in z direction [13].

In the TOB region the radiation and occupancy levels are considerably lower, therefore the granularity can be decreased even further, which means that the strip pitches are

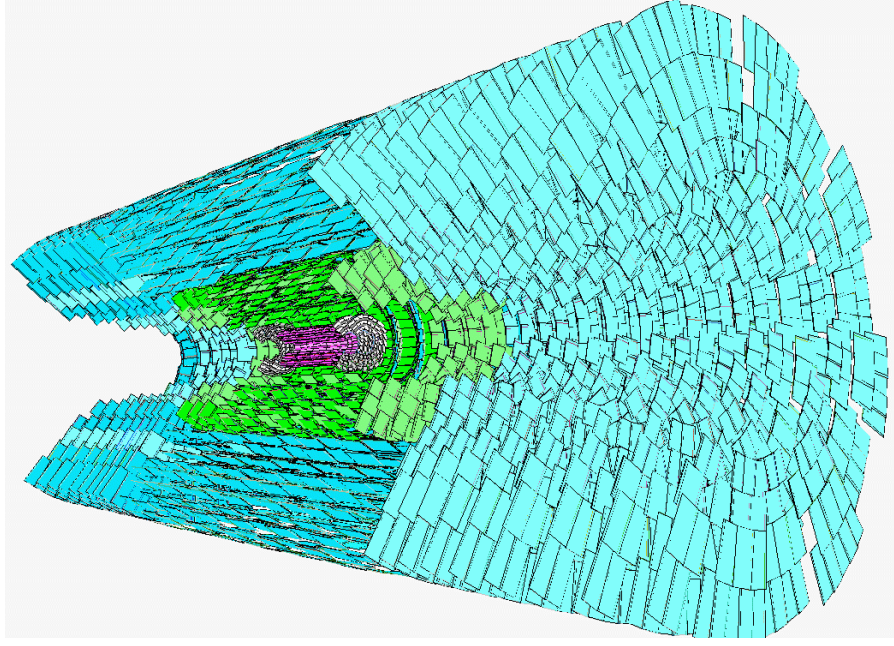


Figure 3.4: 3D drawing of the complete CMS tracker showing the position of all modules.

<http://zitogiuseppe.com/cms/tracker2.gif>

wider and the individual strips longer. In order to maintain the level of signal-to-noise ratio, 500 micrometer-thick silicon sensors are used. The TOB consists of six layers with strip pitches between 120 and 180 μm and the two innermost layers again feature a stereo angle. As the strip pitch is wider, the resolution is lower with 35 - 52 μm in $r - \phi$ - and 52 μm in z direction.

The end caps are divided into the Tracker End Cap (TEC) and Tracker Inner Discs (TID). The TEC consists of nine discs and the three layers of the TID fill the gap between TIB and TEC (see figure 3.1). The wedge-shaped modules are arranged in rings with the strips pointing towards the beam and the first two discs of the TID and discs one, two and five of the TEC feature double-sided modules with a stereo angle. Analog to the barrel region, the thickness of the silicon was chosen to be 320 and 500 μm for TID and TEC respectively. The number of rings for the TID is three and seven for the TEC and they are arranged in a way that they cover the maximum surface with the fewest gaps [20].

Sensors

Due to the large surface and the large number of sensors, a lot of careful consideration had to go into the selection of the technological baseline. The inner and outer barrel and end-cap regions all use AC coupled, poly-silicon biased, single-sided p-on-n devices processed on six-inch wafers [20]. This means that the readout electrodes (the microstrips) are highly-doped p^+ implants in a high-resistivity n-doped substrate. This is a

relatively simple and low-cost process widely used in the semiconductor industry and it has been proven to be sufficiently radiation-hard for the expected fluence over the nominal tracker lifetime. Such devices can be produced in large quantities and with high yields by the industry. The only difference between inner and outer silicon-strip tracker sensors is the thickness, which is larger for the outer regions (500 vs. 320 μm). Due to the various geometries for stereo modules, barrel- and end-cap regions and the varying pitch, a total number of 15 different sensor layouts was used.

The choice of p-on-n technology for the detectors yields some effects that have to be taken into account when planning the operation. Caused by radiation damage with increasing fluence these detectors undergo a process called type inversion where, due to radiation-induced effects, the effective doping of the substrate changes from n- to p-type. Consequently the depletion region will start growing from the back when the detector is biased which does not allow under depleted-operation any more. Details about the individual technologies and radiation damage can be found in Chapter 4. Table 3.1 summarizes the most important parameters of the used silicon sensors.

Table 3.1: Silicon-strip tracker characteristics[13]

Part	Nr. of Detectors	Thickness μm	Mean Pitch μm
TIB	2,724	320	81 / 118
TOB	5,208	500	81 / 183
TID	816	320	97 / 128 / 143
TEC	2,512	320	96 / 126 / 128 / 142
TEC(2)	3,888	500	143 / 158 / 183
Total	15 148		

Modules

A detector module is a basic unit of the the CMS tracker. It consists of one or two chained sensors, a carbon-fibre support frame, a pitch adapter and the readout hybrid (3.5). The sensor is glued to the support structure together with the power cable and wire bonded to the readout hybrid through the pitch adapter. Apart from the front-end chips (amplifiers), the hybrid contains a multiplexer and some other elements of the front-end (section 3.2). The maximum number of connected microstrips per module is 768, corresponding to 6 chips [21].

The carbon-fibre frame serves as a very light, yet rigid support with very low thermal expansion and as a thermal bridge through which the sensors and hybrids dissipate power to the cooling line. Again the large number of different geometries requires different module layouts. The production and assembly have been done at remote centers specializing in a certain geometry.

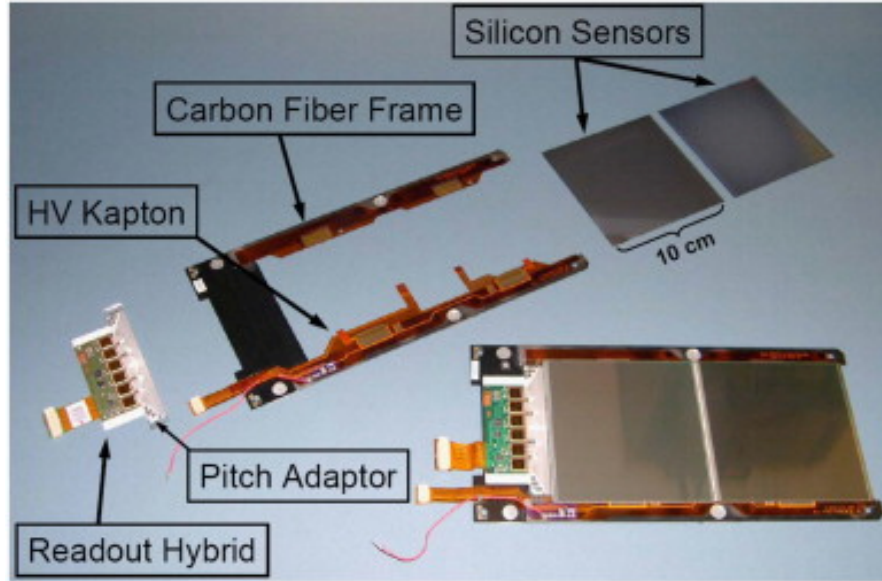


Figure 3.5: Individual components of a CMS silicon-strip tracker module [22].

Mechanical Support

Since the tracker has to be mechanically very well aligned to achieve the desired precision of the position measurements, the support structure has to be very stable structurally and precise, while minimizing material. Although the final alignment is done with particle tracks the initial positions of all sensors have to be known with high precision as a starting point and must remain stable over time and a wide temperature range.

For all these reasons carbon fiber is the material of choice for all mechanical supports. The TIB structure is designed as a series of low-mass cylindrical half shells with additional supporting ribs to increase the mechanical stability and hold the modules and all their services (cabling, optical fibers) [20]. Thin aluminum cooling pipes are routed over the surface of the shells and are in thermal contact with the heat sources on the modules (sensors and hybrids).

In the TOB so-called rods are used to hold the modules in place. The whole length is covered by two rods holding six or seven sensors each. The cabling and cooling pipes are directly incorporated into the rods that also hold part of the front-end electronics, like the optical hybrids. These rods are then inserted into an external support frame called wheel, also made of carbon fiber, which incorporates the final geometry of the system. Both the TIB and TOB have a longitudinal overlap of sensors to ensure full geometric coverage [21].

The TID and TEC support consists of discs that have routing options for all connections and the cooling circuit and are made of a honeycomb structure with carbon fiber reinforcements. They hold the individual rings of wedged modules on both sides so the whole area can be covered by the overlapping rings [20].

The cooling system is common for the whole strip tracker and consists of a closed circuit system with C_6F_{14} as coolant. The thermal contact between the module frames and the piping is established by the screws that hold the modules in place on their respective support structures. The nominal coolant temperature is -15°C , which translates to about -5°C on the silicon sensors. Additionally, the whole volume has to be supplied with dry gas to prevent condensation as an absolutely tight decoupling of the tracker from the surrounding volume is not possible [20].

3.2 Tracker Readout

Silicon-microstrip detectors are usually read out by charge-sensitive amplifiers. Due to the large number of ~ 9 million channels in the CMS tracker, this amplifier is realized as a highly integrated front-end chip that has to meet very tight requirements in terms of particle rate, magnetic field, material budget and radiation tolerance. Since the event rate in the LHC collisions is 25 ns, fast sampling is absolutely necessary but data has to be stored for at least the duration of the Level-1 trigger decision, which takes 3.7 microseconds, a time equivalent to 150 bunch-crossings. The general performance of the tracker in terms of position resolution can benefit from charge-sharing effects between the individual strips and therefore it has been decided to read out the full analog signal from each individual strip and transmit it to the front-end driver boards, where it is processed. The following section will describe the front-end chip of the strip tracker and the general architecture of the readout system.

The Front-End Chip

The readout chip used in the CMS silicon-strip tracker is called APV25 and was specifically developed to meet the strict requirements of the experiment. Excellent radiation-tolerance was considered very important and consequently iterations of the chip were produced in different radiation-hard processes. Finally the implementation in a $0.25\ \mu\text{m}$ CMOS process met the requirements and also provided significant savings of costs.

The chips have 128 input channels split into two groups of 64 channels. Each channel consists of a pre-amplifier stage which is coupled to a shaping stage which produces a $50\ \text{ns}$ CR-RC pulse. A gain inverter between the pre-amplifier and the shaper ensures same-polarity output independent of the input-signal sign, which allows to read detectors with electron- (n-in-n, n-in-p) and hole (p-in-n) signals [23].

The CR-RC pulse of the shaper of each channel is sampled at a clock rate of 40 MHz and written into a 192 cell-deep pipeline, which allows for storage for a maximum time of $4.8\ \mu\text{s}$ and thus longer than the $3.7\ \mu\text{s}$ of a Level-1 trigger decision. Upon the reception of a trigger signal the content of the affected pipeline-cell columns are read out by the Analogue Pulse Shape Processor (APSP), which has two operation modes (figure 3.6a):

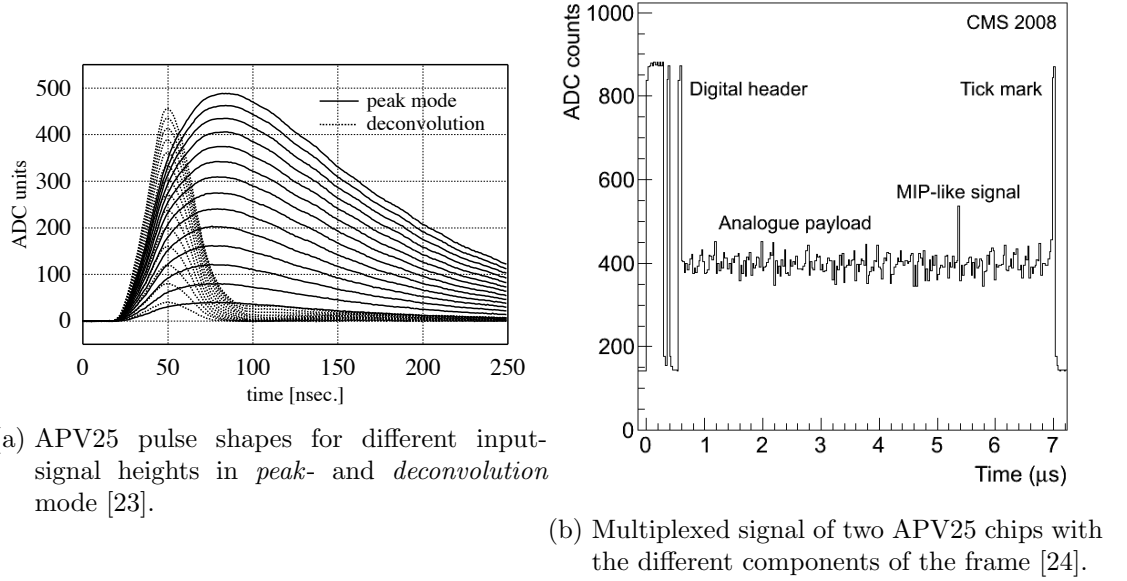


Figure 3.6

Peak-mode: In peak-mode only one cell per input channel is read out and the output is timed to the peak of the analog pulse with a relatively slow rise time of 50 ns.

Deconvolution-mode: In this mode three consecutive samples are read and the output is a weighted sum of the three. This results in a reshaped, shorter pulse that is peaked at 25 ns, which corresponds to a single bunch crossing.

After this stage data of each channel is multiplexed to a differential current with non-consecutive order of channels. The resulting signal is 7 μ s long, has a 12-bit digital header that includes address and error information, followed by the analog signal of 128 strips, and is terminated by a *tickmark* (figure 3.6b), which is used for many purposes like for example the calibration of the absolute signal [23] [24].

The more or less constant ADC count of the channels that show no particle hit in figure 3.6b is called the *pedestal* value and is unique to each channel. Another contribution that varies with time and is small compared to the pedestals but common to all 128 channels of a chip is called *common-mode* shift [24].

Readout System Architecture

Apart from the readout chips the hybrid that is part of each single detector module also has the APVMUX chip, which multiplexes the signal of two front-end chips to a single line, the Detector Control Unit (DCU), for monitoring the module and a Phase Locked Loop chip that synchronizes clock- and control signals.

The multiplexed signal from two chips then is converted to an optical signal using

Linear Laser Drivers (LLDs, optohybrid) and is then transmitted to the front-end drivers (FEDs) in the counting room of the experiment via optical fibers [24].

These front-end drivers each receive signals on 96 optical inputs, which corresponds to 192 APV chips, and digitize them using 10-bit analog-to-digital converters (ADC). This digitized signal is then processed by fast circuitry using Field Programmable Gate Arrays (FPGA) to reduce the amount of data that has to be written to the data acquisition system. There are three operating modes for the FEDs [24]:

Scope mode SM basically writes out raw data as shown in figure 3.6b and includes no further processing.

Virgin Raw VR operation mode removes all digital information from the signal header and the tickmark from the end and provides the digitized signal of all 128 channels.

Zero Suppressed ZS mode makes full use of algorithms implemented through the FPGAs to perform pedestal subtraction and common-mode correction and the output contains only channels above a threshold of five times the detector noise, thus potentially containing a signal from a particle hit. Whenever such a seed signal is found, neighboring channels are checked for signals exceeding two times the detector noise. This clustering process reduces the initial data rate by an order of magnitude.

Since the gain of the laser drivers and the length of the individual fibers vary, the signal of the front-end chips have to be precisely timed and calibrated. The amplitude of the tickmark signal, which is supposed to be constant over time and all chips, is used to calibrate the gain of the laser drivers which are tuned in such a way that the amplitude of the tickmark corresponds to 640 ADC counts. This signal also corresponds to the maximum output of the APV chip, which is 175,000 electrons. Using this, an absolute calibration factor for the detector response in electrons can be obtained [24]:

$$f_c = [ADC]/[e^-] = 640 \pm 20 \% / 175,000 = 274 \pm 14 e^- / ADC \text{ count} \quad (3.1)$$

The control of the modules is performed by the front-end controller (FEC), which distributes the LHC clock, trigger- and control signals to the modules through optical fibers via a digital optohybrid and the Communication and Control Unit (CCU) that is shared by several modules in a control ring (figure 3.7).

3.3 Performance

The all-silicon tracker of CMS was designed to provide robust tracking information along with good momentum resolution of high p_T particles. In the axial magnetic field of 3.8 T the nominal relative momentum resolution is 0.7 % for 1 GeV/c and 5 % for 1 TeV/c particles [26].

In order to get an estimation of the capabilities and useful information about calibra-

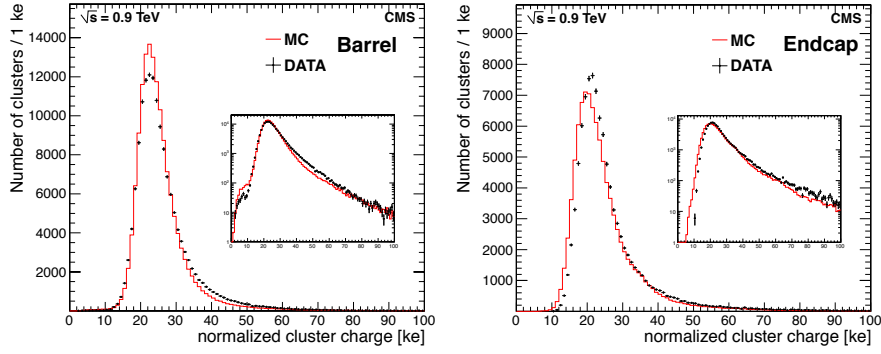
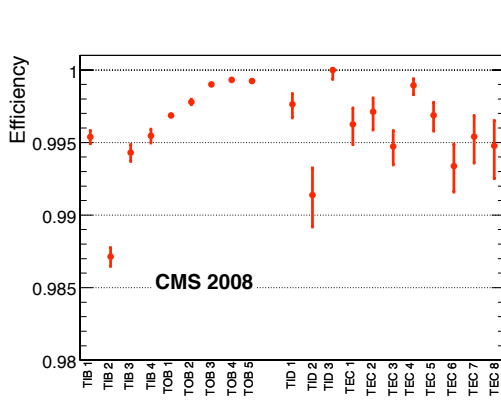
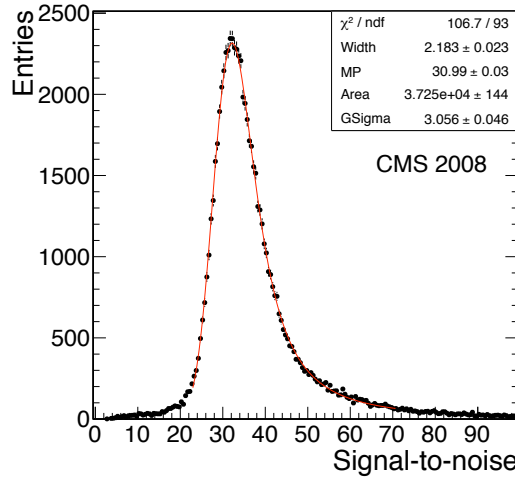


Figure 3.8: Normalized cluster charge distributions fitted with a convolution of a Landau- and a Gaussian distribution for the pixel- barrel and end-cap modules at 0.9 TeV [26].



(a) Hit efficiency for the different barrel- and end-cap layers of the CMS tracker after removal of non-functional modules [24].



(b) Signal-to-noise ratio distribution of the TOB layer-5 modules [24].

Figure 3.9: Examples of the CMS silicon-strip tracker performance.

In the strip tracker the signal-to-noise ratio is used as a benchmark for individual detector performance. Therefore the total cluster signal is divided by the cluster noise, which is defined as $\sigma_c = \sqrt{\sum_i \sigma_i^2} / \sqrt{N_{strips}}$. Since the TIB and TOB are made from detectors of different thicknesses and sizes – thicker detectors having higher signal, longer strips having higher noise – the figures differ for both types. In the results presented in [24] the TIB modules reach values from 25 to 30 as the most probable value of the Landau fit and the TOB values between 31 and 36 (figure 3.9b).

The hit resolution was measured and the results for small incident angles are presented in table 3.2 [24].

Table 3.2: Measured resolution of barrel layers.

Layer	TIB 1-2	TIB 3-4	TOB 1-4	TOB 5-6
Pitch [μm]	80	120	183	122
Resolution [μm]	17.2 ± 1.9	27.7 ± 3.6	39.6 ± 5.7	23.2 ± 3.6

3.4 The Tracker in the HL-LHC Scenario

As described in chapters 1 and 2 the instantaneous luminosity of the LHC will reach $5 \times 10^{34} \text{ cm}^{-2}\text{s}^{-1}$ in the high-luminosity era. For the tracker this translates into a dramatically increased radiation environment of up to $10^{15} \text{ 1 MeV n}_{eq} \text{ cm}^{-2}$ and increased pileup of events in the bunch crossings in the order of 200. Since the current tracker is not able to deal with such conditions in terms of radiation hardness and granularity, it is scheduled to be replaced entirely.

This replacement allows for a complete redesign, starting from the sensors and modules, front-end electronics, powering scheme and cooling system to the general layout. The main requirements are [27]:

- An increase in granularity in the same order of magnitude as the instantaneous luminosity increase to deal with increased pileup and to keep the occupancy low.
- A drastic reduction of the material in the tracking volume and therefore an improvement of momentum resolution for high p_T particles.
- Dramatically improved radiation tolerance of the silicon sensors.
- The possibility of including real-time track-based information in the Level-1 trigger decision, allowing for immediate identification of high p_T tracks and thus greatly reducing the amount of data that has to be processed by the back-end.

To achieve these goals extensive R&D effort is being undertaken by the collaboration and the individual components will be described briefly. The sensors R&D, which is the subject of this thesis, will be described in more detail in later chapters.

Front-End Electronics

Since all services like cabling and cooling infrastructure are to be taken over from the present tracker, the available bandwidth for signals is limited, especially since the granularity increase will dramatically increase the number of readout channels. Therefore the analog signal processing will be dropped and replaced in favor of a binary chip. This CMS Binary Chip (CBC) will read 128 channels and will feature a 256-cell-deep pipeline to store digital event data over a longer period of time (trigger latency up to 6 μs) [27].

In addition, the implementation of a high speed bi-directional trigger- and data link is scheduled to increase the available bandwidth, which is limited by the number of presently installed fibers, and to simplify the control- and readout systems which are presently separated.

Proposed Modules

In order to identify high p_T tracks on the modules themselves, it is necessary to combine the information from closely-spaced sensors with fine pitch. The correlation could be done by the front-end electronics directly but for that purpose strips from both sensors have to be bonded to the same hybrid, which has to be placed at the edge of the sensor. There are two kinds of proposed modules (figure 3.10):

pT-2S

This module consists of two strip sensors with parallel, approximately five-centimeter-long strips and a strip pitch of 90 μm . It can be used for the outer layers of the future tracker but provides no z information.

pT-PS

This module is designed to overcome the limitations of the pT-2S by providing additional z information. A pixel sensor with a bump-bonded readout chip that also takes care of the hit correlation is combined with a strip sensor. The length of the strips will be around two cm and the pixels will be realized in a size of 100 $\mu m \times \sim 1 mm$ to meet the granularity requirements in the inner tracker.

Power and Cooling

Since the power cables that are presently installed in CMS are to be reused, the implementation of DC-DC power converters directly on the modules is studied to deliver power at higher voltage, and thus reducing the ohmic losses, as the general power consumption of the new tracker will likely be higher than that of the present one.

Limiting this consumption can partially be achieved by cooling the tracker to lower operating temperatures but maintaining the same services. Two-phase cooling with CO_2 as coolant has been shown to be a viable solution and operating temperatures of $-20^\circ C$

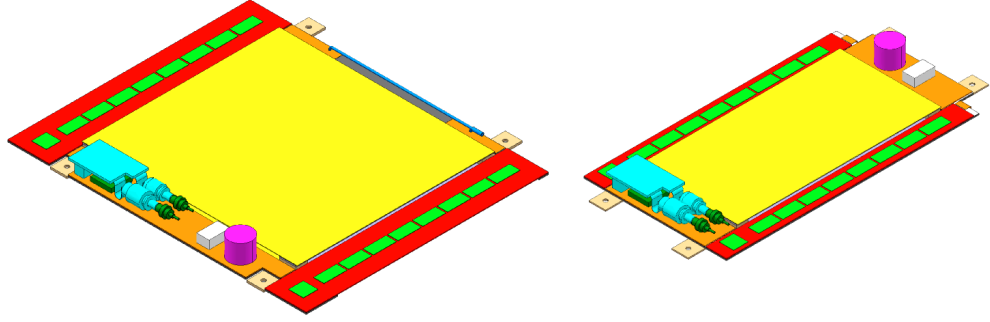


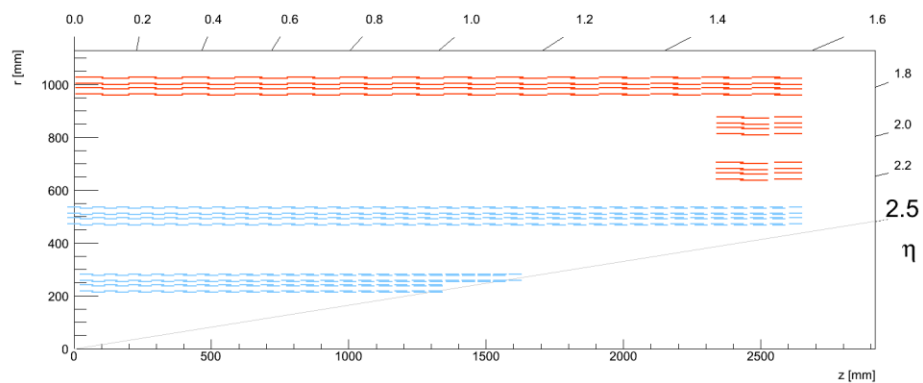
Figure 3.10: Schematics of the pT-2S and pT-PS modules for the CMS tracker upgrade [27]. Each module consists of two closely spaced sensors (second sensor not visible).

could be reached [27].

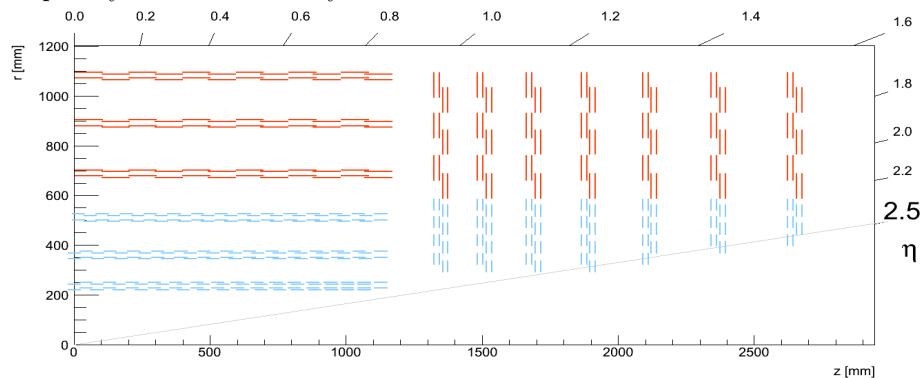
Possible Layouts

Several possible layouts of the future CMS tracker are currently being studied, using simulations [28]. Two approaches are possible. The first one is optimized for fast Level-1 track finding and therefore governed by limitations of the electronics. It features an extended barrel section and no end caps, with three so-called super layers consisting of two layers of closely-spaced pT-PS modules each. The measured signals have to be hierarchically correlated, first on the module itself, then within the super layers, and finally this "tracklet" information has to be combined to tracks with information from the other super layers.

The other approach features a more generic layout with a barrel- and end-cap section which employ both types of modules – pT-PS in the inner layers and pT-2S in the outer ones. Fast track reconstruction is more complex with this layout and the option of using Pattern Recognition Associative Memory (PRAM), which matches signals from the sensors to coarse, pre-determined patterns for the Level-1 trigger, is being studied. This approach is optimized for general tracking performance but associative memory, although it has already been used successfully in high-energy physics, needs to be proven a feasible technology for such a large-scale application. Figures 3.11a and 3.11b show schematics of the two layouts under investigation. pT-2S modules are drawn in red and pT-PS modules are shown in blue.



(a) "Long-barrel" layout optimized for fast (Level-1) track triggering. This layout is governed by the need for hierarchical correlation of information from modules to super layers to the whole system.



(b) A more conventional layout with traditional barrel- and end-cap regions. To simplify the tracking procedure, pattern-recognition associative memory is being studied.

Figure 3.11: Possible layouts for the Phase-2 tracker upgrade created with [28].

4 Silicon Sensors in High-Energy Physics

4.1 Working Principle and Limitations

In this chapter the working principle of silicon sensors in general and the aspects of their operation in high-energy physics will be described briefly. As the investigation of radiation-hard silicon-sensor technology for future experiments is the scope of this thesis, special attention will be paid to the various approaches that have been investigated.

A very detailed and comprehensive summary of the use of silicon sensors in high-energy physics in terms of working principle, technology and operational history can be found in [29], where the information in section 4.1 is taken from unless otherwise stated.

4.1.1 Silicon as a Semiconductor and the pn-Junction

Silicon is a semiconductor material that occurs naturally in the form of silicon dioxide (quartz) and more complex compounds. The pure element, which has to be produced industrially, is a regular crystal and shows the typical properties of a semiconductor:

- At low temperatures it acts as an insulator;
- At higher temperatures it shows conductance in the range between metal and insulator.

This behavior is explained by the quantum-mechanical properties of the regular lattice that the silicon atoms form in the crystal and the bonds between the individual atoms. Silicon is a group-IV element and has four valence electrons that can enter covalent bonds. Those electrons, however, can be excited to a free state by adding energy exceeding a threshold that is characteristic of the material. In silicon this band¹ gap is 1.12 eV and it can be altered by adding artificial impurities to the material. At low temperatures the valence band is full and the conduction band in intrinsic silicon is empty, with the concentration of charge carriers of both signs being equal to the intrinsic charge-carrier density. However, it is possible to change the conductivity behavior by adding additional states inside the band gap of intrinsic silicon. This process is called doping and figure 4.1 shows some levels that can artificially be added to the silicon band structure.

¹The band structure of energy levels is a result of the regularity of the atomic lattice of the material.

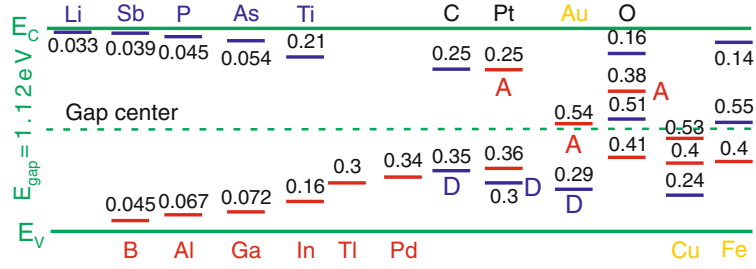


Figure 4.1: Different levels in the band gap that correspond to different impurities in the silicon lattice [29].

Typical dopants are group V elements like phosphorus, which have one more electron than silicon, and therefore act as donors and create 'n-type' silicon and group III elements like boron, which have only 3 valence electrons and therefore an additional hole² (acceptor). The resulting material is called 'p-type' silicon. The resistivity (or conductance) of the material then reads

$$\rho = \frac{1}{e(\mu_e n + \mu_h p)} \quad (4.1)$$

and is dependent on the concentration of charge carriers (electron density n and hole density p), their respective mobilities $\mu_{e/h}$ and the elementary charge. μ itself is dependent on the drift velocity and the electric field via the relation $\mu = v_D/E$. In practice this relation can be rewritten to only take into account the majority-charge-carrier density in p- or n-type silicon. The dopants do not only act as sources of additional charge carriers but can also act as traps. The additional levels that are introduced in the band gap facilitate transitions from one band to the other.

In intrinsic silicon, electron-hole pairs are constantly created by thermal excitation, which does not make it an appealing material for a particle detector as the number of charge carriers created by a traversing particle through ionization is rather small compared to the intrinsic density. In order to get a measurable signal the silicon needs to be depleted of free carriers, which is achieved by applying a reverse bias voltage to a pn-junction (p- and n-type silicon are brought into contact). In this junction, in thermal equilibrium, a space-charge region is created, as the fermi-energy levels (close to the conduction band in n-type and the valence band in p-type) have to be the same. This moves the levels of valence- and conduction band, thus creating the space-charge region through an electrical field that is induced by the diffusion- and recombination currents between the two differently-doped regions. This field then prevents further diffusion and depletes the space-charge region of free carriers. Figure 4.2 shows the energy-band structure and space-charge region at a pn-junction.

In order to exploit the signal that a charged particle traversing the silicon creates fully, the depleted region has to be as large as possible. This is achieved by applying a

²If an electron is excited to the conduction band it leaves an unmatched positive charge in the valence band that can travel through the lattice and therefore, just like an electron, can act as charge carrier.

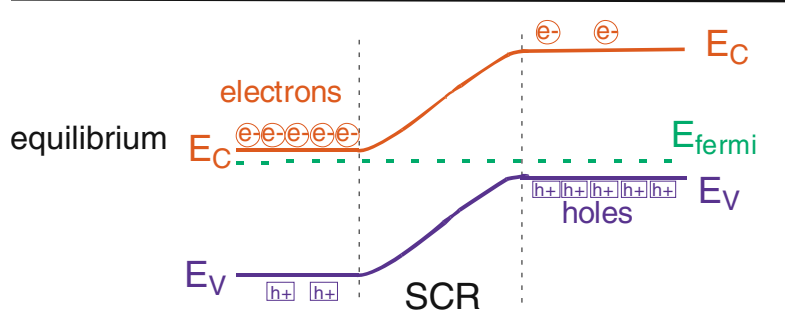


Figure 4.2: Schematica of a pn-junction and energy levels with space-charge region SCR [29].

reverse bias voltage to the pn-junction, which increases the potential barrier and thus the width of the depleted region between the two differently-doped contacts. By varying the voltage the thickness of the carrier-free region can be tuned. Since the signal created in a detector should be as strong as possible, the whole volume has to be depleted. For that reason the **full depletion voltage** V_{fd} is an important operating parameter of a detector and reads

$$V_{fd} = \frac{D^2}{2\epsilon\mu\rho} \quad (4.2)$$

with D denoting sensor thickness, ϵ the dielectric constant, μ the charge carrier mobility, and ρ the resistivity.

If the applied bias voltage exceeds the full depletion voltage, the equilibrium is disturbed and thermally-generated charge carriers are swept out of the depleted region and manifest themselves as a current. This is called 'dark-' or 'leakage current' and the current density reads

$$j_l = \frac{1}{2}en_i\sigma v_{th}N_t w A \quad (4.3)$$

with e the elementary charge, n_i the intrinsic carrier density, σ the conductance, v_{th} the drift velocity, N_t the contamination with impurities with levels close to the middle of the band gap and w the width of the depleted region. This leakage current is also temperature-dependent with $n_i \propto e^{\frac{E_g}{k_B T}}$.

Since the two electrodes of a pn-junction with the depleted bulk of silicon in between can be considered a capacitor, a capacitance measurement can be used to extract the full depletion voltage

$$C = A \sqrt{\frac{\epsilon_0 \epsilon_r S_i}{2\rho\mu V_{bias}}} \quad (4.4)$$

with A the capacitor surface and ϵ the dielectric constants of vacuum and silicon. Above V_{fd} this capacitance becomes constant as the dielectric (the depleted silicon) now fills the whole distance between the electrodes. Figure 4.3 shows the leakage current and $1/C^2$ as a function of bias voltage. The relation $V \propto \frac{1}{C^2}$ arises from equation 4.4 and makes the identification of the full depletion voltage more obvious.

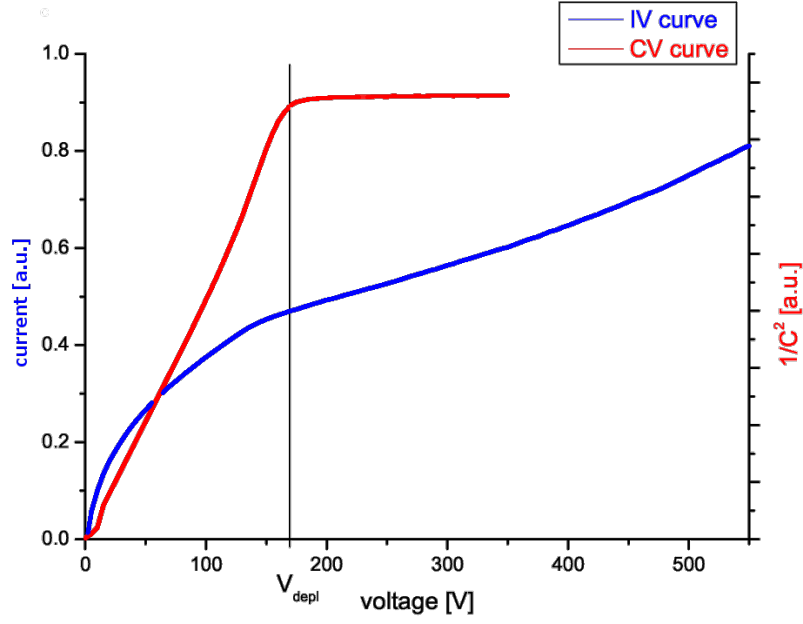


Figure 4.3: IV and $1/C^2V$ relation of a silicon sensor. The 'kink' identifies the full depletion voltage.

4.1.2 Energy Loss – Signal Creation

The principle by which particles are detected is their interaction with matter through ionization. In gaseous detectors the atoms of the gas are ionized and in silicon the traversing particle creates electron-hole pairs. Through this interaction the incident particles lose energy and this energy loss – described by Bethe and Bloch in their famous formula – in differential form reads

$$-\frac{dE}{dx} = 4\pi\rho N_A r_e^2 m_e c^2 z^2 \frac{Z}{A} \frac{1}{\beta^2} \left[\frac{1}{2} \ln\left(\frac{2m_e c^2 \beta^2 \gamma^2 T_{max}}{I^2}\right) - \beta^2 - \frac{\delta(\gamma)}{2} \right] \quad (4.5)$$

with z the charge of the incident particle, T_{max} the maximum kinetic energy that can be transferred to a single electron in a collision, I the mean excitation energy, Z the atomic number, A the atomic mass, N_A the Avogadro number, m_e the electron mass, c the speed of light, r_e the classical electron radius, β the relativistic beta v/c , $\gamma = 1/\sqrt{1 - \beta^2}$ and δ a density effect correction.

Figure 4.4 shows this differential energy loss as a function of incident particle momentum for muons in copper. The minimum around 500 MeV represents the minimum deposited energy in the absorbing material and a muon of that energy is called minimum-ionizing particle (MIP). These MIPs are hardest to detect and therefore serve as benchmarks for detectors.

The number of collisions in a thin layer like a silicon sensor (several hundred μm)

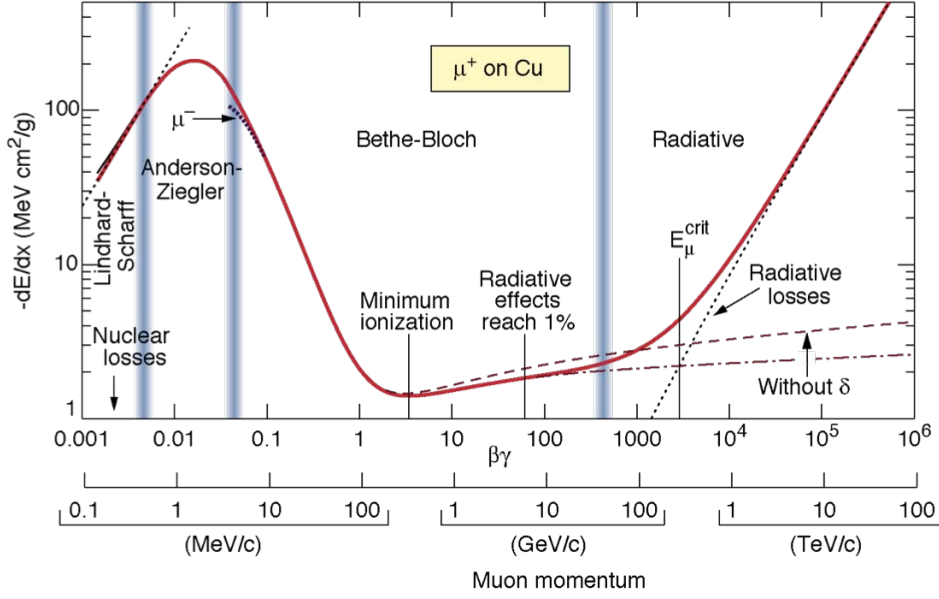


Figure 4.4: Differential energy loss (stopping power) of muons in copper for different incident particle energies calculated with the Bethe-Bloch formula 4.5.

is subjected to statistical fluctuation, as is the energy transfer per scattering process. This was first described by Landau and the deposited charge in a thin layer follows a so-called Landau distribution. It takes high-energetic δ electrons into account, which are responsible for the long asymmetric tail of the distribution. The probability-density function reads

$$p(x) = \frac{1}{\pi} \int_0^\infty e^{-t \log t - xt} \sin(\pi t) dt \quad (4.6)$$

and the characteristic function is

$$\phi(t; \mu, c) = e^{it\mu - |ct|(1 + \frac{2i}{\pi} \log(|t|))} \quad (4.7)$$

with μ being the most probable value, which is approximately 30 percent lower than the mean value, and c being a scale parameter. Figure 4.5 shows an example of such a Landau distribution.

The energy that an incident particle has to deposit in silicon to create a single electron-hole pair is 3.6 eV. This is approximately three times higher than the band gap energy but also accounts for phonon excitation. The most probable number of electron-hole pairs that are created in silicon per μm is 76, while the average is 108 [29]. In a 300 μm -thick detector this results in $\sim 22,000$ electron-hole pairs whereas the charge carrier density in intrinsic silicon is in the order of 10^{10} cm^{-3} . From these numbers the need to operate with depleted pn-junctions becomes obvious as the signal that a particle would create in intrinsic silicon would drown in the thermally-generated charge carriers.

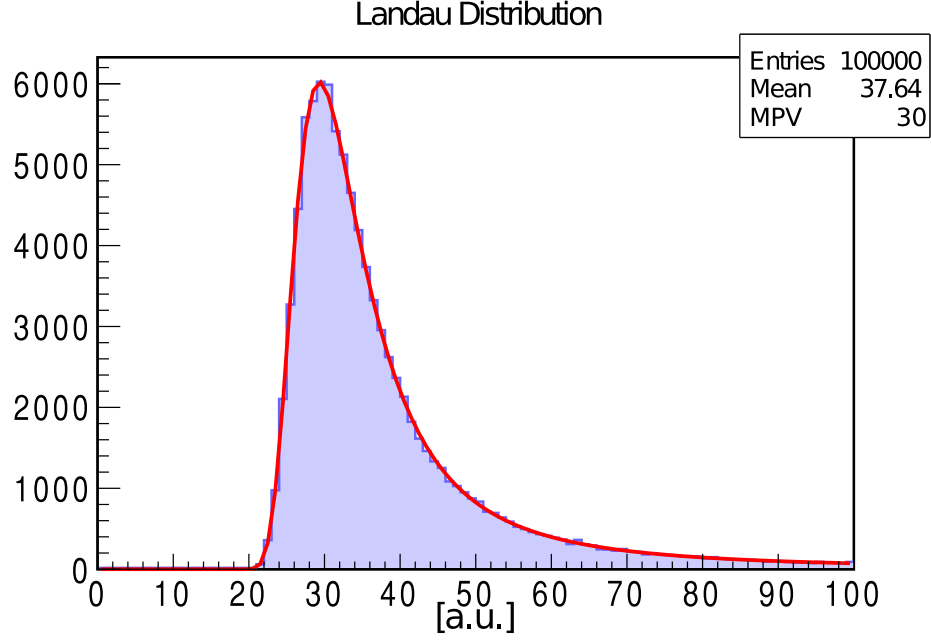


Figure 4.5: Landau distribution with arbitrary scales. The most probable value (MPV) is different from the mean value of the truncated distribution and not defined otherwise.

4.1.3 Design of Position-Sensitive Devices

Silicon sensors in high-energy physics are mostly used as position-sensitive devices. Therefore one or both of the electrodes of the pn-junction are segmented. The starting point is an either n-or p-doped silicon wafer that is implanted with strips or pixels of a certain geometry on one surface. For the sake of simplicity the basic concepts of position-sensitive devices will be presented in the example of a simple, planar, single-sided, p-on-n microstrip sensor. The necessary changes for n-on-p devices will be described later.

On one side of the n-type wafer, p^+ -doped strips are implanted into the bulk, while the other side is doped with donors evenly across the whole surface, making it n^{++} . The strips are then covered by a layer of SiO_2 that acts as isolation. On top of this dioxide layer, the strips are covered with a thin layer of aluminum that is now capacitively coupled to the actual implant. This is also the basic layout of a so-called metal-oxide-semiconductor (MOS) structure and serves the purpose of decoupling the readout electronics from the implant. The strips are connected to an implanted bias ring via a poly-silicon resistor (ohmic resistor) to distribute the bias voltage to all the electrodes evenly. Figure 4.6a shows a lateral cut through a single strip and illustrates the principle of AC coupling and poly-silicon biasing.

When an ionizing particle traverses the biased and fully depleted sensor it creates electron-hole pairs that then separate in the electric field and drift towards the electrodes. In the case of a p-on-n detector, the electrons drift towards the backplane and the holes

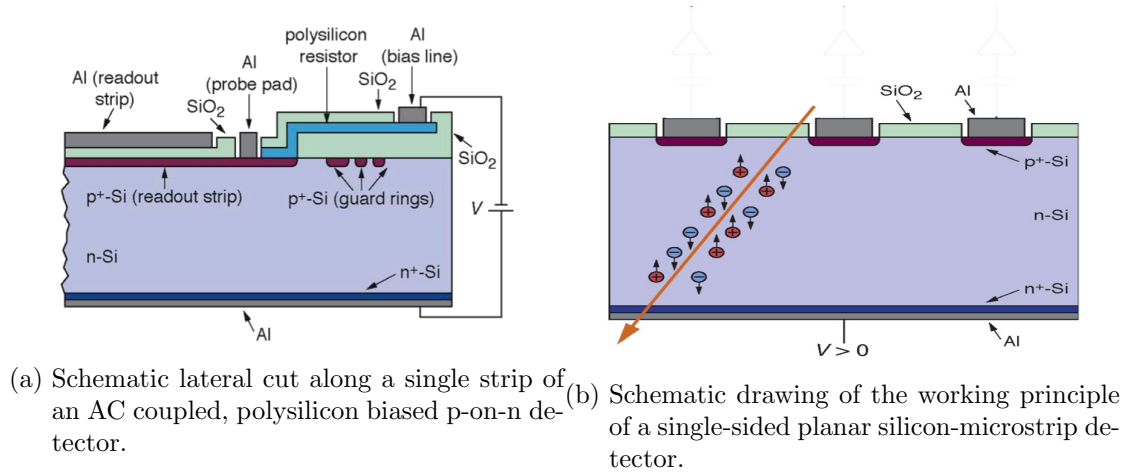


Figure 4.6

drift towards the strips, where they induce a signal on the capacitively-coupled aluminum readout strips that are connected to the readout chip. In n-on-p or n-in-n detectors, the electron signal is collected at the strips and the holes drift to the backplane. The segmentation allows collection of the whole signal of a traversing particle on few strips and therefore a position-sensitive measurement. The process of signal creation and drift is illustrated in figure 4.6b.

The silicon dioxide that is used as dielectric has a very important impact on the surface properties of the sensor. It has a charge density of its own and an important influence on the isolation of the strips through the Si-SiO₂ interface. Depending on the sign of the oxide charge, there are two possibilities:

Oxide charges have the same polarity as majority-bulk carriers:

In this case the majority-bulk carriers are driven into the bulk material and when a reverse bias voltage is applied to the strips, the depleted region grows from the strips, also depleting the volume in between the strips. This ensures electrical isolation of the strips, which is absolutely necessary for position-sensitive devices and is the case for p-strips in n-bulk detectors.

Oxide charges and majority-bulk charge carriers have opposite signs

Here the oxide charges attract the majority carriers from the bulk and they form an accumulation layer at the Si-SiO₂ interface, which shortens the strips and thus ruins the position sensitivity. Prominent examples of this effect are n-on-p devices or the n^{++} strips on the backside of double-sided devices (figure 4.7). The technological possibilities of overcoming this effect will be discussed in chapter 5.



Figure 4.7: Schematic drawing of the accumulation layer for the opposite-sign oxide- and bulk-charge case.

4.1.4 Parameters

Some intrinsic electrical parameters of silicon sensors, like leakage current and the correlation of the full depletion voltage V_{fd} with the detector capacitance have already been described in section 4.1.1. Some other parameters that mainly affect the performance in terms of particle detection will be described briefly in this section.

Interstrip Capacitance

Along with the total detector capacitance, or – in case of segmented detectors – the capacitance of one single strip to the backplane, the capacitance between the individual strips plays an important role for the performance of the detector. Together with the coupling capacitance between the strip implant and the aluminum, this interstrip capacitance C_{int} determines the capacitive network that is connected to the input of the readout chip. Since charge sharing (through capacitive coupling) between strips is a desirable effect to improve the spatial resolution the interstrip capacitance should have a well-defined behavior but it also contributes to the load of the readout and thus affects noise performance.

Noise

Due to quantum-mechanical effects and the finite operating temperatures of silicon sensors in high-energy physics experiments – even in a fully depleted sensor – electron-hole pairs are constantly created. These pairs manifest themselves as noise and compete with the signal from traversing particles and thus affect the performance of the detector. Several factors contribute to this noise which is expressed as **equivalent noise charge** Q_n or **ENC**. Figure 4.8 shows an equivalent network diagram and the individual factors are

- the load capacitance C_l that the charge-sensitive amplifier (readout chip) sees at its input,
- the leakage current I_L of a strip (*shot noise*),
- the parallel resistance of the bias resistor of a single strip R_P ,

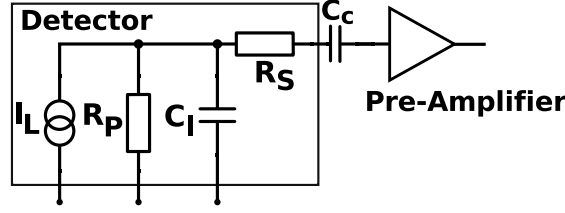


Figure 4.8: Equivalent network diagram of the individual contributions to the detector noise.

- the serial readout resistance of the aluminum metallization R_S
- and the coupling capacitance C_c , which is very large and can therefore be ignored in the calculation of the noise

and they are summed up quadratically,

$$ENC = \sqrt{END_{C_I}^2 + ENC_{I_L}^2 + ENC_{R_P}^2 + ENC_{R_S}^2} \quad (4.8)$$

where the individual contributions read:

$$ENC_{I_L} = \frac{e}{2} \sqrt{\frac{I_L t_p}{q_e}} \quad (4.9)$$

$$ENC_{C_I} = a + b C_I \quad (4.10)$$

$$ENC_{R_P} = \frac{e}{q_e} \sqrt{\frac{k_B T t_p}{2 R_P}} \quad (4.11)$$

$$ENC_{R_S} = C_I \frac{e}{q_e} \sqrt{\frac{k_B T R_S}{6 t_p}} \quad (4.12)$$

In these equations e is Euler's number, q_e is the elementary charge, a and b are constant amplifier parameters, k_B is the Boltzmann constant and t_p is the integration- or peaking time of the amplifier. If this peaking time is very short, as it is the case in the LHC experiments, the noise is determined by the capacitances of a strip as the shot noise ENC_{I_L} caused by the leakage current becomes negligible. In other experiments, where the integration time of the front-end electronics is longer, this becomes the dominating factor.

The detector noise, contrary to the signal, which only depends on the depleted volume, can be tuned by choosing appropriate sensor-design parameters for the specific application.

Spatial Resolution – Charge Sharing – ETA Function

Particles that traverse a silicon detector create electron-hole pairs along their path. This cloud of charges drifts and diffuses in the electric field in the detector and thus the charge

that a single particle creates can spread over several strips, depending on the distance between the strips, called pitch. This charge sharing is heavily affected by the interstrip capacitance C_{int} and can positively affect the spatial resolution if the sensor is read out in analog (the pulse height of each strip is considered).

If the charge of a traversing particle is not shared between strips the resolution is binary³ and dominated by the strip pitch according to

$$\langle \Delta x^2 \rangle = \frac{1}{p} \int_{-p/2}^{p/2} x^2 dx = \frac{p^2}{12} \Rightarrow \sigma = \frac{p}{\sqrt{12}} \quad (4.13)$$

whereas charge sharing allows the use of center-of-gravity- (CoG) or so-called η -algorithms to improve the resolution of hits between two strips with

$$x_\eta = x_{\text{left strip}} + \frac{S_{\text{right strip}}}{S_{\text{left strip}} + S_{\text{right strip}}} (x_{\text{right strip}} - x_{\text{left strip}}) \quad (4.14)$$

the hit position in between the strips and S being the charge of a strip. The spatial resolution is then dependent on the signal-to-noise ratio.

$$\sigma \propto \frac{p}{\text{Signal/Noise}} \quad (4.15)$$

4.2 Radiation Damage

Since the investigation of radiation-hard silicon for a future high-luminosity collider is the subject of this thesis, a short introduction to the mechanisms responsible for radiation damage in silicon detectors and their measurable consequences will be given in the following section [29] [30] [31].

4.2.1 Bulk Damage – Microscopic and Macroscopic Consequences

There are two major mechanisms via which particles can interact with atoms in the silicon lattice. The first is electromagnetic interaction with the hull of the atom, which is responsible for the formation of signals. The second process is interaction with the nucleus, either via the strong- or the electromagnetic force, and this is the main source of bulk damage in the silicon. The two main effects of irradiation are

- displacement of lattice atoms from their initial position and
- nuclear reactions

Displacement can create several different kinds of point defects like interstitials or vacancies, but also more complex combinations of these two (Figure 4.9). The second process

³Strip is hit or not hit.

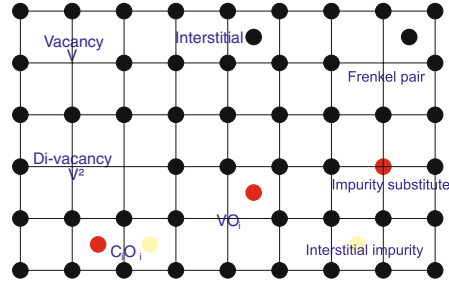


Figure 4.9: Different kinds of point defects in the silicon lattice [29].

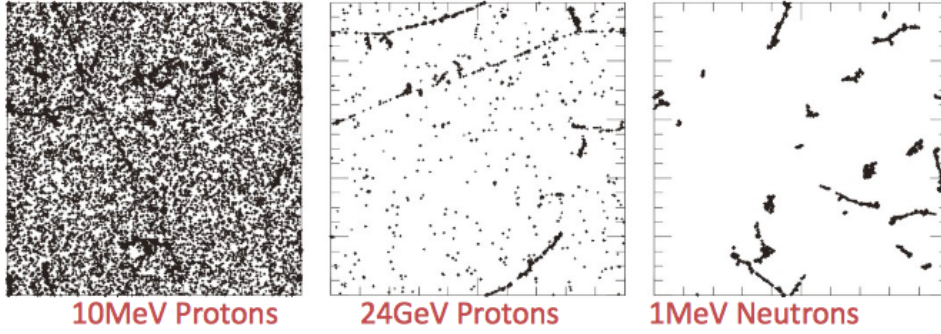
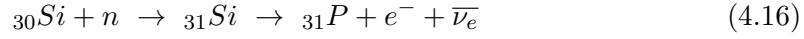


Figure 4.10: Simulation of defects created by different incident particles with different incident energies [32].

is the interaction of incident particles with the nucleus via nuclear interactions leading to processes like for example



which turns a silicon atom into an additional donor. These defects created by displacement and nuclear interactions create new levels in the band gap that have effects on the silicon properties and manifest themselves in changes of macroscopic properties [31]:

- change of the effective doping concentration N_{eff} and thus the full depletion voltage V_{fd} by creation of additional acceptor levels
- increase of the dark current
- decrease of the charge-collection efficiency CCE

Different incident particles and energies create different kinds of lattice-displacement damage. As shown in figure 4.10, high-energy, charged particles and neutrons are more likely to create clusters of defects while lower-energy, charged particles create more point defects. The energy required to displace a silicon atom from its lattice position is ~ 25 eV whilst the threshold for defect cluster creation via a primary knock-on atom (PKA) is around 5 keV.

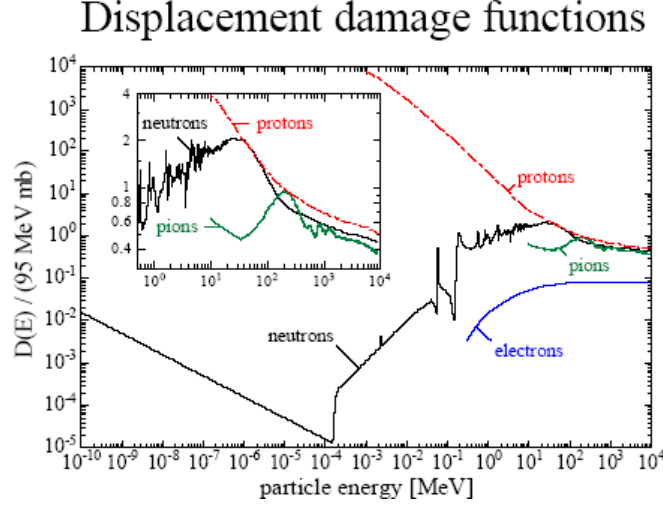


Figure 4.11: Displacement-damage cross-sections for different particles as a function of energy [33].

A common way to quantify the damage produced by a given radiation source is to calculate the Non-Ionizing-Energy Loss (NIEL). Commonly, neutrons of 1 MeV are used as reference particles and the so-called hardness factor κ is calculated according to

$$\kappa = \frac{\int D(E)\Phi(E)dE}{D(E_{neutron=1MeV}) \int \Phi(E)dE} \quad (4.17)$$

with $D(E)$ the total displacement-damage cross-section in barn⁴ and $\Phi(E)$ being the particle fluence. The numeric value for the displacement cross-section of 1 MeV neutrons is 95 MeV mb/cm². Scaling for any particle with any energy can be obtained by calculating the so-called 1 MeV neutron-equivalent fluence Φ_{eq} .

$$\Phi_{eq} = \kappa\Phi \quad (4.18)$$

Figure 4.11 shows the calculated displacement-damage cross-sections for neutrons, protons, pions and electrons.

In the following section, the macroscopic effects of the above mechanisms will be discussed briefly as they are a powerful tool to assess the amount of radiation damage in a detector.

Leakage Current

Irradiation creates additional levels in the middle of the band gap and therefore dramatically increases the probability of electron-hole pair creation and thus leakage current in

⁴1b = 10⁻²⁸m²

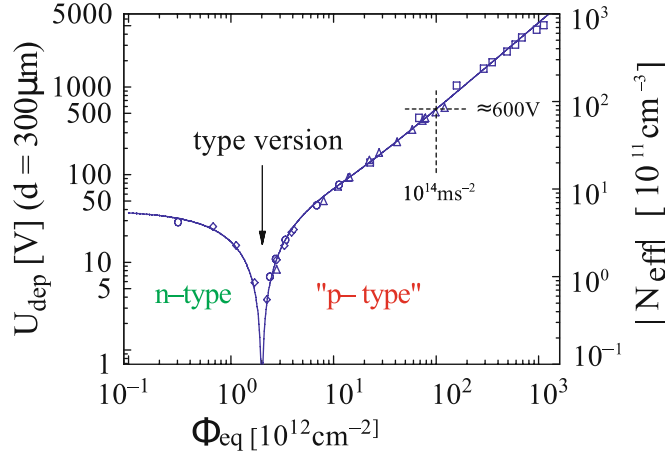


Figure 4.12: Evolution of the effective doping concentration N_{eff} and thus the full depletion voltage V_{fd} with fluence [31].

silicon. It was found out in experiments that the current increase is proportional to the equivalent fluence.

$$\frac{\Delta I}{V} = \alpha \Phi_{eq} \quad (4.19)$$

Here $\Delta I/V$ is the current per unit volume, Φ_{eq} is the 1 MeV neutron equivalent fluence mentioned above and α is the so-called current-related damage rate. This linear dependence is stable over many orders of magnitude and can therefore be used to determine the fluence.

Change of N_{eff} and V_{fd}

Point defects induced by irradiation can combine with impurities in the silicon lattice and form more complex defects (figure 4.9). These combinations lead to a removal of donors (for example the combination of $P + V \rightarrow VP$ removes the donor function of phosphorous [29]) and to an increase of defects that behave like acceptors ($V + V + O \rightarrow V_2O$, oxygen-di-vacancy). In donor-doped n-type silicon this means that the effective doping concentration N_{eff} first decreases to the level of intrinsic silicon before the material effectively becomes p-type (acceptor-doped). The qualitative behavior and the close interplay of V_{fd} and N_{eff} can be seen in figure 4.12. Substrates that initially were p-type keep their properties but show an ever increasing depletion voltage.

Charge-Collection Efficiency

The decrease of the charge-collection efficiency with increasing fluence can be attributed to additional levels in the band gap that act as trapping centers. Charge that would normally contribute to the signal of the detector is trapped in these levels for a time

exceeding the integration time of the readout system. The degradation of the collection efficiency can be parametrized by an exponential decay, depending on the trapping time τ_{eff} , which is different for electrons and holes due to their different mobility.

$$Q_{e,h}(t) = Q_{0,e,h} e^{-\frac{1}{\tau_{eff,e,h}}t} \quad (4.20)$$

Here, the effective trapping time is proportional to the number of defects.

4.2.2 Surface Damage

Surface damage is a general expression for radiation-induced effects on the silicon dioxide layer and the interface between the bulk and the oxide. It is created by ionization only and therefore plays an important role in experiments with high rates of electromagnetically interacting particles (electrons and photons). However, in hadron experiments, the dominant source of damage are hadrons that create bulk damage and therefore surface damage does not play an important role in the work presented in this thesis.

Since SiO_2 is an insulator, the creation of electron-hole pairs is not fully reversible, which leads to polarization effects and to the accumulation of static positive charges at the interface (compare section 4.1.3), which in turn can accumulate charge carriers from the bulk and thus decrease interstrip resistance and increase interstrip capacitance.

These effects strongly depend on the quality of the oxide and the effects can be attenuated by the use of silicon with $\langle 100 \rangle$ crystal orientation instead of $\langle 111 \rangle$ because it features fewer unmatched valence electrons (dangling bonds) that can act as charge traps.

4.2.3 Annealing

Defects in the silicon lattice like interstitials and vacancies are mobile through diffusion processes that depend on temperature. Interstitial and vacancy recombination or combination of vacancies to di-vacancies have a rather short time constant, while the formation of more complex defects (combination of interstitials/vacancies with impurities) happens on a longer timescale.

These processes are called annealing and can be beneficial or bad for the properties of a damaged sensor. Especially the 'healing' of defects by recombination is desired, while the last of the above effects degrades detector performance. The two kinds of annealing are called 'beneficial annealing' and 'reverse annealing' and – as their underlying processes – happen on different timescales. The temperature dependence of diffusion can be used to suppress annealing processes at low temperatures ($< 20^\circ\text{C}$) to a high degree or to accelerate them by heating the sensor. In the following section a short summary of the different effects will be given [31].

Leakage-Current Annealing

The current-related damage rate mentioned in 4.2.1 is temperature-dependent and the parametrization reads

$$\alpha = \alpha_0 + \alpha_I e^{-\frac{t}{\tau_I}} - \beta \ln\left(\frac{t}{t_0}\right) \quad (4.21)$$

with α_I and β being constants fitted from experimental data, t_0 is 1 minute and the time constant τ_I accounts for the temperature dependence of α via the relation

$$\frac{1}{\tau_I} = k_{0I} e^{-\frac{E_{BG}}{k_B T}} \quad (4.22)$$

with E_{BG} being the band gap and k_{0I} another constant that can be found in [31].

Annealing of N_{eff}

The evolution of the full depletion voltage and effective doping concentration can also be parametrized by an empiric model called *Hamburg Model* [31], which describes donor removal and acceptor creation with fluence and annealing.

The parametrization reads

$$\Delta N_{\text{eff}}(\Phi_{eq}, t, T) = N_{C,0}(\Phi_{eq}) + N_A(\Phi_{eq}, t, T) + N_Y(\Phi_{eq}, t, T) \quad (4.23)$$

with the parameters temperature T , time t and 1 MeV neutron-equivalent fluence Φ_{eq} . N_C is a constant contribution that only depends on the irradiation dose, N_A describes the beneficial annealing amplitude as a function of annealing time and -temperature and N_Y describes the undesired reverse annealing. The qualitative shape of the individual contribution is shown in figure 4.13.

Annealing of Charge-Collection Efficiency

The trapping of electrons and holes is also the subject of annealing effects and experimental data indicates that the probability of electron trapping decreases, while hole trapping increases. This basically means that the annealing behavior is different for electron- (p-type) or hole-collecting detectors (n-type).

4.3 Radiation-Hard Sensor Technology

With the increasing luminosities of hadron-collider experiments and thus irradiation doses, radiation hardness of silicon sensors becomes the performance-limiting factor in

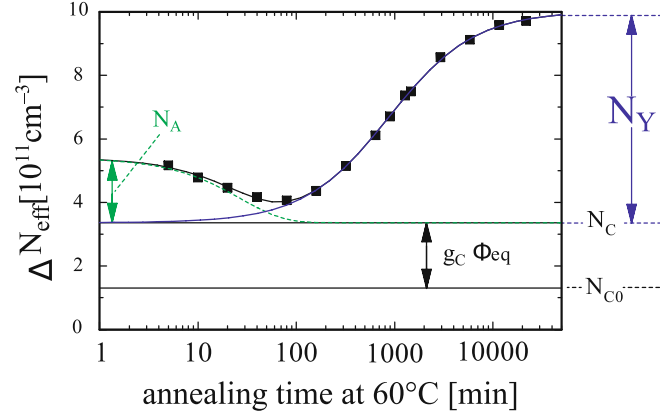


Figure 4.13: Amplitude of the different components of the Hamburg Model as a function of annealing time [31].

their operation. Extensive research by large and dedicated collaborations like RD48 and RD50 at CERN has been carried out on increasing radiation tolerance and understanding the underlying effects.

While the sensors made from n-type (p-strips in n-bulk) standard float-zone silicon presently used in the CMS experiment were found to be sufficiently radiation-hard for the expected LHC lifetime, they would not stand a chance to survive the fluences expected for the high-luminosity phase. There are two approaches to improving radiation tolerance:

Optimization of Design

This approach exploits the fact that design parameters can be altered to improve tolerance to hadron irradiation of silicon and extend the lifetime of a detector in an experiment. These include adequate choice of material (high vs. low resistivity, initial depletion voltage), doping (n- vs. p-silicon) and thickness.

Defect Engineering

The second approach aims at altering the intrinsic properties of the silicon material itself. By tuning the concentration of impurities or defects in the bulk, the formation of certain levels in the band gap can be suppressed or aided, which leads to very different behavior of the material.

In the following the two most relevant technological approaches for this thesis will be explained briefly.

4.3.1 p-Type Silicon

As mentioned in section 4.2, silicon sensors that were initially donor-doped (n-type) undergo a process of type inversion, which leads to the pn-junction growing from the back after a certain fluence. As a consequence, the distance in which the charge carriers

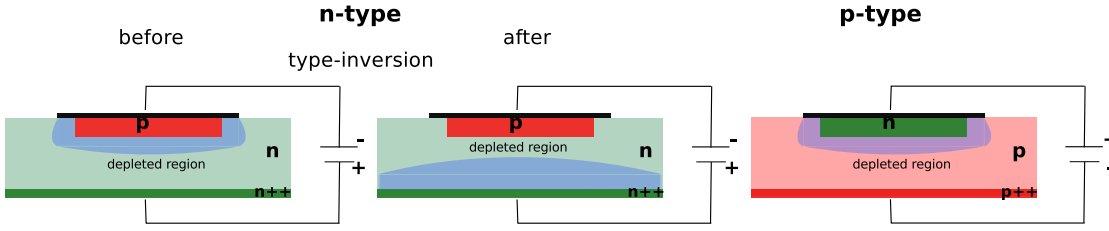


Figure 4.14: Schematic drawing of the depleted region at $V < V_{fd}$ in n- and p-type silicon. After type inversion the depleted region in n-type material does not reach the segmented side.

can drift and induce a signal in the readout circuits is shorter and the signal is overlapped by the drift of thermally-generated charge carriers. Only at higher voltages the depleted region reaches the segmented readout side (figure 4.14). The use of acceptor-doped (p-type) silicon on the other hand avoids this, as the material does not undergo type inversion and the junction will always be at the side of the segmented electrode. The depleted region will therefore also start growing from the segmented side of the detector and the created charge carriers will always induce a signal, thus allowing under-depleted operation of the detector.

This advantage is also present in n-in-n silicon but since the backplane needs an additional processing step and requires double-sided photolithography this technology is much more expensive than the use of p-doped substrate. In addition to the possibility of under-depleted operation, p-type detectors also have the advantage that they collect signals induced by the drifting electrons, which have a higher mobility in the material as compared to holes. This leads to a more pronounced Lorentz-effect in a magnetic field which has to be taken into consideration.

Finally, acceptor-doped material has a very small reverse annealing amplitude as compared to n-type material, which is beneficial for long-term operation as the depletion-voltage increase over time is not overly pronounced (compare figure 4.13).

4.3.2 Oxygen-Rich Silicon

Over the past decades, various defect-engineering-based approaches have been tried to improve the radiation tolerance of silicon. Some empirical findings have later been understood at the microscopic level. Today the most exploited beneficial effect is the increased radiation-hardness of oxygen-enriched material. Figure 4.15 shows the effective doping concentration N_{eff} and full depletion voltage V_{fd} as a function of proton fluence for standard-, oxygen- and carbon-enriched material.

The microscopic and macroscopic consequences on defect formation in different oxygen-rich materials after proton-, neutron- and γ -irradiation have been investigated in [34] and [35]. It has been found that a deep-acceptor level and a bistable donor level are closely related to the performance of a silicon detector and that the former one is largely

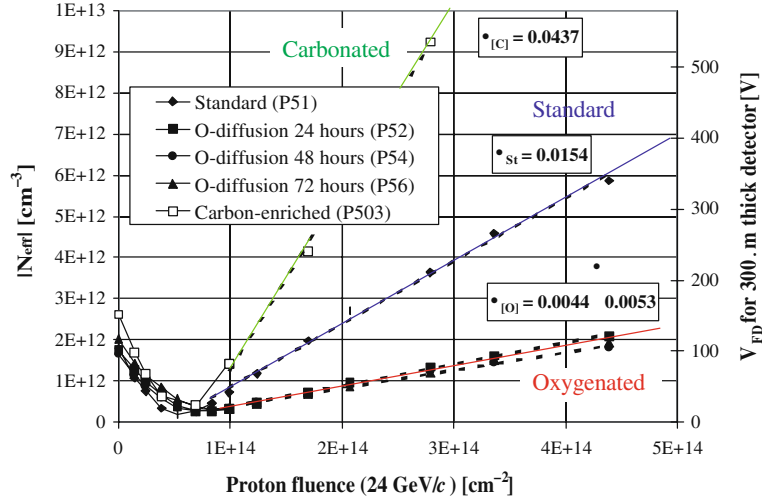


Figure 4.15: N_{eff} and V_{fd} as a function of proton fluence for different defect-engineered silicon substrates [RD48 and RD50].

suppressed and the latter is greatly enhanced in oxygen-enriched silicon. This deep acceptor is believed to be linked to the formation of the complex V_2O in the silicon lattice, which acts as a kind of 'vacancy-getter'.

However, this effect is limited to the point-like defects inflicted by proton irradiation. The defect clusters that are formed by neutrons would require much higher oxygen concentrations than are achievable with the most common methods. Empirical studies by RD48 have found the minimum oxygen concentration required to see a beneficial effect on the radiation-hardness to be in the order of 10^{17} cm^{-3} [36].

Macroscopically speaking, oxygen enrichment leads to a decrease of the stable-damage parameter g_C and an increase in the reverse-annealing time constant τ_γ from figure 4.13. In practice this means that the macroscopic effects of radiation damage are not as severe and the timescale before the undesired reverse annealing happens is longer.

These findings clearly favor any kind of oxygen-rich silicon substrate as base material for high-energy-physics detectors. Presently there are three groups of materials that all have a high oxygen concentration but are produced differently.

Diffusion-of-Oxygen Float-Zone Silicon

Float-zone silicon is the most widely used silicon substrate in high-energy physics. The fabrication process allows the production of very high-purity (and therefore high-resistivity) ingots⁵, as the process can happen in an inert atmosphere or vacuum. A

⁵A large single crystal in cylindrical form with a diameter of several tens of centimeters and heights greater than half a meter. Ingots are cut into parallel discs, which are called wafers, and serve as the starting point for detectors and ICs.

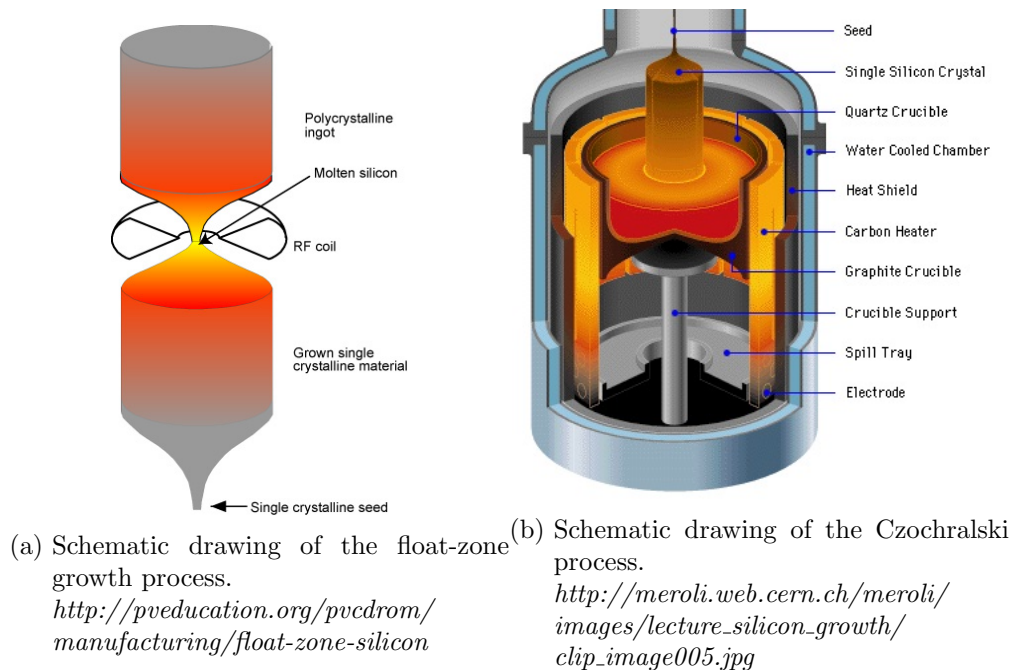


Figure 4.16: Different silicon-ingot-growth processes used for silicon detectors.

polycrystalline silicon rod is brought face-to-face with a seed-single crystal and is then slowly pulled through a RF heating coil, which melts a zone of the rod, which then re-crystallizes as a single crystal (figure 4.16a). As most impurities dissolve more easily in molten silicon than in the crystal, the molten zone 'drags' them out of the material. Doping of the material is achieved by adding the dopants to the atmosphere in which the process takes place.

However, low concentration of impurities also implies a low oxygen content of standard float-zone silicon. To increase oxygen concentration, oxygen can be added to the atmosphere during the growth process or – more commonly used in high-energy applications – thermally diffused into the material from a thick SiO_2 layer which is grown on the final wafer. The resulting material is then called diffusion-of-oxygen float-zone silicon.

Magnetic Czochralski Process

The Czochralski process, named after Jan Czochralski, is the most commonly used process for silicon-ingot production in the IC industry. High-purity silicon is melted in a quartz crucible and dopants are added to the melt to have p- or n-type silicon. Then a seed-single crystal is dipped into the melt and slowly pulled out again and thus the ingot is grown (figure 4.16b). This whole process usually happens in an inert atmosphere. During the growth process, the walls of the quartz crucible (which is SiO_2) dissolve into the melt and therefore Czochralski silicon has a very high natural oxygen concentration in the order of 10^{18} cm^{-3} .

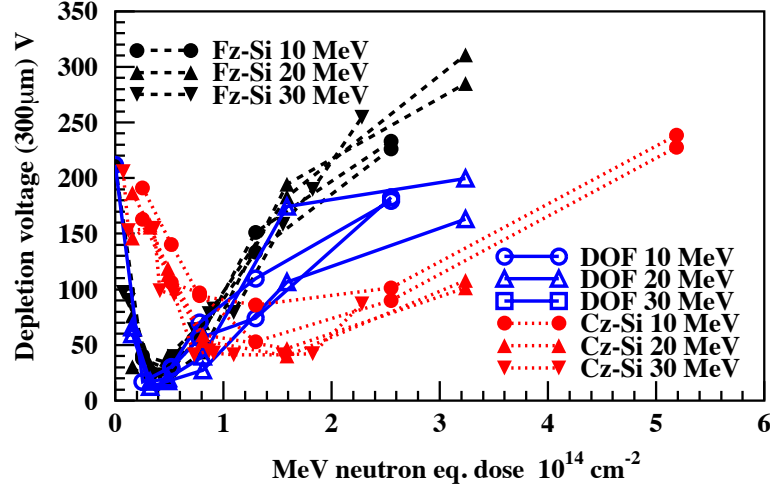


Figure 4.17: Evolution of depletion voltage as a function of fluence [37].

The problem of this process for detector production is the low purity and low resistivity of the material, which is about a factor of ten too small for reasonable depletion voltages in high-energy applications.

Recent development of the so-called magnetic-Czochralski process, however, allows the production of detector-grade silicon with very uniform properties and high resistivities. An external magnetic field is applied, which leads to a reduction of convection in the melt and to the formation of a liquid-silicon crucible around the central section of the melt from which the ingot is pulled. By separating the material in the center from the one that is in contact with the quartz, the oxygen concentration is reduced but the purity of the material is greatly enhanced.

The suitability of such magnetic-Czochralski material for detectors with respect to irradiation was investigated amongst others in [37] and [38]. Figure 4.17 shows the evolution of the full depletion voltage V_{fd} with fluence for standard float-zone-, diffusion-of-oxygen float-zone- and magnetic-Czochralski materials. Further results will be presented in this thesis.

Epitaxial Silicon

Another fabrication process of interest is epitaxial growth of thin layers. Here a layer of single-crystal silicon is grown on a single-crystal substrate (usually low-resistivity Czochralski or magnetic Czochralski) by chemical vapor deposition. In order to form a non-volatile film, the material to be deposited has to be present in a suitable gaseous phase which reacts chemically with the substrate. There are several commercially available gases but the reaction $SiH_4 \rightarrow Si + 2H_2$ illustrates the process.

The main advantage that epitaxial silicon offers for use as a detector is the very thin

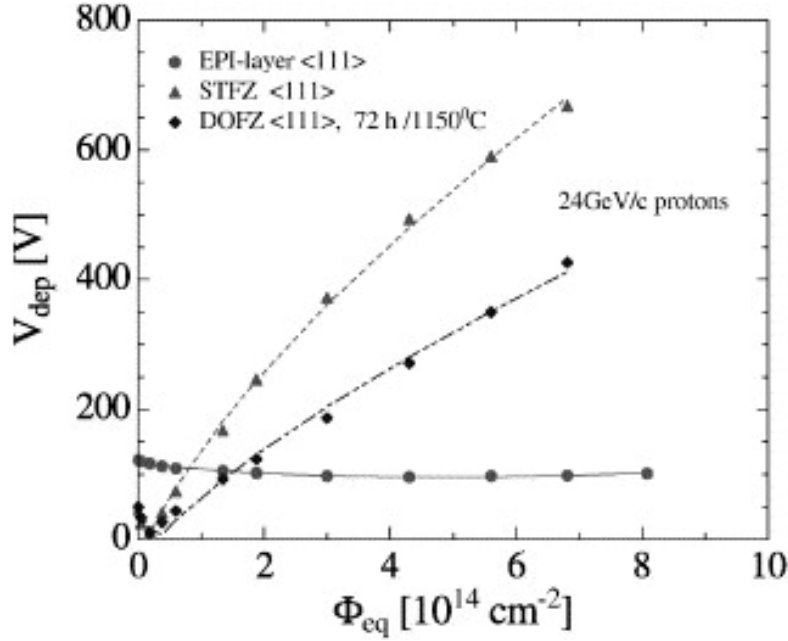


Figure 4.18: Depletion voltage V_{fd} of epitaxial-silicon diodes as a function of normalized particle fluence [39].

active layer. On the one hand this reduces the signal as the traversing particle creates fewer electron-hole pairs but it has beneficial effects on radiation hardness, since thin detectors effectively reduce the necessary depletion voltage. This allows for a dramatic increase of the initial doping concentration of the bulk and thus the effects of radiation-induced donor removal are alleviated. First studies of radiation tolerance of 50 micrometer-thin epitaxial diodes are presented in [39] and it has been found that highly doped, p-in-n epitaxial diodes do not undergo type inversion after irradiation to high fluence (figure 4.18).

Other studies ([40] [41]) have investigated detectors and diodes from material with thicknesses up to $150 \mu m$ and have found similar behavior.

5 The HPK Project

The present CMS tracker was designed to withstand the radiation dose that it will receive during an approximate lifetime of ten years with an integrated luminosity of 500 fb^{-1} . It was constructed from 300 to 500 micrometer-thick sensors, made of standard oxygen-lean float-zone silicon, in a simple, single-sided, planar p-on-n process. After its expected lifetime, the whole tracker must be replaced like discussed in chapter 3, section 3.4, as the integrated luminosity will reach the design value and the silicon sensors will suffer from heavy radiation damage. In addition, the requirements for the sensors in the HL-LHC will change dramatically in terms of granularity and radiation tolerance [17]. For that purpose CMS is running a vast measurement- and irradiation campaign to identify a suitable technological baseline for future sensors that can be used in a large part of the tracker. This so-called HPK project will be presented in detail in the following sections.

5.1 Motivation and Goals

As already mentioned in section 3.4 the expected track density in the HL-LHC scenario will increase by a factor of ten and the accumulated fluence that the pixel detectors close to the interaction point will receive will be in the order of $10^{16} \text{ 1MeV n}_{\text{eq}} \text{ cm}^{-2}$, while the fluence for the innermost strip layers at a radius of 20 centimeters will still be $10^{15} \text{ 1MeV n}_{\text{eq}} \text{ cm}^{-2}$. This requires sensors with increased radiation tolerance and increased granularity compared to the ones used in the present CMS experiment.

The collaboration has therefore launched a large campaign with the Japanese semiconductor company Hamamatsu Photonics K.K. to investigate many different aspects of future sensors in a coordinated effort with respect to:

Material

Results of the RD48 and RD50 collaborations have yielded that oxygen-rich material is more tolerant to radiation damage than the oxygen-lean float-zone silicon used at present and therefore more suitable for the future CMS tracker.

Thickness

Radiation damage increases leakage current – which also increases noise and power to be dissipated – depletion voltage and trapping in a sensor, which makes sensible operation after irradiation to high fluences more difficult. Thin sensors could be used to overcome these problems and also reduce the material budget of the whole tracker. For the 2S module discussed in section 3.4, a reduction of sensor thickness from 300 to 200 μm would correspond to a reduction of the material budget for

the whole module by 30 percent.

Polarity / Doping

As mentioned in section 4.3, the use of p-doped silicon has advantages in terms of radiation hardness compared to n-doped material as there is no inversion of the sign of the effective doping concentration and trapping of the charge carriers is reduced due to the higher mobility of electrons, which induce the signal in this type of material.

Sensor Concepts / Layouts

The increased track density requires sensors with much higher granularity. For that reason new geometrical concepts like short strips or long pixels for the 2S and PS modules and segmented sensors with integrated routing from the active strip area to the bonding pads for the readout or integrated pitch adapters are being studied.

In recent years many studies [42] have investigated different materials and concepts but due to the significantly different conditions of the measurements it is difficult to draw valid conclusions. For that reason the CMS collaboration has agreed on conducting a new study with many of the available materials and technologies but under conditions that ensure comparability. It has been decided to use one single, standardized, planar wafer design that includes small prototype sensors and test structures, to have all the samples produced by the same, high-quality producer and to comply to a standardized measurement protocol. This reduces the parameter space to:

- material
- doping and
- thickness

which still results in many possible combinations but allows sensible conclusions, since the investigated structures are all of the same design. Irradiation of the samples to certain fluences, which correspond to different radii in the future system, are an important part of the campaign and allow drawing individual conclusions in terms of radiation hardness for different parts of the future tracker.

The goal of the campaign is to identify a single, radiation-hard technological baseline for a large part of the future CMS silicon-(strip-)tracker and to test various new sensor designs and -concepts. [43]

The limitation to one (or two) single technology(ies) for the strip- (and pixel) tracker should ensure simple, cost-effective mass production of the huge number of sensors that will be needed for the future tracker.

5.2 Materials, Technologies and Structures

Since a high oxygen content of silicon substrate is beneficial for the radiation hardness of sensors, oxygen-rich materials have been chosen for the HPK project. Diffusion-of-oxygen float-zone silicon is investigated along with magnetic Czochralski and epitaxial silicon in thicknesses ranging from 50 to 300 μm and all material-thickness combinations are available in p-on-n and n-on-p technology. The collaboration designed the wafer as a p-on-n layout and Hamamatsu adapted it for n-on-p technology. The p-type wafers exist in two technologies with different strip-isolation mechanisms that will be covered in the next sub-section. Some thin DOFZ wafers were produced by physical thinning of the material and some make use of a technology called deep diffusion. The nomenclature of materials¹ used is the following.

FZ: Float-zone silicon with a possible reduction of active volume by deep diffusion

FTH: Float-zone material that is physically thinned

MCZ: Magnetic Czochralski silicon

Epi: Epitaxial silicon

Table 5.1 gives an overview of the available materials and thicknesses.

Table 5.1: Overview of the available materials and thicknesses of wafers for the HPK project.

Material	320 μm	200 μm	120 μm	100 μm	50 μm
FZ	✓	✓	✓		
FTH		✓			
MCZ		✓			
Epi				✓	✓

It is important to note that the 320 micrometer-thick, n-type float-zone material is very similar to the sensors used in the tracker at present and therefore serves as reference. The wafers on which the layout was processed were bought from silicon producers by Hamamatsu and the resistivities for the materials are 3 - 8 $k\Omega cm$ for p-type FZ wafers, 1.2 - 2.4 $k\Omega cm$ for the n-type FZ and 0.5 - 2 $k\Omega cm$ for the Epi wafers. The respective resistivities for magnetic-Czochralski material are above 0.5 $k\Omega cm$ for the n-type and above 2 $k\Omega cm$ for the p-type wafers.

A small number of 200 micrometer-thick FZ wafers was produced with a second layer of metallization, separated from the first layer by a thin layer of oxide and connected to it by means of so-called *vias*, to study on-sensor routing. However, these structures have not been investigated for this thesis and will therefore not be considered any further.

¹This will be used for the rest of this thesis.

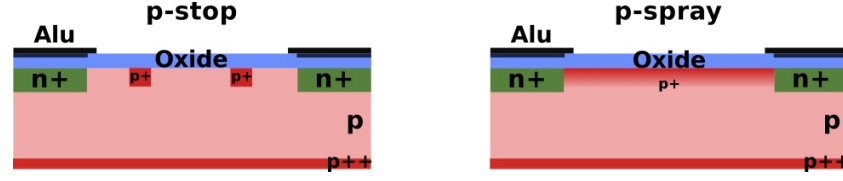


Figure 5.1: Schematic drawing of the section between two strips in a p-bulk strip detector that illustrates the difference between p-stop and p-spray isolation methods.

5.2.1 Strip Isolation on p-Type Sensors

As mentioned in 4.1.3, the technological implementation of n-on-p sensors requires additional processing steps. Positive oxide charges at the Si-SiO₂ interface on the readout side attract electrons (majority carriers in p-type material), which form an accumulation layer underneath the oxide in the bulk and thus shorten the strips (see figure 4.7). This accumulation has to be prevented by isolating the n-strips in the p-bulk artificially, which can be achieved by two means:

p-stop:

P-stop is a technology that surrounds each strip with its own, isolating p-implant that repels the electrons and thus prevents the accumulation layer from forming. It is possible either to execute this implant as a common structure between the strips or as an individual atoll for each individual strip, surrounding it completely. An additional photolithography mask is required to define the structures for the implantation.

p-spray:

This method achieves the same effect as p-stop by doping the whole surface between strips uniformly with acceptors and thus creating a continuous p+ electrode on the surface between the strips. It does not require the additional mask and photolithography step and thus is considerably simpler and cheaper.

Figure 5.1 illustrates the difference between the two methods. For this project the nomenclature was chosen in such a way that n-bulk silicon is abbreviated with the letter **N**, p-bulk, p-stop is referred to with **P** and p-bulk, p-spray with **Y** respectively. This allows for a quick and simple identification of material-thickness-doping combinations by assigning them a code like **FZ200Y**, which would denote 200 micrometer-thick, n-in-p, p-spray float-zone silicon. Figure 5.2 shows the different strip layout for n- and p-spray sensor designs and p-stop with the additional electrode.

5.2.2 Thin Materials

As handling large wafers thinner than 300 micrometers is difficult and usually foundries² do not take the risk, thin sensors are produced by polishing the backside of thick wafers

²Wafer-producing companies

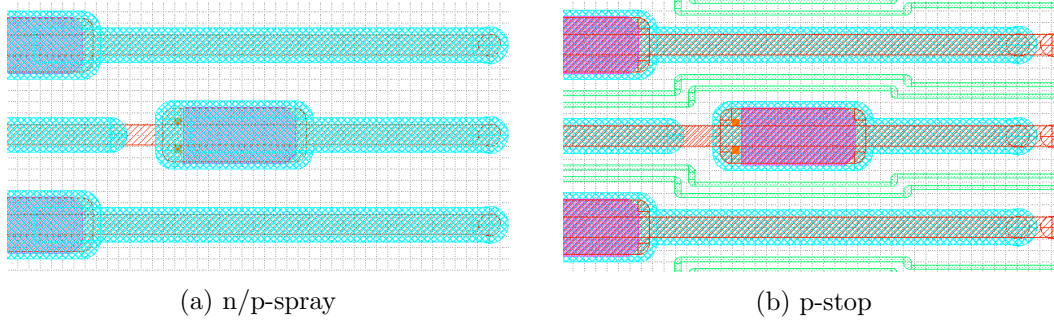


Figure 5.2: Different layouts for n/p-spray- and p-stop sensors.

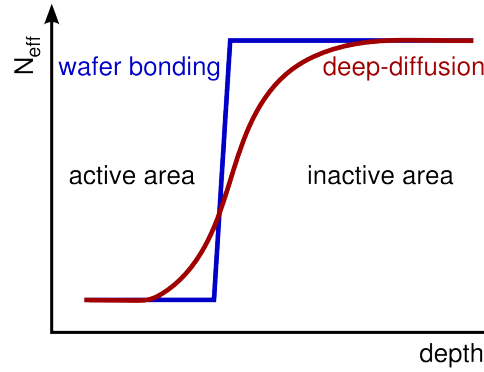


Figure 5.3: Qualitative shape of the effective doping concentration at the interface between backplane and active volume for deep-diffused and physically-thinned or wafer-bonded sensors [44]

after the front side has been fully processed. These thinned wafers are then wafer-bonded to a handling wafer, that reduces the risk of mechanical breaking. An alternative method is a technology called deep diffusion. During this process the backplane of the wafer is heavily doped (p++ or n++) and this layer is then diffused into the bulk material to a given depth by heat treatment. This basically represents an ohmic contact to the remaining active region but also results in a gradual transition from backplane to active bulk in the doping profile (5.3), which means that the active volume is not defined precisely. The float-zone (**FZ**) wafers of active thickness smaller than $320\ \mu\text{m}$ available for this project achieve the reduction of active thickness by this technology.

The deep-diffusion process represents a simple and cost-effective way of reducing active thickness and thus depletion voltage and leakage current after irradiation but the possible benefit of reducing the material budget of the tracking system by using thinner sensors is lost (figure 5.4).

In the HPK project all deep-diffused float-zone (**FZ**) wafers are physically $320\ \mu\text{m}$ thick. Some physically-thinned float zone (**FTH**) wafers were ordered at a later stage to verify and compare the results with the deep-diffused material. Magnetic-Czochralski

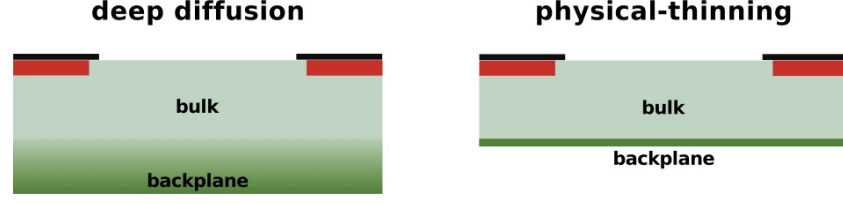


Figure 5.4: Schematic drawing of a deep-diffused and physically-thinned sensor. The physical thickness of the deep-diffused wafer is still $320\text{ }\mu\text{m}$ but the active volume is reduced.

Table 5.2: Physical- versus active-thickness of HPK wafers obtained from mechanical and CV measurements.

Material	Active Thickness [μm]			Physical Thickness [μm]		
	N	P	Y	N	P	Y
FZ 320	301	294	291	320	320	320
FZ 200	224	212	210	320	320	320
FZ 120	148	135	134	320	320	320
FTH 200	204	207	202			
MCZ 200	201	210	202			
Epi 100	103	102	100			
Epi 50	50	49	49			

(**MCZ**) wafers are all physically $200\text{ }\mu\text{m}$ thick and the epitaxial wafers (**Epi**) are grown on a carrier wafer and the thickness code denotes the active volume. Table 5.2 summarizes the active and physical thickness of all wafer types obtained from measurements.

5.2.3 Wafer and Structures

The wafer that CMS ordered for this project contains many different structures to address various issues and problems. These include diodes to investigate material properties and radiation hardness, prototype sensors to investigate new concepts and geometries and dedicated test structures to investigate the quality of the production process. Figure 5.5 shows a schematic drawing of the wafer where the central region is occupied by relatively large sensors and the diodes and test structures are grouped in their vicinity [43] [45].

Diodes

These structures are very basic and only consist of a pn-junction. They have been designed for material studies and for investigating the impact of radiation damage, the defects that are generated and their annealing behavior.

Baby_STD

The Baby_STD is a very basic strip sensor with 256 strips and a strip pitch of 80

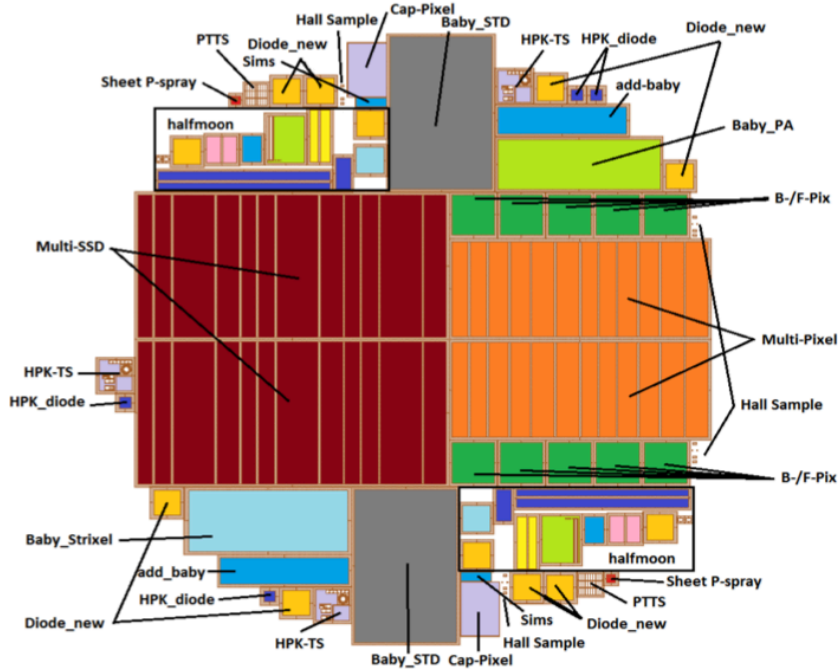


Figure 5.5: Drawing of the layout of the six-inch wafer ordered from Hamamatsu for the CMS Tracker Upgrade.

μm . Charge-collection efficiency and strip parameters before and after irradiation are to be investigated.

Multi-SSD

This is a strip sensor with 12 individual regions to address questions about geometry. It will be described in detail in section 5.4.

Multi-Pixel

This sensor features long pixels of the order of 1 or 2 mm with different pitches, different strip width-over-pitch ratios and different biasing schemes. It was intended as a prototype for the pT modules from section 3.4 with high granularity.

Baby_PA

This small sensor with 128 strips has a pitch adapter from a strip pitch of $80 \mu m$ down to the pitch of the input channels of the APV25 ([23]) readout chip of $44 \mu m$ implemented in the metallization. The influence of on-sensor routing on top of the implants is studied with respect to sensor performance.

Baby_Strixel

A strixel sensor is a new concept that allows higher granularity while maintaining the connection to the front-end electronics on one single side of the sensor. It has two rows of shifted short strips, where the second row is connected to the readout via routing lines in between the strips of the first row. This concept is also

discussed for use with the pT modules.

Baby_Add

The Baby_Add(itional) is a small sensor with 56 strips to study the Lorentz angle before and after irradiation. It is therefore connected to a front-end chip and brought into a high magnetic field. Charge is injected via a laser and the offset of the charge carriers from the expected position is measured.

Halfmoon

This is a set of test structures to monitor the production-process quality and various aspects of the material itself, like the quality of the oxide or the thickness of individual layers on the surface (metallization, oxide). It is an adopted version of the test structures that have been on the wafers for the sensor production of the present CMS detector.

BPix & FPix

These are prototype pixel sensors for the barrel (B-) and forward (F) regions of the future tracker and feature different pixel geometries and bias schemes. They are not part of the project this thesis is about and will be investigated at a later stage.

5.3 Irradiation

The search for radiation-hard silicon that can outperform present-day materials is the main goal of this campaign, therefore irradiation studies of the structures on the wafer are a very important part of it. The different fluence steps that the samples are irradiated to are driven by the expected fluence in CMS during the HL-LHC era. Figure 5.6 shows this fluence corresponding to an integrated luminosity of $3,000 \text{ fb}^{-1}$ as a function of the radius from the interaction point.

As it is intended to equip as much of the future tracker as possible with one single sensor technology, fluence levels at different radii are investigated. For the strip tracker this is practically limited to larger radii over 20 cm and the work presented in this thesis will cover the fluence steps corresponding to radii of 40 cm and 20 cm and structures with an active thickness equal to or larger than $200 \mu\text{m}$. Table 5.3 summarizes the different irradiations. As the radiation environment for the innermost region up to a radius of about 30 cm is dominated by charged hadrons and the outer regions will suffer mainly from neutron damage, the irradiations are designed as mixed irradiations with adequate fractions of protons and neutrons to mimic this fact.

Since the project wafer is designed symmetrically and all structures are available twice, it is theoretically possible to perform a characterization step after each individual irradiation and by that means assess the pure proton-, pure neutron- and mixed damage. To do so, one structure is irradiated with protons first and the other one with neutrons. Then they are qualified in the laboratory before they undergo irradiation with the other particle type and another qualification step. The structures also undergo a small an-

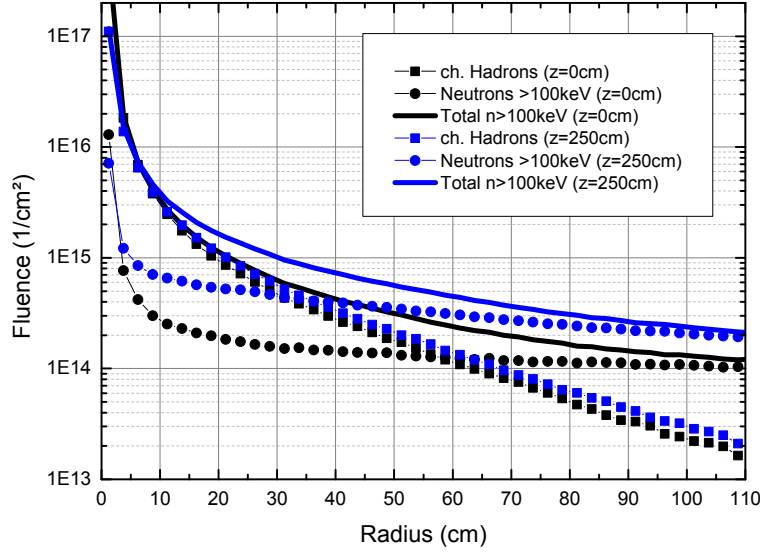


Figure 5.6: Simulated fluence for different particles as a function of the radius from the interaction point inside the CMS detector corresponding to the total integrated luminosity after the HL-LHC lifetime of $3,000 \text{ fb}^{-1}$ [46].

Table 5.3: Neutron- and proton fluences at different radial positions as simulated for the CMS tracker in the HL-LHC era [43]. The fluences investigated in this thesis are printed in bold typeface.

Radius	Protons	Neutrons	Total
5	130	10	140
10	30	7	37
15	15	6	21
20	10	5	13.9
40	3	4	7
$\times 10^{14} \text{ 1MeV } n_{eq} \text{ cm}^{-2}$			

nealing step after each irradiation to equalize the effect of the environmental conditions during the irradiation with the two particle types. This is necessary, as the structures can be cooled during proton irradiation with an accelerator, which prevents annealing, but during the neutron irradiation in a reactor core this is not possible. However, this detailed, particle-dependent study has only been done for diodes so far, as they provide sufficient information on material properties, particle-type-dependent damage.

The proton irradiation is carried out at the cyclotron in Karlsruhe, where the beam energy is 24 MeV and the samples are scanned with the beam inside a cooled box, which is required as most structures are a lot larger than the beamspot and uniform irradiation is desired [47].

The neutron irradiation on the other hand, is done in an irradiation tube that protrudes into the core of the Triga Mk. 2 research reactor at the Jozef Stefan Institute in Ljubljana [48].

During the course of the project, it was decided to add further irradiations with higher-energy protons, as, according to [32], charged hadrons with different energies create different kinds of damage and the NIEL hypothesis is violated [49] [50]. These irradiations are performed with 800 MeV protons at the Los Alamos National Laboratory in the United States and at the CERN Proton Synchrotron, where the beam energy is 23 GeV.

5.4 The Multi-Geometry Silicon-Strip Detector

Motivation

The Multi-Geometry Silicon-Strip Detector — or, abbreviated, **MSSD** — is the largest structure on the HPK wafer and was designed to study various sensor geometries. It has regions with different strip pitches and different implant widths as second varying parameter. Due to the short bunch-crossing interval in the LHC and the resulting short peaking time required for the readout electronics in the CMS tracker, the contribution of shot noise to the overall noise performance of a detector is reduced. As a consequence the capacitive load of the pre-amplifier input, that mostly depends on the strip-capacitances of the sensor, becomes important or even dominant.

During the R&D effort for the present tracker, studies investigating the influence of strip geometry on the strip capacitances have been performed on 300 micrometer-thick, p-on-n, multi-geometry sensor prototypes with six cm long strips before and after irradiation to the expected total LHC fluence ([51], [52]).

It has been found that the strip pitch and the implant width of the strips have considerable influence on the strip capacitance. This capacitance has two contributions:

- the interstrip capacitance C_{int} from section 4.1.4

- the backplane capacitance C_{back} of one strip to the backplane of the sensor

In addition, the geometry of the strip implant and the metallization that covers it affect the high-voltage stability of the detector and its breakdown behavior. This plays an important role in the operation of detectors with high depletion voltages after considerable irradiation.

The purpose of the MSSD sensor is to repeat these studies for thinner sensors, various bulk materials and different doping technologies.

Since the curve-shapes of both of the capacitances mentioned change with irradiation — the backplane capacitance mainly through a change of the dielectric constant of the bulk through the change of N_{eff} and the interstrip capacitance through changed oxide properties (surface damage) — the MSSD sensors are an important part of the irradiation campaign and are irradiated to the fluence steps that represent the strip region of the future tracker. However, they are only qualified after mixed irradiation.

Other interesting parameters than the noise behavior through the capacitances and the high-voltage stability can be studied by connecting the sensor to a readout system and exposing them to radiation while looking at the response of the system. This can either be done by means of a radioactive source or in a particle beam. The latter option allows for studying the effects of the strip geometry on parameters like

- the signal,
- the signal-to-noise ratio,
- the detector efficiency,
- the charge-sharing behavior and
- the spatial resolution

and their respective evolution with irradiation to expected HL-LHC fluences. Thus the MSSD sensor is a powerful tool to assess many aspects of sensor design and -geometry and their impact on the overall performance of the future sensors for the CMS tracker.

The Sensor

The MSSD is a fairly large structure that exists twice on every wafer. It measures 65.7 mm by 32.8 mm and has a total number of 384 strips with an implant length of 30.48 mm. There are 12 regions with 32 strips each and three groups of regions with four pitches and three different width-over-pitch ratios. The available pitches are 70, 80, 120 and 240 μm and the width-over-pitch ratios are around 0.15, 0.25 and 0.35, with slight variations. The exact numbers are summarized in table 5.4.

The different regions all have their own bias- and guard-ring structures and are separated by a deep n+/p+ implant, which penetrates all the way to the backplane, and thus separates the regions, effectively making them individual sensors on a common

Table 5.4: Exact strip-geometry parameters of the MSSD sensor.

Region	1	2	3	4	5	6	7	8	9	10	11	12
Pitch [μm]	120	240	80	70	120	240	80	70	120	240	80	70
Width [μm]	16	34	10	8.5	28	58	18	15.5	40	82	26	22.5
Al [μm]	29	47	23	21.5	41	71	31	28.5	53	95	39	35.5
w/p	0.13	0.14	0.13	0.12	0.23	0.24	0.23	0.22	0.33	0.34	0.33	0.32

piece of silicon. The strips are polysilicon-biased and AC-coupled for direct bonding to a front-end chip. Figure 5.7 shows the schematic drawing and some details from the MSSD structure.

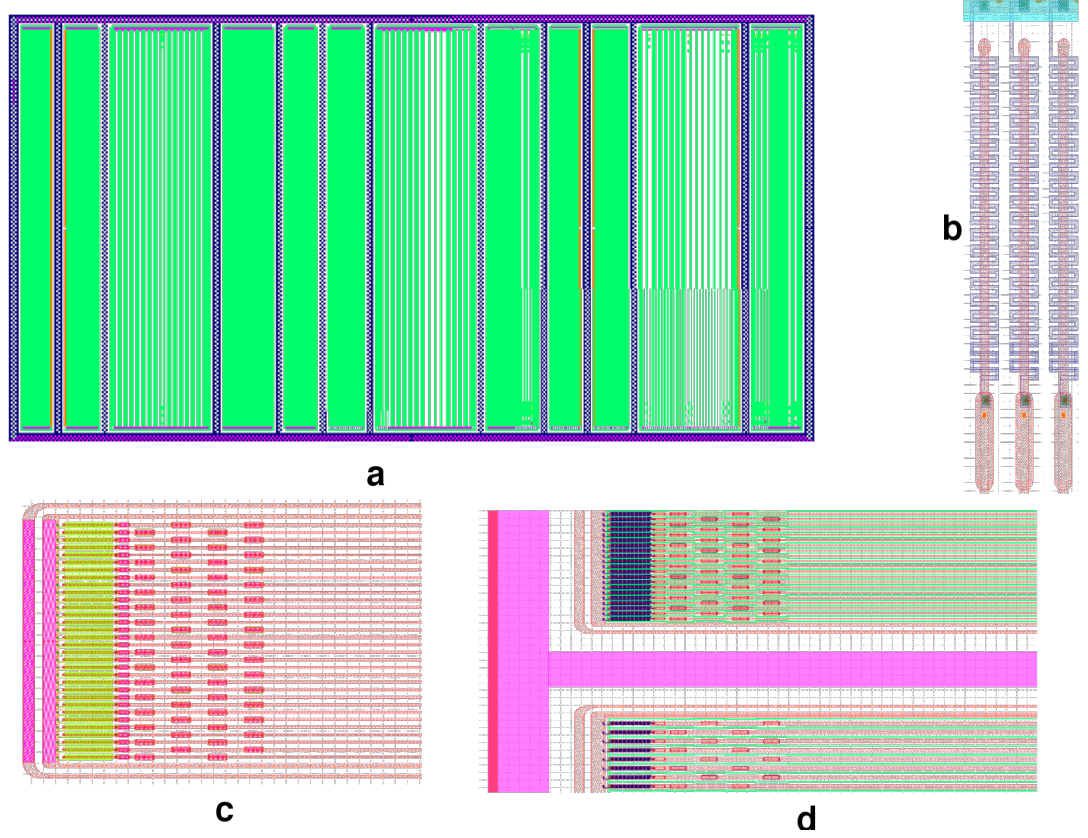


Figure 5.7: Schematics of the MSSD detector. Region 12 is the outer left one and region 1 is on the right (a). (b) shows details of the polysilicon bias resistors, (c) shows a detailed view of a 70 μm region and (d) shows the deep implant to separate the regions in pink.

6 Electrical Qualification of the Multi-Geometry Silicon-Strip Detector

Electrical qualification of silicon sensors in high-energy physics is an important aspect of characterizing the sensor performance and material properties. Not only do the electrical parameters give access to information necessary to understand the production process and -quality, but they also yield important information about radiation damage and general performance as described in chapter 4. One might naively expect that knowing the position resolution and efficiency of a detector is enough to assess its suitability for an experiment, but in order to gain a deeper understanding of the performance, the different characteristics like doping concentration, layer thickness, oxide properties and so forth, which can be derived from the results of the measurement of electrical parameters, have to be known. With this information it is possible to model and simulate different detector technologies and -geometries and thus the performance. These models, in conjunction with a detailed understanding of mechanisms responsible for radiation damage in silicon, also allow for predicting the behavior with increasing fluence and thus drawing conclusions about the long-term operation of a detector.

Extensive measurements on n-bulk silicon with different crystal orientations ($\langle 100 \rangle$ and $\langle 111 \rangle$) and readout schemes (AC and DC coupled strips) have been performed during the R&D phase of the present CMS tracker [51]. For that purpose a multi-geometry detector was produced that was quite similar to the MSSD presented in section 5 but with longer strips and a slightly different strip pitch. It is therefore of great interest for the HPK project presented in the previous chapter to complete and verify the results and models obtained in this previous study with data measured on p-doped silicon of different thicknesses.

Performing electrical measurements on the MSSD structure and building a dedicated setup has been a significant part of this thesis. The measurements, the parametrization of results similar to [51] and [52] in order to obtain comparable results and possible conclusions will be described in section 6.1.

Section 6.2 will present the experimental setup that has been developed throughout this thesis, while section 6.3 presents a survey of the data collected at the participating institutes and the evolution of electrical sensor parameters with irradiation.

6.1 Measurements & Parameters

As described in section 5.4 of the previous chapter, the Multi-Geometry Silicon-Strip Detector was designed to investigate the influence of strip- and sensor geometry on parameters like leakage current, depletion voltage and front-end amplifier input capacitance (compare section 4.1), and thus the performance of a sensor. The total strip capacitance, which is the sum of the interstrip capacitance C_{int} and the backplane capacitance C_{back} together with the leakage current, determine the noise behavior of a sensor and thus its performance. The leakage current furthermore yields information about power dissipation of a detector, high-voltage stability of a certain geometry and radiation damage. The interstrip capacitance determines charge sharing between strips and thus the position resolution and the collected signal, while the depletion voltage that is extracted from the measurement of the depletion-layer capacitance is the most important operating parameter.

6.1.1 Measurements

Leakage Current I_l

To measure the leakage current on a strip sensor, a voltage source for the bias voltage is needed along with a precise amperemeter. The bias voltage is applied on the metallization on the backplane of the detector and the connection to ground is made at the bias ring, which is connected to the strips by polysilicon resistors. This ensures that all strips are at the same potential and that the total current generated in the detector volume is measured. In addition, the guard-ring which surrounds the bias ring can be grounded to have a well-defined detector volume. Depending on the doping of the particular sensor that is to be measured, the high voltage has to have positive polarity for n-type and negative polarity for p-type materials.

Depletion Layer- or Backplane Capacitance C_{back}

According to equation 4.4, the capacitance of the depleted layer in a silicon detector is inversely-proportional to the square root of the applied voltage and thus the depleted thickness. To extract the full-depletion voltage V_{fd} , $\frac{1}{C^2}$ is plotted against the voltage and the kink of the curve defines the depletion voltage (compare figure 4.3).

For the measurement a high-precision LCR meter¹ is necessary in addition to the voltage source. This instrument sources an AC voltage with a selectable frequency and measures the current and phase-angle and thus calculates the desired value from the impedance of the circuit. The connection is again made to the backplane and the bias ring of the sensor to measure the capacitance of all strips. The capacitance of one strip is

¹Inductance-, capacitance-, resistance meter

equivalent to the total detector capacitance divided by the number of strips in first-order approximation.

The measurement frequency for this measurement is temperature-dependent and can be tuned but for the HPK project it was agreed to use 1 kHz to ensure reproducibility of the results. Also, most modern LCR meters have a built-in functionality to correct stray-capacitances in the cables connected to the inputs. This is usually done by measuring capacitance values for an open- and short circuit without the device that is supposed to be tested. For this study, the open correction was used.

Interstrip Capacitance C_{int}

The implant of a strip does not only have a capacitance towards the backplane of the sensor but also to other strips. The depleted bulk again acts as dielectric but in this case, the capacitance is a function of sideways depletion depth. This interstrip capacitance (compare section 4.1.4) determines the charge sharing between the strips and, together with the backplane capacitance of a single strip, the load capacitance of the amplifier and thus the detector noise. It is therefore vital to understand the behavior of the interstrip capacitance also after irradiation, as it is sensitive to surface damage that deteriorates the oxide and consequently decreases strip isolation.

On the MSSD, the interstrip capacitance is a very delicate measurement, as, due to the short strips, the values are very small and close to the sensitivity limit of the instrument. For that reason it is usually measured to two neighboring strips, which can be shorted to even more neighbors, to avoid second-order effects.

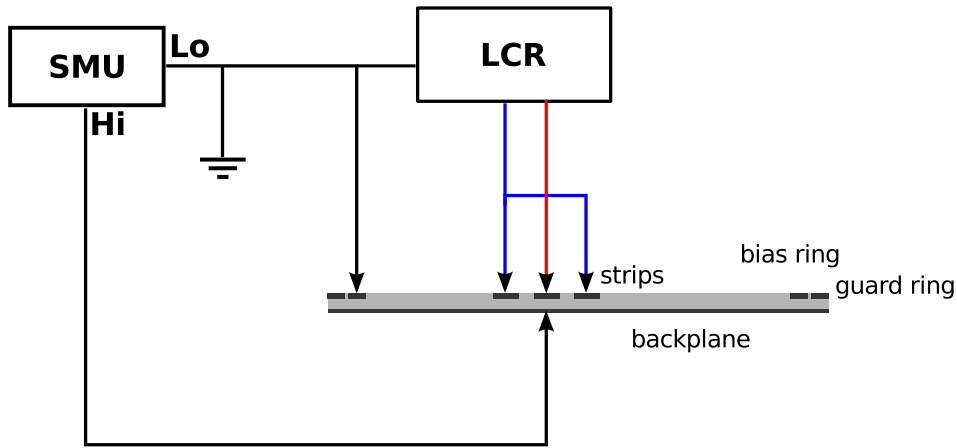


Figure 6.1: Schematic drawing of the connection scheme that is used for the measurement of the interstrip capacitance.

For this project, the interstrip capacitance is measured between a strip and two of its closest neighbors at 1 MHz and as a function of the bias voltage, as shown in figure 6.1.

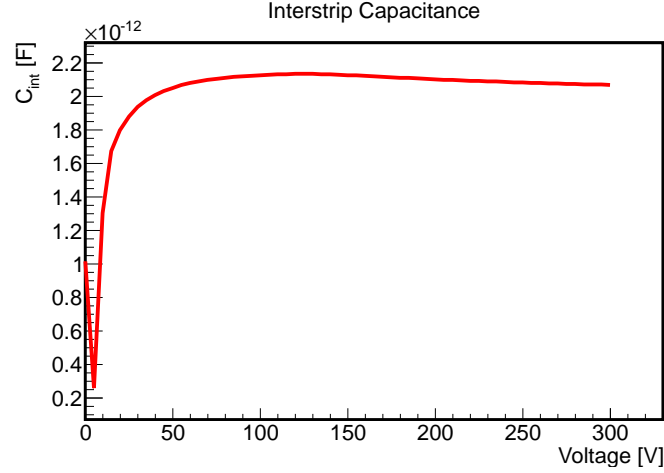


Figure 6.2: Interstrip capacitance C_{int} measured to two neighbors in a region with 70 micrometer pitch. The strips are three cm long.

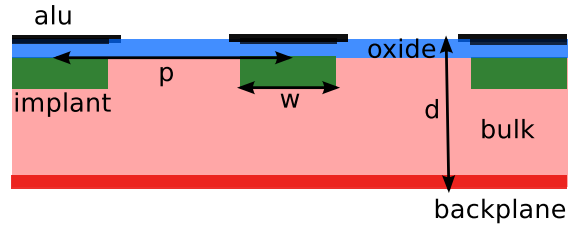


Figure 6.3: Geometrical parameters of a silicon-strip detector.

6.1.2 Parametrization of Results

The HPK project offers a huge parameter space for the comparisons of detectors. When investigating the properties of the MSSD structure and taking into account the geometry, this space grows to

- material
- thickness
- doping
- pitch
- width-over-pitch

which makes it necessary to find parametrizations that allow for summarizing of data in plots and extraction of dependences of parameters on geometry. Furthermore, it is desirable to use these parametrizations to extrapolate the results to geometries that have not been tested. Since studies like these have been performed for the present CMS tracker with very similar structures ([51], [52] and [53]), the nomenclature and parametrization will be retained. Figure 6.3 shows a summary of the geometrical parameters of a strip sensor.

If a simple, planar diode is considered a plate capacitor, the backplane capacitance reads

$$C_{back, Diode} = \epsilon_0 \epsilon_{r, Si} \frac{A}{d} \quad (6.1)$$

with A being the surface and d the thickness of the depleted region, which corresponds to the detector thickness above V_{fd} . This can be modified, since a strip can be modelled as a planar diode of width p and length one.

$$C_{back, Diode} = \epsilon_0 \epsilon_{r, Si} \frac{p}{d} \quad (6.2)$$

In this case the depletion voltage reads

$$V_{fd, Diode} = \frac{q_e N_{eff} d^2}{2 \epsilon_0 \epsilon_{r, Si}} \quad (6.3)$$

with q_e the elementary charge, N_{eff} the effective doping concentration, d the thickness of the detector and $\epsilon_0, \epsilon_{r, Si}$ the dielectric constants of vacuum and silicon. Since the actual implant width of the strip is much smaller than the pitch, these relations have to be modified by a geometrical correction, obtained by a semi-analytical solution of the Poisson equation [54]. The depletion voltage and backplane capacitances then read

$$V_{fd} = V_{fd, Diode} [1 + 2 \frac{p}{d} f(\frac{w}{p})] \quad (6.4)$$

and

$$C_{back} = C_{back, Diode} [\frac{1}{1 + \frac{p}{d} f(\frac{w}{p})}] \quad (6.5)$$

respectively, with $f(\frac{w}{p})$ being a series expansion in w/p .

$$f(\frac{w}{p}) = -0.00111(\frac{w}{p})^{-2} + 0.0586(\frac{w}{p})^{-1} + 0.240 - 0.651(\frac{w}{p}) + 0.355(\frac{w}{p})^2 \quad (6.6)$$

The function 6.6 decreases monotonically in the range of tested width-over-pitch ratios, which means that a higher depletion voltage and lower backplane capacitance for strip sensors are expected. These corrections are greater for large pitches and larger at smaller values of width-over-pitch.

Figure 6.4 shows the function $f(\frac{w}{p})$ and figure 6.5 shows the correction factor between strip sensor and diode for V_{fd} and C_{back} for two different detector thicknesses.

The interstrip capacitance can be computed under the assumption that the strips represent two semi-infinite plates that are separated by p-w.

$$C_{int} = 4 \epsilon_0 \epsilon_{interface} \frac{K(k)}{K \sqrt{1 - k^2}}, \quad k = \frac{1}{2 \frac{p}{w} - 1} \quad (6.7)$$

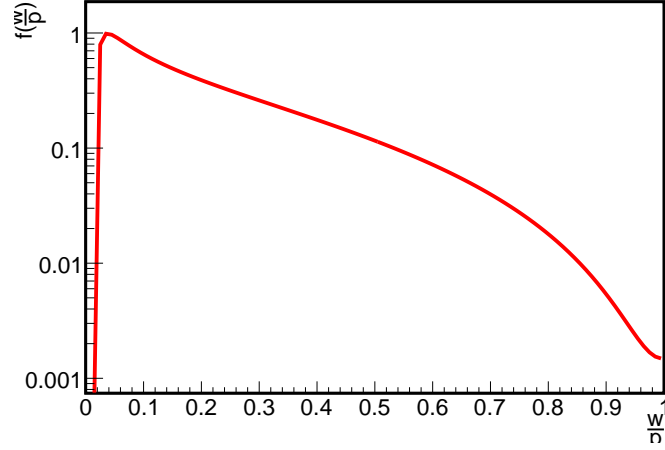


Figure 6.4: The function $f(\frac{w}{p})$ for the geometrical correction of depletion voltage and backplane capacitance [55].

with K an elliptic integral and $\epsilon_{interface}$ the effective dielectric constant of the zone between the strips, which is approximated as $\epsilon_{interface} = (\epsilon_{Si} + \epsilon_{Si_2})/2 = 7.9$ [53]. In practice, a linear dependence of the interstrip capacitance on the width-over-pitch ratio for regions with the same pitch can be expected. But as this model assumes infinite substrate thickness, which does not hold true for the thin sensors that have been investigated in the course of this project, a correction has to be implemented that transforms the dependence to

$$\frac{w}{p} \rightarrow \frac{w + \delta}{p} \quad (6.8)$$

with the parameter δ to be extracted from the fit.

The backplane capacitance is expected to be proportional to the pitch p , corrected by a factor of $1/[1 + p/df(w/p)]$, according to equations 6.2 and 6.5. Combining the dependences of the two equation yields

$$p \frac{1}{1 + \frac{p}{d} f(\frac{w}{p})} = \frac{p}{d + p f(\frac{w}{p})} \quad (6.9)$$

and the proportionality of C_{back} to this factor should be linear. According to [52], C_{back} rises with the above factor, C_{int} decreases and the total detector capacitance C_{tot} , which is a sum of the latter, remains constant (figure 6.6).

In practice, the total capacitance of a single strip in first-order approximation reads

$$C_{tot} = C_{back, 1strip} + C_{int, 2neighbors} \approx \frac{C_{back, all strips}}{N_{strips}} + C_{int, 2neighbors} \quad (6.10)$$

with $C_{back, all strips}$ the backplane capacitance measured on the bias ring and $C_{int, 2neighbors}$ the value obtained from the measurement described in 6.1.1, both above the full depletion voltage.

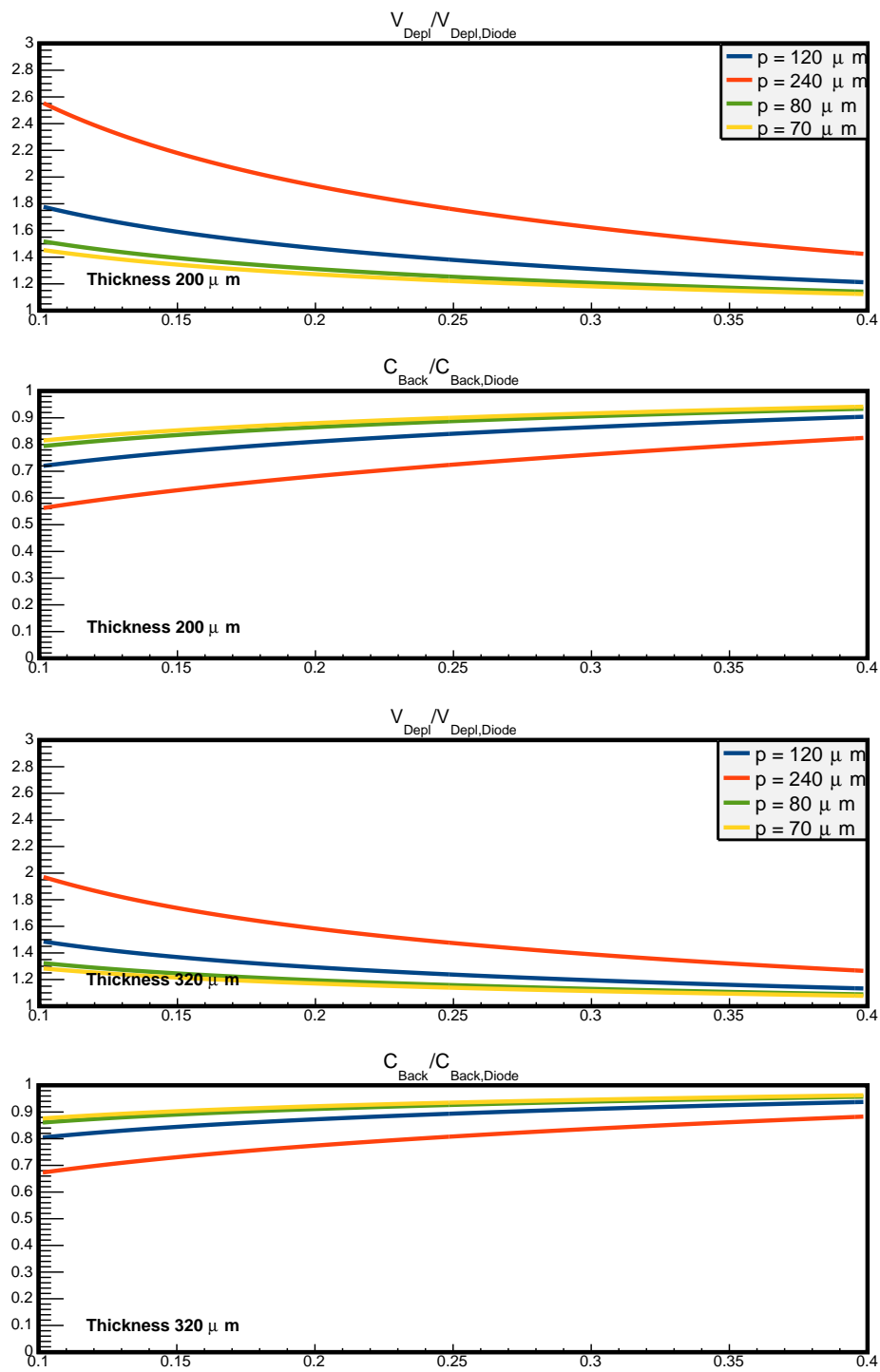


Figure 6.5: Computed correction factors to the diode approximation for a detector thickness of 200 and 320 μm for the pitches p of the MSSD.

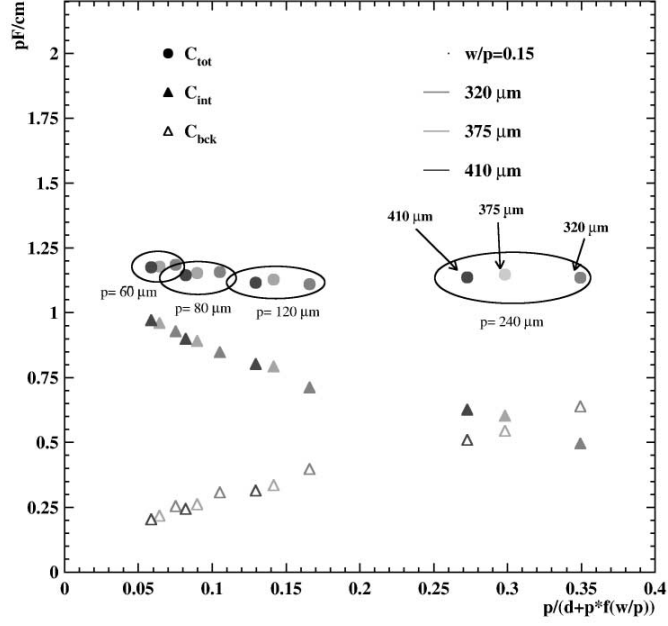


Figure 6.6: C_{back} , C_{int} and C_{tot} as a function of $p/[d + pf(w/p)]$ [52].

The depletion voltage, according to equation 6.3, is proportional to $p/df(w/p)$ and the intercept of a linear fit corresponds to the depletion voltage of a planar diode in this model.

Since capacitances and leakage current are always a function of voltage, an appropriate voltage has to be selected to extract the values for these overview plots. Two principal approaches are possible:

A multiple of V_{fd}

This approach ensures that the detector is depleted and all parameters, especially the capacitances, have reached a saturation value. This represents the operating conditions and the approach also works for irradiated detectors, which might have much higher depletion voltages, thin detectors and detectors made from different materials.

A fixed voltage

Using a fixed voltage for the extraction of sensor parameters does not take different material properties and fluence states of the samples into account but can be a reasonable choice, as the accessible bias voltages in the real experiment are limited due to the power supplies, the installed cables, the power to be dissipated and the cooling system.

In this chapter the first approach will be followed, as the intention is to compare material properties and thus the operating conditions for the specific materials have to be reproduced and therefore all values have been extracted at $1.2 \times V_{\text{fd}}$. Examples of data at a fixed voltage will be shown in the conclusions.

6.2 The Experimental Setup

The measurements described in section 6.1 are all different and require dedicated setups with different connection schemes. Since the MSSD is a multi-geometry structure with twelve regions, performing the three different measurements on all twelve regions on every detector results in a huge number of individual measurements. It is therefore desirable to have an automated test setup to measure one or several detectors at once without user intervention. This is especially important after irradiation of the structures, as it is necessary to perform the measurements at low temperature to keep the leakage current down and prevent annealing. Cooling to -20°C takes a considerable amount of time and thus it is favorable to measure several detectors per cooling cycle.

Part of the work for this thesis has consisted of performing the electrical measurements from the last section on the MSSD structure and setting up an adequate test stand with the available hardware.

6.2.1 Hardware

Cooling

Measurements on biased silicon devices have to be performed in darkness, and — in case of irradiated structures — in a cold environment. Avoiding any exposure of the sensor to light is necessary as light is radiation and would thus immediately saturate the sensor with charge carriers. For that purpose a cooling box, developed at HEPHY Vienna for long-term tests of modules during the production phase of the CMS tracker [56], was used to address both issues. This is basically a custom-made, sealable box that can thermoelectrically be cooled to -20°C and holds up to ten test samples.

Test Board

Before tests can be performed with the MSSD detectors, they have to be prepared for use with the various setups. For that reason a sensor, together with a glass-substrate pitch adapter, is glued to a ceramic (Al_2O_3) frame that acts as a mechanical support, electrical- and thermal isolation and carrier. All 384 strips are then wire-bonded to the sensor-facing side of the pitch adapter. These assemblies are screwed to an aluminum block that holds a printed circuit board; which connects the bias rings of the various regions of the MSSD to ground through a $100\text{ k}\Omega$ resistor and wire bonds. The leakage current and backplane capacitance are measured through wires that are soldered to the PCB and connect to a 64-pin ERNI connector that holds another PCB with bond pads to connect the individual strips for the measurement of the interstrip capacitance.

The backplane of the MSSD is contacted via wire bonds from a small pad that is glued to the ceramic frame, can be removed for irradiation and connects to a wire that is routed to the connector and delivers the high voltage.

Switching System

A two-stage switching system has been used to automatically perform all these measurements on the MSSDs. Stage one multiplexes the lines for the individual regions for the IV- and CV measurement (bias rings) and the C_{int} measurement to three common outputs. Together with the high-voltage connection, these three output lines are then connected to a USB-controlled, custom-built switchboard with high-voltage relays that switches between the schematics for the different measurements and contains the circuitry of the ISO box. The ISO box is necessary to decouple the input of the LCR meter that is only rated to 20 V from the bias voltage, which can exceed this value dramatically. This switchboard allows for the performance of all three measurements from section 6.1 on all twelve regions sequentially without ramping down the high voltage or changing the wiring of the setup. Figure 6.7a shows the schematic wiring of the detector and figure 6.7b shows the interior of the custom-made switchboard with the different lines and relays required for the individual measurements in different colors.

The measurement is done as follows:

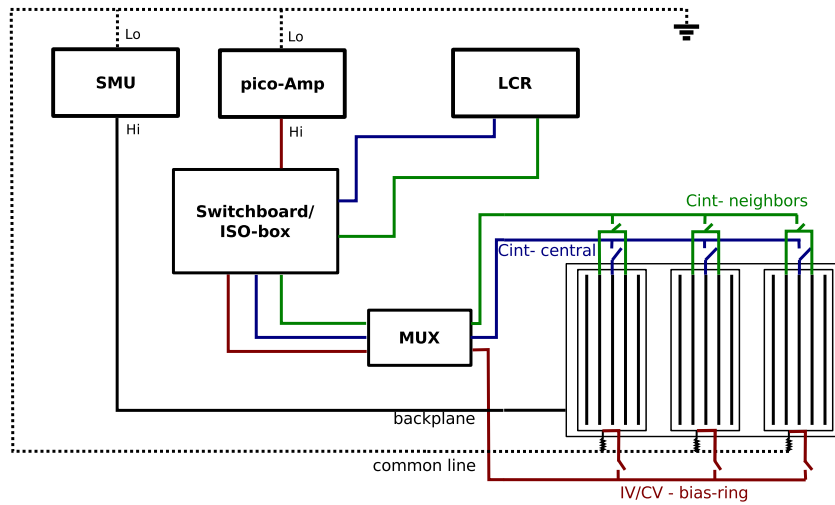
1. set high voltage
2. switch to IV measurement
3. switch through twelve regions and read current
4. switch to CV measurement
5. switch through twelve regions and read backplane capacitance
6. switch to C_{int} measurement
7. switch through twelve regions and read interstrip capacitance
8. set next high voltage and repeat from step two

Using this method, a complete electrical characterization of an MSSD detector with a voltage ramp up to 1,000 V takes about one and a half hours.

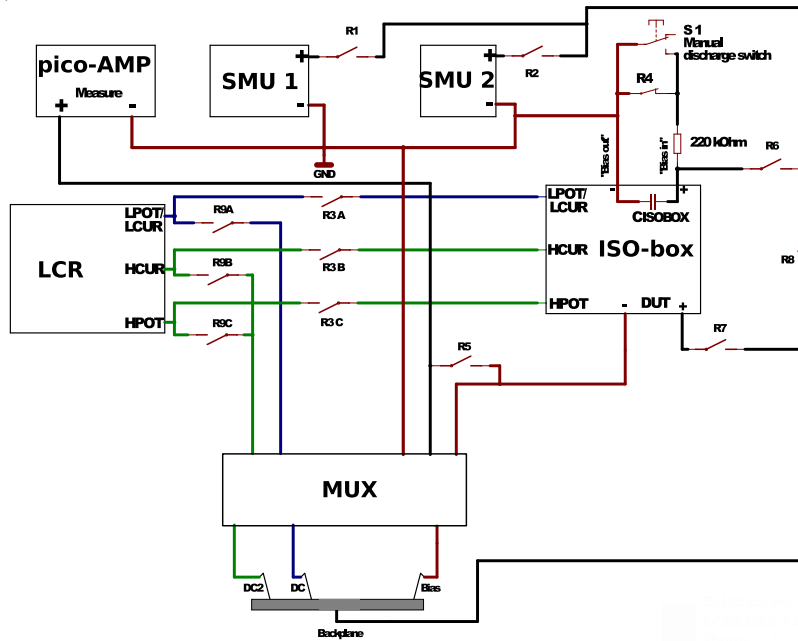
6.2.2 Control Software

In order to exploit the high degree of automation of the measurement setup fully, a control software was implemented in LabVIEW 2010 that performs the measurements and coordinates the instruments. It was designed to be modular and requires minimal user intervention. It consists of two stages that will be described briefly in the following section.

The actual measurement procedure consists of a series of stacked loops that loop over the bias voltage, measurement type and MSSD region. After some input required for correct labelling and storage of the results has been processed, the software sets a given high voltage and performs the following procedure:



(a) Connection- and switching scheme for the different regions of the MSSD.



(b) Relay schematic of the custom-made switchboard with high-voltage relays and all instruments. Courtesy of *F. Boegelspacher* from KIT.

Figure 6.7

1. read temperature on test board
2. apply high voltage and wait
3. set switchboard to leakage-current measurement, loop through twelve regions of the MSSD and read current
4. set switchboard to backplane-capacitance measurement, loop through twelve regions of the MSSD and read C_{back}
5. set switchboard to interstrip-capacitance measurement, loop through twelve regions of the MSSD and read C_{int} .

The last two steps also perform the offset correction and calibration of the interstrip capacitance. In the end, the measured data is restructured and the curves for each individual region are stored as a function of voltage.

Figure 6.8 shows a simplified flowchart of the MSSD-measurement control software that illustrates the functionality and steps described above.

Before starting the measurement campaign for the HPK project, a detailed measurement protocol was developed that states standardized parameters and settings for all the used instruments in order to ensure comparability of results obtained at different centers. As far as the MSSD is concerned, the most important parameters are:

- Voltage: all measurements should be performed in the range from 0 to 1,000 V or to the breakdown voltage
- Temperature: the measurement temperature should be 20°C for unirradiated samples and -20°C for irradiated detectors to prevent annealing and high leakage current.
- Frequency: 1 kHz for the backplane-capacitance- and 1 MHz for the interstrip-capacitance measurement.

Since the HPK project includes a vast number of individual structures from the many wafers that are qualified and used by the whole collaboration, a database has been introduced to keep track of the pieces. It is used to record measurement results and the history of the samples so that it is accessible for every collaboration member.

Before results can be uploaded they need to be reviewed carefully and some basic offline analysis has to be performed. In case of the electrical qualification of the MSSD sensor, three tables have to be filled that include leakage-current-, backplane-capacitance- and interstrip-capacitance data along with analysis results, like the depletion voltage extracted from the CV curve.

Another LabVIEW program is used to extract the parameters for the database tables with minimal user intervention. The only exception is the depletion voltage, as in some cases — due to the deep-diffusion process — the parameter cannot be extracted unambiguously from the $1/C^2$ curve. The user then has to select the fitpoints and ac-

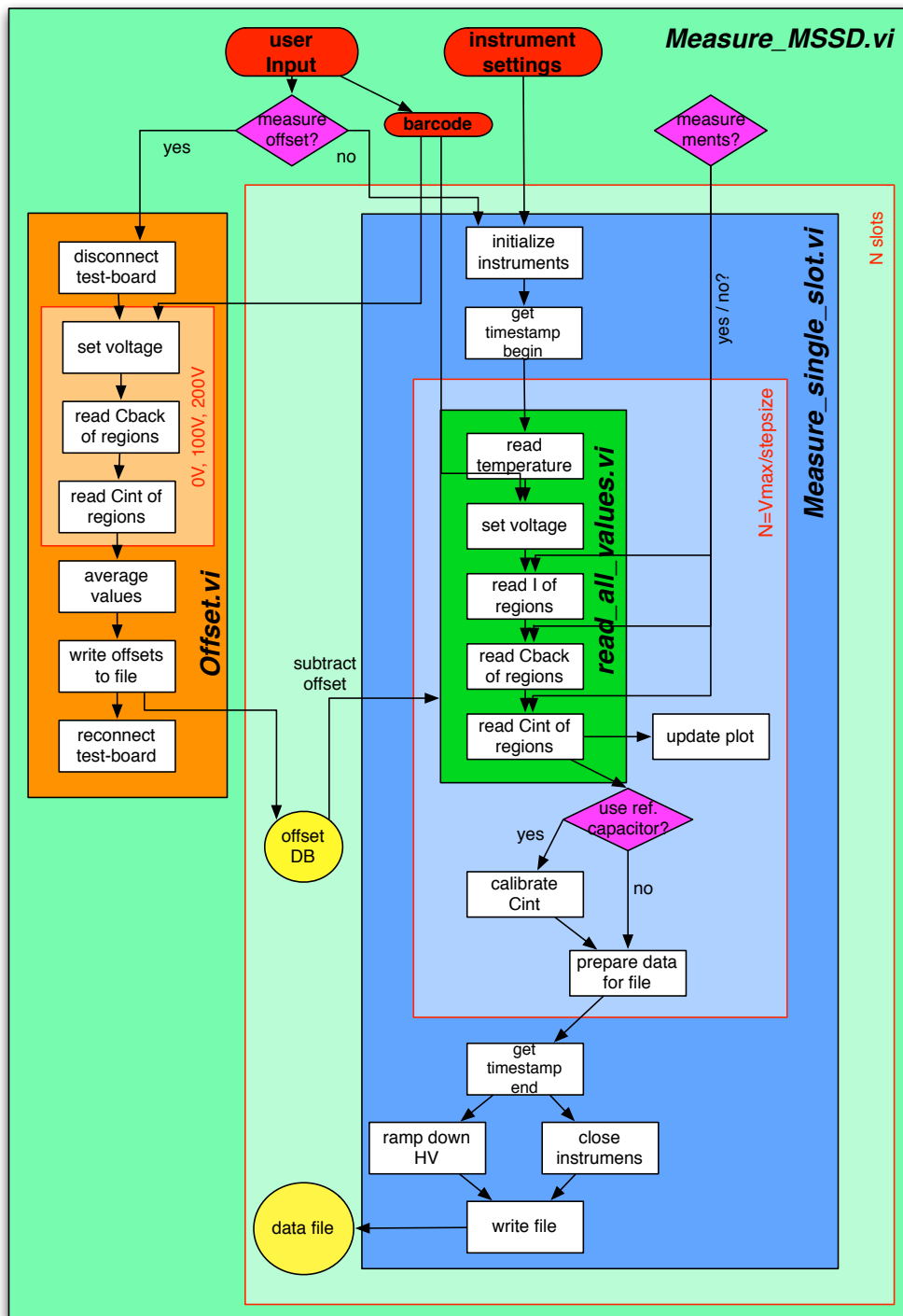


Figure 6.8: Simplified flowchart of the MSSD measurement software. The basic functionality is shown with the different sub-VIs but most parameters and variables are omitted for simplicity.

knowledge the result manually. After this analysis the results are parsed into .xml-format and uploaded to the database.

6.2.3 Calibration

As mentioned before, the measurements of the capacitances on the MSSD detector are very delicate, since there are many long cables and a switching system in the circuit and the strips on the MSSD are very short. This makes a correction and calibration of the measured C_{back} - and C_{int} values necessary to achieve high precision in the automated cooling box setup. The backplane capacitance of a depleted, thick (thickness pitch) detector is usually of the order of several hundred pF, which is far above the precision limit of the LCR meter, and thus the subtraction of the stray capacitance of the cables is sufficient. The backplane capacitance in the database reads

$$C_{back, DB} = C_{back, measured} - C_{stray} \quad (6.11)$$

with C_{stray} the value obtained in the offset measurement with the disconnected detector.

In the case of the interstrip capacitance the measured values are below ten pF, which is considerably smaller than the stray capacitance of the cable. In addition, the influence of the cabling and switching enters with double effect since both strips are connected to the instrument through the switching matrix, which is not the case for the backplane capacitance.

As a result, in addition to the subtraction of the offset values, a normalization of the measurement to the value of a known reference capacitor mounted on each test board is performed. This reference calibration is not linear over the whole range of interstrip capacitances and therefore another scale factor is introduced. It is obtained by measuring a set of known capacitors with different capacitances with the cooling box setup and fitting the known value versus the measured value. The final interstrip capacitance as it is written to the database then reads

$$C_{int, DB} = \frac{C_{int, measured} - C_{stray} - C_{reference\ correction}}{scale\ factor} \quad (6.12)$$

$$C_{reference\ correction} = C_{reference, known} - C_{reference, measured}$$

The scale factor obtained from this calibration is 1.098. Figure 6.9 shows a plot of known versus measured capacitor values and the fit. The measured values are shown with reference-capacitor normalization and without. The offset is almost constant at a value of 1.92 pF, while the actual reference capacitor value was measured to be 2.03 pF with the LCR meter.

Despite all the calibration efforts it has not been possible to fine-tune the measurement of the interstrip capacitance with the cooling box setup in such a way that it matches the values obtained at a dedicated probe station with short cables and without a switching matrix. The measurements are easy to reproduce and the reference capacitor calibration

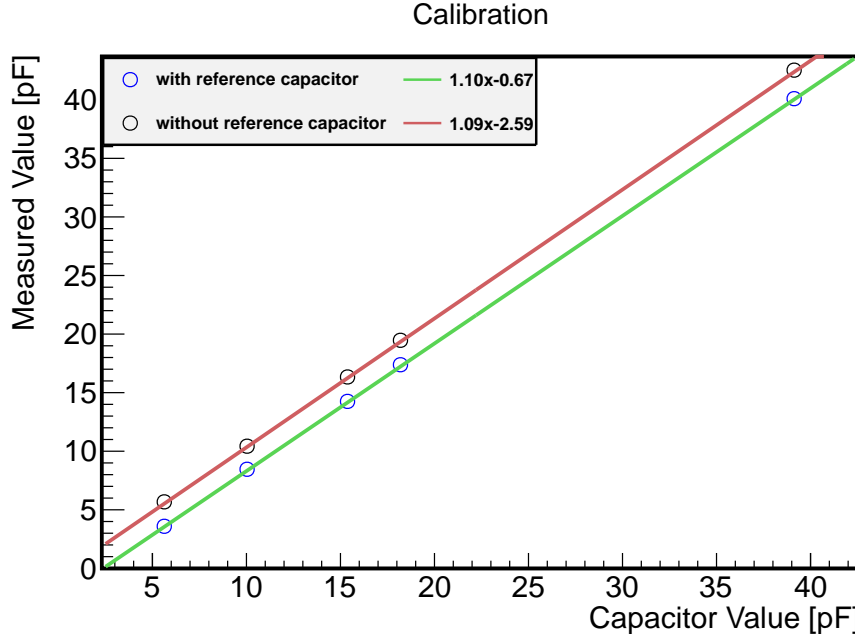


Figure 6.9: Capacitance calibration with and without reference capacitor.

has improved the results a lot but there is still a small, yet noticeable offset between the results obtained with the cooling box and the probe station. Collaboration members from INFN Florence went to extensive lengths to fine-tune their setup with respect to this delicate measurement and finally managed to get precise and verified results. However, it has to be noted that they do not use the switching system and therefore do not achieve such a high level of automation as with the presented setup. When comparing their interstrip-capacitance results and the results obtained during the work for this thesis, the latter are about 20% higher.

6.3 Results

In this section, the results obtained in the course of this thesis with the cooling-box setup and by INFN Florence will be presented according to the parametrization discussed in section 6.1.2. Data shown here was downloaded from the collaboration database on April 27th, 2013.

The plots in the following sections are ordered by not-irradiated and irradiated in columns and the lines represent the different doping schemes (p-on-n, n-on-p / p-stop, n-on-p / p-spray).

In the following, the results for the depletion voltage and total strip capacitance will be shown.

6.3.1 Depletion Voltage

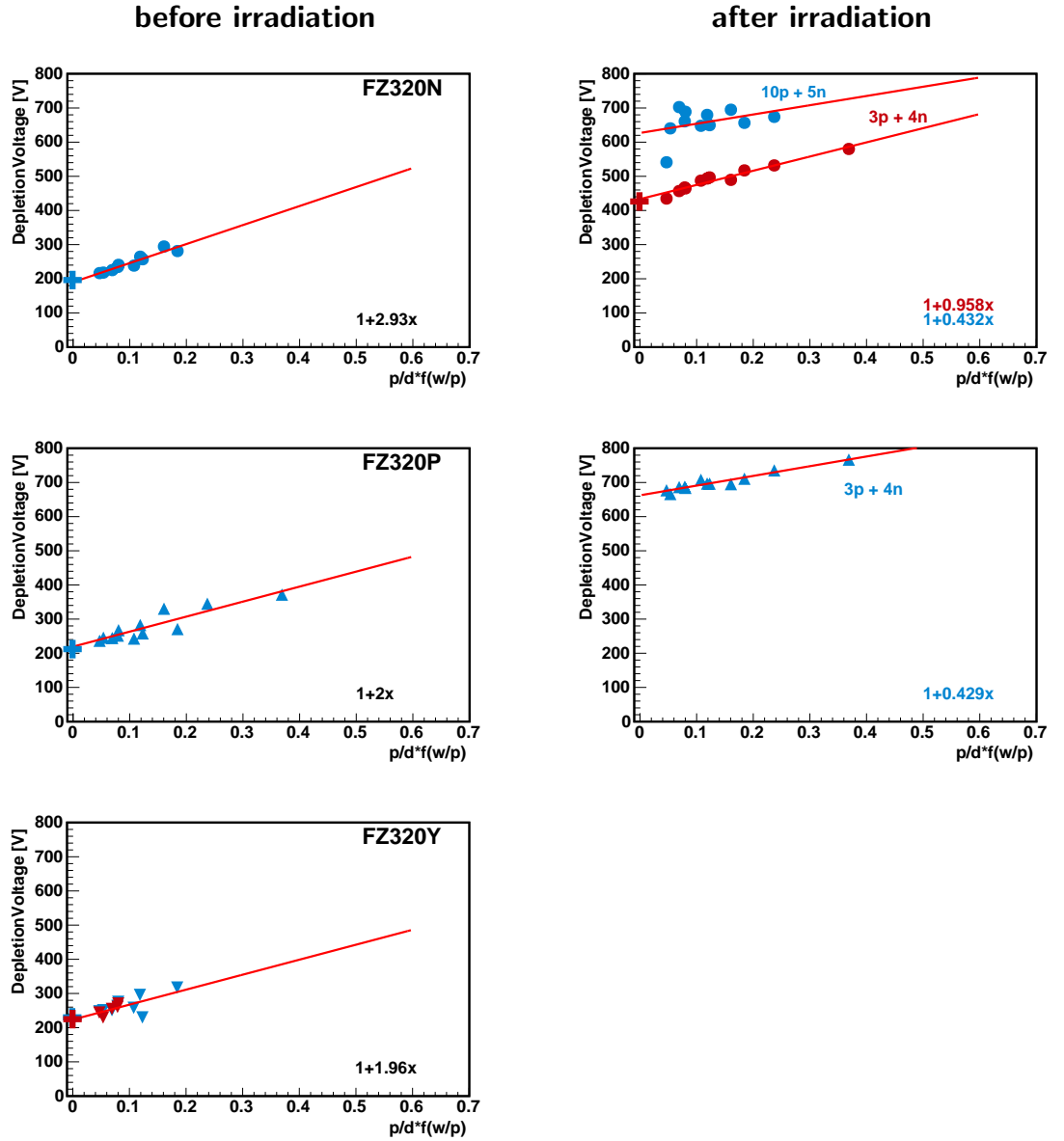
FZ 320 depletion voltage V_{fd} 

Figure 6.10: Depletion voltage for 320 micrometer-thick float-zone material and all three different doping schemes before (left) and after (right) irradiation. The fit parameters and, where applicable, the fluence are indicated in the plots. The plot in the upper right corner shows measurements after two different mixed fluences of 7×10^{14} 1MeV n_{eq} cm^{-2} (3×10^{14} protons and 4×10^{14} neutrons) and 15×10^{14} 1MeV n_{eq} cm^{-2} (10 protons and 5 neutrons).

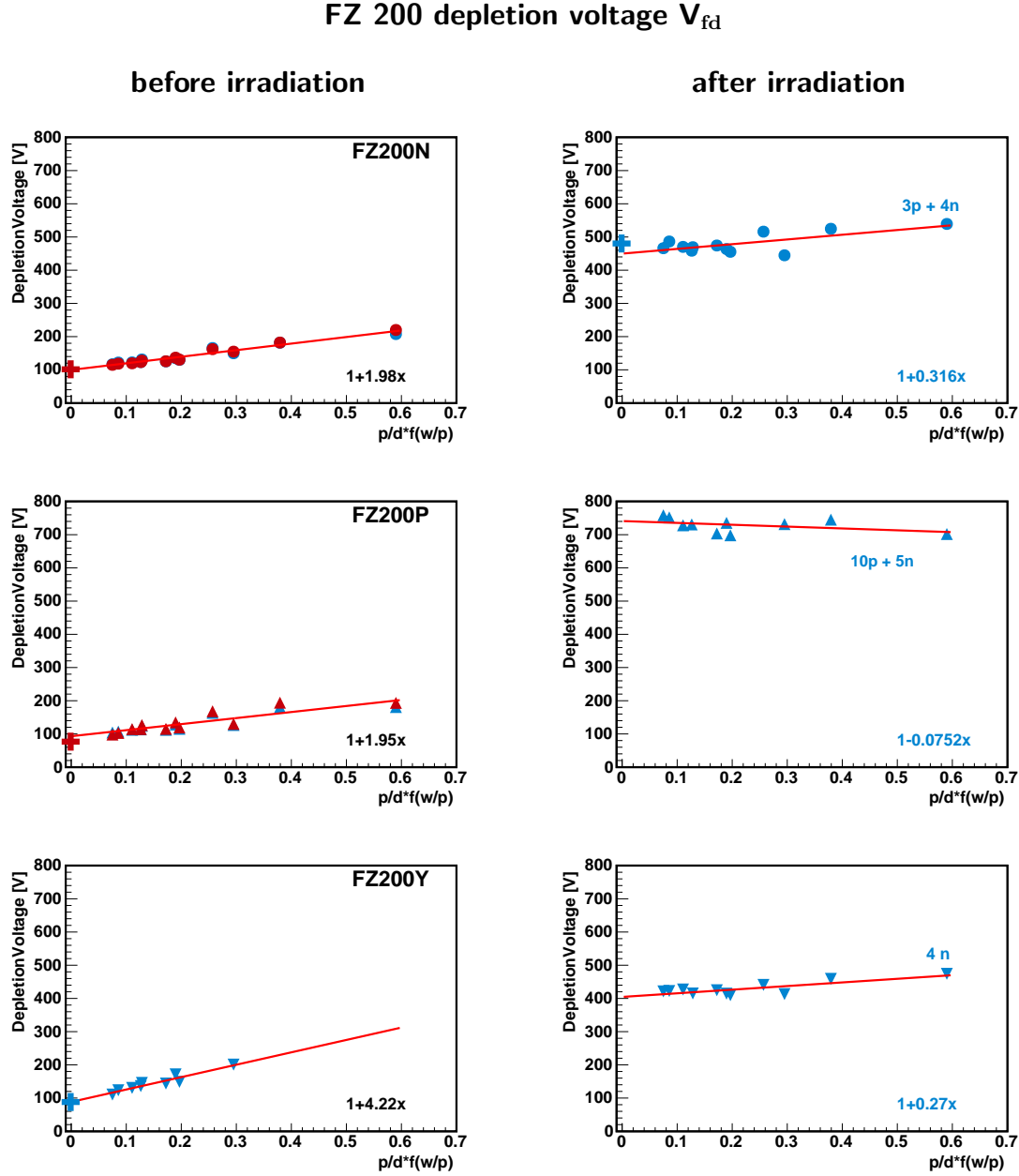


Figure 6.11: Depletion voltage for 200 micrometer-thick, deep-diffused float-zone material and all three different doping schemes before (left) and after (right) irradiation. The fit parameters and, where applicable, the fluence are indicated in the plots.

Figures 6.10 and 6.11 show the depletion voltage of the individual regions of 320 micrometer-thick and 200 micrometer-thick, deep-diffused MSSDs as a function of the parametrization introduced in section 6.1.2. The left column shows the result before and the right one the result after irradiation and the rows represent the different doping

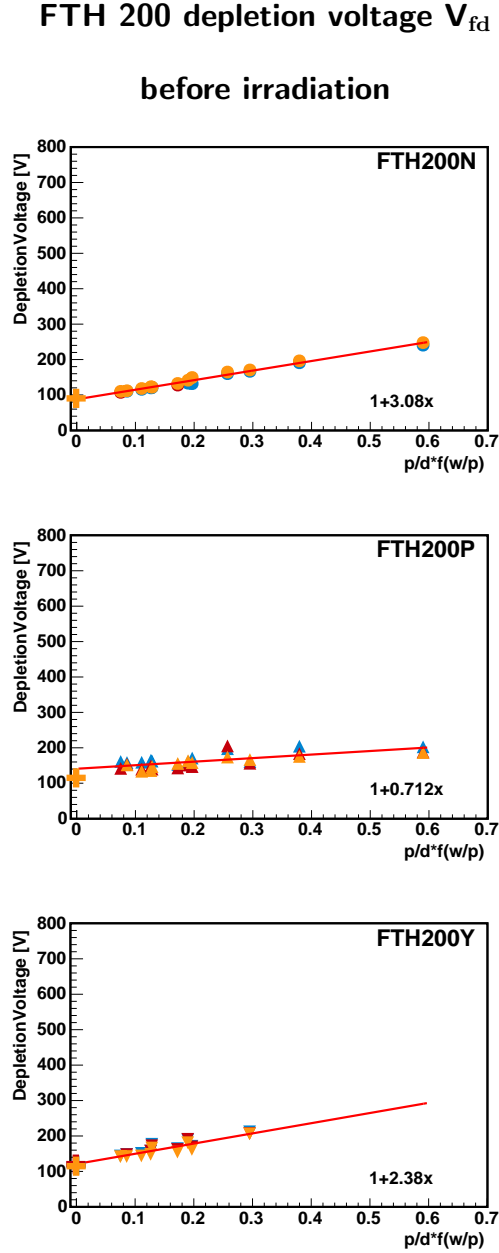


Figure 6.12: Depletion voltage for physically 200 micrometer-thick float-zone material and all three different doping schemes. Data for irradiated, physically-thinned material was not available yet.

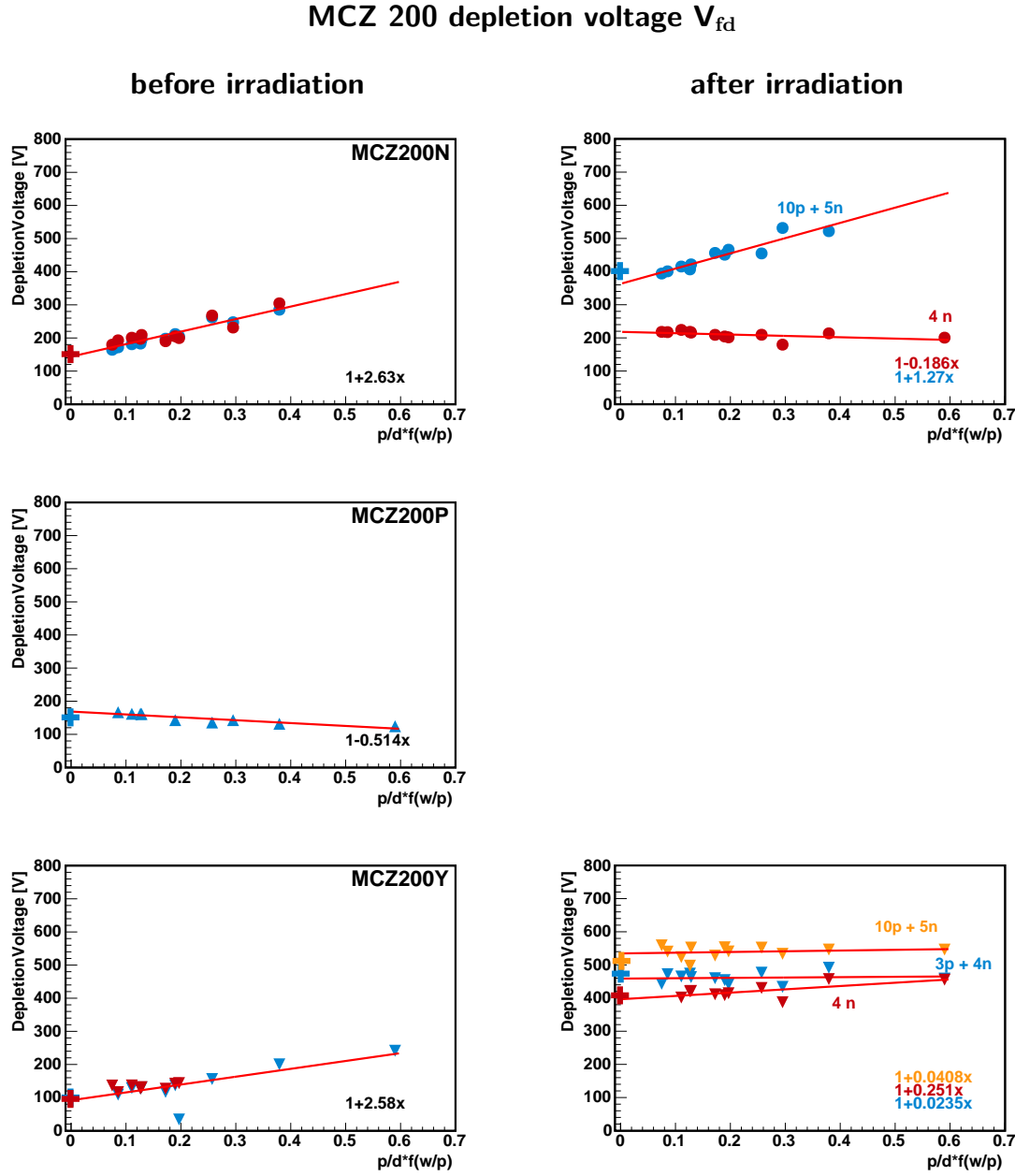


Figure 6.13: Depletion voltage for 200 micrometer-thick magnetic Czochralski material and all three different doping schemes before (left) and after (right) irradiation. The fit parameters and, where applicable, the fluence are indicated in the plots. After irradiation, the plots show measurements corresponding to different fluences of 4×10^{14} 1MeV n_{eq} cm⁻² neutrons, 7×10^{14} 1MeV n_{eq} cm⁻² (3×10^{14} protons and 4×10^{14} neutrons) and 15×10^{14} 1MeV n_{eq} cm⁻² (10×10^{14} protons and 5×10^{14} neutrons).

schemes.

The physically 200 micrometer-thick materials (magnetic-Czochralski- and float-zone silicon) are summarized in figures 6.12 and 6.13.

The datapoints are fitted with a linear function as derived in equation 6.4. According to that equation, the intercept of this fit corresponds to the depletion voltage of a diode, with a correction factor of zero and the slope divided by the intercept should be close to two ($V_{depl}/V_{depl,Diode} \propto (1 + 2x)$). The crosses in the figures 6.10, 6.11, 6.12 and 6.13 at $p/d * f(w/p) = 0$ show the depletion voltage of a diode from the same wafer as the measured MSSD and, together with the normalized fit parameters, confirm the relation deduced in equation 6.4 for the unirradiated sensors.

As mentioned in section 6.1.2, this geometrical correction originates from a semi-analytical solution of the two-dimensional Poisson equation [54]. Unlike a planar diode, where the equipotential lines of the electric field can always be considered parallel to the surface of the diode in first-order approximation, a strip sensor will fulfill this requirement only after the depleted layer underneath the strips has reached a thickness that is of the same order as the strip pitch, therefore increasing the depletion voltage by the correction derived in equation 6.4.

After irradiation, however, the model that assumes circular expansion of the depleted regions from the strips breaks down. The intercept of the fit function is still a very good estimate for the depletion voltage of a diode and also the linearity is still valid (figure 6.11), but the slope that should be two according to equation 6.4 is close to zero, which means that the boundary layer of the depleted region is planar from the beginning and that no geometrical correction between the depletion voltage of a diode and a strip sensor applies. In reality the situation is more complex as the bulk properties and thus the depletion characteristics of irradiated sensors change dramatically. In order to gain a full understanding why the above model breaks down, further studies involving extensive simulations of the electric fields in the bulk would be necessary.

The parameters of all fits for all materials that have been electrically qualified during the HPK project are summarized in figure 6.14, which shows a scatterplot of the fit parameters with their respective errors. The x axis shows the depletion voltage of a diode as extracted from the intercept of the above fit, whereas the y axis shows the normalized slope, thus yielding values around two if the depleted region grows from the strip side according to equation 6.4. The two cases corresponding to depletion from the front- and backside are indicated by the solid black lines in the plot. The yellow datapoints represent unirradiated sensors where the fit parameters are within four sigma from the model prediction, the red points are materials where the pull is actually greater than four sigma, the blue points represent irradiated, n-bulk materials with different fluences and the green points show irradiated p-doped material.

For most unirradiated detectors the model prediction according to 6.4 holds true. The outliers with a pull greater than four σ shown in red correspond to FTH200N at ($x \sim 100/y \sim 3$), FTH200P at ($x \sim 120/y \sim 1$) and MCZ200P at ($x \sim 180/y \sim 0.5$). An

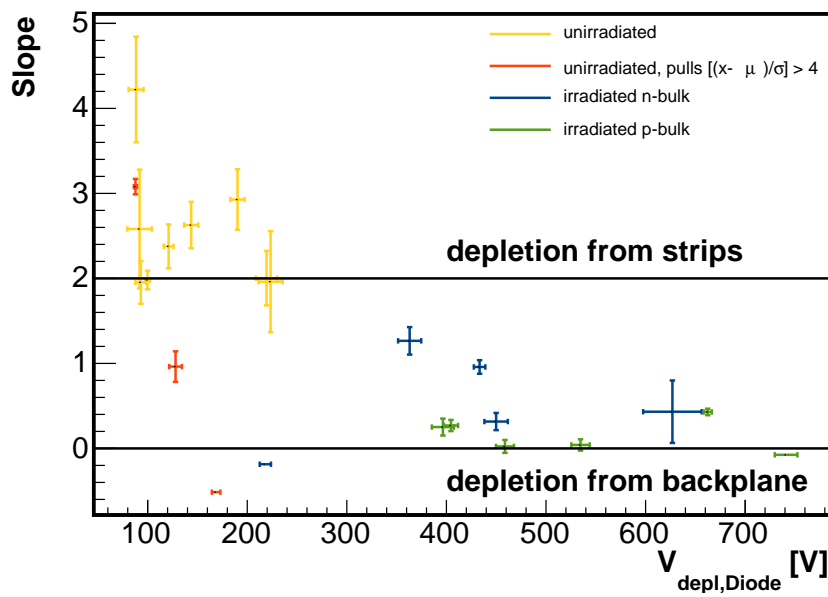


Figure 6.14: Scatterplot of the fit parameters and their errors obtained from fitting the depletion voltage of different regions of the MSSD as a function of the geometrical correction $p/d * f(w/p)$ with a straight line. The x axis shows the actual intercept which corresponds to the depletion voltage of a diode with correction factor 0 and the y axis shows the slope divided by the intercept. The model predictions for front- and backside depletion are indicated by the solid black lines.

interesting feature of figure 6.14 is that only physically thin materials are affected whereas all float-zone- and magnetic-Czochralski (N,Y) materials follow the prediction.

These results represent an interesting extension of the findings of the studies presented in [51], [52] and [53] to n-in-p material and to thinner sensors. The linear dependence of the depletion voltage has been confirmed for all tested materials and the accordance with the prediction from equation 6.4 is even better than in previous studies.

Contrary to [53], where no linear dependence of the depletion voltage on $p/d * f(w/p)$ after irradiation could be observed, this study does find linear behavior. However, the slope of the fit after irradiation is always very close to zero, which indicates a more complex situation that cannot be modelled so easily, taking only the geometry into account. In order to gain a full understanding of the depletion behavior of irradiated sensors, extensive studies and device simulations would be necessary, which is beyond the scope of this thesis.

6.3.2 Total Strip Capacitance

Figure 6.15 shows the total strip capacitance to the backplane and the two closest neighbors as a function of the geometrical correction parameter from equation 6.9. The total capacitance is constant for a given width-over-pitch ratio, whereas the backplane capacitance increases with increasing parameter and the interstrip capacitance decreases. However, different width-over-pitch ratios have different total capacitance values, which originates from the interstrip capacitance that is larger for larger values of w/p . The backplane capacitance on the other hand does not change significantly with w/p .

Since both capacitances depend only on the geometry and the depleted volume, irradiation is not expected to affect the values significantly at voltages above the full depletion voltage. As the values in figure 6.15 were extracted at $1.2 \times V_{fd}$, this behavior is confirmed, which also means that the front-end amplifier input capacitance will stay constant with increasing accumulated fluence. For that reason it is possible to optimize the readout chip solely based on the strip geometry in the future CMS tracker without having to take additional, irradiation-induced effects, into account.

Figure 6.16 shows the same quantity but for three different doping schemes. The width-over-pitch ratio is 0.15.

This result yields several conclusions that are important for the design and specification of new sensors. First of all, they confirm the expectation – and thus the underlying model – that the total capacitance of one strip, which is the dominant source of noise in silicon detectors in the LHC environment with its short peaking time, is constant as a function of $p/[d + p * f(w/p)]$. This holds true over the wide range of tested strip pitches, as the changes of the backplane- and interstrip capacitance with increasing parameter cancel each other out.

The value of the total strip capacitance is quasi-independent of the strip pitch but almost exclusively governed by the width-over-pitch ratio of the strips, with smaller

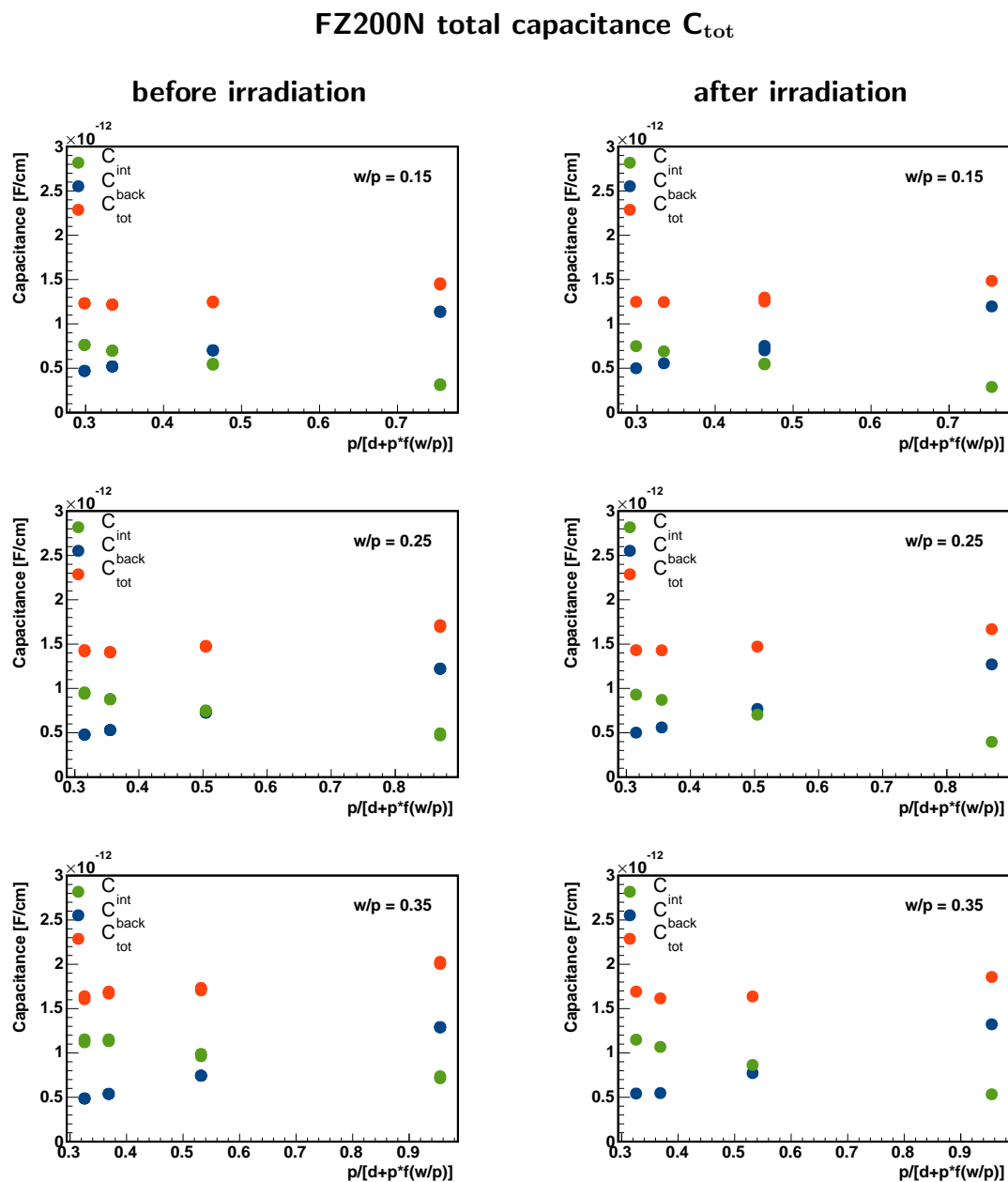


Figure 6.15: Total capacitance of one strip per cm for 200 micrometer-thick, n-bulk float-zone material before (left) and after (right) irradiation.

FTH200 total capacitance C_{tot} , $w/p = 0.15$

before irradiation

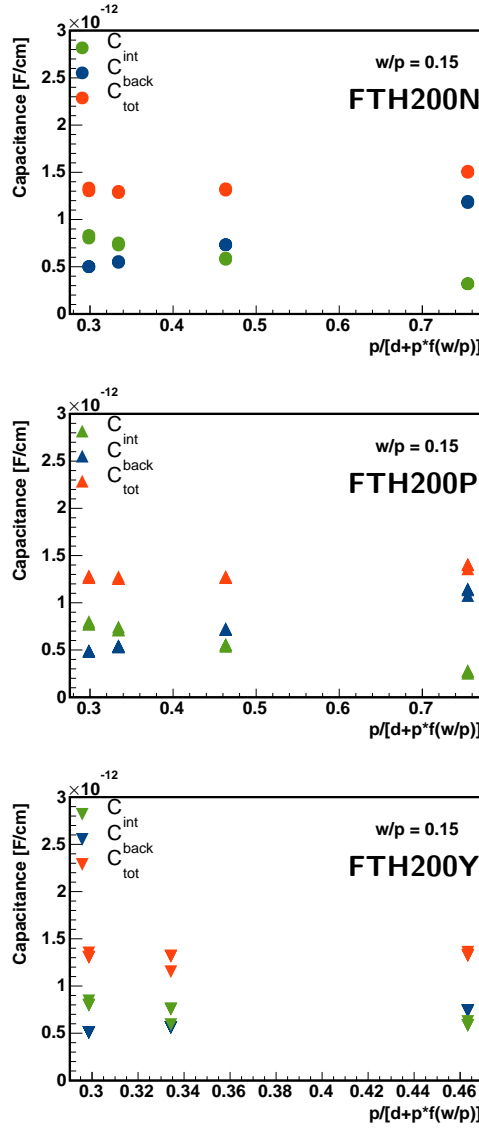


Figure 6.16: Total capacitance of one strip per cm for 200 micrometer-thick, physically-thinned, n-bulk float-zone material before irradiation.

values of w/p having smaller capacitance and thus lower noise. This allows for designing suitable front-end electronics for the future tracker independently of the final strip pitch but matching a given strip length and width-over-pitch ratio.

Although thinner strips with respect to the pitch reduce the capacitance, they result in a higher electric fields underneath the strips which in turn lowers the breakdown voltage and high-voltage stability. For these reasons, it is necessary to find a balance between high-voltage stability and noise performance of a certain geometry that suits the application best. Given the high fluences expected in the High-Luminosity LHC environment and consequently the high depletion voltages that will be necessary to keep charge collection of the sensors at a reasonable level, higher width-over-pitch ratios are more favourable despite the higher noise they imply.

Another, interesting feature of these results is the independence of the total capacitance on the doping technology (figure 6.16) which indicates that this behavior really only depends on the geometry and that the producers have good control over the production process, resulting in similar geometrical conditions independent of the doping scheme and underlying process.

Figure 6.17 shows histograms of all measured values of the total capacitance of the regions on the MSSD, normalized to a strip length of one cm for the different width-over-pitch ratios and before and after irradiation. As already shown in figure 6.15, higher values of w/p have higher total capacitance whereas irradiation has only a very minor effect on the mean values that are grouped around 1.5 pF/cm, independent of pitch and detector thickness as the decrease of C_{int} with increasing strip pitch is almost perfectly compensated by the increase of C_{back} .

Tables 6.1 and 6.2 summarize the parametrization of the total capacitance as a function of the width-over-pitch ratio for all unirradiated- and irradiated materials.

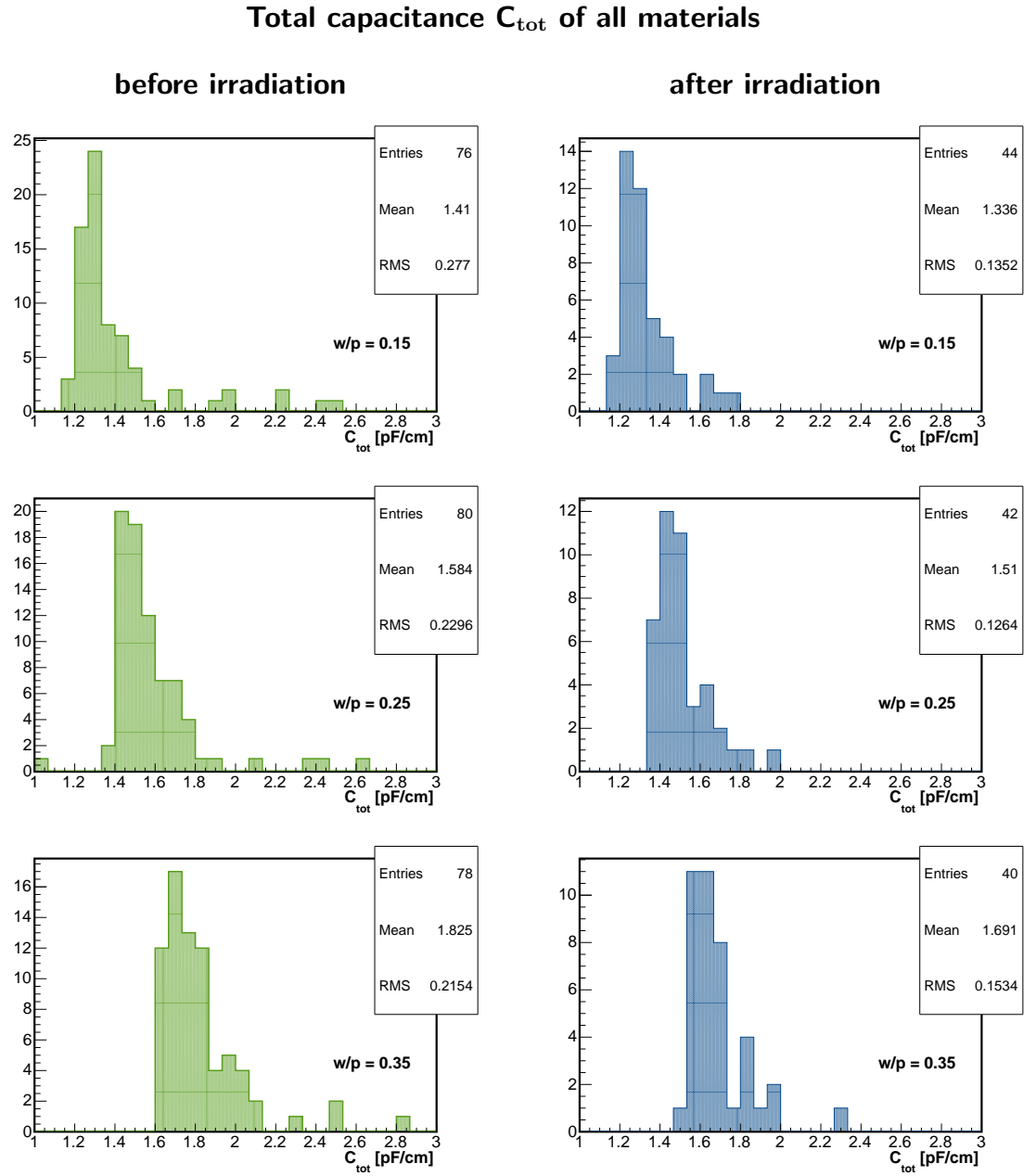


Figure 6.17: Total capacitance of one strip per cm for all pitches, materials and doping schemes for the different width-over-pitch ratios present on the MSSD.

Table 6.1: Parametrization of the total capacitance for all unirradiated materials independent of the doping scheme.

Material	Pitch	$C_{tot}(w/p)$
FZ320	70 μm	$C_{tot} = 0.63(\pm 0.24) + 3.40(\pm 0.88) * (w/p)$
	80 μm	$C_{tot} = 0.96(\pm 0.14) + 2.37(\pm 0.53) * (w/p)$
	120 μm	$C_{tot} = 1.33(\pm 0.32) + 0.64(\pm 1.18) * (w/p)$
	240 μm	$C_{tot} = 0.75(\pm 0.17) + 3.1(\pm 0.65) * (w/p)$
FZ200	70 μm	$C_{tot} = 1.35(\pm 0.31) + 1.07(\pm 1.21) * (w/p)$
	80 μm	$C_{tot} = 1.08(\pm 0.24) + 2.14(\pm 0.91) * (w/p)$
	120 μm	$C_{tot} = 0.89(\pm 0.36) + 2.98(\pm 1.38) * (w/p)$
	240 μm	$C_{tot} = 1.31(\pm 0.43) + 2.47(\pm 1.62) * (w/p)$
FTH200	70 μm	$C_{tot} = 1.01(\pm 0.022) + 1.97(\pm 0.08) * (w/p)$
	80 μm	$C_{tot} = 0.90(\pm 0.035) + 2.44(\pm 0.13) * (w/p)$
	120 μm	$C_{tot} = 0.96(\pm 0.036) + 2.27(\pm 0.14) * (w/p)$
	240 μm	$C_{tot} = 1.09(\pm 0.074) + 2.34(\pm 0.28) * (w/p)$
MCZ200	70 μm	$C_{tot} = 1.12(\pm 0.09) + 1.59(\pm 0.35) * (w/p)$
	80 μm	$C_{tot} = 1.13(\pm 0.15) + 1.72(\pm 0.55) * (w/p)$
	120 μm	$C_{tot} = 1.38(\pm 0.20) + 1.07(\pm 0.73) * (w/p)$
	240 μm	$C_{tot} = 2.02(\pm 0.73) + 0.79(\pm 2.70) * (w/p)$

Table 6.2: Parametrization of the total capacitance for all irradiated materials independent of the doping scheme.

Material	Pitch	$C_{tot}(w/p)$
FZ320	70 μm	$C_{tot} = 0.94(\pm 0.01) + 1.76(\pm 0.06) * (w/p)$
	80 μm	$C_{tot} = 0.96(\pm 0.02) + 1.65(\pm 0.08) * (w/p)$
	120 μm	$C_{tot} = 0.96(\pm 0.02) + 1.70(\pm 0.11) * (w/p)$
	240 μm	$C_{tot} = 1.24(\pm 0.12) + 1.37(\pm 0.46) * (w/p)$
FZ200	70 μm	$C_{tot} = 0.98(\pm 0.03) + 1.91(\pm 0.14) * (w/p)$
	80 μm	$C_{tot} = 1.01(\pm 0.035) + 1.8(\pm 0.13) * (w/p)$
	120 μm	$C_{tot} = 1.05(\pm 0.04) + 1.74(\pm 0.19) * (w/p)$
	240 μm	$C_{tot} = 1.34(\pm 0.16) + 1.51(\pm 0.65) * (w/p)$
MCZ200	70 μm	$C_{tot} = 0.90(\pm 0.14) + 2.48(\pm 0.57) * (w/p)$
	80 μm	$C_{tot} = 1.04(\pm 0.02) + 1.68(\pm 0.11) * (w/p)$
	120 μm	$C_{tot} = 1.06(\pm 0.03) + 1.74(\pm 0.13) * (w/p)$
	240 μm	$C_{tot} = 1.25(\pm 0.07) + 1.85(\pm 0.27) * (w/p)$

7 Beam Tests

The second and major part of the work that has been carried out throughout this thesis has been devoted to testing the MSSD sensors' response to ionizing particle beams. Four such beam tests, carried out at beam lines at Fermilab and CERN, have been analyzed. The experimental setup, the data-analysis procedure and the most important results will be summarized in this chapter.

Although ionizing sources like ^{90}Sr and ^{106}Ru can be used to measure the signal in the laboratory, full position resolution and detection efficiency studies can be done only with high-energy beams or cosmic rays.

Both approaches require a dedicated readout system with multi-channel charge amplifiers and shaping circuitry. For this study the APV25 [23] chip produced for the present CMS tracker was used.

Using an external beam telescope to measure the trajectories of the beam particles, it is possible to study parameters like charge sharing, spatial resolution, signal and efficiency of a silicon sensor by comparing the data recorded by the detector that is tested to the reference tracks 7.2. This can be done because the angular spread of the beam is negligible and multiple scattering is small with respect to the resolution of the telescope.

7.1 The Beam-Test Setup

A readout module (figure 7.1) was designed that is similar to the test boards used for the electrical qualification. The MSSD, which is permanently glued to a ceramic support and bonded to a pitch adapter, is mounted on an aluminum baseplate that holds the sensor, a front-end hybrid from the present CMS tracker and a bias circuit. A low-pass RC filter is added to the high-voltage line that is connected to the backplane of the sensor to reduce noise introduced by the bias voltage. A front-end hybrid with 4 APV25 [23] chips, developed for the present CMS tracker (chapter 3, section 3.2), is used for readout.

The aluminum plate serves as a mechanical support and thermal contact for the sensors during testing. As with the electrical qualification, cooling is essential when biasing irradiated detectors to keep the dark current and thus the noise low, prevent thermal runaway and suppress annealing.

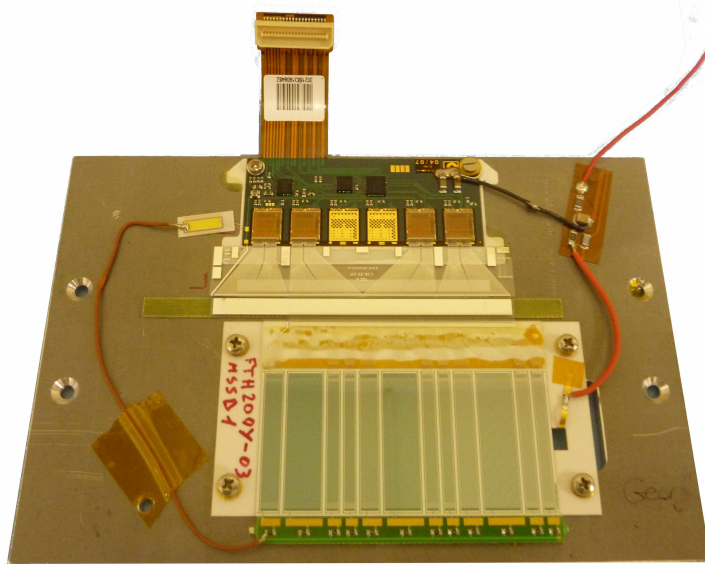


Figure 7.1: Readout module designed for testing the MSSD in beam tests and source setups. The sensor is connected to the front-end chips through three pitch adapters that ensure rebondability for multiple use.

7.1.1 The Silicon Beam Telescope

The Silicon Beam Telescope or SiBT [57] is a dedicated setup developed by the CMS group of the Helsinki Institute of Physics (HIP) to test silicon microstrip- and -pixel detectors in a test-beam environment. In order to reproduce the expected operating temperatures of HL-LHC detectors and to be able to measure irradiated detectors it was installed inside a Vienna Cooling Box identical to the one described in chapter 6.

Cooling Box, Detectors and Trigger

This box has ten slots with a spacing of four centimeters, which has been found to provide a sufficient lever arm for the precise tracking of passing particles. Measuring the tracking efficiency of the telescope itself requires a minimum of four space points: three to provide the space points to reconstruct the track and one is used as the detector under test to calculate the resolution and efficiency. Since the telescope makes use of strip detectors, eight reference planes are necessary to provide the four two-dimensional space points and these planes occupy the first and last four slots inside the box, while the two central ones can hold detectors that are tested.

The reference detectors used as telescope in the SiBT are single-sided, AC-coupled strip detectors manufactured by Hamamatsu Photonics on high-resistivity float-zone material for the D0 experiment at the Tevatron. These have a thickness of $320\ \mu\text{m}$ and a readout pitch of $60\ \mu\text{m}$ [57]. In between the 639 strips that are connected to the front-end chips, electrically-floating intermediate strips improve the charge sharing and

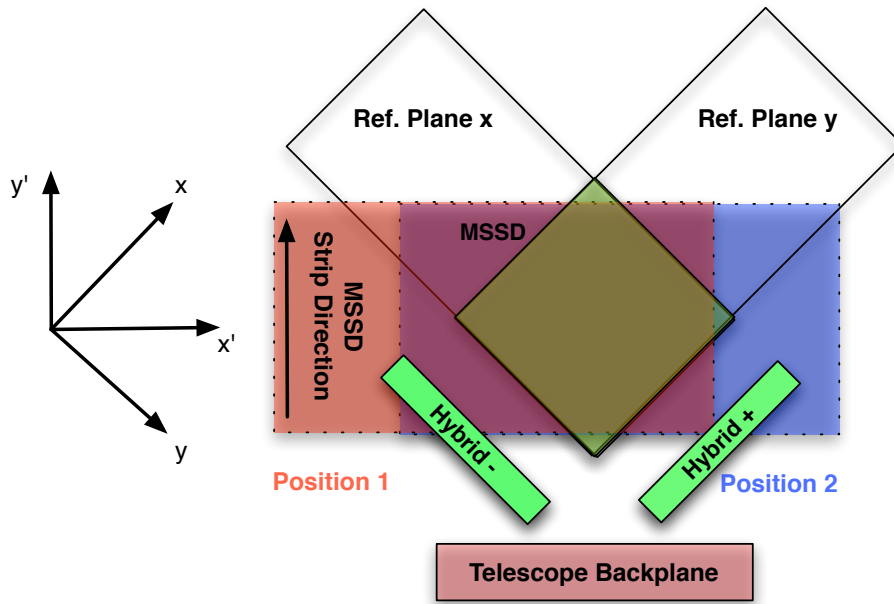


Figure 7.2: Schematic drawing of the geometrical relations of reference detectors and DUT in the SiBT.

thus the resolution, which is claimed to be 4.2 micrometer [57]. Their depletion voltage was determined by means of CV measurements to be around 150 V, which is also the operating voltage in the system.

These sensors are mounted on a carrier PCB holding six-chip CMS TOB (Tracker Outer Barrel) hybrids, which in turn is mounted to a brass plate that is inserted into the cooling box. Due to the restricted space inside the box, the sensor orientation was chosen to be plus and minus 45° alternatingly, effectively resulting in pairs of orthogonally-orientated sensors with an active overlapping area of four by four centimeters. The hybrids are connected to the front-end electronics and data acquisition system through the backplane of the Vienna Box by so-called VUTRI adapters, which are mounted on the brass plates, and VUTRI cards on the outside of the box [57]. Figure 7.2 shows a schematic drawing of this assembly.

In 2011 a new, larger cooling box was successfully commissioned for use with the SiBT. It has slots for twelve detectors, maintaining the spacing of four centimeters for the reference planes. On the other hand, the four slots for the Detectors Under Test (DUTs), are spaced by eight centimeters. Figure 7.3 shows the geometry of the old and new SiBT, while figure 7.4 shows the new cooling box with the increased DUT spacing.

The trigger is provided by two scintillators coupled to photomultipliers that are mounted in front and behind the cooling box together with NIM modules that form a coincidence signal.

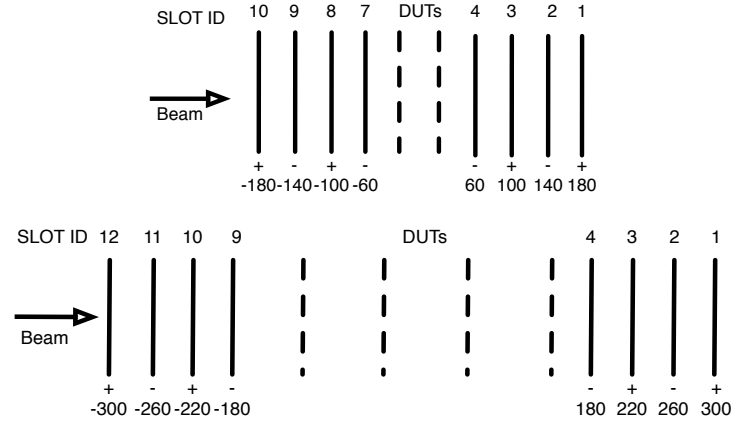


Figure 7.3: Position and orientation of the reference planes and DUTs inside the old (top) and new (bottom) cooling box used for the SiBT. The origin of the coordinate system was chosen such that the layout is symmetrical around the center of the box. + and - denote the orientation of the detectors $\pm 45^\circ$.



Figure 7.4: Picture of the Silicon Beam Telescope at the H4 beam line at the SPS North Area at CERN. The first and last four slots are occupied by the reference detectors. The picture shows the new cooling box that can hold up the four detectors under test (DUTs).

Readout and Data-Acquisition Software

The readout system of the Silicon Beam Telescope is based on a prototype version of the CMS data-acquisition system and therefore the basic concept resembles the one presented in chapter 3. It consists of PCI card-controlled electrical front-end controller boards (FEC) and front-end driver (FED) boards and a Communication- and Control

Unit (CCU). The front-end controller distributes clock- and trigger signals to the readout chips and sets tunable chip parameters [57].

The multiplexed chip signals from the APVMUX (section 3.2) are transmitted to the front-end drivers via the VUTRI interface at the backplane of the cooling box, which amplifies the signal. These data frames are read and digitized by the front-end driver upon reception of a trigger signal. All data is recorded in *virgin raw mode* in the SiBT. The total number of front-end chips per FED is 16, which means that a total of four FED cards is required to read the whole SiBT [57].

7.1.2 Test-Beam Facilities

All data presented here was taken at four beam tests. The first one took place at the FNAL in Illinois, United States, in March 2011 and the following three experiments were carried out at CERN in September 2011, May 2012 and October 2012.

MTest Beam Line at FNAL

This is a dedicated test-beam facility providing a 120 GeV proton beam from the Main Injector synchrotron at Fermilab. The particle rate is less than 100 kHz and the spills are usually 3.6 seconds long and one spill per minute is available [58].

H2 Beam Line at CERN

The H2 beam line is part of the SPS North Area experimental facility that is supplied by the SPS with a 450 GeV primary proton beam, which is then directed onto a primary target, where a secondary beam is created that contains hadrons, electrons and muons. The available energies range from ten to 360 GeV secondaries and the maximum achievable energy is 400 GeV with the primary proton beam. A system of beam optics, collimators and targets gives the user the possibility of changing beam shape, -size, -energy and particle type [59].

The experimental area H2B was used during the September 2011 and May/October 2012 beam tests together with the CMS calorimetry group, where the Silicon Beam Telescope ran in parasitic mode, meaning that it was placed before the absorbing calorimeter in the beam line. This was possible as the total material budget of the telescope and thus the energy loss of the beam as seen by the calorimeter is negligible. However, the calorimeters as the main users had the choice of beam parameters and therefore the particle type and -energy was varied.

7.2 The Analysis

In this section the analysis of the data recorded in the beam tests will be described in detail. A two-step approach has been chosen and two different software packages have been used to process the raw data:

1. The **EUTelescope** [60] [61] [62] package within the ILCSoft framework has been

used to process telescope data and reconstruct tracks.

2. A special **TBAnalysis** software written for the analysis of the MSSD detectors takes the parameters of the reconstructed telescope tracks as input and does the detailed analysis of the MSSDs performance.

This has the advantage that the complicated task of telescope alignment and track reconstruction is carried out by a well-tested software framework that requires minimal user intervention. Although initially developed for a silicon-pixel telescope, the code was easily adapted to process data recorded with strip sensors.

The detailed analysis of the MSSD with its special geometry could not easily be implemented in the **EUTelescope** framework and therefore it was decided to write a dedicated analysis code. It has been developed in the course of this thesis and has been optimized for studies of the multi-geometry detector.

7.2.1 Tracking with the EUTelescope Framework

The EUTelescope software package [60] was initially developed for the analysis of data recorded with the EUDET telescope, which uses silicon-pixel sensors and is based on the ILCSoft [63] framework.

The implementation of the EUTelescope package into the ILCSoft framework consists of a series of procedures with a modular structure, which perform the track reconstruction. The parameters that define the analysis are passed to the analysis steps via XML files [60]. Figure 7.5 shows the structure of the track-reconstruction analysis chain adapted for the Silicon Beam Telescope.

It has been modified for use with silicon-strip sensors, as the original version [60] demands two-dimensional hit coordinates for every sensor plane, which a strip sensor cannot provide. In the geometry description this was accounted for by modelling the strip sensors as pixel sensors, with one pixel in y direction, and a step of *hit faking* had to be introduced in the analysis chain to interpolate the missing coordinates on a given sensor plane after the initial, separate alignment in x - and y direction.

The raw data is first converted into a format readable by the EUTelescope package and then pedestal- and noise calculations are performed. A cluster search on the calibrated data then yields clusters which correspond to hits of traversing particles. These clusters can be filtered to reduce the combinatorial background for later track fitting and the filtered clusters are used to calculate the η -correction, which in turn is used to translate the clusters into actual coordinates in the telescope-coordinate system according to

$$\tilde{x} = x_i + \frac{S_{i+1}}{S_i + S_{i+1}}(x_{i+1} - x_i) = x_i + \frac{S_{i+1}}{S_i + S_{i+1}}\tilde{p}$$

with \tilde{x} the calibrated position, x_i the position of strip i and S_i the signal of strip i . These hits are then used to align the individual planes of the beam telescope with respect to each other. This has to be done in x - and y direction separately, as each plane of the SiBT

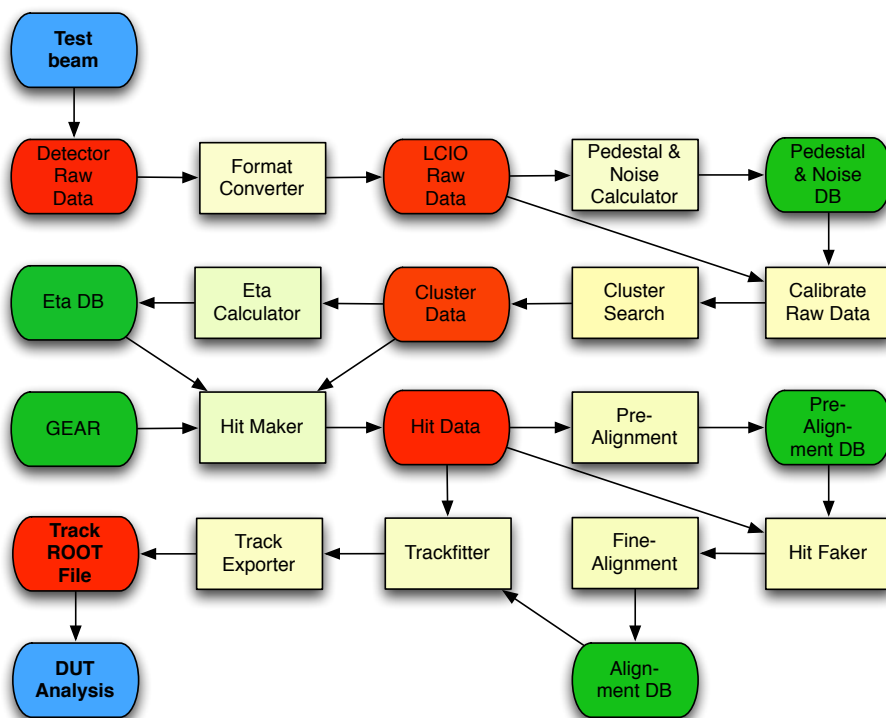


Figure 7.5: Modified analysis chain for the reconstruction of telescope tracks with the EUTelescope framework as used for the Silicon Beam Telescope.

can only provide a one-dimensional measurement. After the alignment corrections are added to the hit coordinates calculated by the hitmaker, the missing coordinate of every plane is interpolated, using the measurements of the other planes. This means that the y coordinate on a plane that measures only in x direction is computed by interpolating the measurements of all planes that measure in y direction. This is necessary, as separate alignment in x - and y direction is not able to correct angular misalignment, which requires two coordinates for every telescope plane.

For that reason, a second step of alignment is performed before the final tracks are fitted with straight lines. In order to get a pure sample of tracks, only events with tracks meeting the following criteria are selected for the analysis:

- no ambiguous hits and thus only events with one hit per telescope plane
- no missing hits
- $\chi^2 < 500$ ($N_{D.O.F.} = 8$)

After this step, the track parameters are exported to a ROOT file, which is used for the further analysis with a standalone software.

MSSD data is also processed with the EUTelescope framework but here the analysis steps are limited to the format conversion and calibration of the raw data. Finally the calibrated raw data and the pedestal and noise collections for the DUT are also written to a ROOT file, which acts as input for the further analysis of the MSSD.

Resolution of the SiBT Beam Telescope

During the analysis of the data recorded with the MSSD, the tracking performance of the SiBT (section 7.1) has also been studied in order to have an independent estimate of the uncertainty of the reconstructed tracks. For that reason, the hits in the telescope planes as reconstructed by the EUTelescope framework were exported to a ROOT tree for several single runs that represent different beam tests.

With these hits, the resolution of the individual telescope planes was computed with a double-iterative method, taking all planes that measure a coordinate (four in x direction and four in y direction) and assigning an a-priori error of 20 micrometers to each of them. In the first loop, one plane is excluded at a time and the track is fitted with the datapoints of the remaining ones. The residual distribution $\sigma_{Residuals}$ on the excluded plane is a convolution of the intrinsic reference-plane sensor resolution σ_{Sensor} and the error of the fitted track, which is determined by the resolution of the other planes σ_{Track} .

$$\sigma_{Sensor} = \sqrt{\sigma_{Residuals}^2 - \sigma_{Track}^2} \quad (7.1)$$

Using this method, the intrinsic resolution of each plane is computed and can be used as measurement error to repeat the above procedure in a second loop, which converges after the second iteration.

As soon as the resolution of all planes is known, the telescope resolution can be computed as a function of the position along the z axis (beam axis). The individual reference-sensor resolutions determine the error of the fit parameters of the track and thus the error of the track itself. Propagating these parameter errors along the z axis yields the telescope resolution $\sigma(z)$ according to

$$\sigma(z) = \sqrt{\sigma_a^2 z^2 + \sigma_b^2 + 2 \sigma_{ab}} \quad (7.2)$$

with a and b the slope and intercept of the fit, σ_a and σ_b their respective errors and σ_{ab} the covariance. Doing this for both measured coordinates yields the telescope resolution σ_x and σ_y in x - and y direction, which can be combined to the telescope resolution in the direction orthogonal to the MSSD strips by applying the transformation

$$\sigma_{x'} = \sqrt{\sigma_x^2 \cos^2(\theta) + \sigma_y^2 \sin^2(\theta)} \mid \theta \approx 45^\circ \quad (7.3)$$

with $\sigma_{x'}$ the resolution in the measurement direction of the MSSD. Figure 7.6 shows the computed resolution as a function of z for four example runs that correspond to the four different beam tests. Table 7.1 summarizes the resolution $\sigma_{x'}$ at the DUT positions (along z) for the four runs.

Table 7.1: Telescope resolution at the DUT positions for the four beam tests.

		March 2011 3,623	September 2011 4,164	May 2012 5,208	October 2012 5,695	
Box	DUT	z Position [mm]	$\sigma_{x'}$ [μm]	$\sigma_{x'}$ [μm]	$\sigma_{x'}$ [μm]	$\sigma_{x'}$ [μm]
new	0	140		7.33	7.05	6.78
	1	60		6.47	6.24	6.04
	2	-20		6.24	6.06	5.92
	3	-100		6.71	6.56	6.45
old	0	20	6.12			

7.2.2 MSSD Analysis

The **TBAnalysis** software has been developed for the detailed analysis of the MSSD detectors and is based on C++ and ROOT libraries [64]. It takes the calibrated raw data of the MSSD and the track parameters of the reconstructed telescope tracks as input and performs the analysis described below in a two-step approach.

1. low-level data processing
2. filling plots and histograms and extracting the relevant parameters

Figure 7.7 shows a flowchart of the software with its input and different analysis paths that will be explained in more detail on the following pages.

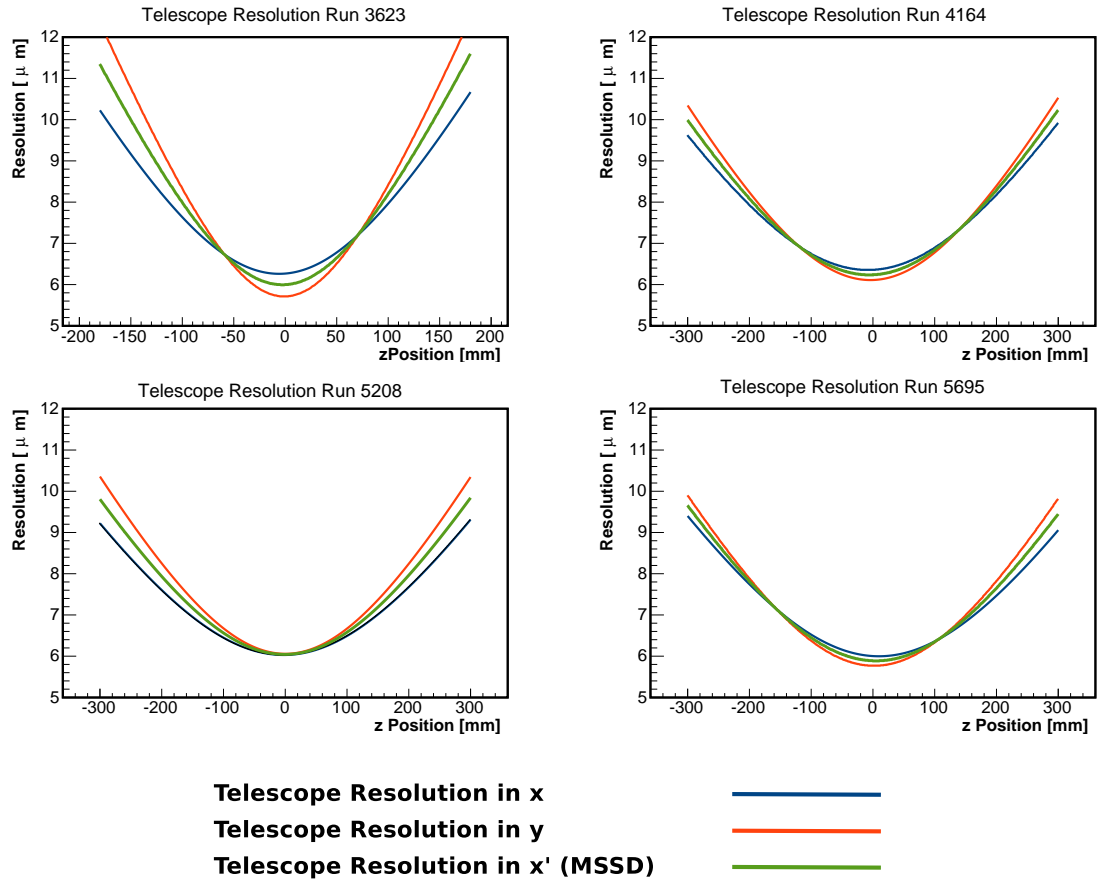


Figure 7.6: Computed SiBT resolutions for four runs corresponding to different beam tests (clockwise: March 2011, September 2011, October 2012, May 2012).

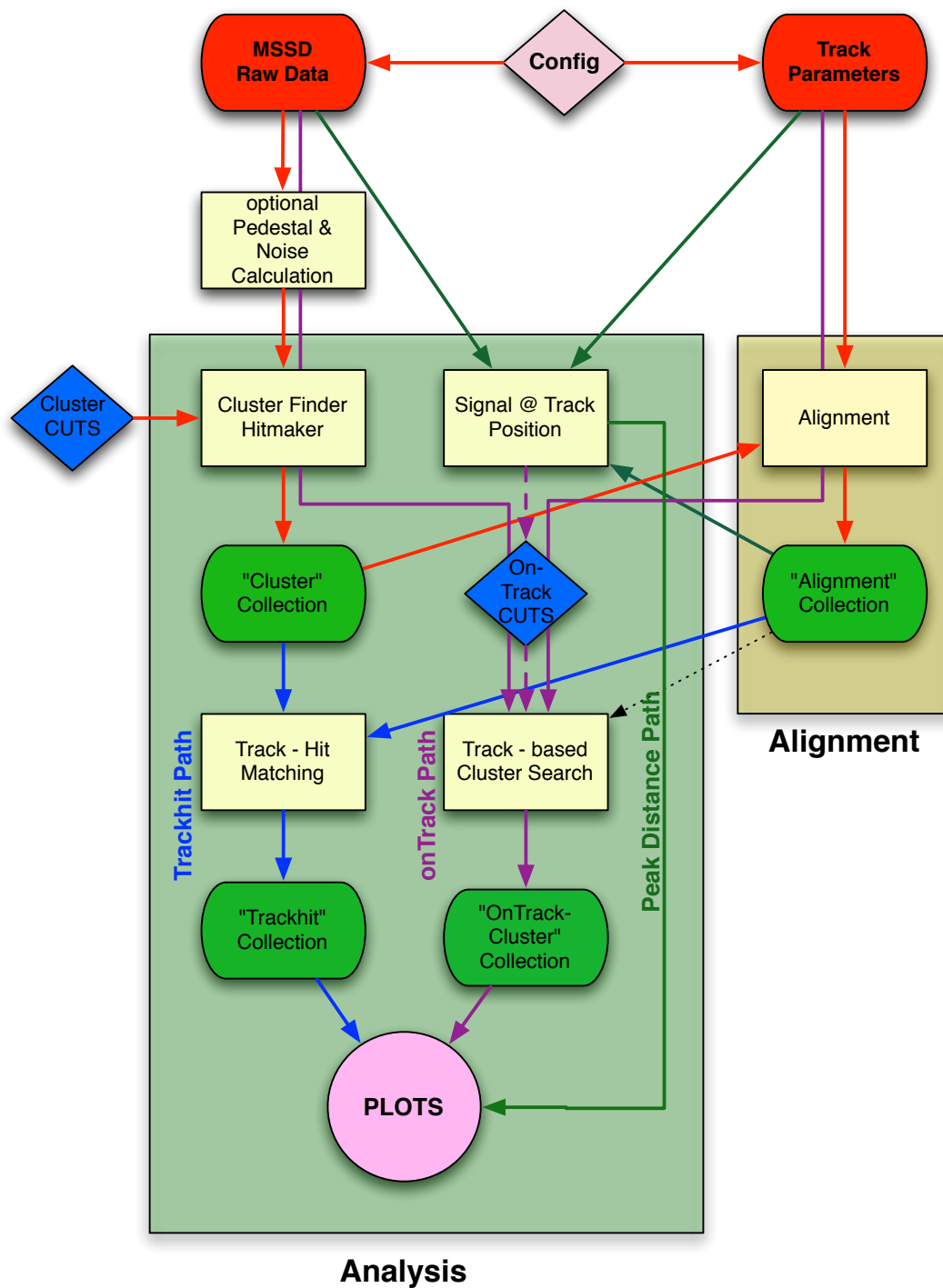


Figure 7.7: Flowchart of the TBAAnalysis software for MSSD data analysis. The different paths/procedures are highlighted in different colors.

Low-Level Data Processing and Algorithms

The first step is the low-level processing of the raw data, which is indicated by the red arrows in figure 7.7. It includes clustering and alignment of the MSSD with respect to the telescope and is done by a separate executable. Since it is necessary for the alignment to match tracks recorded with the beam telescope to hits on the MSSD, the clustering step has to be taken first. The whole procedure is done as follows:

A class called **ConfigReader** reads a configuration file that contains information about the high-voltage settings, the fluence, particle type, annealing, cooling-box slot number and all run numbers that are to be used for the analysis. This is necessary, as the area of the MSSD is much larger than the area of the reference planes of the Silicon Beam Telescope and therefore several mounting positions inside the telescope are necessary to cover the whole sensor area. In addition the MSSD is rotated at an angle of 45° with respect to the reference planes due to geometrical restrictions, which is illustrated in figure 7.2. With the information from the configuration file the telescope tracks and DUT data are loaded to objects called **Data** and **Track**.

In a first step the pedestal- and noise calculation is performed on the **Data** object, rejecting particle hits by only taking events and strips into account where the signal is smaller than 2.5 times the noise. Either the *mean* or the *median* of the signal distribution of the strips considered for the common-mode calculation (chapter 3, section 3.2) in each event can be used to calculate the correction, with the latter yielding lower noise. Finally the pedestal- and noise collections are written to a separate file.

Figure 7.8 shows a comparison of the noise distribution without the common-mode correction, the distribution with the EUTelescope algorithm and the final result using the **TBAnalysis** algorithm with the *median* and two iterations.

A **Cluster** class then takes the MSSD data in the **Data** object and starts performing a cluster search on the common-mode corrected, pedestal-subtracted raw data of each event. The criteria that define a cluster are as follows:

$$S_{seed\ strip} > 3\sigma \quad , \quad S_{neighbor\ strip} > 2\sigma \quad (7.4)$$

with S the CM-corrected, pedestal-subtracted signal of a strip and σ the corresponding noise of the strip. The algorithm first looks for a strip exceeding the seed-strip threshold and then adds neighboring strips to the cluster as long as their signals are above the neighbor-strip threshold. The following properties of the cluster are calculated, taking the geometry into account, and afterwards the information is written to a separate file.

- first strip
- cluster charge
- cluster noise
- cluster signal-to-noise ratio
- cluster width
- center-of-gravity (in mm and strip units)
- signal of all strips contributing to the cluster

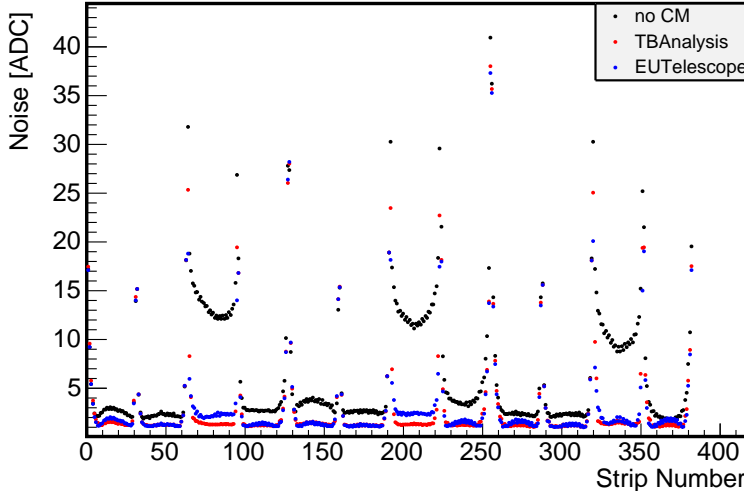


Figure 7.8: Comparison of the noise profile without using CM correction, the EUTelescope algorithm and the **TBAAnalysis** algorithm.

The next step in the data processing is the alignment of the DUT with respect to the beam telescope. To do so, an **Alignment** class reads the slot number from the **ConfigReader** and extrapolates the track from the **Track** object to the z position of the slot. Then the track's x - and y coordinates are rotated to the MSSD-coordinate system (rotated by 45°) according to the coordinate transformation

$$x' = x \cos(\theta) + y \sin(\theta) \quad (7.5)$$

$$y' = -x \sin(\theta) + y \cos(\theta) \quad (7.6)$$

with θ the rotation angle that is close to 45° . For the angular alignment, an angle range around 45° is scanned and the RMS of the residual distribution plotted versus the tested angles. The minimum of the resulting curve can be fitted with a parabola, allowing for the extraction of the true alignment angle.

The next step is the alignment in x direction perpendicular to the strips. The track coordinates are rotated by the angle determined in the previous step and then the mean value of the residual distribution is the alignment correction in x direction. Figure 7.9 shows the width of the residual distribution as a function of the rotation angle and the residual distribution for the ideal angle, the mean of which corresponds to the alignment shift in x direction for a specific run.

An alignment in y direction is only possible with an error corresponding to the strip length of the MSSD since the DUT only offers position information in the direction perpendicular to the strips. However, it is possible to extract cuts in y direction to make sure that only tracks that have actually hit the active area of the DUT are used for the

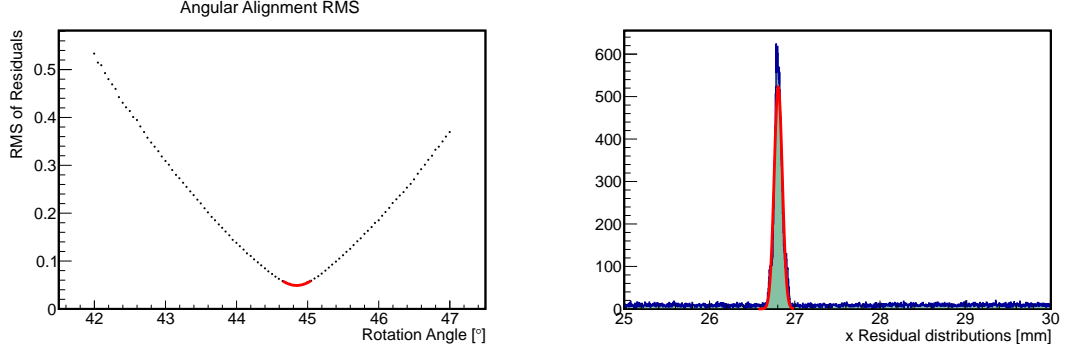


Figure 7.9: Width of residual distributions for the angular alignment and residual distribution for the ideal angle, which contains the alignment constant in x direction for run 5,208.

analysis. To do so, the value 1 is assigned to a track if a matching cluster is found or the value is 0 if there is none. Then these values are filled into a profile histogram with the y coordinate of the track determining the bin. The size of the beamspot is determined by the bins which are not empty. Algorithmically searching for the first and last bin to exceed a threshold of 95% the mean value in y direction of that distribution then yields the minimum and maximum y coordinates of tracks that are to be accepted for the further analysis (figure 7.10).

Finally the alignment corrections are saved to another file that can be associated to a specific detector and run. After successful alignment of the MSSD with respect to the telescope three methods are available for the further analysis.

Peak-Distance Method

With this method, the expected impact point of the track on the MSSD is calculated and the x coordinate is translated back to a strip number. With this information, the charge of five adjacent strips around the impact point is histogrammed. In addition, a second charge distribution is built with five strips that are within the same region of the sensor but 15 strips away from it. This ensures that no particle-induced signal is picked up as only events with one track are used. Figure 7.11 shows an example of such distributions.

The distribution at the position of the track is the *track-induced signal* and the one away from it is the *noise*. This is fitted with a Gaussian distribution, while the signal is fitted with a convolution of a Landau- and a Gaussian distribution to account for electronic noise and intrinsic fluctuations in the detector signal (right side of figure 7.11). The distance between the mean value of the Gaussian distribution and the most probable value of the Landau distribution is – per definition – the signal of the detector and as such used for the further analysis.

On-Track Method

The second method uses a threshold of 0.4 times the signal obtained in the previ-

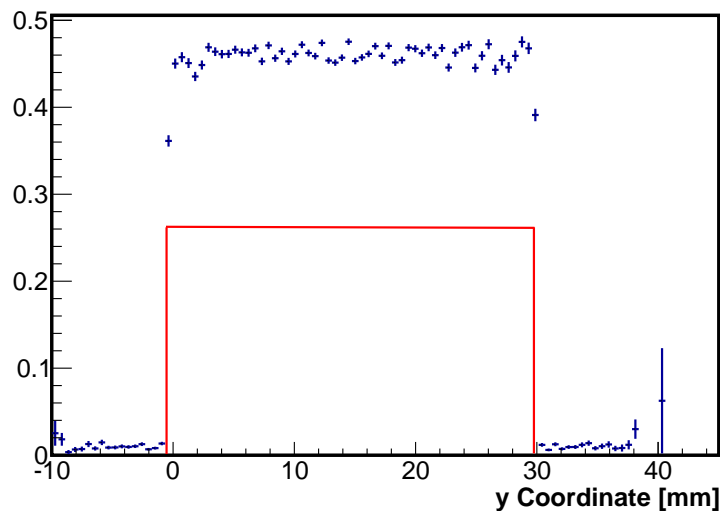


Figure 7.10: Profile histogram showing the efficiency along the y coordinate of the MSSD. Only tracks between the minimum- and maximum y value, indicated by the red lines (and thus measured on the MSSD), are used for the further analysis.

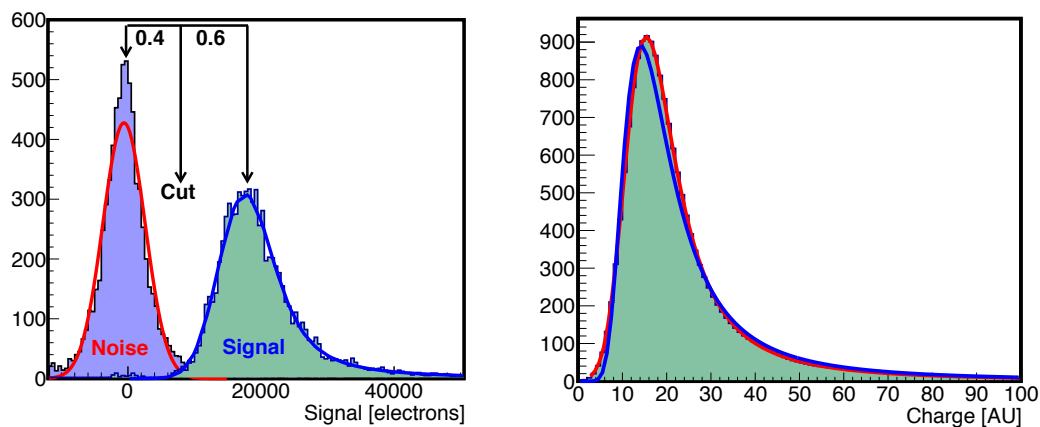


Figure 7.11: The signal distribution at the track position and noise distribution away from the track are shown on the left side. The right plot shows the difference between a pure Landau distribution (blue) and a convoluted Landau- and Gaussian distribution (red) when fitting a real detector signal.

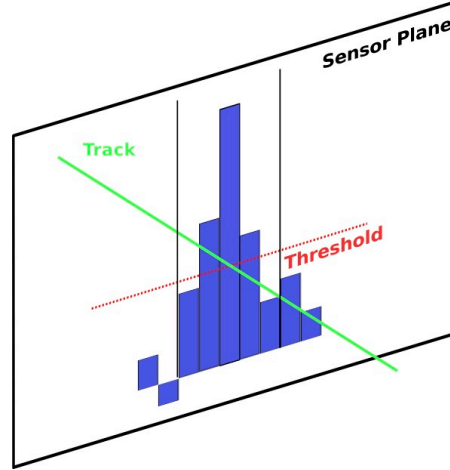


Figure 7.12: Illustration of the principle of track-induced clustering. The threshold is derived as 0.4 times the signal defined in the **Peak-Distance** method and the clustering window is five strips wide.

ous step for track-induced clustering. Again a five-strip-wide window around the calculated impact position of the track is used to build a cluster from all adjacent strips with a signal exceeding the calculated threshold. These `onTrackClusters` are needed to match tracks to the hits measured on the DUT. Figure 7.12 illustrates the clustering process within the five-strip window.

Trackhit Method The last method is called *trackhit* method. The clusters that have been found for the alignment are matched to the telescope tracks from the same event, with the restriction that the distance between the track impact point and the hit measured on the detector must not exceed three strip pitches of the particular region. The properties of the resulting track-hit pair are written to a `Trackhit` object that is derived from the same base class as the `onTrackCluster`.

After the `process` executable has finished the low-level processing and all the above collections have been created, they can be used to extract the relevant parameters for this analysis. Before these parameters will be described in more detail the calibration of the detector signal will be explained.

Calibration

There are several methods of calibrating the detector signal that is recorded by the front-end drivers in units of analog-digital-converter counts (or ADC counts) back to electrons, which is the more natural charge unit for this application. For this analysis a method of calibration using the signal of the well-known reference detectors in the SiBT was implemented. With an active thickness of $300\ \mu\text{m}$ and 78 electron-hole pairs that are created by a traversing MIP per micron of silicon, the reference planes have a signal of $\sim 23,400$ electrons each. Since there are eight of these detectors in the telescope at all

times and they are all identical, the average value of their signal can be used to obtain the DUT signal in electrons according to the formula

$$S_{DUT,electrons} = S_{DUT,ADC} \frac{23,400}{\overline{S_{ref\ planes,ADC}}} \quad (7.7)$$

with S the signal and $\overline{S_{ref\ planes,ADC}}$ the mean signal of all eight reference planes in the telescope, which is retrieved from a lookup file.

7.2.3 Parameters

In this section the parameters that are extracted from the recorded data will be presented. These are:

- noise
- signal
- resolution
- efficiency

All of the following plots have been created by another `plot` executable that is called after the processing of the raw data. It reads the same config file as the first analysis step and loads the collection specified in the `collection` variable from the MSSD-data file. The possible values are:

- 0** onTrackCluster
- 1** Trackhit
- 2** PeakDistance

The **PeakDistance** method is always used to calculate the signal of a specific region as it avoids any bias introduced by clustering. Even if the actual cluster is smaller than five strips the signal is the same as the mean pedestal-subtracted signal of a strip that is not hit is "zero" per definition. One of the two cluster collections is needed to compute the resolution of the detector, as the reference tracks need to be compared to the actual measurement on the MSSD which requires clustering.

Unless otherwise stated, all plots show data for an unirradiated 320 micrometer-thick p-on-n float-zone detector with a bias voltage of 300 V applied, tested in the March 2011 beam test at Fermilab. For most plots the data for the individual regions is arranged in a matrix style, where the columns correspond to the different pitches and the rows correspond to the width-over-pitch ratios (table 7.2).

Noise Profile Fig. 7.13

This plot shows the noise value for each strip of the MSSD for each individual run considered in the analysis. This allows for the identification of noisy strips, which are found at the borders of the regions. If the noise behavior changes over different runs (the pedestal- and noise values are calculated from the data run) it is a hint at changing conditions during data taking. The average noise value of

Table 7.2: Order of Regions in the Plots.

	Pitch 120 μm	Pitch 240 μm	Pitch 80 μm	Pitch 70 μm
w/p = 0.15	1	2	3	4
w/p = 0.25	5	6	7	8
w/p = 0.35	9	10	11	12

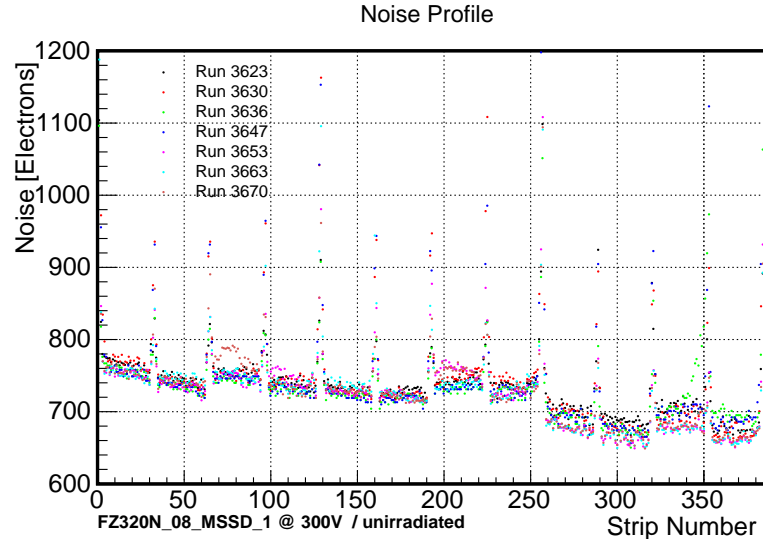


Figure 7.13: Noise versus strip number for the different runs.

the 28 central strips of each region is used at a later stage to plot the noise as a function of the bias voltage.

Signal Fig. 7.14

This plot is used for the calculation of the `onTrackCluster` threshold and the signal of the DUT, which is the distance between the mean of the noise distribution and the most probable value of the charge distribution.

Residual Distribution Fig. 7.15 and Resolution Fig. 7.16

The calculation of the spatial resolution requires two steps. First, the residual distribution is fitted with a Gaussian distribution of which the σ (RMS) is extracted. This is used to restrict the range for a second histogram, which is then again filled with the residuals, to five σ . The RMS of this new histogram is equivalent to the resolution of the detector in the specific region. These values are then plotted as a function of the region's pitch (figure 7.16).

The second histogram is necessary, as extracting the width of the original residual

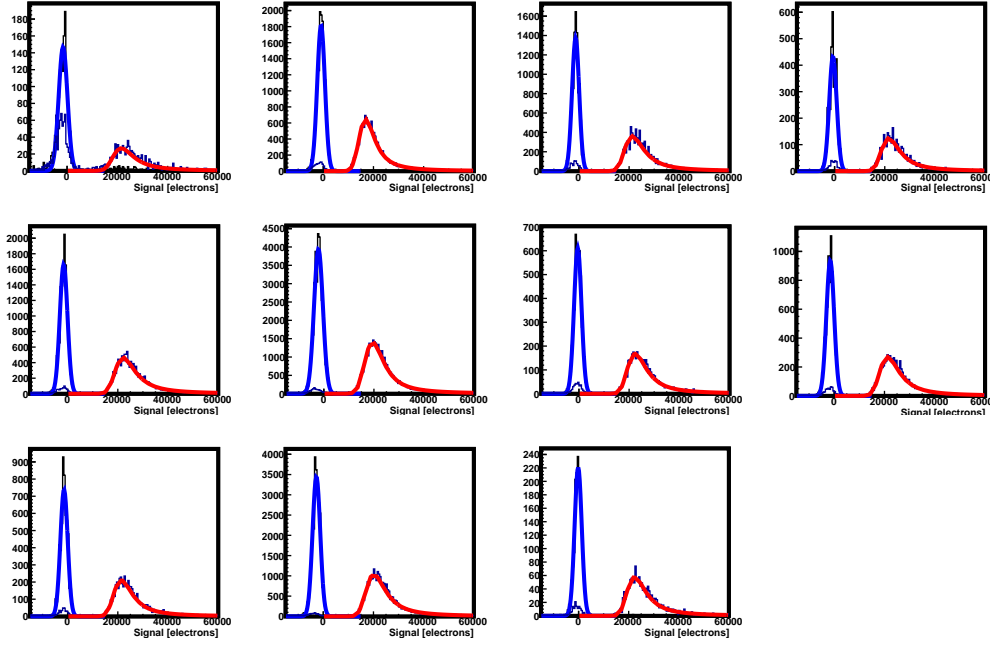


Figure 7.14: Track-induced signal and noise away from the track for eleven regions of the MSSD. Region twelve was not illuminated by the beam and is therefore not shown.

distribution yields a much higher RMS because of the background, which is considered when the RMS is calculated. Thus, this overestimates the real resolution.

However, this measured resolution is not the intrinsic detector resolution, as it has a contribution from the resolution of the beam telescope, which is a function of the z position along the beam axis as described in section 7.2.1. For the new cooling box geometry, a resolution of $\sim 6.5 \mu\text{m}$ has been computed (section 7.2.1, table 7.1).

An additional estimation of the telescope resolution can be made by taking into account that the measured resolution as a function of the strip pitch reads

$$\sigma_{\text{measured}}^2(p) = \sigma_{\text{DUT}}^2(p) + \sigma_{\text{Telescope}}^2 \quad (7.8)$$

with the DUT resolution assumed to be proportional to the pitch according to equation 4.13.

$$\sigma_{\text{DUT}}^2(p) = \kappa p \text{ with } \kappa = \frac{1}{\sqrt{12}} \quad (7.9)$$

Using this relation, the measured values for each region of a given width-over-pitch ratio can be fitted with

$$\sigma(p) = \sqrt{\kappa^2 p^2 + \sigma_{\text{Telescope}}^2} \quad (7.10)$$

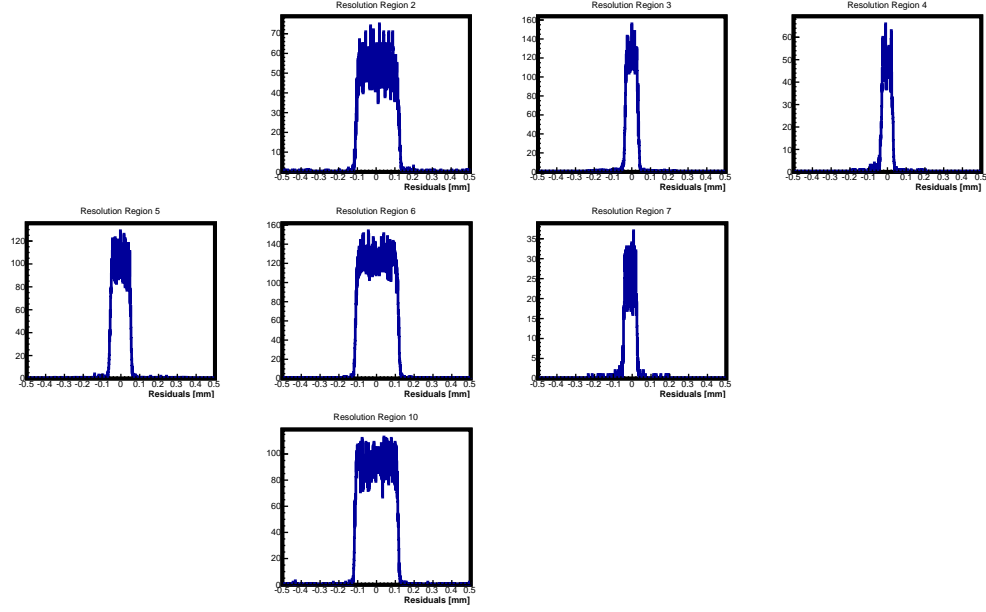


Figure 7.15: Residual distributions for regions two to eight and ten. The plot shows data for an unirradiated 320 micrometer-thick p-on-n float-zone detector.

which allows for the estimation of the telescope resolution as the intercept of the fit function. The open triangles in figure 7.16 represent the resolution corrected for the telescope resolution according to the formula 7.8, while the dashed blue line shows the calculated telescope resolution from table 7.1. The fit with σp from equation 7.10 is shown in red.

Efficiency and Noise Occupancy

To obtain the efficiency of the DUT a method similar to the one used for the signal is applied. The raw data is scanned for a strip exceeding the threshold computed for the `onTrackCluster` method in a window around the calculated impact point of the track on the DUT, provided that the track has passed through the active area of the specific region. The width of that search window in strip units is derived from the measured resolution of a specific region as

$$w = \frac{3 \sigma \sqrt{12}}{p} \quad (7.11)$$

with w the width of the search window, σ the resolution and p the pitch. The number of strips in the search window has to be odd because the strip closest to the track is always considered. For that reason the number of neighboring strips to be included in the search is given by

$$n_{\text{neighbors}} = \text{ceil}\left(\frac{\sigma \sqrt{12}}{p}\right) \text{ and } n_{\text{window}} = 1 + 2 n_{\text{neighbors}} \quad (7.12)$$

At the same time the probability of measuring one fake hit is computed by counting

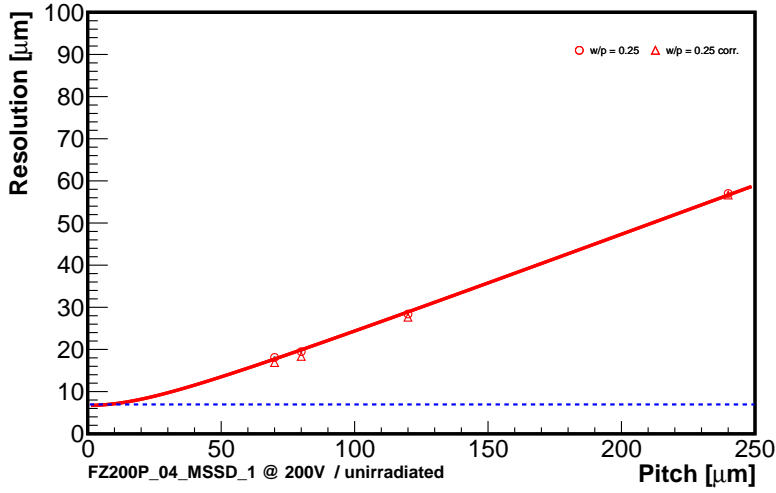


Figure 7.16: Measured resolution of a DUT in run 5,208 for regions with $w/p = 0.25$. The estimation of the telescope resolution yields $6.715 \mu m$ for this run, while the calculated value at this z position is $6.56 \mu m$ (blue line, see section 7.2.1).

the number of strips above the threshold that are not within the search window, divided by the number of strips not contributing to the search window. This is equivalent to the noise occupancy ω .

$$\omega = p_{n_{fake}=1} = \frac{n_{above\ threshold}}{32 - n_{window}} \quad (7.13)$$

The probability of not measuring a fake hit is therefore given by $1 - p_{n_{fake}=1}$ and the probability of at least one fake hit in a search window of size w reads

$$p_{n_{fake} \geq 1} = 1 - (1 - p_{n_{fake}=1})^w \quad (7.14)$$

which can be used to compute the efficiency ϵ . The latter depends on the fraction of measured tracks in the search window n_A and the probability of measuring at least one fake hit $p_{n_{fake} \geq 1}$.

$$n_A = 1 - (1 - \epsilon)(1 - p_{n_{fake} \geq 1}) \quad (7.15)$$

where the number of measured tracks n_A is given by one minus the combined probability of not measuring a track ($1 - \epsilon$) and not measuring a fake track ($1 - p_{n_{fake} \geq 1}$). Simplification and solving for ϵ yields

$$\epsilon = \frac{n_A - p_{n_{fake} \geq 1}}{1 - p_{n_{fake} \geq 1}} \quad (7.16)$$

which is one if n_A is one (if all tracks are detected, there is no method of telling which fraction originates from noise).

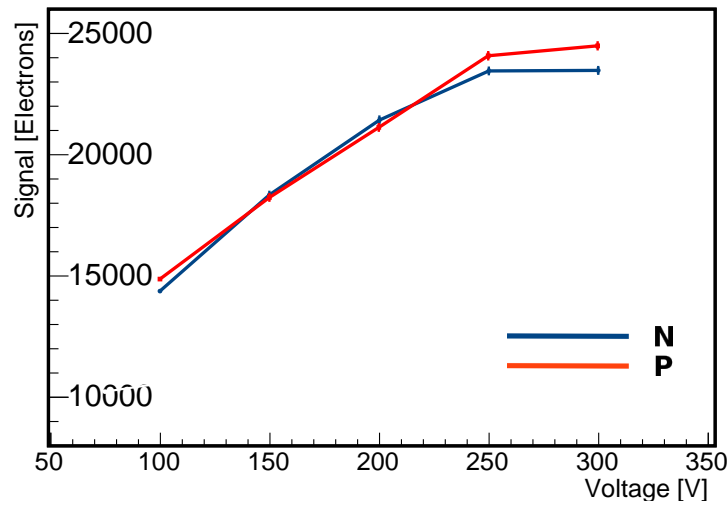


Figure 7.17: Signal in electrons as a function of the bias voltage for FZ320 N and P measured in the March 2011 beam test at Fermilab.

All the parameters above can be plotted as a function of voltage or fluence to visualize the impact of the bias voltage or radiation damage on them.

To do so, all relevant parameters of the analysis are written to a ROOT file that can then be read by another executable `compare`, which creates graphs for individual detector objects and fluences. A `Detector` object has the following properties

- detector name, which includes all information about material, thickness and doping
- region
- fluence
- particle type
- annealing

which ensures that measurements of the same detector/region in the same irradiation- and annealing state will be summarized in a single graph. Figure 7.17 shows, as an example of such a plot, the signal of 320 micrometer-thick float-zone silicon as a function of the bias voltage.

7.3 Results

In this section the results of the analysis presented above will be summarized. Table 7.3 gives a survey of the detector materials and the fluence- and annealing states in which they were tested.

The complete set of detector names in the different beam tests is summarized in table 7.4. A set of three reference DUTs that were always the same was used in two of the

Table 7.3: Survey of tested materials in the different beam tests and their respective fluence- and annealing status. The numbers denote the fluence in multiples of 10^{14} 1MeV n_{eq} cm^{-2} .

Test beam	March 2011	September 2011		May 2012	October 2012
Irradiation	0	3.5 protons	4 neutrons	15 mixed	15 mixed
		$\times 10^{14}$ 1MeV N_{eq} cm^{-2}			
320 μm FZ	N P Y		N P	N P Y	N* P** Y**
200 μm FZ	N P Y	P Y	P Y	N P Y	N* Y**
200 μm MCZ	N	P	P	N P Y	N* P** Y**
200 μm FTH	N P Y				

N: p-on-n, P: n-on-p p-stop, Y: n-on-p p-spray
mixed: 10 protons and 5 neutrons
annealing: * 166 minutes at 60°C, **80 minutes at 60°C

three CERN beam tests for reference purposes. One of these detectors was also tested in the March 2011 beam test.

7.3.1 Data-Taking Conditions

Data recorded in four beam tests with the MSSD will be presented in this section. Due to the fact that the beams at Fermilab's MTEST facility and at CERN's H2 beam line are different in their structure, energy and the particle type used, different conditions apply to the four tests. In the beam tests at CERN, where SiBT was always the secondary user in the beam line — meaning that it was not possible to influence the beam parameters — along with the calorimetry group of CMS, this holds especially true. The particle types and energies ranged from 15 to 150 GeV electrons and 50 to 300 GeV pions to 150 GeV muons. Since the beam parameters were changed continuously it was not possible to take these changes into account for the analysis.

Pick-Up Noise

The measured noise of a detector is the sum of the intrinsic sensor noise and the noise of the readout electronics. This latter part is small compared to the first, but due to a design flaw in the module constructed for the MSSD, it has become a major contribution. The readout hybrid, which is directly glued to the aluminum base plate, was insufficiently grounded and this introduced a large contribution of electronic pick-up noise.

The two beam tests in September 2011 and May 2012 were particularly affected by this problem, which was solved by adding an additional grounding connection. Figure 7.18 shows the improvement of the noise behavior after adding this additional grounding, using the example of an unirradiated 200 micrometer-thick n-on-p float-zone sensor.

As shown in figure 7.18 the noise of the strips before the introduction of the additional

Table 7.4: Detector names of tested MSSDs. The numbers and letters denote the fluence in multiples of 10^{14} $1\text{MeV } n_{eq} \text{ cm}^{-2}$ and the particle type.

Detector Name	March 2011	September 2011	May 2012	October 2012
FZ200N_02_MSSD_1	0			
FZ200P_04_MSSD_1	0	0	0	0
FZ200Y_02_MSSD_2	0			
FZ320N_08_MSSD_1	0			
FZ320P_01_MSSD_1	0			
FZ320Y_04_MSSD_2	0			
FZ200P_06_MSSD_1		4 n		
FZ200P_06_MSSD_2		3.5 p		
FZ200Y_02_MSSD_2		3.5 p		
FZ200Y_10_MSSD_2		4 n		
FZ320N_04_MSSD_1		0	0	0
FZ320N_08_MSSD_2		4 n		
FZ320P_04_MSSD_2		4 n		
MCZ200P_07_MSSD_2		3.5 p		
FZ200N_04_MSSD_2			15 m	15 m [*]
FZ200P_01_MSSD_2			15 m	
FZ200Y_06_MSSD_1			15 m	15 m ^{**}
FZ320N_05_MSSD_1			15 m	15 m [*]
FZ320P_02_MSSD_2			15 m	15 m ^{**}
FZ320Y_05_MSSD_1			15 m	15 m ^{**}
MCZ200N_02_MSSD_2			0	0
MCZ200N_04_MSSD_1			15 m	15 m [*]
MCZ200P_01_MSSD_2			15 m	15 m ^{**}
MCZ200Y_05_MSSD_1			15 m	15 m ^{**}
FTH200N_24_MSSD_2				0
FTH200P_08_MSSD_1				0
FTH200Y_03_MSSD_1				0
Fluence: $10^{14} \text{ 1MeV } n_{eq} \text{ cm}^{-2}$				
protons, neutrons and mixed irradiation (10 p + 5 n)				
annealing: * 166 minutes at 60°C, **80 minutes at 60°C				

grounding connection is of the same order but the fluctuations between the strips are enormous. Grounding the hybrid to the aluminum plate leads to a much more uniform noise profile, with only the border-of-region strips showing elevated noise, which is a known effect.

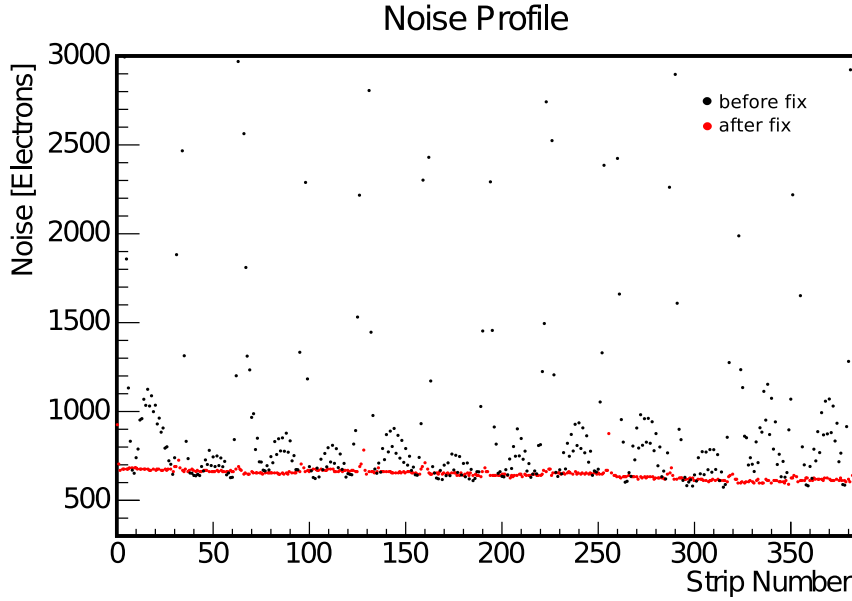


Figure 7.18: Noise profile before and after the implementation of the additional grounding on the module of a 200 micrometer-thick, unirradiated n-on-p float-zone sensor at 200 V that served as a reference in all four beam tests.

Data Selection

According to simulation studies [65], in which different tracker layouts were investigated with respect to their overall physics performance and parameters, the new CMS tracker will have a strip pitch around $90\ \mu\text{m}$ and a strip length of $\sim 5\ \text{cm}$ to meet the requirements of the tracker in the HL-LHC era in terms of granularity. This pitch is not available on the MSSD but similar pitches are — with the regions having a pitch of $80\ \mu\text{m}$. Furthermore, the results presented in chapter 6 yield that it is possible to extrapolate the electrical behavior to other pitches and width-over-pitch ratios.

7.3.2 Signal and Noise

The following section gives an overview of the results that have been obtained from the four beam tests with the MSSD. Not all regions of the sensors were covered in every beam test. Only the relevant regions with pitches of 80 micrometer will be presented in this chapter¹. Each group of regions with their different width-over-pitch ratios was connected to a different pair of readout chips and thus amplification chains with gain differences in the order of 10 %. For that reason, variations in the signal cannot be reliably identified as inherent properties of the geometry.

¹The full set of results can be found in the electronic appendix

Comparison of Doping Schemes and Thicknesses

Figure 7.19 shows the signal of all unirradiated detectors and illustrates the scaling of the signal with the detector thickness. The open triangles represent thick, 320 micrometer-thick float-zone silicon, the filled, upwards-facing triangles represent the deep-diffused, 200 micrometer-thick float-zone material, the downwards-facing triangles represent FTH material and the circles indicate sensors made from magnetic-Czochralski substrate. The color scheme is adapted to the different materials but the different shades of blue represent n-bulk, the shades of red represent p-stop and the green colors represent p-spray silicon.

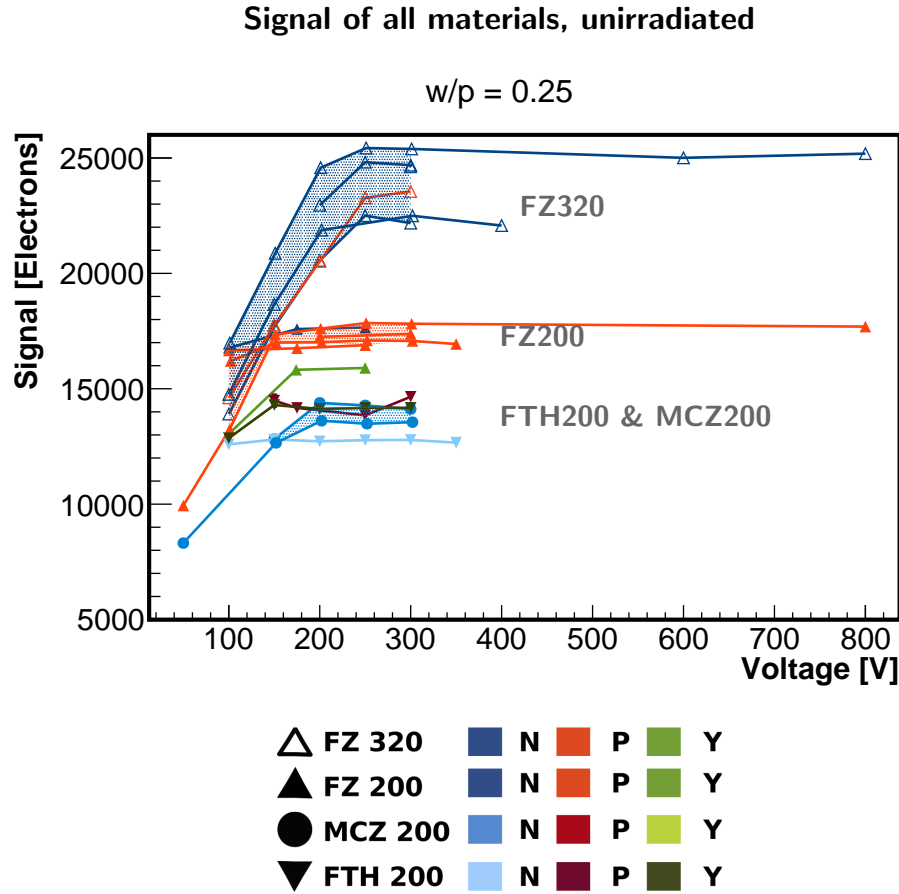


Figure 7.19: Comparison of the signals of all unirradiated materials. Different shades of the same color represent the same doping scheme but different materials. For detectors for which more than one measurement is available, the shaded area indicates the range of the measurements.

The 300 micrometer-thick, n-bulk float-zone material has the highest signal of all materials before irradiation, with a spread of $\sim 10\%$ indicated by the shaded blue area. This spread originates from the fact that sensors from two different wafers were measured with different readout hybrids. The signal of the p-bulk sensor is around

23,000 electrons, which was to be expected, given a measured active thickness of 295 micrometer.

The deep-diffused, 200 micrometer-thick float-zone silicon is the material with the second-greatest active thickness and thus also the second largest signal before irradiation, with n-bulk and p-spray samples having higher signal than the p-spray material. Again, FZ200P was used as reference detector in all four beam tests and thus four curves are shown.

Physically-thinned material shows different behavior, as the N type shown in light blue has approximately 20 % lower signal than the detectors made from p-doped substrates, which have the same signal as the 200 micrometer-thick, n-bulk magnetic-Czochralski detector that was measured twice and is of the same active thickness.

Figure 7.20 shows the measured signal of all detectors that were irradiated to the intermediate fluence step of 3.5×10^{14} 1MeV n_{eq} cm^{-2} protons or 4×10^{14} 1MeV n_{eq} cm^{-2} neutrons. These are made from 300 micrometer-thick float-zone silicon, which served as reference, because this material has been investigated and used by CMS for the present tracker, and deep-diffused, 200 micrometer-thick float-zone material. Whereas for the thick sensors only data after neutron-irradiation is available, the samples for the deep-diffused silicon cover irradiations with both particle types.

After these fluences, the thick detectors have higher signal, but the maximum extracted signal at the tested bias voltages shows signs of saturation around 18,000 electrons, which is approximately 25 % lower than that of unirradiated samples. Furthermore, the signal of the n-bulk detector indicates a higher depletion voltage after irradiation. The p-stop detector does not show any signs of saturation, which can be attributed to the fact that p-bulk material does not type-invert and thus has higher depletion voltages after irradiation than n-bulk material.

The deep-diffused FZ200 material shows similar saturation values of the signal after the irradiations with the same particle type. The overall amplitude of the signal, however, is different, depending on the particle type used for irradiation. Proton-irradiated detectors reach a saturation value which is ~ 25 % lower than that of the unirradiated detectors but the depletion voltage of the p-spray sample is higher than for the p-stop sensors. Neutron-irradiated detectors on the other hand only have a maximal signal that corresponds to 55 % of the unirradiated reference but with lower depletion voltages than after pure proton irradiation.

The scaling with thickness is still evident after this intermediate fluence step, which corresponds to the fractions of protons and neutrons a sensor would receive at a radius of 40 cm from the beam axis in the future CMS tracker, but radiation-induced effects start to play an important role.

Figure 7.21 shows data for the same materials as above but after irradiation to the highest equivalent fluence of 1.5×10^{15} 1MeV n_{eq} cm^{-2} with protons (1×10^{15}) and neutrons (0.5×10^{15}). This is equivalent to the amount of irradiation a sensor would receive at a radius of 20 cm from the center after the full expected lifetime of the HL-LHC

Signal FZ (200 & 300 μm), 3.5×10^{14} protons or 4×10^{14} neutrons

$w/p = 0.15$

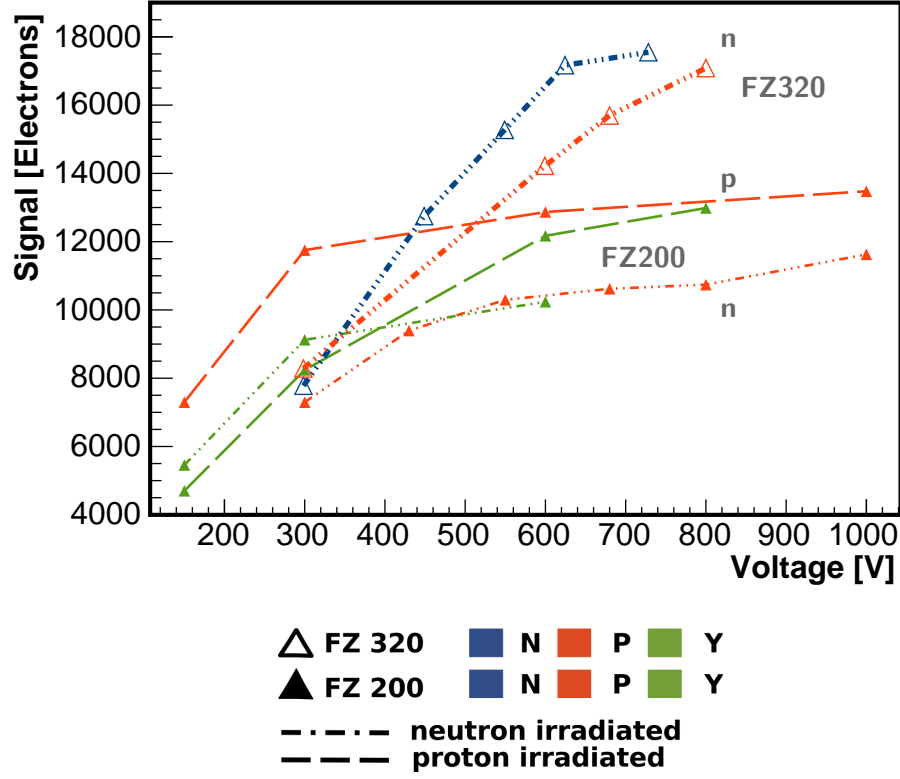


Figure 7.20: Comparison of signals of all materials after pure proton- or neutron irradiation to fluences of 3.5 and 4×10^{14} $1\text{MeV } n_{\text{eq}} \text{ cm}^{-2}$ respectively.

CMS tracker and thus is a "worst-case scenario".

At this fluence the signal does not saturate below 600 V and the linear scaling with the detector thickness is not given any more.

While the 300 micrometer-thick p-spray detector that performs best after this fluence reaches a signal of $9,000$ electrons at 550 V, the p-stop sensor of the same thickness hardly reaches more than $8,000$ electrons at this voltage and the 200 micrometer-thick sensor of the same technology reaches $\sim 7,200$ electrons. The thick n-bulk sensor has such a high shot noise, induced by leakage current, after this fluence that the signal itself cannot be distinguished from the noise any more and thus the sensor is not able to measure any tracks.

High leakage current is an issue when operating detectors irradiated to such high fluences because the power that needs to be dissipated from the sensor can lead to an effect called thermal runaway. This means that the increased current leads to a warming of the bulk materials, which in turn increases the leakage current. By dimensioning the

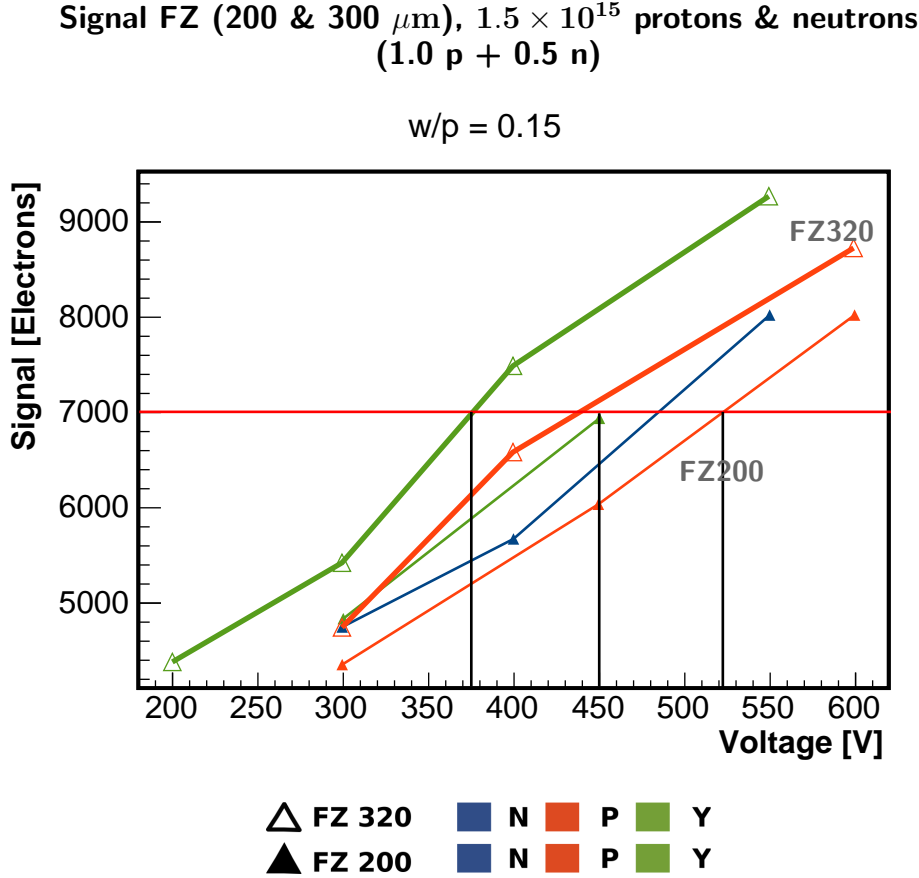


Figure 7.21: Comparison of signals of 200 and 300 micrometer-thick float-zone materials after mixed irradiation to 1.5×10^{15} 1MeV n_{eq} cm^{-2} (1p, 0.5n).

cooling system that is required to measure irradiated detectors appropriately, this effect can be suppressed. However, an element on the readout hybrid called PLL (Phase-Lock Loop) used in this setup, had shown signs of failure at temperatures below -20°C before and therefore cooling below that temperature was not possible. In addition, the built-in compliance of the used power supplies was not sufficient to bias irradiated detectors to voltages higher than $\sim 600\text{V}$ and as a result of the two problems, the signal plateau on structures irradiated to 1.5×10^{15} 1MeV n_{eq} cm^{-2} could not be reached.

The relatively low signal of the thick detectors as compared to the deep-diffused thin ones can be attributed to the trapping of charge carriers in radiation-induced trap levels and to underbiasing, as the bias voltage to deplete these thick sensors fully is definitely above the tested 600 V.

Thin detectors are favourable for application in the future tracker, because they have the advantage of less material in the path of a particle and lower leakage current, which means that less power has to be dissipated and a lighter cooling system can be built.

Under the assumption that the current increase on heavily irradiated sensors is linear

with voltage and volume within the tested range, an increase of the detector thickness from 200 to 320 micrometer yields 60 % higher current while, as shown in figure 7.21, the required voltage increase to reach a signal level of 7,000 electrons is 20 % if the best thick and thin materials are compared and 29 % if the 300 micrometer-thick p-spray sensor is compared to the 200 micrometer-thick p-stop sensor that performs worst (vertical lines in figure 7.21). Consequently, the increase of dissipated power for the same signal is much larger if the sensor thickness is increased as compared to the required increase of bias voltage on the thin sensors.

Comparison of 200 Micrometer-Thick Materials

Given the considerations from the previous section and the fact that 300 micrometer-thick, n-bulk float-zone material cannot be used any more after irradiation to 1.5×10^{15} 1MeV n_{eq} cm^{-2} (1×10^{15} protons and 0.5×10^{15} neutrons), sensors with an active thickness of 200 micrometer are more promising candidates. Two such materials have been tested after irradiation to this highest fluence:

- deep-diffused float-zone silicon
- magnetic-Czochralski silicon

in all three available doping schemes. Physically-thinned float-zone devices might have been a better choice for this comparison, as the deep-diffused material has approximately 20 micrometer more active thickness but the thinned material had not yet been irradiated at the time of the beam test.

Figure 7.22 shows the signal and noise of all materials mentioned above. Magnetic-Czochralski silicon has higher signal than the float-zone material over the entire range of tested voltages, with the n-bulk and p-spray detectors performing better than the p-stop sample. The behavior of the float-zone detectors is similar but the overall signal is about 10 to 20 % lower than that of the Czochralski silicon.

However, when looking at the noise in the bottom figure, it is evident that the irradiated n-bulk detectors have higher noise than the p-bulk materials.

The signals shown in these plots are track-induced and have been obtained by the method described in section 7.2.2. No noise-cuts have been applied for the selection of the strips and therefore the signal of the n-bulk material in figure 7.22 is different from what would have been measured if a clustering algorithm had been used, due to the elevated noise. Figure 7.23 illustrates this by showing the track-induced charge distribution and noise distribution for n-bulk and p-bulk magnetic-Czochralski material irradiated to the highest fluence of 1.5×10^{15} 1MeV n_{eq} cm^{-2} . In the case of the n-bulk material the long tail of the wider noise distribution protrudes far into the regime of the signal distribution and thus a considerable fraction of hits at the low end of the cluster charge distribution – depending on the threshold for clustering – is not identified correctly.

**Signal & Noise 200 μm -thick Materials, 1.5×10^{15} protons & neutrons
(1.0 p + 0.5 n)**

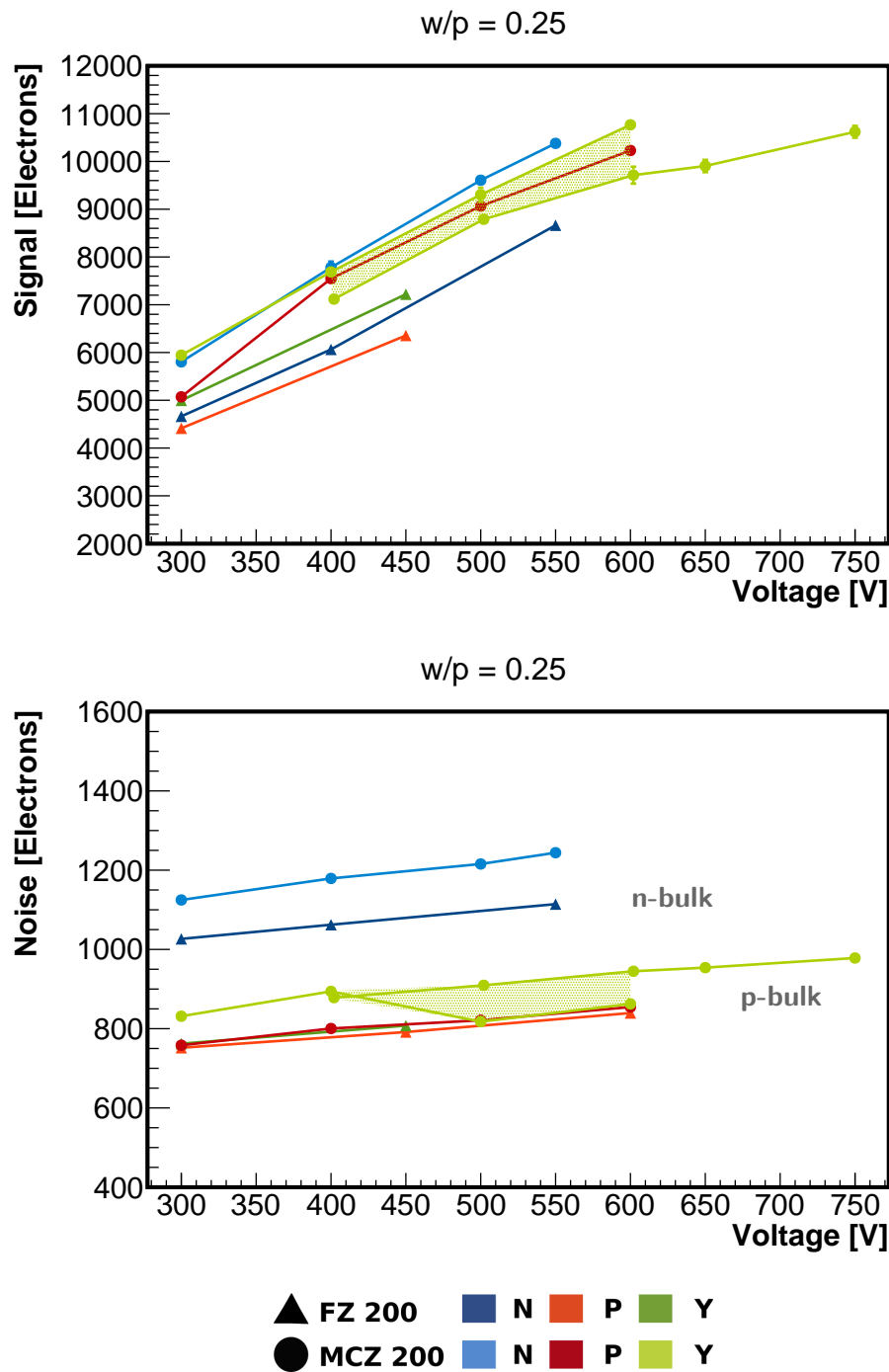


Figure 7.22: Comparison of the signal and noise of 200 micrometer-thick material after mixed irradiation to 1.5×10^{15} 1MeV $n_{\text{eq}} \text{ cm}^{-2}$ (1p, 0.5n).

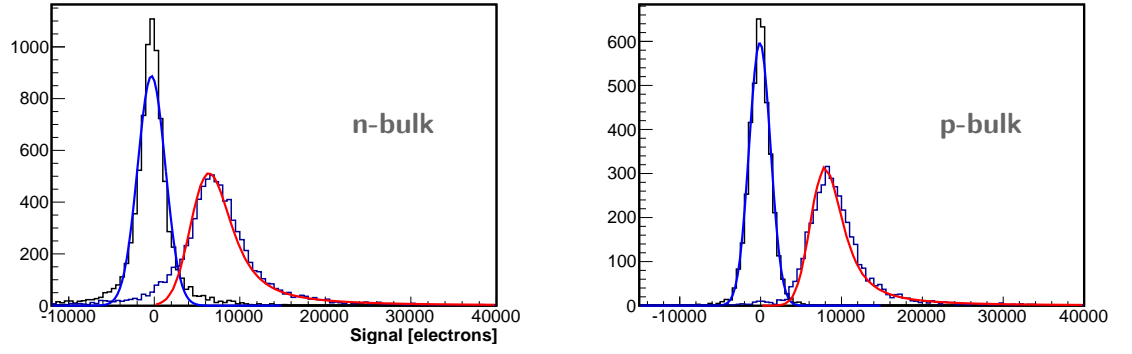


Figure 7.23: Comparison of the track-induced signal and the noise of n- and p-doped magnetic-Czochralski material.

Annealing

In addition to the many degrees of freedom introduced by having different thicknesses, materials and doping schemes, the annealing behavior of these combinations of properties also plays a role in the performance evaluation of possible materials for the future CMS tracker. Since the investigation of annealing behavior is not the main scope of this specific study, only little data with annealed samples is available. Furthermore, many of the irradiated detectors received considerable annealing time during shipping between the participating institutes and the assembly of the modules, which is not accounted for in the figures presented in table 7.4 as it was not tracked. To illustrate the effects on the signal, non-annealed and annealed samples of the materials with an active thickness of 200 micrometer are compared. All samples have received a fluence of 1.5×10^{15} 1MeV n_{eq} cm^{-2} and the annealing specified in table 7.4.

Figure 7.24 shows the signal and noise of three detectors made from 200 micrometer-thick, deep-diffused float-zone material in all three doping schemes before and after annealing. The n-bulk detector was annealed for 166 minutes at 60°C, which is in the reverse part of the annealing curve in figure 4.13. This results in reduced signal and increased noise. The p-spray sensor with an annealing of only 80 minutes at 60°C shows increased signal and high-voltage stability, which yields a reduction in leakage current. The p-stop detector was damaged and could therefore not be measured after annealing.

The magnetic-Czochralski sensors in figure 7.25 show similar behavior, with a clear increase of signal for the p-stop detector shown in red, whereas the signals of the n-bulk- and p-spray detectors are unaffected. The noise on the other hand is only increased for the p-spray detector. No reasonable explanation has been found for this phenomenon. Again, the n-bulk device was annealed for 166 minutes at 60°C, while the p-stop- and p-spray samples received only 80 minutes at 60°C.

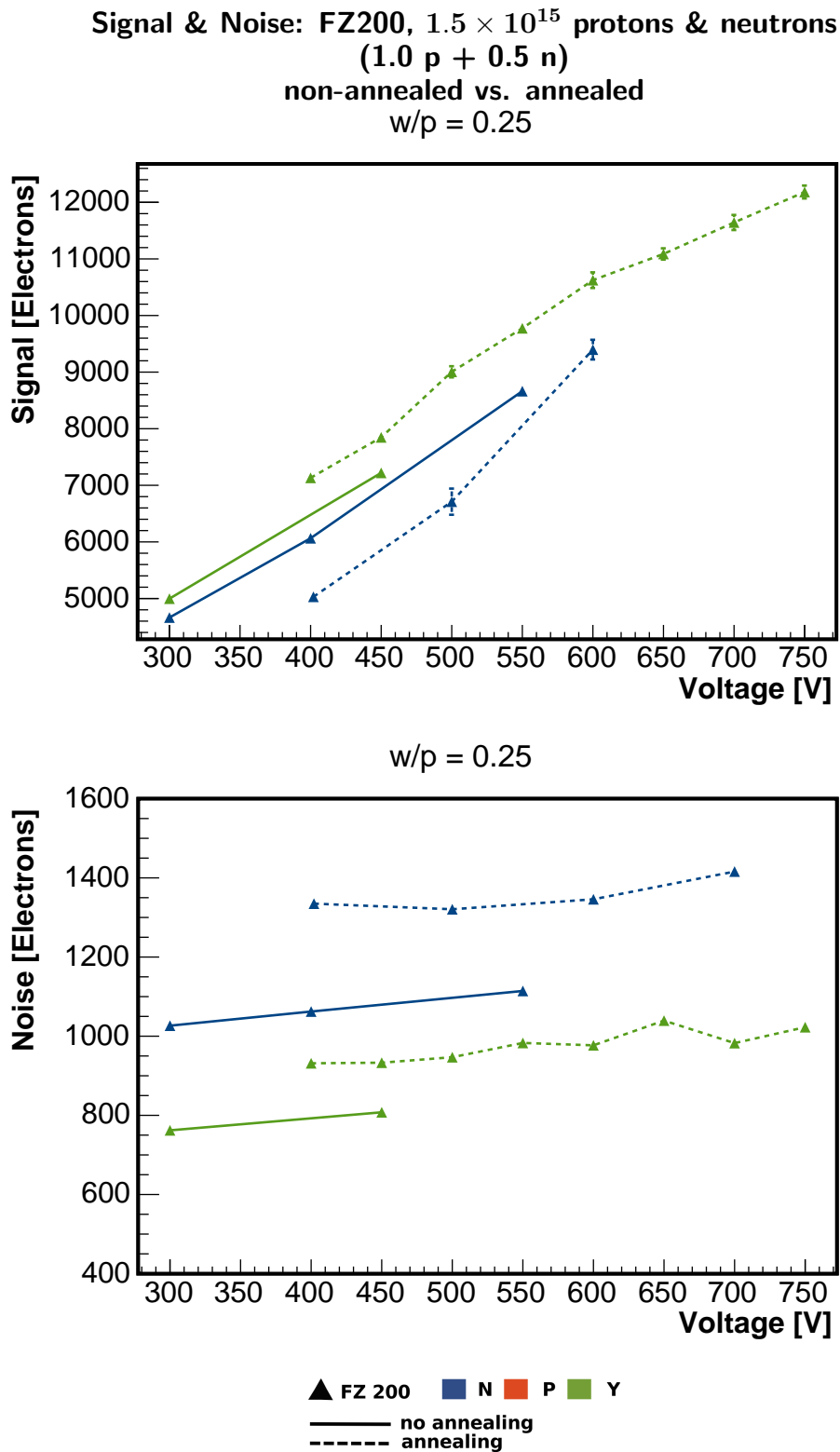
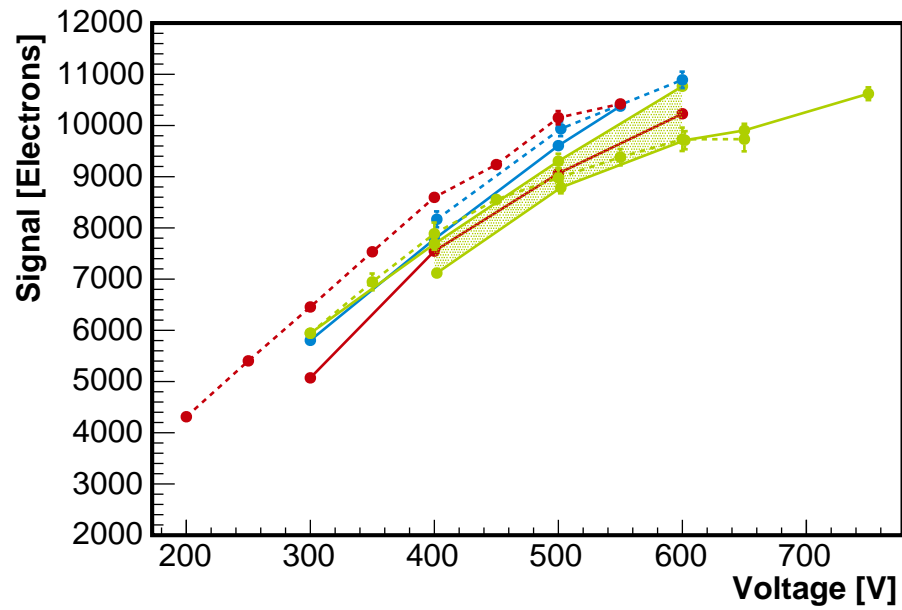


Figure 7.24: Signal and noise of deep-diffused, 200 micrometer-thick float-zone silicon irradiated to 1.5×10^{15} 1MeV n_{eq} cm⁻² (1p, 0.5n) before and after annealing.

**Signal & Noise: MCZ200, 1.5×10^{15} protons & neutrons
(1.0 p + 0.5 n)
non-annealed vs. annealed
w/p = 0.25**



w/p = 0.25

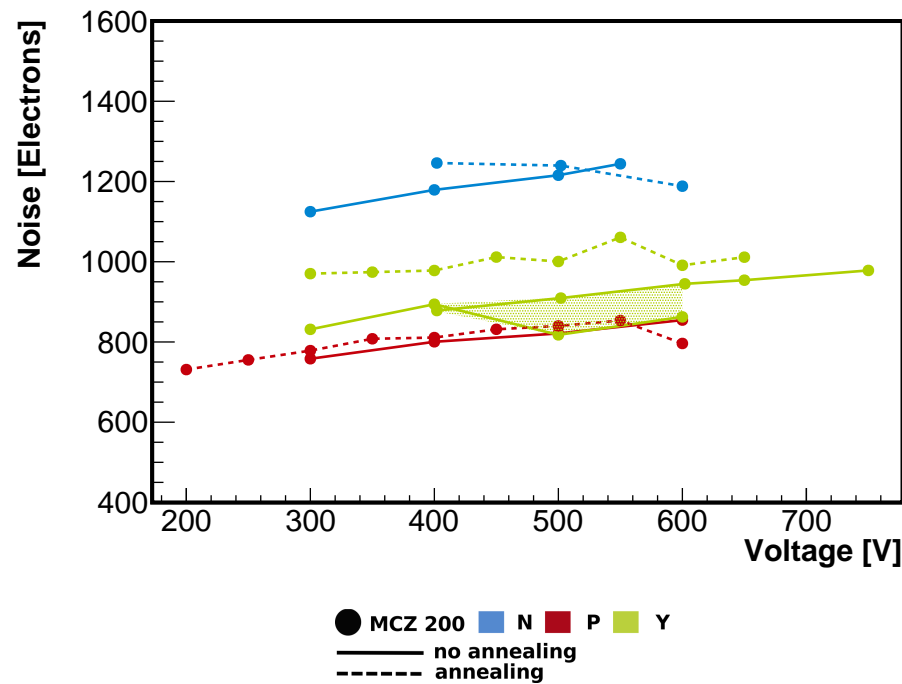


Figure 7.25: Noise of 200 micrometer-thick magnetic-Czochralski silicon irradiated to 1.5×10^{15} 1MeV n_{eq} cm^{-2} (1p, 0.5n) before and after annealing.

7.3.3 Resolution and Efficiency

Resolution

In the following section, all quoted resolutions are the intrinsic DUT resolution, which is derived from the width of the residual distribution according to equation 7.1 with the track-uncertainty values from table 7.1. Given the large pitch of the MSSD the correction is small with respect to the RMS of the residual distribution. The red line marks the expected binary resolution of a sensor with a readout pitch of 80 micrometer derived as $p/\sqrt{12}$ (equation 4.13).

The structure of the MSSD with the different regions of different pitch and size results in a very different number of tracks in the individual regions. Furthermore, many tracks are not used as they hit the non-active area between the regions. The resolution is obtained as the RMS of the residual distribution of the remaining tracks and can be affected by the number of events in the histogram. For that reason, a cut on the minimum number of tracks in a specific region of 1,500 was introduced. This ensures that regions with very low statistics are not counted, as this increases the influence of the background on the RMS of the residual distribution with respect to the peak.

Figure 7.26 shows a correlation plot for the regions with width-over-pitch ratios of 0.15 and 0.25 from the same detector. The correlation is linear with a slope of one, which means that the resolution is independent of w/p . Data for one region per material will therefore be shown in this section, illustrating the dependence on fluence and bias voltage.

Furthermore, figure 7.26 reveals that the resolution depends on the material, as the datapoints that indicate lower resolution below the binary limit of $p/\sqrt{12} \approx 23\mu m$ all represent p-stop or p-spray material, while the other materials that cluster around this value are mostly n-bulk devices.

Figure 7.27 shows the spatial resolution of the region with a width-over-pitch ratio of 0.15 and a pitch of 80 micrometer on 320 micrometer-thick float-zone devices before irradiation, after a fluence of 4×10^{14} 1MeV n_{eq} cm^{-2} neutrons and after irradiation with 1.5×10^{15} 1MeV n_{eq} cm^{-2} protons (1×10^{15}) and neutrons (0.5×10^{15}).

Before irradiation, the resolutions of p- and n-bulk materials are very similar and below the binary limit. After irradiation, the charge sharing between the strips of p-bulk detectors increases, which leads to wider clusters that have a beneficial impact on the resolution. The resolution of n-bulk detectors is unaffected by this phenomenon, as their interstrip isolation is not changed by bulk damage.

Figure 7.28 shows the resolution for 200 micrometer-thick, deep-diffused float-zone devices before and after irradiation. Many unirradiated devices did not fulfill the requirement of at least 1,500 tracks in the region and thus no data is shown. After irradiation to the highest fluence of 1.5×10^{15} 1MeV n_{eq} cm^{-2} (1×10^{15} protons and 0.5×10^{15} neutrons), a significant difference in the performance of n- and p-bulk materials

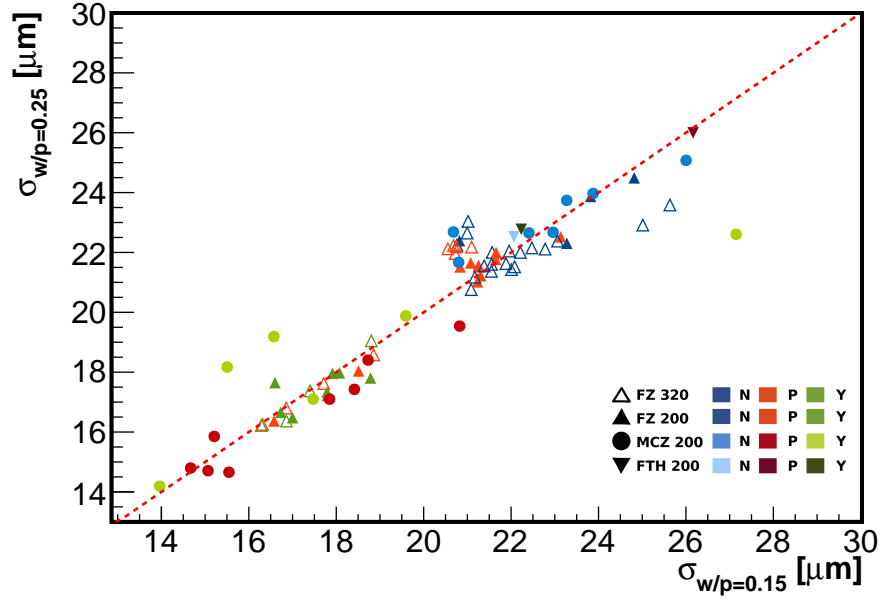


Figure 7.26: Correlation plot between the spatial resolution σ of the regions with width-over-pitch ratios of 0.15 and 0.25 and a pitch of 80 micrometer of all tested MSSDs.

is observed. Again the resolution of p-bulk materials is improved due to charge sharing, resulting in wider clusters and confirming the behavior seen in figure 7.27.

The data for magnetic-Czochralski devices shown in figure 7.29 corresponds to the region with a width-over-pitch ratio of 0.25, as the regions with the lower value of w/p show faulty behavior and the data is therefore not reliable. Again, the trend that p-bulk material benefits from increased charge sharing after irradiation, which has also been observed in the other figures of this section, is confirmed. N-bulk material has a spatial resolution around the binary limit of ~ 23 micrometer, independent of the fluence.

Figure 7.30 represents the 200 micrometer-thick, physically-thinned float-zone material that could only be tested before irradiation. As the number of tracks in the region with $w/p = 0.15$ is very small and thus the datapoints fail the selection criteria, the region with $w/p = 0.25$ is presented here. While the n-bulk and p-spray materials are below the binary resolution, the only available datapoint for p-stop material is considerably above it.

By taking the individual curves corresponding to the different detectors that were tested at different voltages and at different fluence levels into account, the separation of the datapoints in the correlation plot in figure 7.26 can be explained. All tested p-bulk materials show signs of increased charge sharing after irradiation with hadrons, which benefits the spatial resolution due to a larger fraction of wider clusters with respect to

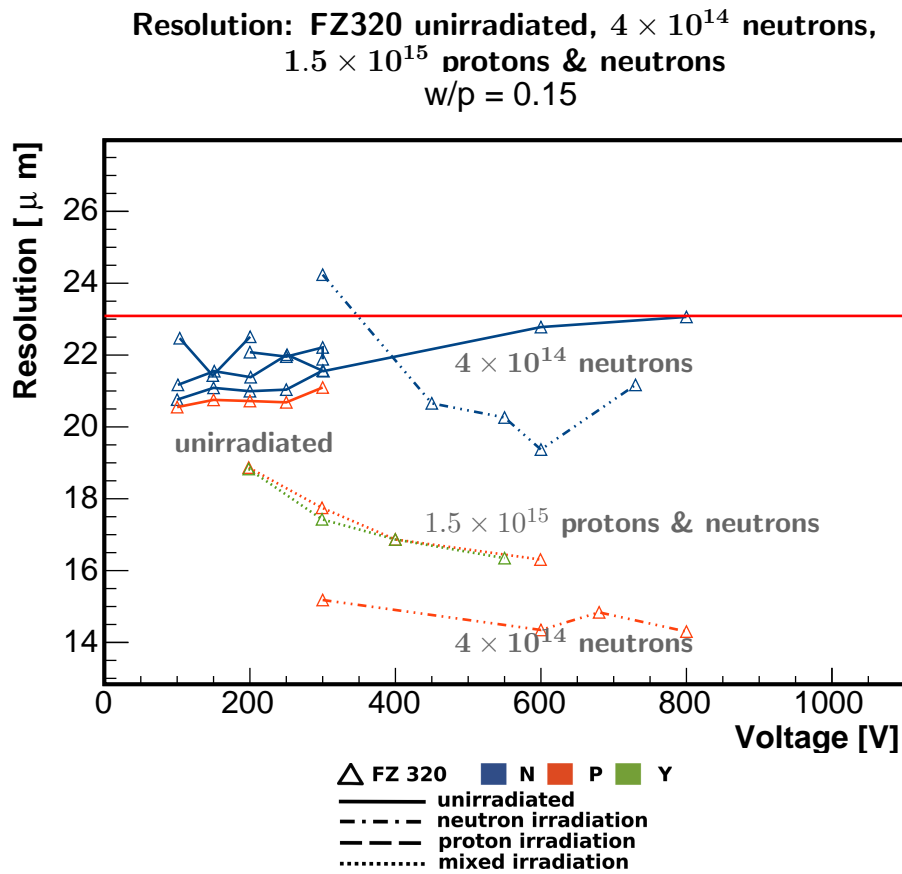


Figure 7.27: Resolution of 320 micrometer-thick float-zone silicon in three different fluence states.

n-bulk material. These, on the other hand, do not experience a change of resolution with fluence, which explains the clustering of blue datapoints around the binary resolution of $\sim 23\mu\text{m}$ in figure 7.26.

**Resolution: FZ200 unirradiated, 3.5×10^{14} protons or 4×10^{14} neutrons,
 1.5×10^{15} protons & neutrons
 $w/p = 0.15$**

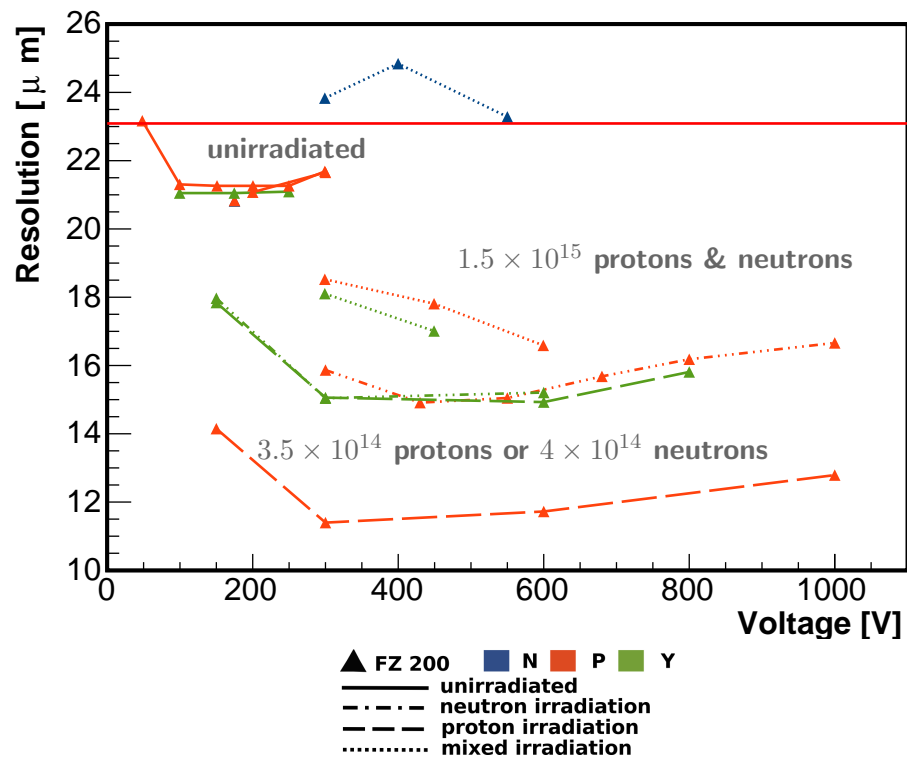


Figure 7.28: Resolution of 200 micrometer-thick float-zone silicon in four different fluence states.

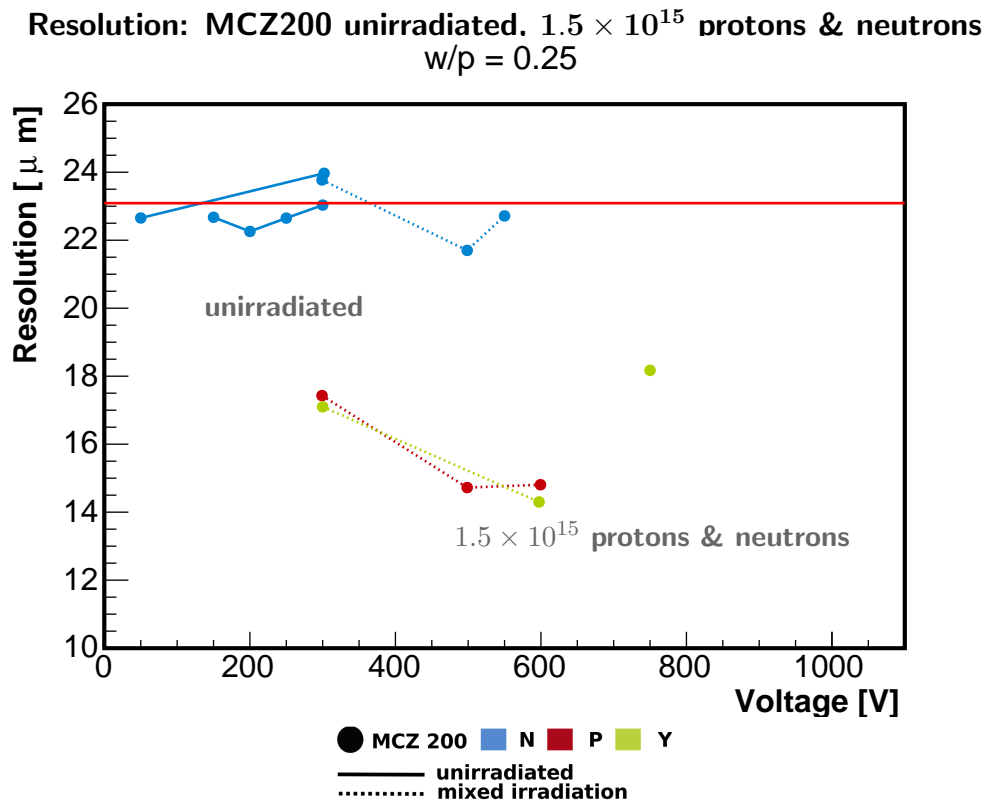


Figure 7.29: Resolution of 200 micrometer-thick magnetic-Czochralski silicon in two fluence states.

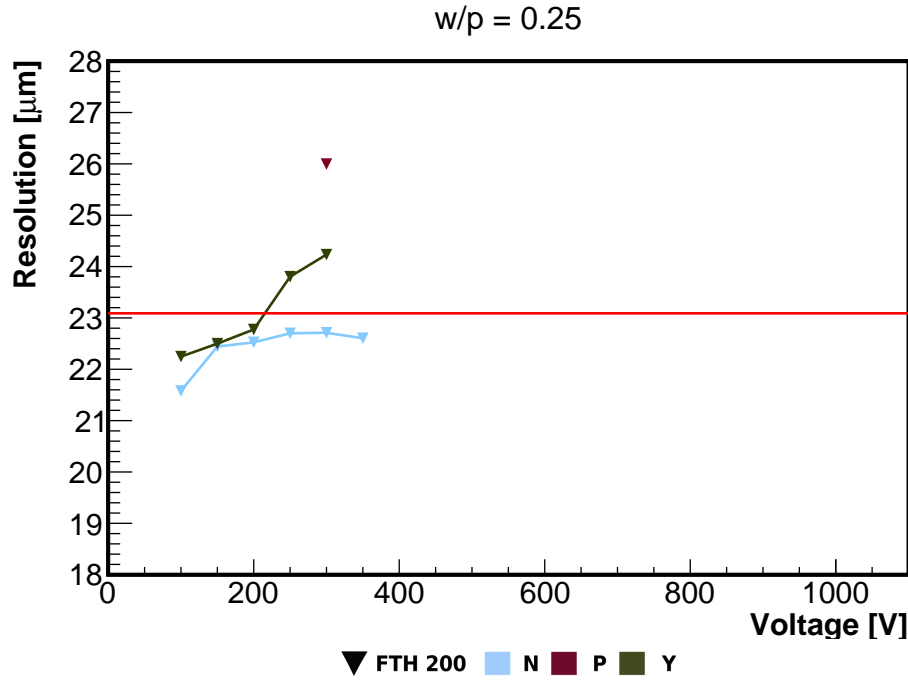


Figure 7.30: Resolution of 200 micrometer-thick, physically-thinned float-zone silicon.

Efficiency

All efficiency- and noise occupancy figures presented in this chapter have been obtained using the method described in section 7.2.2. Similar to the `onTrackCluster` method described, a threshold of 0.4 times the absolute signal (the distance between the mean of the noise distribution and the MPV of the signal) is used as threshold. A window around the calculated impact point of a track is searched for strips exceeding that threshold. From the ratio of detected tracks and the probability of having a noise strip in the same region that is misinterpreted as signal, the efficiency and noise occupancy are calculated according to equations 7.16 and 7.13.

Figure 7.31 illustrates the origin of reduced efficiency and increased noise occupancy: If the noise distribution has very long symmetric tails, the fluctuations of the front-end amplifier output around the pedestal are larger and thus it is possible that the signal created by a traversing particle is not identified as such, which makes the detector inefficient.

Figure 7.32 presents the efficiency and noise occupancy as a function of the bias voltages for regions with 80 micrometer pitch and width-over-pitch ratios of 0.15 on 320 micrometer-thick float-zone devices. Four different measurements are available from unirradiated FZ320N detectors from two different wafers that served as reference. Two of these curves, corresponding to the March 2011 beam test and the one in October 2012, have almost 100 % efficiency, while the other two measurements have increased

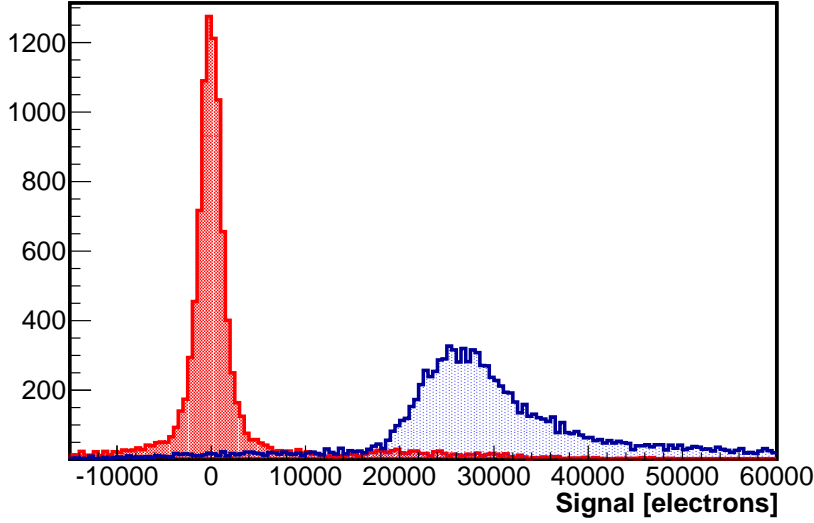


Figure 7.31: Example of the cluster charge and noise distribution of a detector tested in September 2011. The long symmetric tails of the noise distribution reduce the signal, as the fluctuations around the pedestals are larger. This leads to a reduction of the number of identified hits, which reduces the efficiency.

noise occupancy and thus reduced efficiency of only 96 to 98 %. This difference relates to the presence of the additional grounding connection described in section 7.3.1 and illustrated in figure 7.18, or, in the case of the March 2011 beam test, to a generally lower noise level, for which no satisfactory explanation could be found.

The detectors irradiated to the highest fluence of 1.5×10^{15} 1MeV n_{eq} cm^{-2} (1×10^{15} protons and 0.5×10^{15} neutrons) have reduced efficiency and in addition the efficiency- and noise occupancy curves follow a ramp shape, meaning that the efficiency increases with increasing high voltage and the noise occupancy decreases to values below one percent.

The two detectors irradiated with 4×10^{14} 1MeV n_{eq} cm^{-2} neutrons have significantly reduced efficiency as compared to all other detectors, which correlates with increased noise (figure 7.31). The datapoint corresponding to unirradiated n-bulk material at a voltage of 800 V also has reduced efficiency, which can be linked to the increased shot noise caused by increased leakage current at this high voltage.

The result is similar for deep-diffused float-zone silicon with 200 micrometer active thickness as shown in figure 7.33. All unirradiated detectors have efficiencies close to 100 %. The p-stop- and p-spray devices irradiated to the highest fluence of 1.5×10^{15} 1MeV n_{eq} cm^{-2} show the distinctive ramp shape and the actual efficiency climbs well over 96 %, whereas the n-bulk detector performs significantly worse with a much larger influence of the applied bias voltage. Also the noise occupancy for this detector is significantly increased up to 16 %, which is consistent with the elevated noise for the

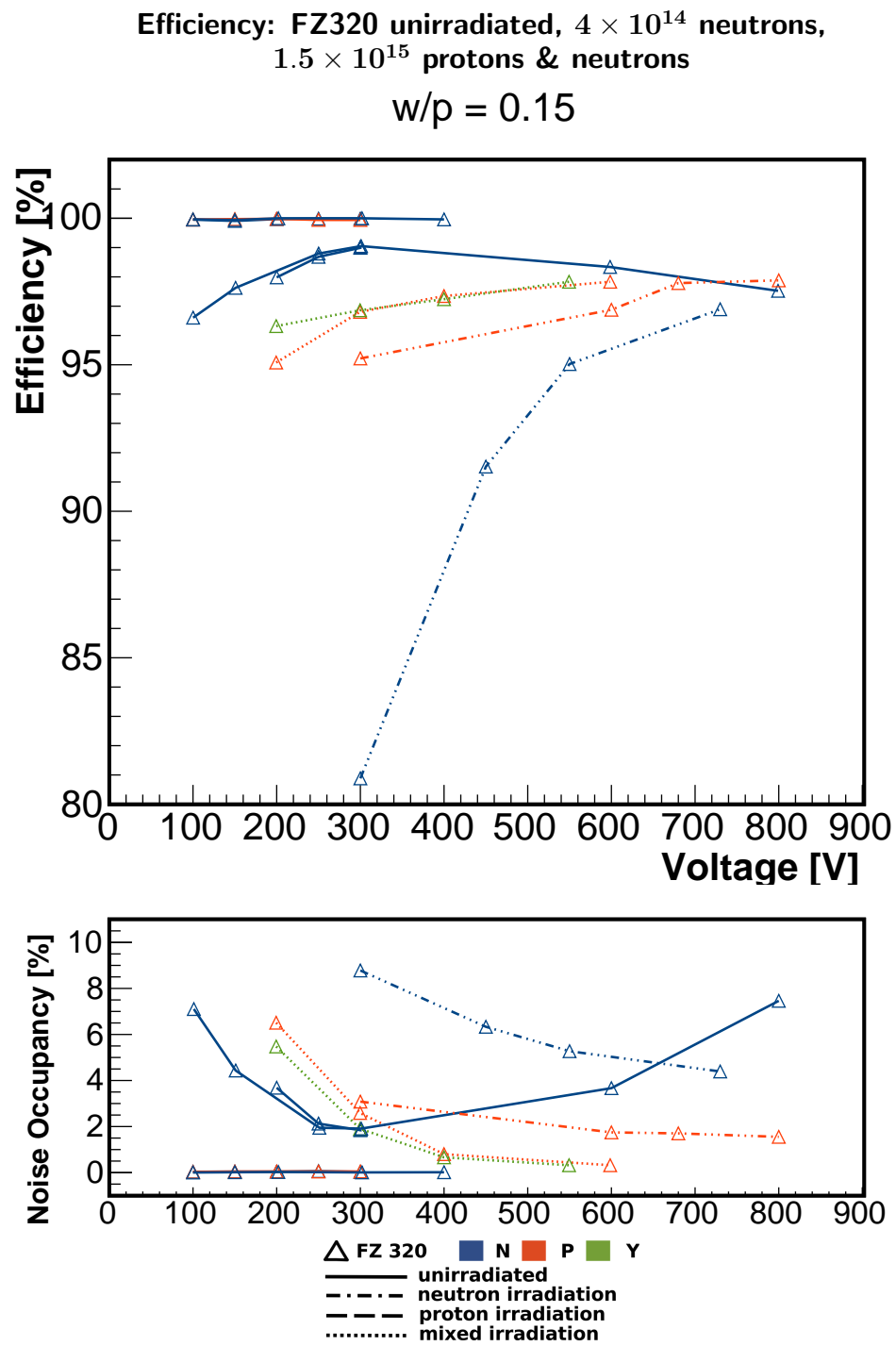


Figure 7.32: Efficiency of 320 micrometer-thick float-zone silicon in three different fluence states.

n-bulk detectors observed in figure 7.22.

Similar to figure 7.32, the efficiency of the unirradiated reference detector decreases at the highest tested voltage. This correlates with a dramatic increase of the noise of the detector, with a voltage increase from ~ 300 to ~ 800 V, which in turn can be attributed to the increase of the leakage current (shot noise). This noise increase also manifests itself in the noise occupancy in the lower sections of figures 7.32 and 7.33.

Figure 7.34 presents the efficiency- and noise occupancy figures for magnetic-Czochralski material. A problem that affected all four regions with $w/p = 0.15$ on the unirradiated n-bulk reference detector was found and therefore no data for this w/p is shown. The irradiated sensors all have efficiency figures around 96 %, with the N material performing worst. Furthermore, this doping scheme also has a high noise occupancy at the level of 5 % at the highest tested voltage, which is consistent with the noise (figure 7.22). The two measurements of the unirradiated reference detector illustrate the influence of the additional grounding on the readout hybrid described in section 7.3.1 on both efficiency and noise occupancy.

Physically-thin float-zone material (figure 7.35) has very high efficiency and exceptionally low noise occupancy, as these detectors were only measured in the last beam test, where the additional grounding connection was made on all modules.

The presented results yield several conclusions about the performance of the tested devices before and especially after irradiation. The spatial resolution of p-bulk detectors improves with increasing fluence as the average clusterwidth and thus the charge sharing between the strips increases. N-bulk detectors, on the other hand, do not show such an effect and the resolution stays around the binary limit of $p/\sqrt{12} \approx 23\mu m$.

Furthermore, the efficiency, as calculated in this section, is closely linked to the noise occupancy and therefore the noise. Low and uniform noise, as measured after the implementation of the additional grounding connection, results in almost 100 % efficiency and ~ 0 % noise occupancy of the tested detectors. Irradiation, on the other hand, increases the noise and thus also reduces the efficiency. Higher bias voltages can recover some efficiency similar to the signal in section 7.3.2, but the difference between n- and p-bulk material is still evident.

Efficiency: FZ200 unirradiated, 3.5×10^{14} protons or 4×10^{14} neutrons,
 1.5×10^{15} protons & neutrons
 $w/p = 0.25$

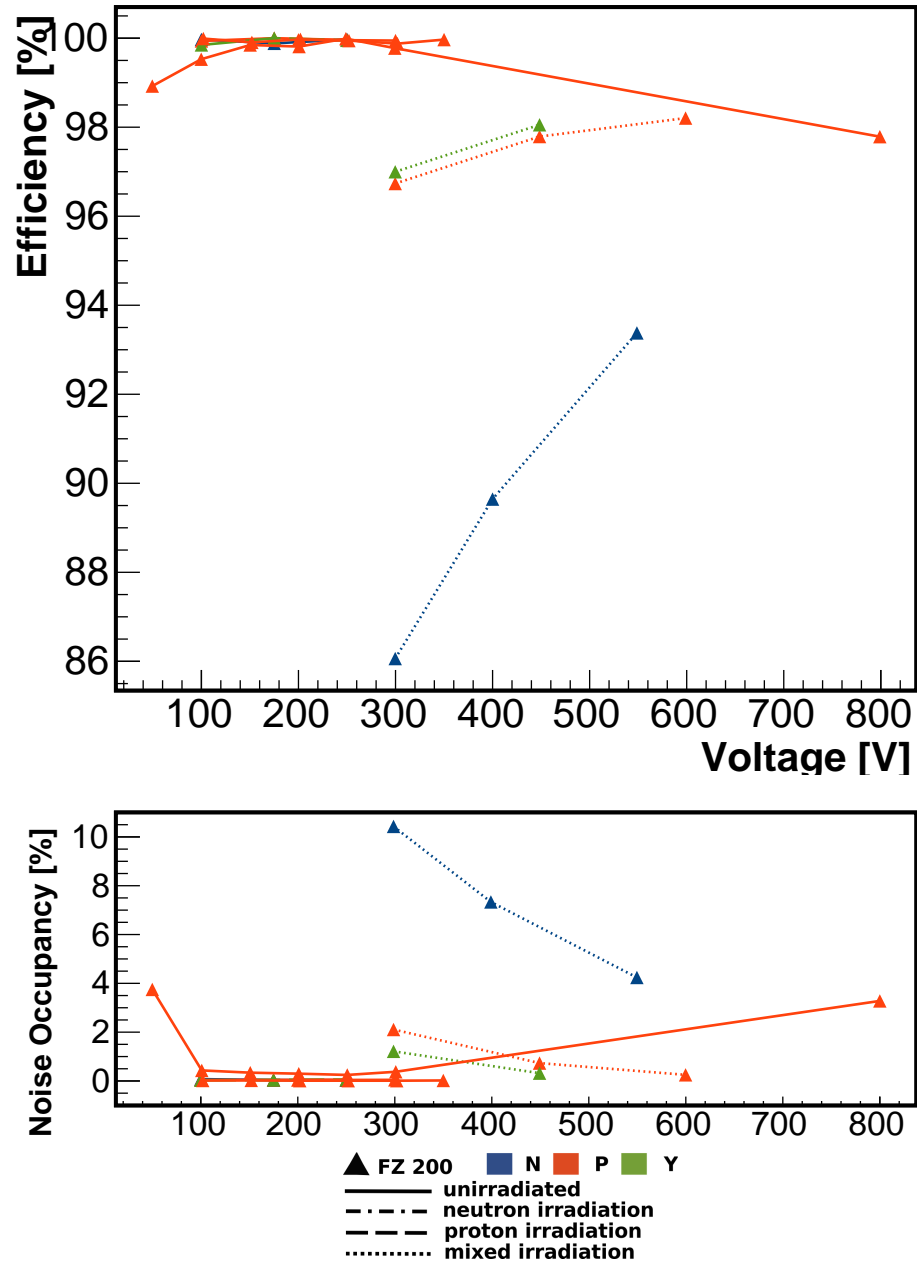


Figure 7.33: Efficiency of 200 micrometer-thick, deep-diffused float-zone silicon in three different fluence states.

Efficiency: MCZ200 unirradiated, 1.5×10^{15} protons & neutrons
w/p = 0.25

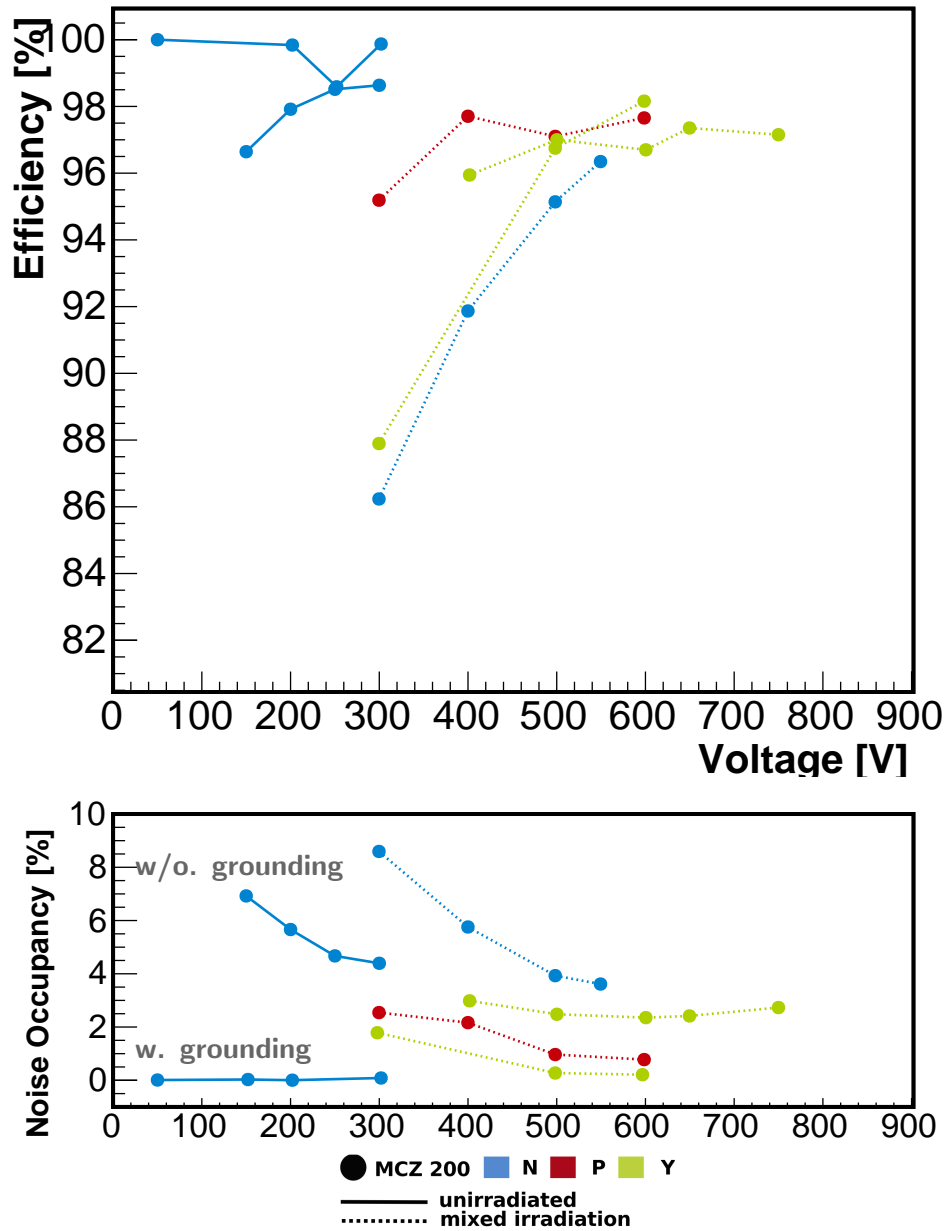


Figure 7.34: Efficiency of 200 micrometer-thick magnetic-Czochralski silicon in two different fluence states.

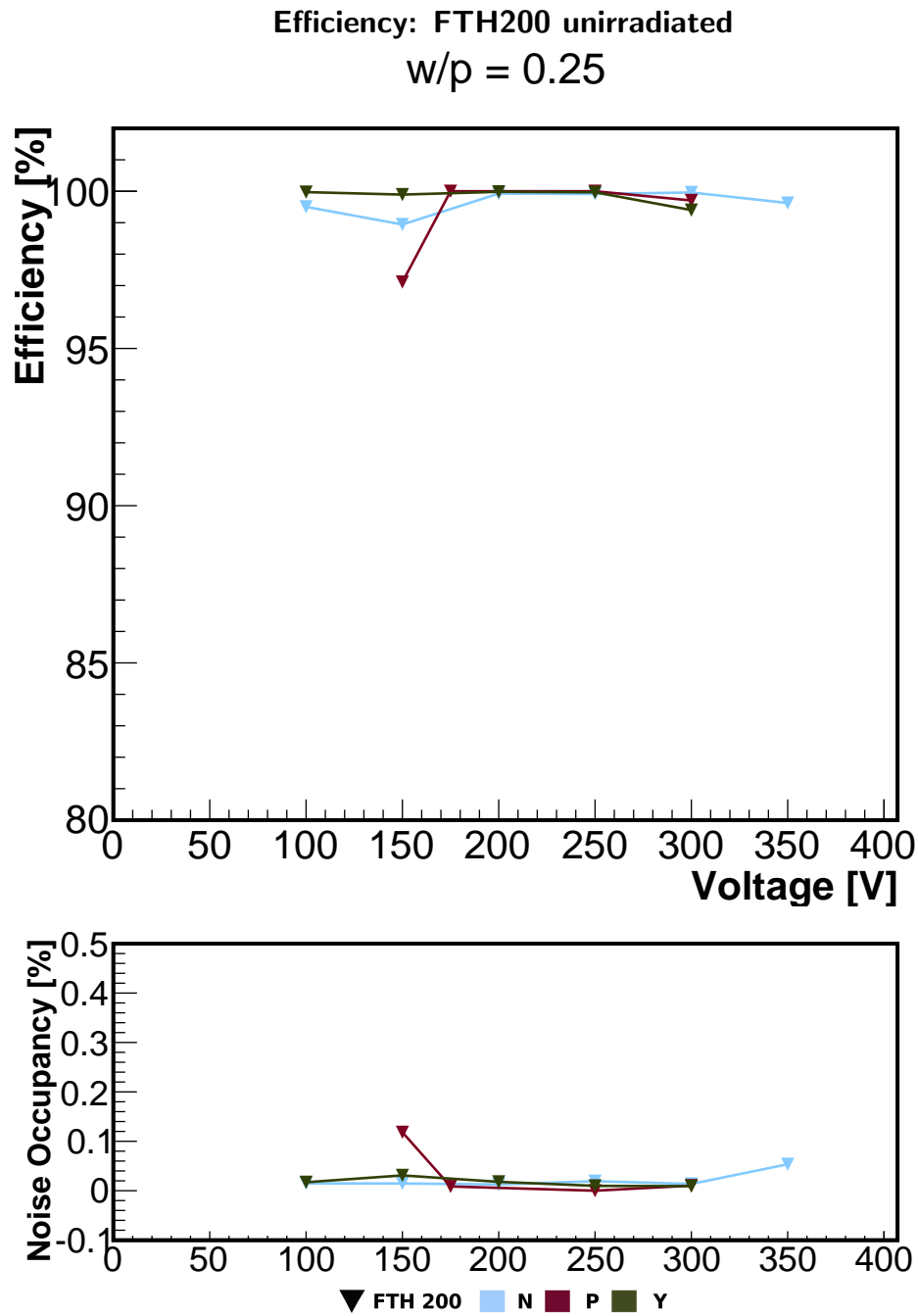


Figure 7.35: Efficiency of 200 micrometer-thick, physically-thinned, unirradiated float-zone silicon.

8 Simulation of Binary Clustering with the CBC

As the Phase-2 tracker upgrade will use a binary readout chip called CMS Binary Chip (CBC) (chapter 3), the response of such a system to possible geometries is of particular interest. For that reason, a simulation of a binary readout system with recorded MSSD data has been carried out.

Binary clustering means that a fixed charge threshold in units of electrons is programmed into the front-end chip and that strips with a signal above this threshold are considered hits. Due to the high granularity of the future tracker, the data from sensors will have to be reduced directly on the module in order to keep the amount of data to be read out and the necessary bandwidth low. The CMS collaboration has therefore developed the second iteration of the CBC prototype called CBC2, which features a total of 254 channels and a correlation logic to correlate hits on the two vertically stacked sensors that form a p_T module. This logic also vetos clusters that are wider than two strips because they indicate a low p_T track. The noise of the prototype was measured to be around 1,000 electrons, independent of the polarity of the signal. The clustering threshold has to be selected such that the noise occupancy (channels that measure noise above the threshold) is zero and the detector efficiency is 100 %.

With the data recorded in the four beam tests, four different algorithms for calculating the center of a cluster that could be integrated into the chip using simple logic functions are simulated. The goal of this study is to evaluate the impact of these algorithms on the position resolution, the average clusterwidth of a sensor and the impact of the threshold on the detector efficiency before and after irradiation.

In the following sections the different binary algorithms and their implementation in the analysis will be explained. The last section is devoted to a few selected results for specific materials that are promising candidates for application in the future tracker.

8.1 Binary Clustering Algorithms

Four algorithms that are relatively easy to implement in a front-end chip and that can be divided into two subgroups have been studied.

- algorithms with full-strip resolution
- algorithms with half-strip resolution

The first type implies that the hit position on the sensor will always be an integer strip number and the expected resolution will be around $p/\sqrt{12}$ (compare equation 4.13). The latter algorithms have some kind of weighting implemented that allows for the calculation of the hit position with a higher precision than an integer strip number.

Binary (1 strip resolution)

This algorithm searches the detector for a sequence of N strips with a signal exceeding a certain pre-programmed threshold. The center is calculated as the mean strip number according to

$$\bar{n} = \frac{\sum_{i=1}^N n_i}{N} \quad (8.1)$$

with n_i denoting the strip number. For odd N , this number is always an integer, while it has to be rounded to an integer for even N , since the remainder of the above division is always 0.5. All rounding conventions are equally possible and have to be decided on.

Leading strip (1 strip resolution)

The second algorithm also searches for a sequence of strips with a signal exceeding the threshold, but returns only the strip with the highest signal. This can be implemented by means of a simple comparator logic. If a strip signal exceeds the threshold, the strip number is written to a buffer. If another adjacent strip has a higher signal, the buffered value is overwritten until the leading strip is found.

Binary (1/2 strip resolution)

This binary algorithm is very similar to the first one presented here, with the difference that non-integer values are accepted as the center of the cluster. It requires a more complex logic since the level of precision of the sent-out data has to be increased. Clusters with an odd number of strips still have integer centers but values in the middle of two strips are also considered.

Barycentric

The last algorithm is more complex and requires a much more sophisticated logic. The center of gravity is built with each strip weighted by its signal S_i . This is very similar to traditional clustering without η correction and to the algorithm used for the `onTrackCluster` method described in the previous chapter. The formula reads

$$\bar{n} = \frac{\sum_{i=1}^N S_i n_i}{\sum_{i=1}^N S_i} \quad (8.2)$$

with n the strip number. This algorithm is very similar to analog readout and too complex to be built into a front-end chip, but it is a good method of comparing the performance to the full analog system.

Figure 8.1 shows the resolution as a function of the threshold for the four presented algorithms. At low thresholds, with many noise strips included in the clusters, the algorithms with half-strip resolution show a better performance. If the threshold is raised, the fraction of included noise strips is reduced. For very high thresholds only

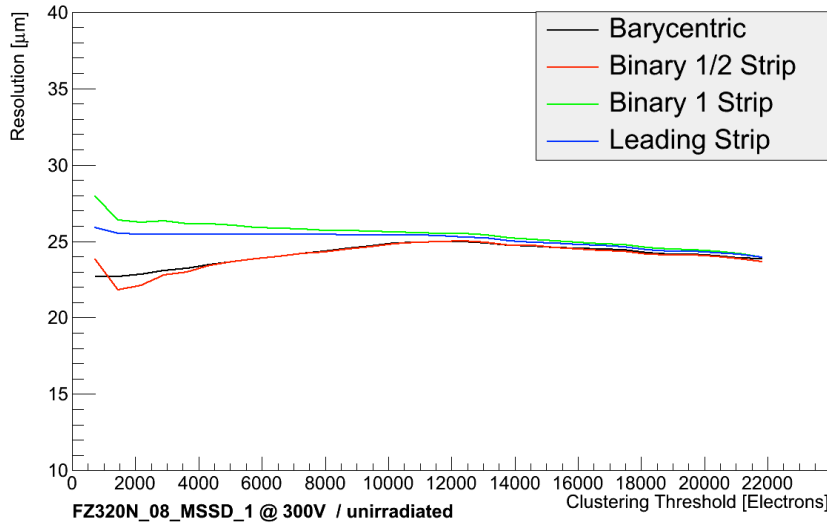


Figure 8.1: Resolution of the four binary algorithms as a function of the threshold.

strips with a large signal remain as one-strip clusters. In this case the performance of the algorithms with full-strip resolution becomes identical with the other ones. The gain in the resolution at low thresholds for the barycentric and binary method with half-strip resolution has to be weighted with the effort that has to be put into implementing the respective logic on the front-end chip.

It should be pointed out that the detector efficiency is only a function of the threshold and independent of the algorithm for computing the cluster center.

8.2 Simulation of the CMS Binary Chip

In this section the implementation of binary clustering as a function of the threshold into the **TBAnalysis** framework will be described briefly. As a loop over many different thresholds is necessary for the simulation of these algorithms, a dedicated executable named **binary** reproduces all the steps that are necessary to find clusters. First a given threshold is set and then the **Track** and **Data** objects are loaded for a given sensor by reading a config file. The **Alignment** collection is applied to the tracks and then clusters are searched for in the common-mode corrected raw data. It will not be possible to implement a common-mode correction algorithm on the CBC itself, but the common-mode noise in the available data originates mainly from the readout system and is thus corrected in this specific study.

The cluster search is done by scanning a window of fixed size around the calculated impact point of the track for seed strips, similar to the **onTrackCluster** method described in section 7.2.2. If a seed is found, adjacent strips are added to the cluster as

long as they exceed the threshold. If two separate seeds are found in the search window, only the closer one is considered for the computation of the resolution. This enhances the resolution for very low thresholds artificially but it still is a good approximation and limits the CPU time needed for the analysis.

After the clusters have been found, the residuals are calculated by subtracting the calculated hit coordinate from the track coordinate for the four different binary algorithms and the RMS of each distribution, corrected by the calculated telescope resolution (table 7.1), is plotted as a function of the threshold, as is the average cluster width.

The detector efficiency, together with the noise occupancy, is calculated with the method described in section 7.2.2 according to equations 7.13 and 7.16. Instead of a threshold derived from the signal- and noise distributions, the different clustering thresholds are scanned in a loop.

The sample of tracks that are used for these calculations are limited by the condition that they have to pass through the active part of the MSSDs' regions.

8.3 Results

Running the analysis steps described in the previous section requires a lot of CPU time, since the clustering procedure has to be repeated for many thresholds and thus it is only done for selected detectors. Taking the better performance of p-bulk sensors after irradiation and the fact that the future CMS sensors will have a pitch around 90 micrometer into account, only regions with a pitch of 80 micron are presented, like in the previous chapter. Furthermore, only the results for the two simplest algorithms, which are the binary algorithms with full- and half strip resolution, will be shown.

The resolution and clusterwidth are presented together with the efficiency and noise occupancy as a function of the threshold in absolute charge and as multiples of the average noise of a region (top scale). Only one unirradiated reference detector (FZ200P at 250V) is shown together with results for detectors that perform best after irradiation to the highest fluence of 1.5×10^{15} 1MeV n_{eq} cm^{-2} and thus are the most promising candidates for the future tracker. These are thin, p-doped detectors and for the specified fluence, data is available for FZ200P/Y and MCZ200P at 450 and 500 V respectively.

Figure 8.2 shows the resolution and clusterwidth on the unirradiated p-stop detector. The efficiency is constant up to very high thresholds in the order of 16σ (multiple of the average noise), while the noise occupancy drops from $\sim 15 \%$ to almost zero around 3σ . This yields a large range of possible thresholds in which the detector can be operated efficiently and by changing the threshold, the spatial resolution can be adjusted accordingly. The resolution for both binary algorithms converges to the same value at high thresholds and the average clusterwidth constantly decreases asymptotically to values close to one.

The irradiated detectors shown in figures 8.3, 8.4 and 8.5 all show the same behavior.

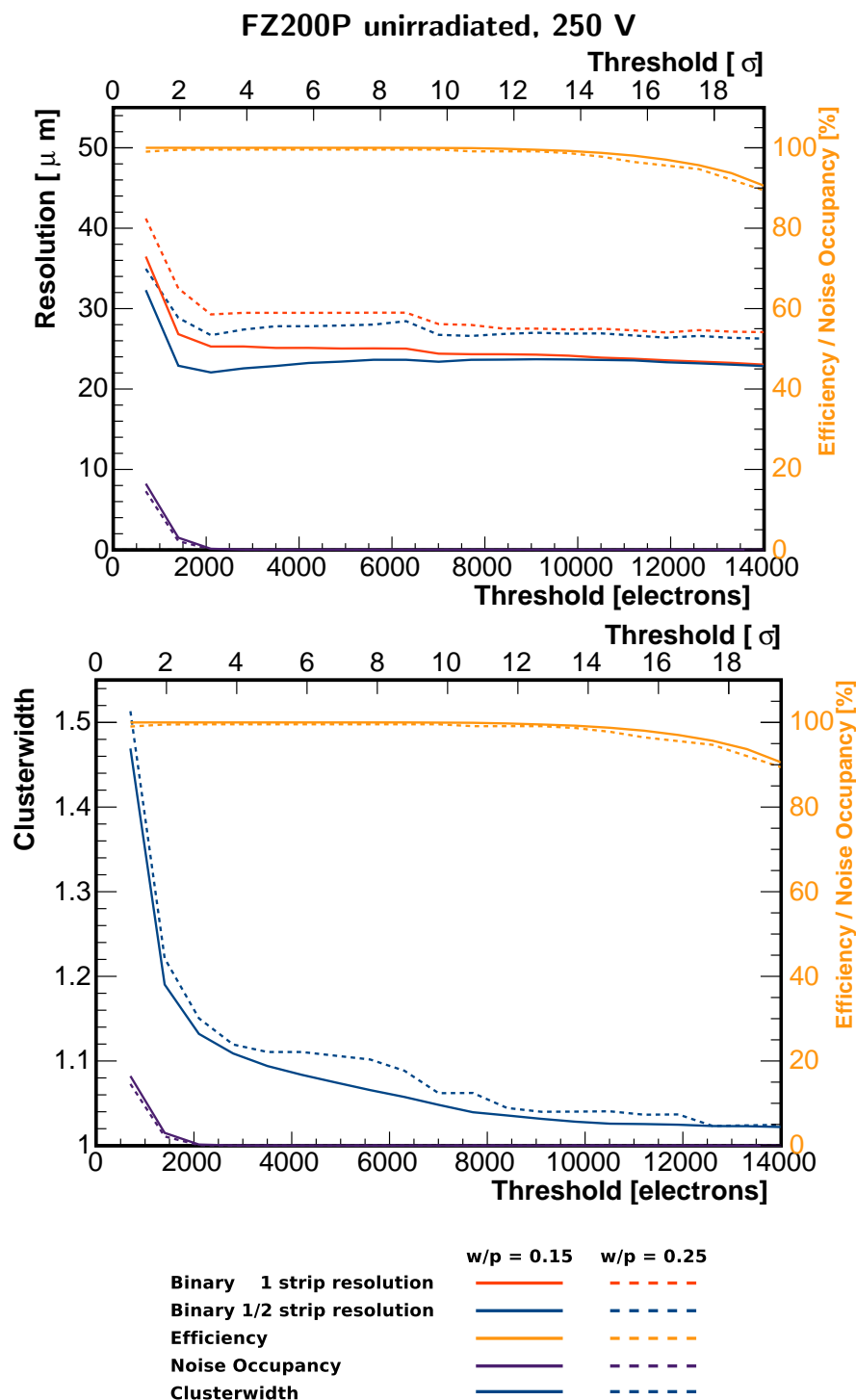


Figure 8.2: Binary resolution and -clusterwidth together with detector efficiency and noise occupancy as a function of the binary threshold for cluster identification extracted from analog data recorded with an unirradiated, 200 micrometer-thick, deep-diffused p-spray float-zone detector biased to 250 V for regions with a pitch of 80 micrometer.

The noise occupancy of the sensor approaches zero for thresholds in the regime of 3σ but at the same thresholds, the detector efficiency starts to fall dramatically. This limits the range in which the detector can be operated efficiently and thus a precise tuning of the threshold is necessary after a fluence of $1.5 \times 10^{15} \text{ 1MeV n}_{\text{eq}} \text{ cm}^{-2}$. The decreasing efficiency originates from the fact that after irradiation strips collect less charge and thus a fraction of clusters at the low end of the Landau distribution fall below the threshold.

This also manifests itself in the average clusterwidth, which reaches values below 1.1 at much lower thresholds than the unirradiated reference device. This implies that only clusters where a central strip collects the largest fraction of the charge are found, while wider clusters, where the charge is more evenly distributed among several strips, are not detected any more.

The resolution eventually converges to the same value, independent of the precision of the used algorithm at very high thresholds, where only one-strip clusters are included. At the lower thresholds that will be required after irradiation, however, the gain in spatial resolution with an algorithm with half-strip precision is significant. The measured resolutions as a function of the threshold fluctuate between ~ 18 and $30 \mu\text{m}$ and the best values are below the binary limit given by $p/\sqrt{12} \approx 23 \mu\text{m}$. Similar to what has been observed with the analog readout in section 7.3.3, irradiation benefits the charge sharing and therefore the resolution of p-bulk materials.

Of all tested materials, the p-stop magnetic-Czochralski device has the widest range of efficient operation after irradiation.

The results presented in this chapter yield that it will be necessary to adapt the CBC threshold to the fluence state of the future sensors, in order to find a balance between noise occupancy and detector efficiency. The window available for selecting an appropriate threshold decreases with increasing fluence. In order to fully exploit the beneficial effects of enhanced charge sharing on the resolution of p-bulk sensors, it makes sense to implement a clustering algorithm that is able to calculate the hit position with half-integer precision as the gain in resolution can be significant, especially for the lower thresholds that will be required after irradiation. Doing so would result in a slightly inferior, but comparable performance of the whole system in terms of resolution to the present, full analog readout system with the additional benefit of significantly decreased bandwidth as it is not necessary to send the full analog data out for processing.

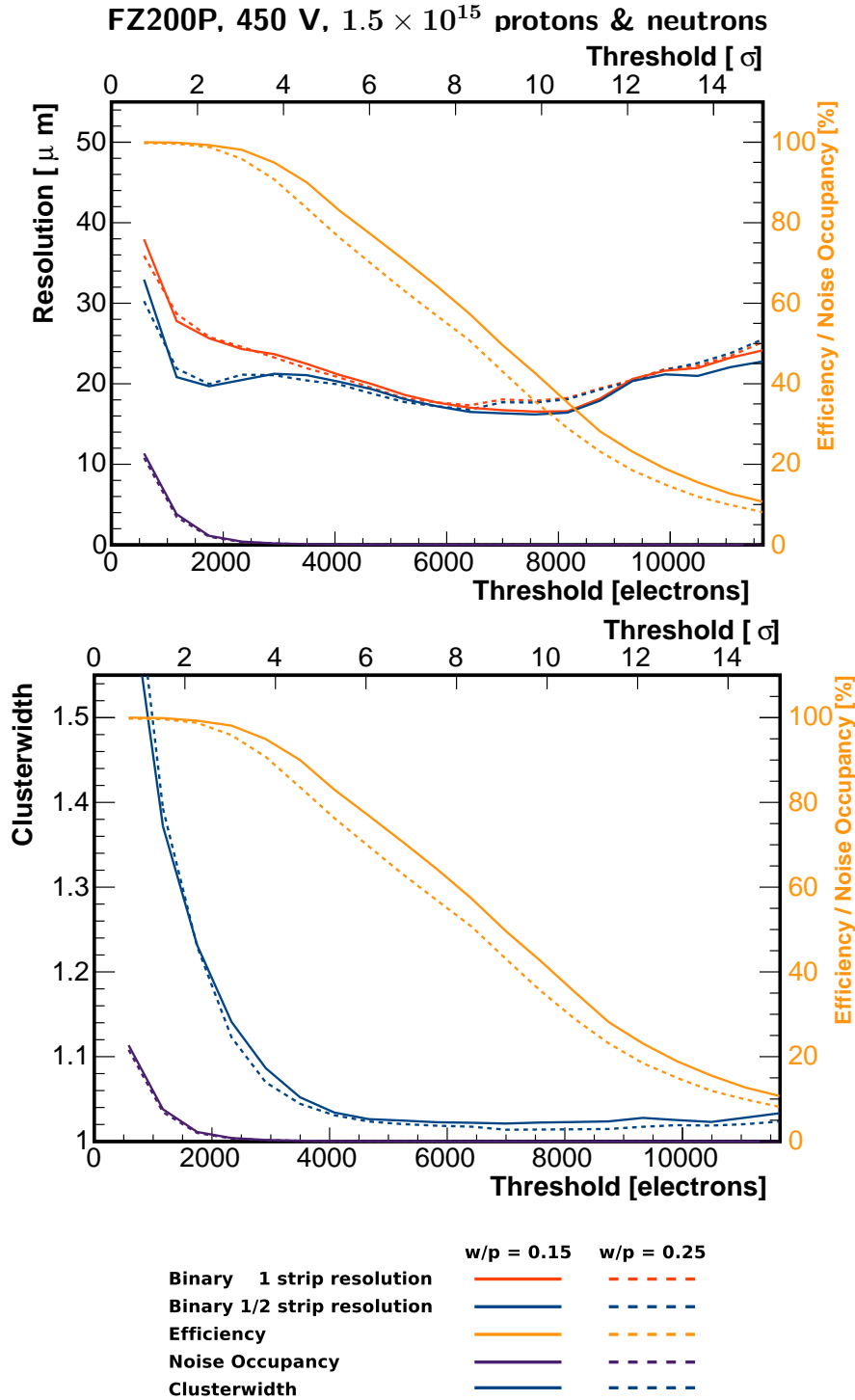


Figure 8.3: Binary resolution and -clusterwidth together with detector efficiency and noise occupancy as a function of the binary threshold for cluster identification extracted from analog data recorded with a 200 micrometer-thick, deep-diffused, p-stop float-zone detector irradiated to 1.5×10^{15} 1NeV n_{eq} cm^{-2} with protons and neutrons and biased to 450 V. The pitch is 80 micrometer.

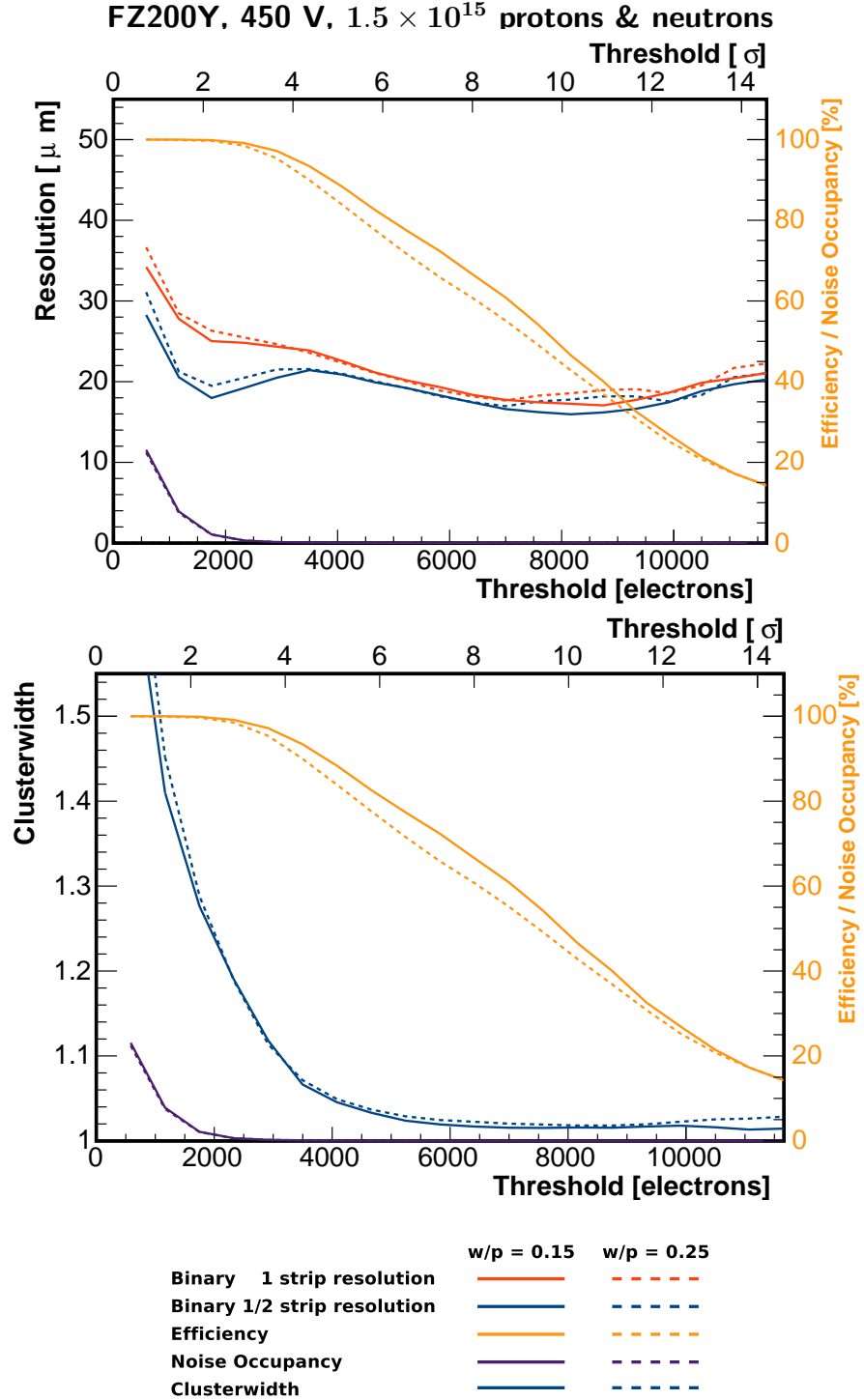


Figure 8.4: Binary resolution and -clusterwidth together with detector efficiency and noise occupancy as a function of the binary threshold for cluster identification extracted from analog data recorded with an unirradiated, 200 micrometer-thick, deep-diffused, p-spray float-zone detector irradiated to 1.5×10^{15} $1\text{NeV } n_{\text{eq}} \text{ cm}^{-2}$ with protons and neutrons and biased to 450 V. The pitch is 80 micrometer.

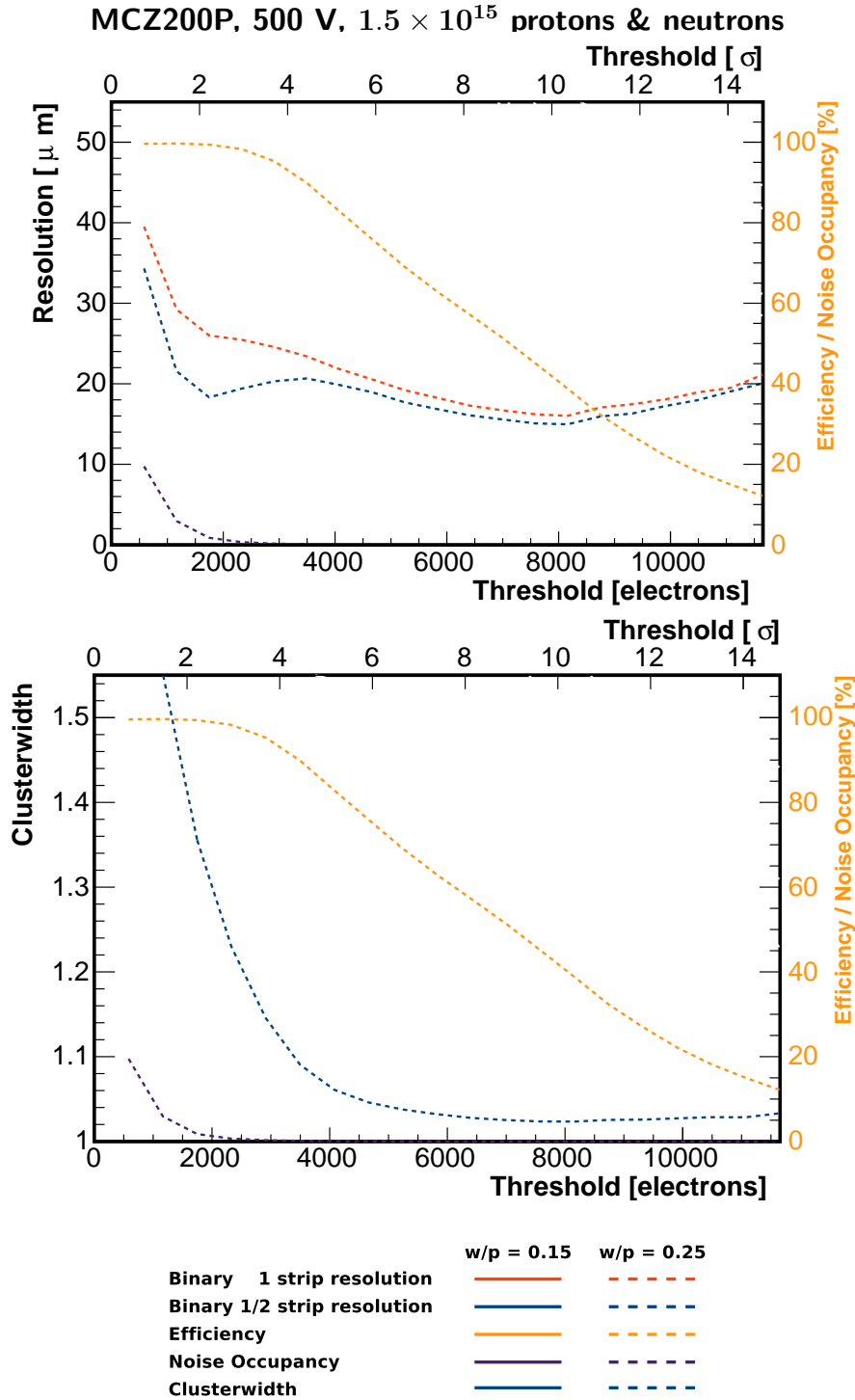


Figure 8.5: Binary resolution and -clusterwidth together with detector efficiency and noise occupancy as a function of the binary threshold for cluster identification extracted from analog data recorded with an unirradiated, 200 micrometer-thick, p-stop magnetic-Czochralski detector irradiated to 1.5×10^{15} 1NeV $n_{eq} \text{ cm}^{-2}$ with protons and neutrons and biased to 500 V. The pitch is 80 micrometer. No reliable data is available for the region with $w/p = 0.15$.

9 Selected Results from the Collaboration

The presented results are only one part of a large collaborative effort involving many institutions to find a suitable material and geometry for sensors to be used in the future Phase-2 tracker of CMS. For that reason, the individual aspects to be investigated and the different measurements are distributed between the institutes participating in the CMS Tracker collaboration.

Some very interesting results – contributing massively to the final decision on a suitable material that is to be taken – have not been mentioned in this thesis. This chapter will give an overview on some selected highlights concerning measurements aimed at understanding the material properties of the available materials at a microscopic level on planar diodes, and on other aspects of strip-sensor qualification that are not within the scope of this thesis.

9.1 Diodes and Material Properties

Planar diodes are the simplest structure and yield important information on material properties on a microscopic level, such as impurity concentrations, the depletion voltage as a function of the effective doping concentration and its response to irradiation with hadrons and subsequent annealing.

Measurements of the oxygen concentration, which is an important parameter with respect to radiation tolerance (compare chapter 4), have been done using secondary-ion mass-spectroscopy (SIMS). The results yield above-average concentrations on all purchased materials between 0.2 to $5 \times 10^{17} \text{ cm}^{-3}$ for the "standard" deep-diffused float-zone silicon, around $0.9 \times 10^{17} \text{ cm}^{-3}$ for the physically-thinned float-zone material and between 3 to $6 \times 10^{17} \text{ cm}^{-3}$ for the magnetic-Czochralski silicon. This means that all float-zone materials have concentrations that are more in the regime of DOFZ¹ material, which was found to be more radiation-hard in previous studies.

Diodes also allow for measuring the effective doping concentration of the bulk material through the depletion voltage. By repeating these measurements over a wide fluence range, data points that can be fitted with the so-called Hamburg model from chapter 4, which allows conclusions on the level of radiation damage, have been obtained. These measurements yield interesting findings about the different damage done by different particles at different energies and about the process of type inversion.

¹diffusion-of-oxygen float-zone

While all materials with an active thickness of 200 micrometer have depletion voltages below 600 V for all investigated fluences, these different fluences have different implications on the effective doping concentration. It has been found that after irradiation with 23 GeV protons, n-bulk float-zone material type-inverts, which is expected, but n-bulk magnetic-Czochralski silicon does not. On the contrary, here the P material shows signs of type inversion, which is unexpected. Irradiation with lower-energy protons on the other hand yields type-inversion of both n-bulk materials. Another interesting feature of particle-type-dependent damage is a phenomenon called compensation: it has been observed that neutron irradiation can compensate for the damage inflicted by 23 GeV protons to a limited extent in oxygen-rich magnetic-Czochralski material.

Annealing studies on these planar diodes have also shown that the depletion voltage can be significantly reduced by annealing at higher temperatures after irradiation, thus decreasing the effective doping concentration. Charge-collection efficiency measurements, where the signal response of a diode to a laser beam is measured with an oscilloscope, have also shown results similar to what can be seen in the beam test analysis in chapter 7: 320 micrometer-thick material collects more charge at lower fluences or at higher voltages than the thin materials, but at intermediate bias voltages around 600 V the thin detectors collect almost as much charge. This discrepancy can be attributed to increased trapping and underdepletion effects in the thicker sensors.

9.2 Other Aspects of Strip-Sensor Performance

In addition to the beam test studies carried out with the MSSD and presented in this thesis, many other parameters have been investigated on other small strip sensors from the HPK wafer. Furthermore, extensive fluence-dependence- and annealing studies have been done on these smaller structures.

Charge-collection efficiency measurements with a radioactive source in the laboratory do not provide tracking information but can be very useful for repeating measurements after every irradiation or annealing step, as the measurements are a lot less complicated and hardware-demanding than a beam test. These laboratory tests yield that at lower fluences below $7 \times 10^{14} \text{ 1MeV n}_{\text{eq}} \text{ cm}^{-2}$ n-bulk sensors collect more charge and have a higher seed-strip signal, which is the charge of the leading strip in a cluster. This is understandable if the fact that the interstrip isolation of p-bulk material decreases with fluence is taken into account, and thus the charge sharing between the strips and the cluster size increase. Above fluences of $1 \times 10^{15} \text{ 1MeV n}_{\text{eq}} \text{ cm}^{-2}$, however, n-bulk detectors show extremely low or even no signal, which is consistent with what can be seen in the beam test analysis (chapter 7).

Another advantage of the p-bulk materials is the fact that these sensors have virtually no reverse annealing amplitude, meaning that the collected charge stays constant over a large range of annealing times, whereas it decreases on n-bulk detectors.

The superiority of magnetic-Czochralski material over float-zone sensors has also been

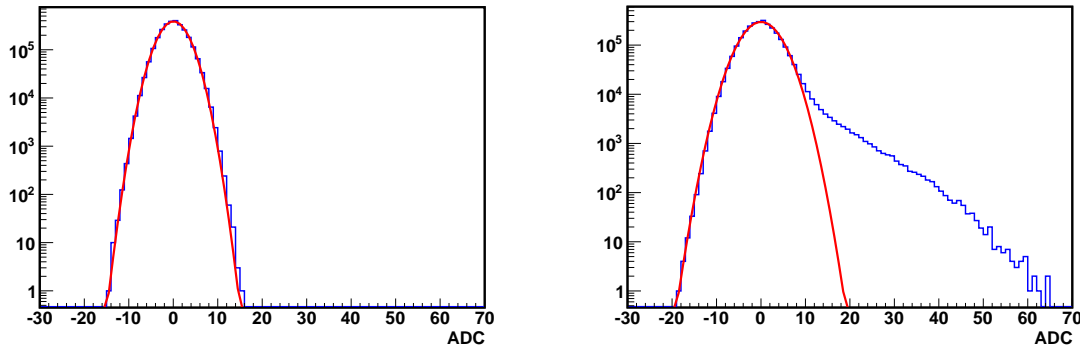


Figure 9.1: Example of a normal noise distribution and a noise distribution with a long, non-Gaussian tail on a logarithmic scale. Courtesy of *M. Naseri, CERN*.

confirmed by the laboratory measurements of the charge-collection efficiency, which might be caused by the much higher oxygen content of MCZ.

An important aspect of sensor operation within the magnetic field of a large-scale collider experiment is the Lorentz angle, which describes the offset of the measured track position from the actual track position due to the drift of the created charge carriers in the magnetic field. As p-bulk detectors collect the signal induced by the drift of electrons, which are more mobile in the silicon lattice, this effect is more pronounced on these detectors. The Lorentz angle has been observed to decrease with irradiation but to increase with annealing.

9.3 Random Ghost Hits

Random ghost hits or micro discharges are a feature that has been observed on irradiated n-bulk material in laboratory measurements. It originates from a long, asymmetric, non-Gaussian tail in the noise distribution that can stretch well above five σ of the distribution, which is the seed-strip threshold for most clustering procedures. Strips that have these long tails can therefore be identified as fake hits on the sensor, resulting in a non-negligible noise occupancy in the order of few percent. As the overall design occupancy of the CMS tracker in the HL-LHC scenario is only $\sim 2\%$, this is a very serious concern for the operation of n-bulk detectors at higher fluences. Figure 9.1 shows a normal noise distribution and one with a long, asymmetric tail resulting in random ghost hits on a logarithmic scale.

These random ghost hits occur mostly on heavily irradiated sensors that are biased to very high voltages and have received no or only little annealing. These sensors show a strong increase of the noise with increasing high voltage and it has been observed that the random ghost hits follow the leakage current, which is responsible for this shot noise. Figure 9.2 shows the dependence of the occurrence of micro discharges as a function of

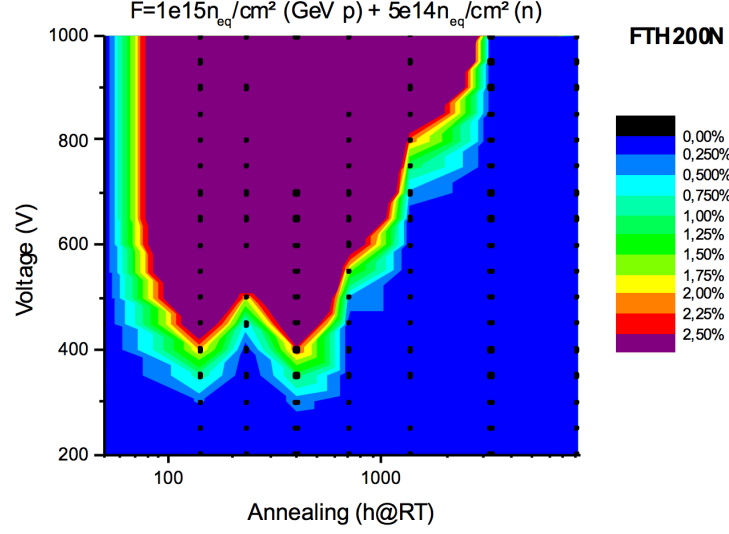


Figure 9.2: Fake occupancy caused by random ghost hits as a function of bias voltage and annealing time on n-bulk, physically-thinned, 200 micrometer-thick float-zone silicon after irradiation to $1.5 \times 10^{15} \text{ 1MeV n}_{\text{eq}} \text{ cm}^{-2}$ [66].

the bias voltage and the annealing time.

By testing MSSD detectors for these random ghost hits it has been discovered that there is a strong dependence on the sensor- and strip geometry: regions with higher pitch and smaller width-over-pitch ratios are affected more severely, which is explained by the strong focussing of electrical field lines in these geometries and consequently the favorable conditions for micro discharges. Furthermore, a so-called "turn-on" voltage, at which the occurrence of micro discharges sets in and that depends on the sensor geometry has been identified.

10 Summary & Conclusions

In the previous chapters different results from very different measurements that have been used to qualify the performance of silicon-strip detectors and their operational parameters have been presented. In addition, an overview over the most interesting findings of other collaboration members has been given.

In this chapter a short summary will be given and the conclusions drawn from the presented results will be related to other aspects described in chapter 9. Special attention will be paid to the implications of these results for the binary readout system that is currently developed for the future tracker and finally a material recommendation, taking all aspects into account, will be given.

10.1 Summary of the Presented Study

This thesis presents a set of different measurements and results obtained in the framework and on sensors of the so-called HPK project introduced in chapter 5. The scope of this project is to do extensive research and development work on different silicon substrates and sensor technologies to find a combination of these two that will be able to fulfill the extremely challenging requirements imposed by the High-Luminosity LHC scenario in terms of radiation tolerance and granularity as described in chapters 1 and 3.

For that reason, a wafer containing different sensors and test structures was purchased from one single vendor with exactly the same layout and design but made of different silicon substrates of different thicknesses and produced in different technologies. The available thicknesses range from 50 to 320 micrometers but for this study only the thicker devices of 200 and 300 micrometer have been investigated. The available materials are oxygen-rich standard float-zone silicon, deep-diffused float-zone material with reduced active volume, physically-thinned float-zone silicon and magnetic-Czochralski silicon — each available in two different polarities and with two strip-isolation mechanisms for the p-bulk samples — yielding a total of three different technologies per material.

From these wafers, a structure called Multi-Geometry Silicon-Strip Detector or MSSD with twelve regions, featuring strip pitches of 70, 80, 120 and 240 micrometer and three width-over-pitch ratios from 0.15 to 0.35, has been investigated in the course of the work leading to this thesis. The MSSD sensor was designed to study the implications of different strip geometries on the electrical properties and operational parameters of a sensor and the performance of these geometries.

Due to the conditions in the HL-LHC scenario and the requirements for the new sensors in terms of granularity and physics performance, their possible strip pitch is constrained to values around 90 micrometer according to simulations [65]. For that specific reason and in order to restrict the huge parameter space given by the different materials, technologies and geometries on the MSSD, the focus is put on regions of the latter, with a strip pitch of 80 micrometer, as this value is closest to the requirements.

Three different, but closely interlinked aspects of sensor qualification are presented in this work. The electrical qualification, presented in chapter 6, especially with respect to the depletion voltage and strip capacitance of different geometries, yields important information on operating parameters that are crucial for the design of the front-end electronics and the sensor operation. Furthermore, it provides the means of verifying a model that allows for making predictions on the parameters of other geometries than the tested ones, which can be used to tailor the future sensors according to the needs in the experiment.

The second aspect is the investigation of the response of a sensor to a particle beam and the properties that can only be accessed in a beam test, like the resolution, hit-detection efficiency, signal and noise. A dedicated analysis of the recorded data is shown in chapter 7. Finally, a binary readout system is simulated in chapter 8, using analog data recorded in the beam tests, to predict the performance with the new CMS binary chip that is currently being developed.

10.2 Conclusions from the Electrical Qualification

The electrical parameters measured on the MSSD are the leakage current, the detector depletion-layer capacitance or backplane capacitance and the interstrip capacitance. From the second, the depletion voltage can be extracted and the combination of the last two measurements yields results on the total strip capacitance, which is an important parameter that determines the detector noise and thus influences the design of the readout electronics. Since the MSSD features regions with three different width-over-pitch ratios and four different pitches, a parametrization of the geometry can be applied, which allows for modelling the above parameters as a function of the strip geometry and extrapolating properties to other geometries.

Depletion Voltage

The ratio of the depletion voltage of a strip sensor to the depletion voltage of a planar diode can be parametrized as a function of the geometry, which is introduced in section 6.1.2, equation 6.4. The parametrization is derived from a semi-analytical solution of the Poisson equation [54]. The parameters of this solution yield a dependence on the strip pitch, the width-over-pitch ratio and the thickness that reads $p/df(w/p)$ with $f(w/p)$ from equation 6.6. The dependence of equation 6.4 can be reduced to $1 + 2 p/d f(w/p)$

if both sides of the equation are divided by the intercept, which is the depletion voltage of a planar diode.

One of the initial goals of the study with the MSSD was to find out if this relation, which was confirmed in studies carried out at the time when the sensors for the present tracker were designed [51], [52], also holds true for p-bulk devices and thin detectors. The results presented in chapter 6, section 6.3 confirm this parametrization with even better accuracy than in the original studies. The results are summarized in figure 6.14 and indicate that, except for some outliers, the normalized slope of the parametrization is very close to two.

After irradiation the presented model breaks down, as the assumptions made in terms of depletion behavior do not hold true any more, because the situation in a heavily irradiated sensor is more complex. The fit intercept is still a valid estimate for the depletion voltage of a planar diode and the dependence on the geometrical parameter $p/df(w/p)$ is still linear but the slope is close to zero. In order to understand this fully, further studies and extensive simulations would be necessary, which is beyond the scope of this thesis.

Strip Capacitance

A similar parametrization as in the previous section can be applied to the backplane capacitance (equations 6.5 and 6.9), which is proportional to the depletion voltage. The total capacitance of one strip is constant as a function of $p/(d + p f(w/p))$. This applies because the decrease of the interstrip capacitance with this parameter is exactly compensated by the increase of the backplane capacitance. Figure 6.15 confirms this behavior and furthermore indicates that the total strip capacitance, which determines the noise of the sensor with the short peaking times in the LHC environment, only depends on the width-over-pitch ratio (figure 6.17) and not on the selected doping scheme (figure 6.16). This allows for tuning the strip capacitance according to the requirements for the readout chip or vice versa.

Geometries with higher width-over-pitch ratios have the advantage of collecting more charge if the sensor is not fully depleted, but they also have higher capacitance and thus noise. On the other hand, small width-over-pitch ratios yield lower noise but the high-voltage stability is worse, resulting in lower breakdown voltages. This is understandable, as the electric field lines are more focussed in the vicinity of smaller electrodes, which favors discharges.

Both of the findings mentioned above make it possible to take the results obtained within the HPK project and apply them to the next prototype sensors and tailor them to the requirements in the future tracker with the binary readout system.

10.3 Conclusions from the Beam-Test Results

The analysis of beam test data has yielded some very interesting findings with respect to the performance of the tested MSSD detectors before and after irradiation.

Signal and Noise

One of the major goals has been to measure the absolute signal that can be extracted from the different materials and doping schemes before and after irradiation. Before irradiation, all tested materials perform exactly as expected, with signals that match the charge that one would expect. No doping scheme is favorable and the signal scales with the measured active thickness of the devices.

After irradiation to an intermediate fluence, which corresponds to the fraction of pure proton- or pure neutron irradiation at a radius of 40 cm from the beam axis in the future CMS tracker (3.5×10^{14} 1MeV n_{eq} cm^{-2} protons or 4×10^{14} 1MeV n_{eq} cm^{-2} neutrons), the signal also scales with thickness but the amplitude is reduced by $\sim 20\%$ due to radiation-induced defects.

After the highest fluence of 1.5×10^{15} 1MeV n_{eq} cm^{-2} (1.0×10^{15} protons and 0.5×10^{15} neutrons), which corresponds to the total fluence at a radius of 20 cm, the signal becomes almost independent of the thickness. At the tested voltages, sensors with an active thickness of 200 micrometer perform almost as well as thick ones, due to the increased trapping in the thick devices. Furthermore, the bias voltages were not high enough to deplete 320 micrometer-thick sensors after this fluence, which leads to signal loss due to underdepletion.

When comparing all thin materials and all doping schemes, the difference in absolute (track-induced) signal of both polarities (n- and p-bulk) is negligible but when the noise is factored in, it becomes clear that a non-negligible fraction of the measured signal on the n-bulk devices originates from noise. This difference is even more important when a clustering procedure is used instead of the signal at the calculated impact point of the track, as the clustering would either not find all signal strips or include a large fraction of fake hits caused by noise, depending on the selected clustering threshold.

Overall, p-bulk magnetic-Czochralski sensors have the highest signal after irradiation, although they are thinner than the deep-diffused float-zone devices. This can be explained with the very high oxygen concentration that has been found and is mentioned in chapter 9, section 9.1.

Measurements of the charge-collection efficiency in the laboratory (section 9.2) indicate that irradiated thick sensors show similar or even better performance than thin ones at very high voltages but as it is absolutely vital to reduce the material budget of the tracker and keep the power to be dissipated low, thin sensors that have comparable signal at lower voltages are favorable and the required voltage increase to get the same signal as from a thick detector outweighs the current increase by the added volume, as shown in

section 7.3. The power dissipation actually has a direct impact on the material budget, as thicker sensors generate more current and thus power, which in turn requires a more capable cooling system, which again adds material.

Resolution and Efficiency

The performed analysis has shown that the resolution of the tested detectors is better than the binary limit given by the approximation

$$\sigma = \frac{p}{\sqrt{12}} \quad (10.1)$$

if the tracking resolution of the Silicon Beam Telescope is taken into account and subtracted from the RMS of the residual distribution. With increasing irradiation, the interstrip-isolation of p-bulk material deteriorates and thus the average clusterwidth increases due to increased charge sharing between the strips. This implies an improvement of the resolution on such devices after irradiation, which can also be seen in this analysis.

On the other hand, wider clusters with lower signals on the individual strips are problematic for the binary readout system sketched in chapter 8, as the resolution gain is zero for clusters wider than two strips. Furthermore, there are plans to reject wide clusters completely in the future system as they are an indication of a track with low transverse momentum, which is not interesting for physics analysis. For that reason it will be necessary to put further R&D efforts in the isolation of the strips on p-stop and p-spray devices.

The hit detection-efficiency has been found to be almost at 100 % for all detectors for which reliable data is available and no pick-up noise was present. This presence can be seen in the noise occupancy figures presented alongside the efficiency and a clear correlation with the grounding of the hybrid is seen. Irradiated devices, especially n-bulk devices, have lower efficiency due to the increased noise and lower signal, which means that a fraction of tracks is not detected or that fake tracks caused by noisy strips are found.

10.4 Implications for the Binary Readout

A binary readout system was simulated with the analog data recorded in the different beam tests to verify the performance of the sensor materials after irradiation to high fluence with such a system. Studies of the resolution with four binary algorithms, the average clusterwidth, the efficiency and the noise occupancy as a function of the clustering threshold are presented in chapter 8.

The resolution that can be achieved with a binary readout system depends on the selected threshold and the algorithm that is used. As can be seen from the figures and results from section 8.3, a chip design that has a precision of "half-strip" units can greatly improve the resolution by almost ten micron, especially at lower thresholds.

It has been shown that all the investigated detectors work with binary readout. The unirradiated, 200 micrometer-thick, deep-diffused p-bulk detector in figure 8.2 shows very high efficiency over a wide range of thresholds due to the large seed signal and small clusterwidth. For that reason, even at very high thresholds, hits will efficiently be detected, as at least one strip is still above the threshold if a particle has traversed the detector. The noise occupancy, on the other hand, decreases to zero already at low thresholds, which yields a large window of possible thresholds.

After irradiation to the highest fluence of 1.5×10^{14} 1MeV n_{eq} cm^{-2} , however, the results change drastically.

The efficiency quickly drops and the average clusterwidth saturates at values close to one already at very low clustering thresholds (figures 8.3, 8.4 and 8.5), independent of the technology. It is an inherent property of p-bulk detectors that the interstrip isolation decreases with increasing fluence. This behavior has been found and confirmed in strip-scans in the laboratory (section 9.2). The consequences are twofold:

- With decreasing interstrip isolation, the charge that a traversing particle deposits in the detector is spread out over more than one strip, thus resulting in lower seed signal and wider clusters. This has a negative impact on the hit-detection efficiency, as the clustering threshold is soon above the seed charge of some clusters at the low end of the Landau distribution, which are therefore not detected.
- On the other hand, a clusterwidth larger than one is very beneficial for the spatial resolution, especially if the chip design is adapted accordingly. As one of the requirements for the Phase-2 tracker is to provide fast information on the transverse momentum of tracks for the trigger decision, clusters wider than two or three strips will be discarded by the chip as they indicate tracks with low p_T .

The noise occupancy on these irradiated devices also decreases to values in the percent range at low thresholds but the window of feasible thresholds before the efficiency also starts to decrease is significantly smaller. As a consequence, the final threshold that is used at any given fluence state of the sensors will have to be adapted such that a balance is found between resolution, hit-detection efficiency and noise occupancy.

10.5 Recommendation

The results presented in this thesis and the findings of other collaboration members presented in chapter 9 make it possible to draw valid conclusions about the performance of different silicon substrates and sensor polarities.

A single polarity of sensors for all parts of the future tracker seems a sensible choice, since it allows for concentrating the R&D effort and facilitates the design of the readout chips and the possible vendors can focus on a single production process, which can therefore be optimized, resulting in higher yield and lower cost.

P-bulk sensors have been found to be robust at high voltage and to have higher signal and lower noise at intermediate voltages after irradiation to high fluences. Interstrip isolation, although decreasing with increasing fluence, is also sufficient for operation at the expected fluence levels, whereas the impact of the increased Lorentz angle for the resolution with a binary readout has to be investigated further.

On the other hand, all n-bulk detectors show random ghost hits after irradiation over a wide range of bias voltages and annealing times, with thinned detectors and lower width-over-pitch ratios affected more severely. This is explained by the increased focussing of field lines beneath the implants, resulting in conditions that favor micro-discharges. Furthermore, simulations yield a higher intrinsic electrical field in irradiated n-bulk detectors.

Taking all these considerations and the results presented in this thesis into account, sensors made from p-doped, thinned silicon are the most sensible choice for the application in the future tracker. Although further beam test studies of the available, physically-thinned detectors, especially after irradiation, will be necessary, the results obtained in laboratory tests and on diodes yield a very good performance of these devices. One of the main goals of the upgrade is to reduce the material budget of the tracker and thin sensors benefit this by actually reducing the material and also by the lower power consumption and thus heat that needs to be dissipated.

While magnetic-Czochralski substrates have a very high oxygen concentration, they are also very expensive to manufacture and thus physically-thinned float-zone silicon seems favorable from the financial point of view.

In terms of the strip-isolation mechanism, p-stop technology shows better stability and breakdown behavior at high voltage, especially before irradiation. Furthermore, the shape of the electrical field and the properties are tunable by adjusting the geometry of the implant and the doping concentration, while the p-spray technology only allows for modification of the doping concentration.

The width-over-pitch ratio makes it possible to adapt the strip capacitance and electrical properties according to the desired application. Given all findings from chapters 6 and 7, an intermediate w/p value around 0.25 seems the most obvious and sensible choice, as it is a good balance between signal-, noise- and breakdown performance, while the resolution is not affected.

For all these reasons, a physically thin, p-bulk, p-stop sensor with parameters optimized for small clusterwidths and with improved interstrip isolation for the binary readout system is the best candidate for the application in the future tracker. Further prototype runs will be necessary to tailor the sensor to the final requirements, but in terms of the substrate and the strip-isolation mechanism, the conclusions from this study clearly point towards this material and technology.

Appendix: Detailed Results

Given the vast amount of recorded data and analysis results, an electronic appendix, containing the individual analysis results for every tested detector and the results not mentioned in this thesis, is available.

It contains the following additional figures from the electrical qualification described in chapter 6:

- Leakage Current at $V_{fd} \times 1.2$ for all tested detectors.
- Breakdown voltage for the tested detectors
- Backplane capacitance as a function of the pitch
- Interstrip capacitance as a function of the pitch

Furthermore, the low level plots and intermediate analysis results for every detector that was tested in the various beam tests (chapter 7) are available. These figures include:

- Alignment results
- Average clusterwidth for every region
- Map of not detected tracks
- Parameters of not detected tracks
- Efficiency and noise occupancy figures for every region
- Noise profile
- Average noise of every region
- Track induced signal
- Residual distribution and resolution of all regions
- ROOT file with all plots

The mentioned figures can be found at: gauzinge.web.cern.ch/PhD_Data

References

- [1] Fabiola Gianotti. Physics during the first two years of the LHC. *New Journal of Physics*, 9, 2007.
- [2] LHCb Collaboration. First evidence of the $B_S^0 \rightarrow \mu^+ \mu^-$ decay. *arXiv:1211.2674*, Nov 2012.
- [3] The LHCb Public Page: <http://lhcb-public.web.cern.ch/lhcb-public/Welcome.html>, Nov. 2012.
- [4] Andreas Schopper. Flavour Physics and CP Violation at LHC. *arXiv:hep-ex/0605113*, May 2006.
- [5] Oliver Brüning; Paul Collier; Paul Lebrun; Stephen Myers; Ranko Ostojic; John Poole; Paul Proudlock. *LHC Design Report*. CERN, 2004.
- [6] Lyndon Evans. The Large Hadron Collider. *New Journal of Physics*, 9(335), 2007.
- [7] The High Luminosity LHC Project webpage: <http://hilumilhc.web.cern.ch/HiLumiLHC/index.html>, 2013.
- [8] Lucio Rossi. Lhc upgrade plans: LHC Upgrade Plans: Options and Strategy. Talk at the IPAC 2011, San Sebastian, Spain, September 2011.
- [9] Oliver S. Brüning. HL-LHC Parameter Space and Scenarios. *Proceedings of Chamonix 2012 workshop on LHC Performance*, 2012.
- [10] Julien Baglio; Abdelhak Djouadi. Higgs production at the LHC. *JHEP*, 03(055), 2011.
- [11] The CMS Collaboration. Observation of a new boson at a mass of 125GeV with the CMS experiment at the LHC. *Phys. Lett. B*, 2012.
- [12] Alex Tapper for the CMS Collaboration. Searches for Supersymmetry with the CMS detector at the LHC. In *Proceedings of the CIPANP 2012*, 2012.
- [13] The CMS Collaboration. CMS Physics Technical Design Report Volume I: Detector Performance and Software. *CMS-doc-3449-v1*, 2006.
- [14] The CMS public web page: <http://cms.web.cern.ch/>.
- [15] The CMS Collaboration. The Hadron Calorimeter Technical Design Report. *CERN-LHCC-97-031 ; CMS-TDR-2*, 1997.

- [16] The CMS Collaboration. The Muon Project Technical Design Report. *CERN-LHCC-97-032 ; CMS-TDR-3*, 1997.
- [17] The CMS Collaboration. Technical Proposal for the Upgrade of the CMS Detector through 2020. *CERN-LHCC-2011-006 ; CMS-UG-TP-1 ; LHCC-P-004*, 2012.
- [18] Wolfgang Erdmann. The CMS pixel detector. *International Journal of Modern Physics A*, 25(7), 3 2010.
- [19] H. C. Kastli et al. Design and performance of the CMS pixel detector readout chip. *Nuclear Instruments and Methods A*, 565:188–194, 2006.
- [20] The CMS Collaboration. The Tracker Project Technical Design Report. *CERN-LHCC-98-006 ; CMS-TDR-5*, 1998.
- [21] The CMS Collaboration. Addendum to the CMS Tracker TDR. *CERN/LHCC 2000-016*, 2000.
- [22] Frank Hartmann. Silicon tracking detectors in high-energy physics. *Nuclear Instruments and Methods A*, 666:25–46, 2012.
- [23] Mark Raymond et al. Design and Results from the APV25, a Deep Sub-micron CMOS Front-End Chip for the CMS Tracker. *Nuclear Science Symposium Conference Record, 2000 IEEE*, 2:9/113– 9/118 vol.2, 2000.
- [24] The CMS Collaboration. Commissioning and performance of the CMS silicon strip tracker with cosmic ray muons. *JINST*, 5, March 2010.
- [25] M. Pesaresi. *The CMS Tracker: Front End Readout and Control Systems & DAQ*. PhD thesis, Imperial College London, August 2006.
- [26] The CMS Collaboration. CMS Tracking Performance Results from Early LHC Operation. *European Physics Journal*, C(70):1165–1192, 2010.
- [27] S. Mersi. CMS Silicon Tracker upgrade for HL-LHC. *Proceedings of the 10th International Conference on Large Scale Applications and Radiation Hardness of Semiconductor Detectors (RD11), Proceedings of Science*, CMS CR -2012/137, 2012.
- [28] S. Mersi et al. CMS Tracker Layout Studies for HL-LHC. *Physics Procedia*, 37:1070–1078, 2012.
- [29] Frank Hartmann. *Evolution of silicon sensor technology in particle physics*. Springer tracts in modern physics. Springer, Berlin, 2009.
- [30] Renate Wunstorf. *Systematische Untersuchungen zur Strahlenresistenz von Silizium Detektoren fuer die Verwendung in Hochenergiephysik-Experimenten*. PhD thesis, University of Hamburg, DESY, 1992.
- [31] Michael Moll. *Radiation Damage in Silicon Particle Detectors*. PhD thesis, University of Hamburg, DESY, 1999.
- [32] M. Huhtinen. Simulation of Non-Ionising Energy Loss and Defect Formation in

- Silicon. *Nuclear Instruments and Methods A*, A491:194–215, 2002.
- [33] G. Lindstroem. Radiation Damage in Silicon Detectors. *Nuclear Instruments and Methods A*, 512(30), 2003.
- [34] J. Stahl, E. Fretwurst, G. Lindstroem, and I. Pintilie. Radiation hardness of silicon - a challenge for defect engineering. *Physica B: Condensed Matter*, 340-342(0):705–709, 2003.
- [35] Z. Li et al. Radiation hard detectors from silicon enriched with both oxygen and thermal donors: improvements in donor removal and long-term stability with regard to neutron irradiation. *NIM A*, (476):628–638, 2002.
- [36] L. Fonseca et al. Silicon wafer oxygenation from SiO_2 layers for radiation hard detectors. *Microelectronics Reliability*, 40:791–794, 2000.
- [37] J. Härkönen et al. Radiation hardness of Czochralski silicon, Float Zone silicon and oxygenated Float Zone silicon studied by low energy protons. *Nuclear Instruments and Methods A*, (518):346–348, 2004.
- [38] Z. Li et al. Radiation Hardness of High Resistivity Magnetic Czochralski Silicon Detectors After Gamma, Neutron and Proton Radiations. *IEEE Trans.Nucl.Sci.*, 51(4), 2004.
- [39] G. Kramberger et al. Superior radiation tolerance of thin epitaxial silicon detectors. *Nuclear Instruments and Methods A*, (515):665–670, 2003.
- [40] Z. Li et al. Investigation of epitaxial silicon layers as a material for radiation hardened silicon detectors. *Nuclear Science Symposium, 1997. IEEE*, 1:46–50, 1997.
- [41] H. Hoedlmoser et al. Characterization of thick epitaxial silicon detectors from different producers after proton irradiation. *Nuclear Instruments and Methods A*, 580(3):1243–1249, 2007.
- [42] The RD50 Collaboration. RD50 Status Report 2008. CERN-LHCC-2010-012, 2010.
- [43] K. H. Hoffmann on Behalf of the CMS Tracker Collaboration. Campaign to identify the future CMS tracker baseline. *Nuclear Instruments and Methods A*, 658(1):30–35, 12 2011.
- [44] J. Erfle. Silicon Sensor Developments for the CMS Tracker Upgrade. *Proceedings of the 10th International Conference on Large Scale Applications and Radiation Hardness of Semiconductor Detectors (RD11), Proceedings of Science*, [PoS(RD11)020], 2011.
- [45] A. Dierlamm. Characterization of silicon sensor materials and designs for the CMS Tracker Upgrade. *Proceedings of Science, Vertex 2012*, 2012.
- [46] S. Müller. *The Beam Condition Monitor 2 and the Radiation Environment of the CMS Detector at the LHC*. PhD thesis, CERN, CERN-THESIS-2010-175, CMS-TS-2010-42, 2010.

- [47] Irradiation Center Karlsruhe. http://www.ekp.kit.edu/english/irradiation_center.php.
- [48] Ljubljana Irradiation Facility. <http://www-f9.ijs.si/~mandic/ReacSetup.html>.
- [49] A. Junkes. Planar silicon sensors for the CMS tracker upgrade. *submitted to NIM A, Proceedings of the 14th VCI*, 2013.
- [50] G. Steinbrück. Towards Radiation Hard Sensor Materials for the CMS Tracker Upgrade. *submitted to proceedings of IEEE-NSS-MIC-RTDS2012*, 2013.
- [51] N. Demaria et al. New results on silicon microstrip detectors of {CMS} tracker. *Nuclear Instruments and Methods A*, 447(1–2):142 – 150, 2000.
- [52] S. Albergo et al. Optimization of the silicon sensors for the {CMS} tracker. *Nuclear Instruments and Methods A*, 466(2):300 – 307, 2001. 4th Int. Symp. on Development and Application of Semiconductor Tracking Detectors.
- [53] S. Braibant et al. Investigation of design parameters and choice of substrate resistivity and crystal orientation for the CMS silicon microstrip detector. *CMS Note*, (011), 2000.
- [54] J.Rahn. Depletion Characteristics of Silicon Microstrip Detectors. SCIPP 93/12, October 1993.
- [55] E. Barberis et al. Capacitances in silicon microstrip detectors. *Nuclear Instruments and Methods A*, (342):90–95, 1994.
- [56] M. Pernicka, T. Bauer, and M. Friedl. Vienna Cooling Box. http://www.hephy.at/project/electronic2/ELEC2/direct_CB.html, 01 2002.
- [57] T. Maenpaa et al. Silicon beam telescope for LHC upgrade tests. *Nuclear Instruments and Methods A*, A593:523–529, 2008.
- [58] C. Johnstone. Experimental, test and research beamlines at Fermilab. *Proceedings of EPAC 2006*, 2006.
- [59] CERN. Introduction to the use of the H2 beam. <http://sba.web.cern.ch/sba/BeamsAndAreas/resultbeam.asp?beamline=H2>.
- [60] Eutelescope webpage. <http://eutelescope.web.cern.ch/>.
- [61] A. Bulgheroni, T. Klimovich, P. Roloff, and A.F. Zarnecki. EU Telescope: tracking software. *EUDET Memo*, 20, 2007.
- [62] I. Rubinskiy. EU Telescope. Offline track reconstruction and DUT analysis software. *EUDET Memo*, 12, 2010.
- [63] Ilcsoft webpage. <http://ilcsoft.desy.de/portal>.
- [64] R. Brun and F. Rademakers. ROOT- An Object Orientated Data Analysis Framework. *Nuclear Instruments and Methods A*, A389(81), 1997.
- [65] S. Mersi et al. Software package for the characterization of Tracker layouts. *Pro-*

ceedings of the 13th ICATPP Conference, CMS-CR-2011-261, 2011.

- [66] M. Prinz on Behalf of the CMS Tracker Collaboration. Radiation Hard Sensor Materials for the CMS Tracker Upgrade, The CMS HPK Campaign. Talk at the 9th International Hiroshima Symposium, Japan, Sept. 2nd 2013.

Georg Auzinger

✉ georg.auzinger@gmail.com

Education

- 2010 – 2013 **PhD**, *Vienna University of Technology & CERN*, Geneva, *PhD*
Austrian Doctoral Student Programme at CERN
- 2003 – 2010 **Master of Science / Diplomingenieur in Physics**, *Vienna University of Technology*, Vienna, *MSc*
with Distinction
- 1994 – 2002 **High School Diploma**, *Bundesrealgymnasium Krems*, Krems
Matura / Reifeprüfung

Military Service

- 2002 / 2003 obligatory military service in the Austrian Army

PhD Thesis

- title *Silicon Sensor Development for the CMS Tracker Upgrade*
- supervisors Univ. Doz. Dr. Manfred Krammer & Dr. Anna Elliott-Peisert
- description Detailed evaluation and study of prototype R&D silicon sensors for the upgrade of the CMS Tracker in the High Luminosity LHC era in terms of geometry and radiation tolerance

Master Thesis

- title *Design of a Cooling Device for the Characterization of Irradiated Silicon Sensors*
- supervisors Univ.-Doz. DI Dr. Manfred Krammer
- description Design and construction of a temperature-controlled, peltier-cooled cold-chuck structure for the qualification of irradiated silicon sensors for high energy physics applications